MASARYK
UNIVERSITY

Investigating the Physics of Hot Galactic Atmospheres

Doctoral Thesis

Mgr. Tomáš Plšek

Faculty of Science
Department of Theoretical Physics and Astrophysics

Supervisor: prof. Mgr. Norbert Werner, Ph.D. **Brno 2026**

Bibliographic Entry

Author:	Mgr. Tomáš Plšek
Title of Thesis:	Investigating the Physics of Hot Galactic Atmospheres
Degree Programme:	Physics Faculty of Science, Masaryk University Department of Theoretical Physics and Astrophysics
Supervisor:	prof. Mgr. Norbert Werner, Ph.D.
Academic Year:	2025/2026
Number of Pages:	xi + 158
Keywords:	AGN feedback; X-ray cavities; hot atmospheres; giant ellipticals; galaxy clusters; chemical enrichment

Abstract

The thesis investigates hot X-ray-emitting atmospheres in massive early-type galaxies and galaxy clusters, with a focus on radio-mechanical AGN feedback and chemical enrichment. Using X-ray spectroscopy, X-ray and radio imaging, and machine-learning methods, the work examines how hot atmospheres feed central black holes, how measurements of jet powers from X-ray cavities can be automated, and how AGN feedback, ram-pressure stripping, and multiphase structure shape the observed distribution of metals.

The first part of the thesis studies the relation between accretion and jet production in nearby early-type galaxies. A strong correlation is found between supermassive black hole mass and mechanical jet power in galaxies with thermally unstable atmospheres, indicating that the thermodynamic state of the hot gas plays an important role in regulating AGN feedback. To further support such studies, a new machine-learning pipeline, CADET, has been developed for the detection and size estimation of X-ray cavities. This tool provides a more systematic and reproducible approach to identifying X-ray cavities and has the potential to automate and improve cavity-based measurements of jet energetics across large samples of galaxies and clusters.

The second part focuses on the chemical composition of hot atmospheres. In the infalling elliptical galaxy M89, the hot gas is found to have super-Solar abundance ratios relative to iron, suggesting that AGN activity and ram-pressure stripping may have helped remove the original atmosphere and replace it with fresh stellar mass-loss material. In the Centaurus cluster, the classical deep central Fe abundance drop is shown to be strongly reduced when the core is modelled with deprojected multi-temperature plasma models and current atomic data, although a weaker residual drop remains. Overall, the thesis shows that AGN feedback, thermal instability, ram-pressure stripping, and metal transport are closely linked processes, and that their interpretation requires both physically motivated models and careful treatment of observational biases.

List of annexed publications

The thesis is based on four publications authored or co-authored by me, Mgr. Tomáš Plšek (TP).

Annex 1: *The relation between accretion rate and jet power in early-type galaxies with thermally unstable hot atmospheres*, **Plšek T.**, Werner N., Grossová R., Topinka M., Simionescu A., Allen S. W., 2022, MNRAS.

As the first author, TP carried out the data analysis and wrote most of the manuscript. The radio data were pre-processed by R. Grossová.

Annex 2: *CAvity DEtection Tool (CADET): pipeline for detection of X-ray cavities in hot galactic and cluster atmospheres*, **Plšek T.**, Werner N., Topinka M., Simionescu A., 2023, MNRAS.

As the first author, TP prepared the training dataset, trained and tested the network, applied it to real data, and wrote most of the manuscript.

Annex 3: *The infalling elliptical galaxy M89: the chemical composition of the AGN disturbed hot atmosphere*, Kara S., **Plšek T.**, Protušová K., Breuer J.P., Werner N., Mernier F., Ercan E.N., 2024, MNRAS.

As the second author, TP pre-processed the *Chandra* data, developed the spectral fitting scheme needed to account for background and foreground contamination of the source signal, and significantly contributed to writing of the manuscript and preparing the figures.

Annex 4: *Missing metals in the central parts of the Centaurus cluster's ICM*, **Plšek T.**, Werner N., Mernier F., Simionescu A., Majumder A., Štofanová L., in preparation.

Except for the preprocessing and spectral extraction of the *XMM-Newton* data, performed by F. Mernier, TP carried out all data analysis and spectral fitting, and prepared most of the manuscript and figures.

Contents

Introduction

Massive elliptical galaxies, galaxy groups, and galaxy clusters span a wide range in mass and physical size, yet they share an important common feature – they are embedded in extended atmospheres of hot, diffuse gas. With characteristic temperatures of about ten million Kelvin, this plasma represents a major baryonic component of massive haloes and provides the medium in which many of the key processes shaping these systems take place, including radiative cooling, accretion onto the central supermassive black hole, AGN feedback, and chemical enrichment (Werner and Mernier, 2020). Although galaxies, groups, and clusters are often studied separately, their hot atmospheres are governed by the same basic interplay between gravity, gas cooling, and energy injection from the central galaxy, specifically its active galactic nucleus (AGN). For this reason, hot atmospheres provide a natural framework for studying the evolution of massive haloes from galaxy to cluster scales.

Hot atmospheres are not static, but continuously lose energy through X-ray radiation. In the central regions of many massive systems, where the gas density is highest, the radiative cooling time becomes sufficiently short ($\sim 10^7$ yrs), and the gas is expected to cool out of the X-ray phase, giving rise to the classical cooling-flow picture (Fabian, 1994). Without a sufficient heat source to balance it, this cooling would lead to substantial accumulations of cold gas and, eventually, to relatively high star formation rates. Nonetheless, the measured star formation rates in giant ellipticals are rather low, and their stellar populations are predominantly composed of old stellar populations – these systems are often described as 'red and dead'. High-resolution grating X-ray spectra obtained with *XMM–Newton*/RGS later showed that the amount of gas cooling out of the X-ray phase is also much smaller than predicted by simple cooling-flow models, establishing what is now commonly referred to as the cooling-flow problem (Peterson and Fabian, 2006).

The currently favoured solution to the cooling-flow problem is heating by AGN feedback. In massive elliptical galaxies and in the central galaxies of groups and clusters, the dominant AGN mode is typically radio-mechanical rather than radiative. In this mode, relativistic jets inflate radio lobes and displace the surrounding X-ray-emitting gas, producing cavities, shocks, and other disturbances in the hot atmosphere (McNamara and Nulsen, 2007; Fabian, 2012). Owing to its high spatial resolution, *Chandra* has been crucial for identifying these structures and for estimating the mechanical power of AGN outbursts from the properties of X-ray cavities (e.g., Birzan et al., 2004). Such estimates show that the enthalpy of the cavities is often sufficient to offset the radiative cooling losses. However, the exact channels by which this energy is dissipated and distributed through the atmosphere are still not fully understood. Candidate processes include shocks, sound waves, and turbulence driven by the inflation and buoyant rise of cavities. More recently, XRISM has begun providing the first direct measurements of gas motions in hot atmospheres (Xrism Collaboration, 2025; Zhang et al., 2026), opening a new way to study how AGN-injected energy is redistributed throughout the surrounding medium.

Another key question is how the central supermassive black holes in these systems are fuelled. Proposed fuelling channels range from hot-mode accretion from the ambient atmosphere to accretion of cooler gas produced by thermally unstable cooling and multiphase condensation (Bondi, 1952; Allen et al., 2006; McNamara and Nulsen, 2012). In many central galaxies, cooler gas phases traced by Hα

emission and by molecular gas detected in CO are closely associated with AGN activity, and recent work suggests that these tracers may be more directly linked to SMBH fuelling than the mere presence of cooling X-ray gas (Lakhchaura et al., 2018; Ubertosi et al., 2025). The picture gets even more complicated, since the inflation and buoyant uplift of X-ray cavities can not only offset cooling of the hot atmosphere but can also further influence this cycle by uplifting low-entropy gas from the centre to larger radii, where it may cool more efficiently and condense into colder phases (Churazov et al., 2001; McNamara and Nulsen, 2007; Fabian, 2012). The relation between cooling, condensation, uplift, and accretion is therefore an important part of the AGN feedback cycle in hot atmospheres.

Besides their thermodynamic structure, hot atmospheres also carry information about their chemical history and that of their hosts. The heavy elements observed in the hot gas were produced by stellar evolution and supernova explosions, primarily by core-collapse and Type Ia supernovae, and were subsequently released and well mixed into the surrounding medium (Mernier and Biffi, 2022). Measurements of elemental abundances and abundance ratios provide an important way to constrain the origin of the gas and the relative contributions of different enrichment channels. Over the past two decades, X-ray observations have shown that the hot atmospheres of ellipticals, groups, and clusters are enriched to a significant level, and that many abundance ratios are remarkably close to Solar (Mernier et al., 2016; de Plaa et al., 2017; Simionescu et al., 2019). The chemical composition of the hot gas is thus not only a record of stellar nucleosynthesis, but also of the processes that mixed, transported, and redistributed the metals throughout the atmosphere.

This redistribution is reflected in the radial metallicity profiles of hot atmospheres. In ellipticals, groups, and clusters, these profiles often show centrally peaked metal distributions, indicating that enrichment is closely linked to the central galaxy and to the subsequent transport of metals through the surrounding gas (Mernier et al., 2017). In a significant fraction of systems, however, the metallicity does not continue to rise to the centre, but instead shows an apparent central drop (Panagoulia et al., 2015; Mernier et al., 2017). Such features are particularly interesting because they suggest that the observed metal distribution is shaped not only by the sites of enrichment, but also by the complex interplay of gas dynamics and observational or modelling effects. Processes such as AGN uplift, mixing, sloshing, stripping, dust depletion, and resonance scattering have all been proposed as possible contributors. Spatially resolved abundance measurements with *Chandra* and *XMM–Newton* therefore provide an important tool for understanding how metals are redistributed within hot atmospheres and how these processes connect to the broader feedback cycle.

This thesis studies the physics of hot galactic atmospheres from multiple perspectives. In the following sections of this introductory chapter, I first summarise the basic properties of the gas and the main observational diagnostics used to study its thermodynamic and chemical structure. I then introduce the physical processes central to this thesis: radiative cooling, AGN feedback, the fuelling of the central supermassive black hole, and the enrichment and redistribution of heavy elements in hot atmospheres. The main body of the thesis is composed of individual publications that focus on radio-mechanical AGN feedback in nearby systems (Annex 1), X-ray cavities and their automated detection (Annex 2), and the chemical enrichment of the hot atmosphere of galaxy M89 (Annex 3), including radial metallicity structure and central abundance drop in the Centaurus cluster (Annex 4).

Hot atmospheres of galaxies and clusters

The hot gas associated with massive haloes is referred to by different names depending on the scale of the system. In massive elliptical galaxies, it is usually described as the hot interstellar medium (ISM) or circumgalactic medium (CGM), in galaxy groups as the intragroup medium (IGrM), and in galaxy clusters as the intracluster medium (ICM). Despite this difference in terminology, the underlying physical picture is the same: these systems are embedded in extended atmospheres of hot diffuse plasma whose thermal,

Figure 1: Composite images of a galaxy group NGC 5813 (*left*) and nearby galaxy cluster Abell 2261 (*right*) showing the extent of thermal X-ray emission (purple) overlaid on the optical image showing individual group/cluster galaxies (NGC 5813 credit: X-ray: NASA/CXC/SAO/Randall et al., 2015, optical: SDSS; Abell 2261 credit: X-ray: NASA/CXC/Univ of Michigan/Gültekin et al., 2021; Optical: NASA/STScI and NAOJ/Subaru).

dynamical, and chemical properties are shaped by the depth of the gravitational potential and by the balance between cooling and heating processes (Mathews and Brighenti, 2003; Werner and Mernier, 2020). In the following sections, I will use the term *hot atmosphere* as a generic description for this hot diffuse gas across all three environments.

The characteristic temperature of this plasma ranges from about 10^6 K in massive galaxies to about 10^8 K in the most massive clusters, with more massive haloes generally hosting hotter atmospheres, as expected from the increasing depth of the gravitational potential well (Sarazin, 1986; Voit, 2005). The atmosphere generally extends far beyond the stellar body of the central galaxy (see Figure 1) and, particularly in groups and clusters, contains a large fraction of the baryons associated with the halo (Mulchaey, 2000; Böhringer and Werner, 2010). Because of its large scale and long dynamical time-scales, the gas can often be treated, to first approximation, as a quasi-hydrostatic medium. In sufficiently relaxed systems, the atmosphere is close to hydrostatic equilibrium, and its radial structure provides a record of how the gas has settled within the halo and how it has subsequently been modified by radiative losses, AGN activity, mergers, and gas motions. In many systems, however, this approximate equilibrium is perturbed by processes such as mergers, sloshing, turbulence, and AGN-driven disturbances (Markevitch and Vikhlinin, 2007; Ettori et al., 2013).

The physical state of the gas is described primarily by its density, temperature, and pressure, linked by the ideal gas law $P = nkT$. In relatively relaxed systems, these quantities vary smoothly with radius, with the density generally decreasing outwards and the temperature structure depending on both halo mass and the thermodynamic history of the gas. Although density and temperature are the most directly measured quantities, it is often more useful to interpret hot atmospheres in terms of derived quantities, such as pseudo-entropy and cooling time, which more directly trace the plasma's thermodynamic evolution.

X-ray diagnostics of hot atmospheres

The existence of extended hot atmospheres was first established through the discovery of diffuse X-ray emission associated with massive haloes (e.g. Gursky et al., 1971; Kellogg et al., 1971). A decisive step came with the detection of the Fe K-shell emission line in cluster spectra by Mitchell et al. (1976) and Serlemitsos et al. (1977), which firmly established that the emission arises in hot thermal plasma and that the gas contains heavy elements. Subsequent observations demonstrated that similar atmospheres are present not only in galaxy clusters, but also in galaxy groups and massive ellipticals (Mulchaey, 2000; Mathews and Brighenti, 2003). These early results established the basic observational picture that still underpins the field today: the X-ray spectrum of the gas reveals its physical and chemical state, while its spatial distribution traces the structure and dynamics of the atmosphere.

In practice, the most direct physical information comes from X-ray spectroscopy. The spectrum of a hot atmosphere consists of thermal continuum emission together with a large number of emission lines from highly ionised elements. These spectra are usually interpreted with models of an optically thin plasma in collisional ionisation equilibrium (CIE). In current X-ray analysis, widely used implementations of such models include `apec` from AtomDB (Smith et al., 2001; Foster et al., 2012) and `cie` from SPEX (Kaastra et al., 1996). Spectral modelling then allows constraining the gas temperature, emission measure, and elemental abundances, while more sophisticated models can account for multi-temperature structure (`gadem`, `wdem`), or projection effects (`projct`, `clus`).

X-ray imaging provides a complementary spatial view of the atmosphere. Since the emissivity of hot optically thin plasma depends strongly on density, surface-brightness maps are especially sensitive to the projected gas distribution. In relatively relaxed systems, azimuthally averaged profiles are often described with simple empirical models, most commonly the β-model, in which the electron density is written as

$$n_{\rm e}(r) = n_0 \left[1 + \left(\frac{r}{r_{\rm c}}\right)^2\right]^{-3\beta/2}, \tag{1}$$

where n_0 is the central density and $r_{\rm c}$ is a core radius (Cavaliere and Fusco-Femiano, 1976). Although such models are only approximations, they provide a useful reference for identifying deviations from a smooth atmosphere, including asymmetries, cold fronts, stripped tails, shocks, and cavities.

Different X-ray observatories provide complementary diagnostics of hot atmospheres. *Chandra*, with its sub-arcsecond imaging capabilities, has been particularly important for resolving small-scale structures in nearby systems, such as rims, shocks, and X-ray cavities (Weisskopf et al., 2002). *XMM–Newton* complements this with its large effective area and, through the Reflection Grating Spectrometer (RGS), high-resolution soft X-ray spectroscopy that is especially useful for abundance measurements and studies of cooling gas (Jansen et al., 2001; den Herder et al., 2001). More recently, XRISM has opened a new window on hot atmospheres by combining imaging with high-resolution calorimeter spectroscopy, allowing direct measurements of gas kinematics in systems where such motions were previously inferred only indirectly (Xrism Collaboration, 2025; Zhang et al., 2026).

Taken together, these approaches make X-ray observations uniquely powerful for the study of hot atmospheres. Spectroscopy constrains the gas's thermal and chemical state, while imaging reveals its spatial structure and deviations from simple equilibrium models. The same observations using telescopes such as *Chandra* or *XMM-Newton* can therefore be used to investigate both the thermodynamic evolution of the atmosphere and the physical processes that disturb it.

Cooling and cool-cores

Having outlined the main observational diagnostics, I now turn to the thermodynamic state of hot atmospheres. A fundamental property of this gas is that it continuously loses energy through radiation, and because the emissivity of an optically thin plasma depends strongly on density, cooling is most effective

in the dense central regions of massive haloes. For this reason, the thermodynamic structure of the atmosphere is often described in terms of the cooling time and entropy, which are more directly related to the gas's thermal history than density or temperature alone. The cooling time is commonly written as

$$t_{\rm cool} = \frac{3(n_{\rm e} + n_{\rm i})kT}{2n_{\rm e}n_{\rm i}\Lambda(T,Z)}, \tag{2}$$

where $n_{\rm e}$ and $n_{\rm i}$ are the electron and ion number densities, T is the gas temperature, and $\Lambda(T,Z)$ is the cooling function (Sarazin, 1986). Systems with short central cooling times and low central entropies are commonly classified as cool-core systems (Hudson et al., 2010), while entropy itself is usually characterised through the proxy $K = kTn_{\rm e}^{-2/3}$ (Ponman et al., 2003; Voit, 2005). In this form, entropy provides a convenient measure of how strongly the gas has been affected by gravitational collapse, radiative losses, and feedback.

In the classical cooling-flow picture, gas in the centre radiates away energy, loses pressure support, and is gradually replaced by gas flowing in from larger radii (Fabian, 1994). In its simplest isobaric form, the corresponding mass cooling rate can be approximated as

$$\dot{M}_{\rm cool} \approx \frac{2\mu m_{\rm p} L_{\rm X}}{5kT}, \tag{3}$$

where $L_{\rm X}$ is the X-ray luminosity of the cooling gas (Fabian, 1994). Later observations, however, indicated that this simple picture is incomplete. High-resolution grating spectra obtained with *XMM–Newton*/RGS showed that the emission expected from large amounts of gas cooling below about 1–2 keV is much weaker than predicted (Peterson et al., 2001; Peterson and Fabian, 2006). The amount of gas cooling out of the X-ray phase, therefore, appears to be substantially smaller than in the original cooling-flow model, which is the essence of the cooling-flow problem.

A more widely adopted view is that hot atmospheres can remain globally hot while still being locally susceptible to cooling. In this framework, thermally unstable perturbations in low-entropy gas may condense out of the hot phase without requiring a steady cooling flow over a wide temperature range. The tendency of the gas to condense is often discussed in terms of the ratio of the cooling time to the free-fall time, $t_{\rm cool}/t_{\rm ff}$, which has been argued to approach a threshold value of order ten in systems prone to multiphase condensation (Voit and Donahue, 2015). Thermal instability, therefore, provides a more natural framework for understanding how cooler gas can form within an atmosphere that, on average, is still hot. This immediately leads to the question of how such a multiphase structure appears observationally.

Multiphase gas

The multiphase character of cool cores is apparent already within the X-ray-emitting plasma itself. Part of the observed temperature spread is expected from projection, because spectra extracted in annuli inevitably mix emission from different radii along the line of sight. However, deprojected analyses and high-resolution X-ray spectra have shown that, in many systems, the gas in the core is better described by intrinsically multi-temperature models than by a single-temperature plasma. Such descriptions include simple two-temperature models as well as differential emission measure distributions, for example, Gaussian or power-law forms implemented as `gdem` or `wdem` models (Kaastra et al., 2004; de Plaa et al., 2010; Sanders et al., 2010). In this sense, cool cores are often multiphase already within the X-ray-bright phase itself.

At lower temperatures, the multiphase nature of the gas becomes even more evident. Many massive systems host warm ionised gas traced by Hα+[N II] emission (see Figure 2) and cold molecular gas traced by CO. These phases are not distributed randomly, but are closely linked to the thermodynamic state of the surrounding hot atmosphere. In nearby giant ellipticals, line-emitting systems tend to have higher central densities, lower entropies, shorter cooling times, and more disturbed X-ray morphologies than

Figure 2: Mutli-wavelength composite images of galaxy group NGC 5044 (*left*) and Persues galaxy cluster (*right*) showing X-ray emission of the hot atmosphere (*blue*) as well as warm filaments (*red*) visible in Hα+[N II] (NGC 5044 credit: NASA Chandra/Digitised Sky Survey/Southern Observatory for Astrophysical Research/Very Large Array; Perseus cluster credit: NASA, ESA, NRAO and STScI).

systems without detected optical line emission (Lakhchaura et al., 2018). The presence of warm and cold gas is therefore widely interpreted as evidence that cooling, although strongly suppressed relative to the classical picture, still proceeds in a residual and spatially inhomogeneous form.

Radio-mechanical AGN feedback

Among the processes capable of influencing the thermal state of hot atmospheres, AGN feedback appears to be the most important in nearby giant ellipticals and in the central galaxies of groups and clusters. In these systems, the dominant form of activity is usually radio-mechanical rather than radiative (McNamara and Nulsen, 2007; Fabian, 2012; McNamara and Nulsen, 2012). A significant fraction of the energy released by accretion onto the central supermassive black hole is channelled into jets and relativistic outflows, which interact with the surrounding gas on scales far larger than the accretion flow itself. Radio-mechanical feedback is therefore not confined to the nucleus but affects the thermodynamic evolution of the hot atmosphere as a whole.

In the current picture, cooling of the hot atmosphere, fuelling of the central black hole, and the subsequent release of mechanical energy are closely linked. Gas that cools or condenses in the central regions may trigger AGN activity, while the resulting outburst injects energy back into the atmosphere and suppresses further cooling (McNamara and Nulsen, 2012; Gaspari et al., 2012). The main observational signatures of this interaction are radio lobes, X-ray cavities, shocks, sound waves, and gas motions. Taken together, these features indicate that heating, cooling, and accretion are not independent processes, but different aspects of the same feedback cycle.

This cycle is likely to evolve over time rather than remain in a steady state. When feedback is weak or temporarily absent, radiative cooling can lower the central atmosphere's entropy and promote the formation of cooler gas phases. As the central black hole is fuelled, a new AGN outburst can inflate radio lobes and X-ray cavities, drive shocks and gas motions, and heat or redistribute the surrounding

plasma. The atmosphere may then remain in a more weakly cooling or temporarily heated state until cooling again becomes sufficiently important to restart the cycle. In this sense, radio-mechanical AGN feedback is often understood as a sequence of alternating cooling and heating phases, whose details can be studied observationally through the structures it imprints on the hot gas.

Feeding the SMBH

An important part of the feedback cycle is the fuelling of the central supermassive black hole. In the simplest picture, hot gas from the surrounding atmosphere is accreted in a roughly spherical manner, as described by the Bondi model (Bondi, 1952). Although this approximation is highly idealised, it provides a useful first-order estimate, and Bondi accretion rates inferred from X-ray data have been shown to correlate with jet power in samples of nearby X-ray-bright ellipticals (Allen et al., 2006). At the same time, many systems also contain substantial multiphase gas in their central regions, which suggests that hot accretion alone is unlikely to provide a complete description of SMBH fuelling in all hot atmospheres.

Observations increasingly suggest that cooler gas phases are closely connected to SMBH fuelling. In many central galaxies, Hα emission and molecular gas traced by CO are more closely associated with AGN activity than the mere presence of cooling X-ray gas (Lakhchaura et al., 2018; Ubertosi et al., 2025). This indicates that the fuelling of the black hole is linked not only to the global cooling state of the atmosphere, but also to the formation, distribution, and dynamics of condensed gas within the core. The situation is further complicated by the fact that AGN feedback can itself influence where and how this gas forms: rising X-ray cavities can uplift low-entropy gas from the centre to larger radii, where it may cool more efficiently and condense into colder phases (Churazov et al., 2001; McNamara and Nulsen, 2007; Fabian, 2012). Cooling, condensation, uplift, and accretion are therefore likely to be coupled parts of the same feedback loop, which naturally leads to the discussion of radio lobes and X-ray cavities in the next subsection.

Radio lobes and X-ray cavities

Radio lobes are among the most direct manifestations of radio-mechanical AGN feedback. Radio observations with facilities such as the VLA, GMRT, and LOFAR reveal extended lobes of synchrotron-emitting plasma inflated by AGN jets (Bîrzan et al., 2008; Giacintucci et al., 2011; Bîrzan et al., 2020). In many systems, X-ray images show surface-brightness depressions at the same locations, indicating that these lobes have displaced the surrounding thermal gas (Fabian et al., 2002; Bîrzan et al., 2004). Radio lobes and X-ray cavities, therefore, represent two complementary views of the same outburst (see Figure 3): the radio data trace the relativistic plasma injected by the AGN, while the X-ray data show how that plasma reshapes the hot atmosphere. Together, they provide one of the clearest observational signatures of radio-mechanical feedback.

X-ray cavities appear as surface-brightness depressions in the hot atmosphere and are often accompanied by bright rims, weak shocks, ghost cavities, and multiple generations of bubbles produced in successive AGN outbursts (Fabian et al., 2002; Panagoulia et al., 2014; Shin et al., 2016). Because they trace the displacement of the thermal gas by AGN-inflated relativistic plasma, they provide one of the clearest observational signatures of jet feedback in massive galaxies, groups, and clusters. The energy associated with a cavity is commonly estimated from its enthalpy, which for relativistic plasma is usually approximated as

$$E_{\rm cav} \simeq 4pV, \tag{4}$$

where p is the pressure of the surrounding gas and V is the cavity volume (Bîrzan et al., 2004). Dividing this energy by a characteristic cavity age, estimated for example from buoyancy, sound-crossing, or refill

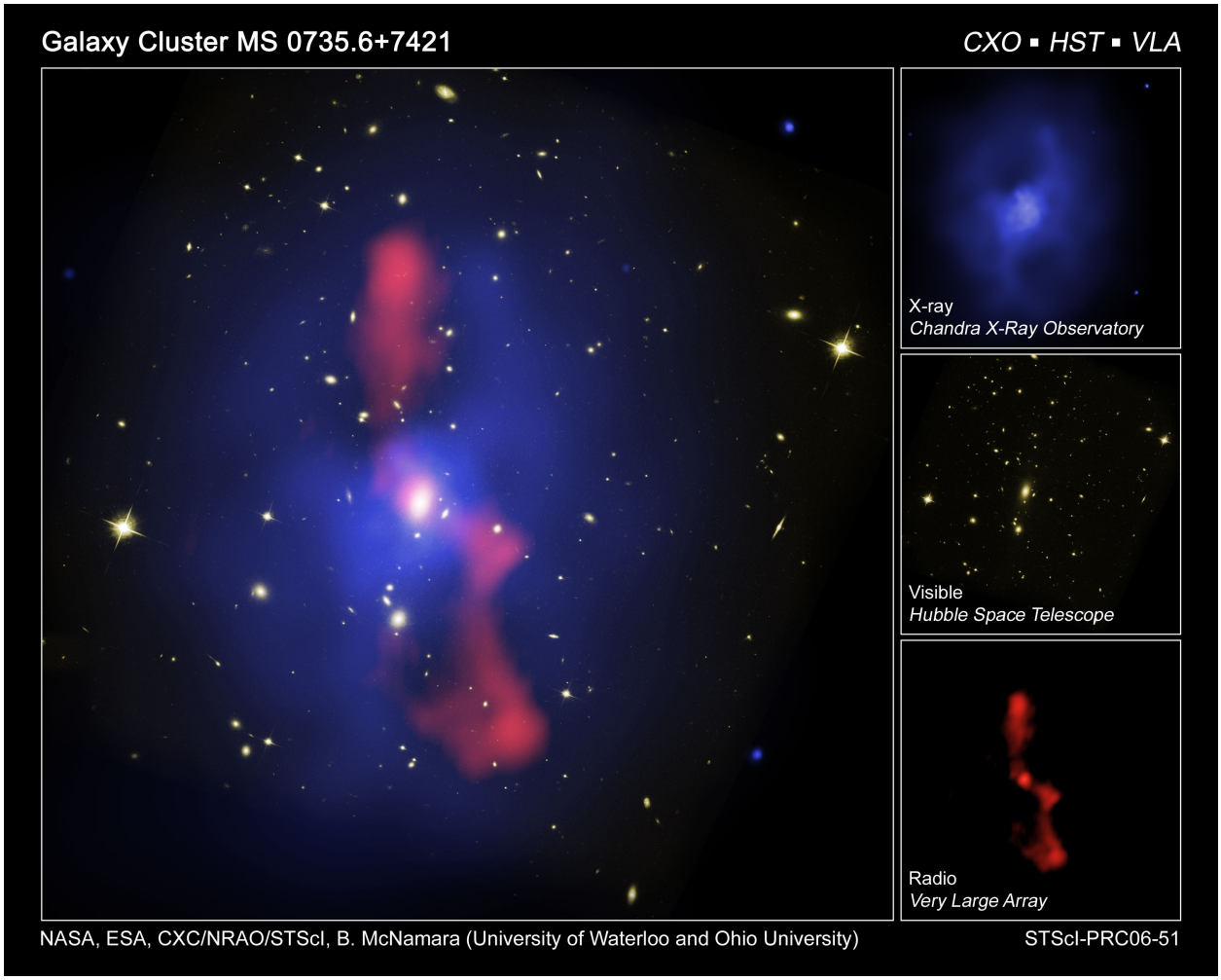

Figure 3: Composite image of galaxy cluster MS 0735.6+7421 consisting of optical image (*yellow*) displaying individual cluster galaxies, X-ray image (*blue*) showing the hot atmosphere rippled by X-ray cavities, and radio image (*red*) with radio lobes, emission of relativistic plasma filling cavities (Hubble and Chandra Credit: NASA, ESA, CXC, STScI, and B. McNamara, Very Large Array Telescope Image Credit: NRAO, and L. Birzan).

time-scales, gives the cavity power,

$$P_{\rm cav} = \frac{E_{\rm cav}}{t}, \tag{5}$$

which is often interpreted as a measure of the AGN outburst's mean mechanical power.

Estimates based on cavity enthalpy show that AGN outbursts frequently carry enough energy to offset a large fraction of the radiative cooling losses, at least on average (Bîrzan et al., 2004; Rafferty et al., 2006). What remains less certain is how this injected energy is actually distributed through the hot atmosphere and converted into heat. Candidate channels include shocks, sound waves, turbulent dissipation, and mixing induced by the inflation and buoyant rise of cavities (McNamara and Nulsen, 2007; Fabian, 2012). More recently, XRISM has begun providing direct constraints on gas motions in hot atmospheres, opening the possibility of linking cavity energetics to the actual kinematics of the surrounding plasma (Xrism Collaboration, 2025; Zhang et al., 2026). This makes X-ray cavities not only a tracer of AGN power, but also an important starting point for understanding how mechanical feedback heats hot atmospheres.

Detection of X-ray cavities

Although X-ray cavities are among the clearest signatures of radio-mechanical AGN feedback, identifying them in practice is not always straightforward. Cavities can be subtle, especially in data of limited exposure depth, and their appearance is strongly affected by noise, projection effects, and departures of the atmosphere from smooth symmetry (e.g., sloshing). These effects influence not only whether a cavity can be detected at all, but also its apparent size and contrast, and therefore the inferred energetics. In most studies, cavities are identified as depressions in the X-ray surface brightness relative to a smooth underlying gas distribution, often with the help of residual images, unsharp masking, or simple empirical models such as the β-model (Dong et al., 2010; Shin et al., 2016; Panagoulia et al., 2014).

Once identified, cavities are usually approximated as ellipsoids (Bîrzan et al., 2004; Dong et al., 2010; Shin et al., 2016). The accuracy of the inferred cavity power, therefore, depends not only on the adopted age estimate but also on how reliably the cavity boundaries are determined. This becomes particularly important when comparing jet powers across samples or relating them to cooling losses and other properties of the host system. The limitations of manual identification and simple geometric assumptions motivate the use of more systematic and reproducible approaches to cavity detection and measurement, which will be discussed later in this thesis (Chapter 2).

Chemical enrichment

The chemical composition of hot atmospheres no longer reflects their original primordial state, but instead records the cumulative effects of enrichment and mixing over cosmic time. The heavy elements observed in the hot gas were synthesised by stellar evolution and supernova explosions, primarily by core-collapse supernovae and Type Ia supernovae, and were subsequently released into the surrounding medium (Mernier and Biffi, 2022). Their abundances and abundance ratios therefore provide a way to connect the present-day hot atmosphere to the past star-formation and enrichment history of the host system. In this sense, the hot gas offers a complementary view of chemical evolution to that obtained from stars alone, because it traces the cumulative products of enrichment after they have been expelled, mixed, and redistributed throughout the halo.

Over the past decades, X-ray observations have shown that the hot atmospheres of ellipticals, groups, and clusters are enriched to a significant level, and that many abundance ratios are remarkably close to Solar (Mernier et al., 2016; de Plaa et al., 2017; Simionescu et al., 2019). In galaxy clusters, the mean metal abundance shows little evolution with redshift (Mushotzky and Loewenstein, 1997; Finoguenov et al., 2000), while the outskirts are enriched to a relatively uniform level of about 0.2–0.3 Solar out to large radii (Fujita et al., 2008; Urban et al., 2017; Mernier et al., 2018a) (see Figure 4). These results are commonly interpreted as evidence that a large fraction of the enrichment took place early and that the metals were mixed efficiently through the gas before or during cluster assembly. At the same time, the observed chemical composition reflects not only nucleosynthesis, but also the subsequent transport and redistribution of metals by processes such as uplift, mixing, sloshing, and ram-pressure stripping. For this reason, understanding chemical enrichment in hot atmospheres requires both accurate abundance measurements and spatially resolved studies of metallicity structure.

Abundance measurements and uncertainties

The heavy elements present in hot atmospheres are measured through their X-ray emission lines, making X-ray spectroscopy the primary tool for chemical studies of the hot gas. In practice, abundance measurements are often expressed either as elemental abundances relative to Solar or as abundance ratios such as O/Fe, Ne/Fe, Mg/Fe, Si/Fe, and S/Fe, which are especially useful for constraining the relative contributions of core-collapse and Type Ia supernovae (Mernier and Biffi, 2022). Different instruments pro-

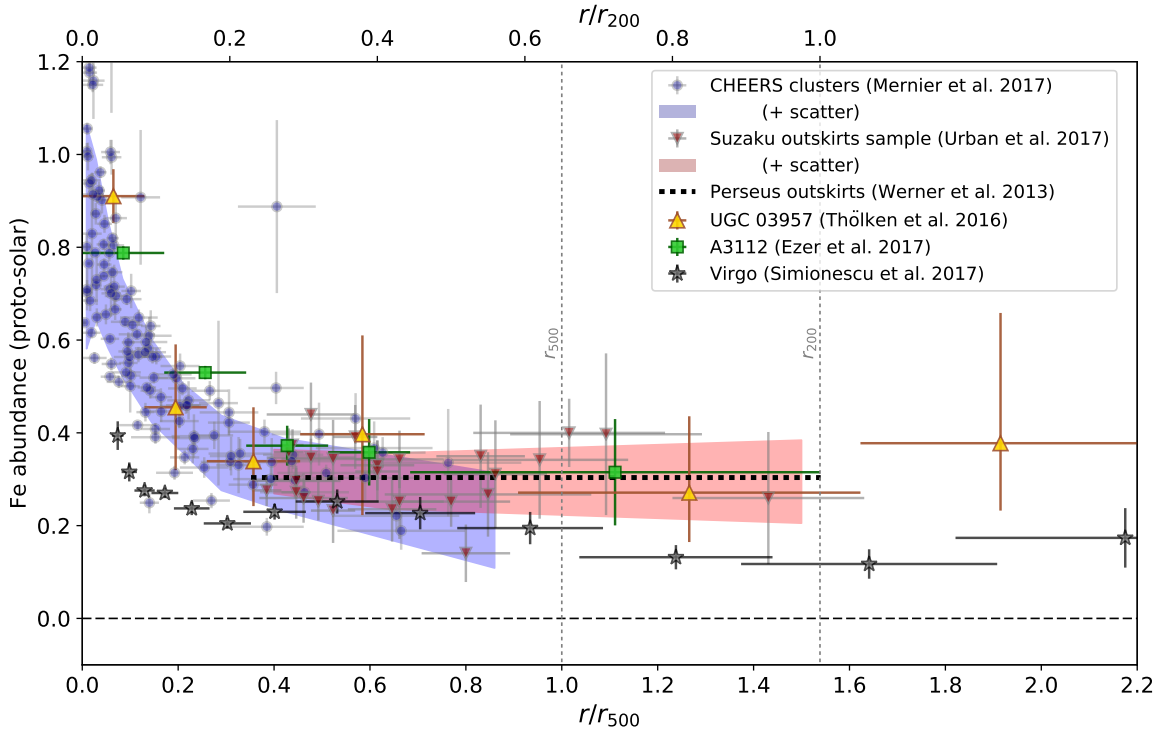

Figure 4: Comparison of the average iron metallicity profiles of the CHEERS cluster sample with those of nearby cool-core clusters (e.g. Virgo, Perseus), extending to large radii and, in some cases, out to or beyond r_{500} (Mernier et al., 2018a)

vide complementary information. CCD detectors are well suited to measuring the broad thermal structure and the strongest elemental features, while high-resolution grating spectra from *XMM–Newton*/RGS are especially valuable for the lighter elements and for detecting weak line complexes in the soft X-ray band (de Plaa et al., 2017; Mernier et al., 2016). The interpretation of these spectra, however, depends sensitively on the adopted spectral model.

A major challenge in abundance work is that the gas in cool atmospheres is often not well described by a single-temperature component. If intrinsically multi-temperature plasma is fitted with an overly simple single-temperature model, the derived Fe abundance can be significantly underestimated, an effect commonly referred to as the Fe bias (Buote, 2000; Wu et al., 2000). Projection effects can further complicate the interpretation by superposing gas with different temperatures and abundances along the line of sight, which is why spatially resolved analyses often rely on direct deprojection methods such as `dsdeproj` (Sanders and Fabian, 2007; Russell et al., 2008) or forward-modelling approaches such as `projct`. Additional uncertainties arise from the choice of plasma code and atomic database, as well as from calibration differences between instruments. Resonance scattering and intrinsic absorption can also affect the observed line fluxes in dense cool cores, thereby biasing abundance measurements if they are not properly accounted for (Gilfanov et al., 1987; Werner et al., 2009; Ogorzalek et al., 2017; Fabian et al., 2024). Accurate abundance work, therefore, requires not only high-quality data but also careful modelling of the source and of the line-of-sight structure.

Metal redistribution

The chemical enrichment of hot atmospheres is reflected not only in integrated abundance measurements but also in their radial metallicity profiles. In ellipticals, groups, and clusters, these profiles often

show centrally peaked metal distributions, indicating that enrichment is closely linked to the central galaxy and to the release of metals into the surrounding atmosphere over long time-scales (Fukazawa et al., 1994; De Grandi and Molendi, 2001; Mernier et al., 2017). At the same time, the radial distribution of metals is shaped not only by where they are produced, but also by how they are transported. Processes such as AGN uplift, mixing, sloshing, and stripping can all redistribute metal-rich gas and modify the observed metallicity structure (Panagoulia et al., 2015; Liu et al., 2019). In this way, metallicity profiles trace both chemical evolution and gas dynamics.

In a significant fraction of systems, the metallicity does not continue to rise to the centre, but instead shows an apparent central drop (Panagoulia et al., 2015; Mernier et al., 2017; Liu et al., 2019). Such central abundance drops have now been reported in giant ellipticals, galaxy groups, and clusters, suggesting that they are not restricted to a single mass scale. They are particularly interesting because they likely reflect a combination of physical redistribution and observational or modelling effects. Proposed explanations include AGN uplift of metal-rich gas to larger radii, depletion of reactive elements into dust grains embedded in cold filaments, resonance scattering, projection effects, and biases introduced by fitting intrinsically multiphase gas with overly simple models (Panagoulia et al., 2015; Liu et al., 2019). Spatially resolved abundance measurements with *Chandra* and *XMM–Newton* are therefore essential for disentangling these possibilities and for understanding how metal transport connects to the broader feedback cycle.

Annex 1

The relation between accretion rate and jet power in early-type galaxies with thermally unstable hot atmospheres

T. Plšek[1], N. Werner[1], R. Grossová[1,2], M. Topinka[1,3], A. Simionescu[4,5,6] and S. W. Allen[7,8,9]

[1] DTPA, Faculty of Science, Kotlářská 2, Masaryk University, Brno, 611 37, Czech Republic
[2] Astronomical Institute of the Czech Academy of Sciences, Boční II 1401, 141 00, Prague, Czech Republic
[3] INAF-Istituto di Astrofisica Spaziale e Fisica Cosmica, Via A. Corti 12, I-20133 Milano, Italy
[4] SRON Netherlands Institute for Space Research, Niels Bohrweg 4, 2333 CA Leiden, The Netherlands
[5] Leiden Observatory, Leiden University, PO Box 9513, 2300 RA Leiden, The Netherlands
[6] Kavli Institute for Physics and Mathematics of the Universe (WPI), The University of Tokyo, Chiba 277-8583, Japan
[7] Department of Physics, Stanford University, 382 Via Pueblo Mall, Stanford CA 94305
[8] SLAC National Accelerator Laboratory, 2575 Sand Hill Road, Menlo Park, CA 94025
[9] Kavli Institute for Astrophysics and Cosmology, Stanford University, 452 Lomita Mall, Stanford, CA 94305

Abstract: We use *Chandra* X-ray data and Very Large Array radio observations for a sample of 20 nearby, massive, X-ray bright, early-type galaxies to investigate the relation between the Bondi accretion rates and the mechanical jet powers. We find a strong correlation ($\rho = 0.96^{+0.03}_{-0.09}$; $\mathrm{BF}_{10} > 100$) between the Bondi accretion power, P_{Bondi}, and the mechanical jet power, P_{jet}, for a subsample of 14 galaxies, which also host cool Hα+[NII] line emitting gas and thus likely have thermally unstable atmospheres. The relation between the Bondi accretion power and the mechanical jet power for this subsample is well described by a power-law model $\log \frac{P_{\mathrm{Bondi}}}{10^{43}\,\mathrm{erg\,s^{-1}}} = \alpha + \beta \log \frac{P_{\mathrm{jet}}}{10^{43}\,\mathrm{erg\,s^{-1}}}$, where $\alpha = 1.10 \pm 0.25$ and $\beta = 1.10 \pm 0.24$ with an intrinsic scatter $\sigma = 0.08^{+0.14}_{-0.06}$ dex. The results indicate that in all galaxies with thermally unstable atmospheres the cooling atmospheric gas feeds the central black holes at a similar jet-to-Bondi power ratio. For the full sample of 20 galaxies, the correlation is weaker and in a subset of galaxies with no signs of Hα+[NII] emission, we see a hint for a systematically lower jet-to-Bondi power ratio. We also investigate the dependence of jet power on individual quantities in the Bondi formula such as the supermassive black hole mass ($M_\bullet$) and the specific entropy of the gas (K) at the Bondi radius. For the subsample of Hα+[NII] emitting galaxies, we find a very tight correlation of P_{jet} with $M_\bullet$ ($\rho = 0.91^{+0.06}_{-0.11}$; $\mathrm{BF}_{10} > 100$) and, although poorly constrained, a hint of an anti-correlation for P_{jet} and K ($\rho = -0.47^{+0.60}_{-0.37}$; $\mathrm{BF}_{10} = 1.1$).

Key words: accretion, accretion discs – galaxies: active – galaxies: jets – galaxies: nuclei – radio continuum: galaxies – X-ray: galaxies

Published in Monthly Notices of Royal Astronomical Society (MNRAS), Volume 517, Issue 3, December 2022, Pages 3682–3710.

1.1 Introduction

All massive early-type galaxies harbour supermassive black holes (SMBH) in their centre and are permeated by extended, hot, X-ray emitting atmospheres. Although the central black holes represent a small fraction in terms of total mass and size compared to the proportions of the host galaxy, they are often outperforming its energetic output and thus playing a substantial role in the energetics of the whole galactic atmosphere.

As the supermassive black holes accrete the surrounding material, a big part of its rest mass (up to 40 % for fast rotating black holes) may be turned into energy. Part of the energy is then expelled in the form of electromagnetic radiation or outflows of relativistic particles (jets), typically depending on the type and rate of the accretion flow. However, the vast majority of low-redshift active galactic nuclei (AGNs) in early-type galaxies operate in the radio-mechanical (kinetic) mode, which is observed in the form of radio lobes and X-ray cavities (e.g. Fabian, 2012; Shin et al., 2016; Grossová et al., 2022).

A detailed description of the accretion of supermassive black holes is nontrivial. Assuming a matter-to-radiation conversion efficiency of $\epsilon = 10$ per cent, a spherical Bondi accretion (Bondi, 1952) from the hot atmospheres of early-type galaxies would result in luminosities that are several orders of magnitude above the observed values. However, it is likely that most of the accretion power in early-type galaxies is converted into jets and the estimates of mechanical jet powers from the observed X-ray cavities are within an order of magnitude comparable to powers predicted from the Bondi formula (Böhringer et al., 2002; Churazov et al., 2002; Di Matteo et al., 2003; Allen et al., 2006).

Allen et al. (2006) studied the relation between Bondi accretion powers and mechanical jet powers in nine nearby giant ellipticals using a combination of *Chandra* X-ray and VLA radio observations finding a tight power-law correlation. Their result indicates that $2.2^{+1.0}_{-0.7}$ per cent of the rest mass energy of the accreted material is converted into jet power. A relation with a much larger scatter has been observed by Russell et al. (2013); however, these authors derived their estimates of jet powers using X-ray data only.

Detailed studies of the gas distribution within the Bondi radii were performed using very deep *Chandra* observations of NGC 3115 (Wong et al., 2011, 2014) and M87 (Di Matteo et al., 2003; Russell et al., 2015, 2018). These observations reveal shallow density profiles, which are consistent with the presence of significant outflows and multi-phase gas at the Bondi radii of central black holes. The clumpy cool gas within the hot multi-phase flow could reach the core episodically, triggering larger outbursts than the continuous activity driven by a more steady hot inflow (Werner et al., 2019).

Here, we study how the presence of thermal instabilities and multi-phase gas affects the relationship between the Bondi accretion power and the mechanical jet power in 20 nearby early-type galaxies. Ten galaxies in our sample harbour extended Hα+[NII] nebulae, four systems display nuclear optical line emission, and six galaxies show no indications for the presence of cool gas. The Bondi accretion rates are calculated from density and temperature profiles of the hot atmospheric gas in the centre of the galaxies determined using *Chandra* data and using black hole mass measurements from the literature (see Sect. 1.1.1). The jet powers are estimated from the energies and time scales needed to inflate cavities in the X-ray emitting gas, where the cavity volumes are estimated based on the extent of the most recent generation of radio lobes. The relation between Bondi accretion powers and jet powers is studied for both the full sample and separately for galaxies which also show nebular line emission and their atmospheres are thus presumably prone to thermally unstable cooling (e.g. Lakhchaura et al., 2018). We also investigate the correlations of the jet power, separately, with the mass of the central SMBH and with the gas entropy within the Bondi accretion radius and examine whether the estimated jet power offsets the radiative cooling within radii where the cooling time is shorter than 1 Gyr.

1.1.1 Sample selection

We selected a sample of galaxies with high-quality archival *Chandra* observations that allow us to determine the properties of their X-ray emitting atmospheres within an order of magnitude of the Bondi radii of their central supermassive black holes (SMBH). Importantly, all of the selected galaxies host radio lobes, which appear to have been inflated recently or still undergoing inflation. The sample galaxies and their basic parameters are listed in Table 1.1. SMBH masses were taken either from direct measurements reported by Kormendy and Ho (2013) and Saglia et al. (2016) or derived from the $M_\bullet - \sigma_v$ scaling relation (see Table 1.1)

$$\log\left(\frac{M_\bullet}{10^9\,M_\odot}\right) = \alpha + \beta \log\left(\frac{\sigma_v}{200\,\mathrm{km/s}}\right), \tag{1.1}$$

where $\alpha = 8.49 \pm 0.05$ and $\beta = 4.38 \pm 0.29$ (Kormendy and Ho, 2013) and velocity dispersions were taken from the *HyperLeda*[1] database (Makarov et al., 2014). Galactic redshifts were taken from *Nasa Extragalactic Database* (NED). The distances were derived from measurements of Surface Brightness Fluctuations (Blakeslee et al., 2001; Jensen et al., 2003; Cantiello et al., 2005; Blakeslee et al., 2009) except for NGC 507 and NGC 6166 (Fundamental Plane method; Tully et al., 2013), and NGC 1600 and NGC 4778 (Tully-Fisher relation; Theureau et al., 2007).

1.2 Data reduction and analysis

The parameters of Bondi accretion were determined using observations from the *Chandra X-ray Observatory*. The mechanical powers of relativistic jets emanating from AGNs were approximated by the work performed by the jet to inflate the radio lobes, where the volumes were estimated from the extended radio emission observed by the Karl G. Jansky Very Large Array (VLA) telescope and the pressure was inferred from *Chandra* data. The exact positions of SMBHs were either determined as the centre of hard X-ray emission (3 – 7 keV) observed with the *Chandra X-ray Observatory* or small scale radio emission observed with Very-long-baseline interferometry (VLBI), or they were taken from Atacama Large Millimeter Array (ALMA) measurements (NGC 4636, NGC 5846; Temi et al., 2018) (see Table 1.1).

1.2.1 *Chandra* data

Throughout this analysis, we used archival *Chandra* observations of 20 nearby early-type galaxies. The *Chandra* data were reprocessed using standard CIAO 4.14 procedures (Fruscione et al., 2006) and current calibration files (CALDB 4.9.6). For most objects, the observations were obtained by the ACIS-S chip in the VFAINT mode, but for some galaxies (NGC 507, NGC 4636, NGC 5846 and NGC 6166) we also included ACIS-I observations (see Table A.1.2).

Point sources, as well as regions of strong nonthermal emission emanating from relativistic jets (e.g. NGC4261, NGC4486), were found using the `wavdetect` procedure both in the hard (3 – 7 keV) and broad (0.5 – 7 keV) band, visually inspected and excluded from further analysis. The light curves, extracted in the 0.5 – 7.0 keV band, were deflared using the `lc_clean` algorithm within the `deflare` routine and good time intervals were obtained.

For objects with multiple observations, the individual OBSIDs were reprojected onto one of the observations via the `reproject_obs` script. For background subtraction, we used blanksky background files, which were reprojected onto the observations, filtered for VFAINT events, and scaled to match the particle background of observations in the 9 – 12 keV band.

[1] http://leda.univ-lyon1.fr/

Table 1.1: Initial parameters for the sample of galaxies: right ascension and declination coordinates of the SMBH position, morphology of cool gas tracer Hα+[NII] emission (adopted from Lakhchaura et al., 2018; extended emission extends beyond central 2 kpc), total ACIS exposure time, VLA configuration used for radio lobe size-estimation, distance d, redshift z (*Nasa Extragalactic Database*), hydrogen column density $n_{\rm H}$ (HI4PI Collaboration et al., 2016), velocity dispersion σ_v (*HyperLeda* database; Makarov et al., 2014), supermassive black hole masses $M_\bullet$ and their references.

Galaxy	RA [a]	DEC [a]	Hα+[NII] morphology	Exptime (ks)	VLA conf. [b]	d (Mpc)	z	$n_{\rm H}$ (10^{20} cm^{-2})	σ_v (km s^{-1})	$M_\bullet$ [c] ($10^9\,M_\odot$)	Ref.
IC 4296	$13^{\rm h}36^{\rm m}39.03^{\rm s}$	-33°57'57.07"	Extended	28.5	D	49.0	0.0125	3.96	327 ± 5	$1.30^{+0.24}_{-0.20}$	[1]
NGC 507	$01^{\rm h}23^{\rm m}39.94^{\rm s}$ *	33°15'21.86" *	No	62.2	C	64.6	0.0165	5.24	292 ± 6	$2.14^{+0.58\,\ddagger}_{-0.46}$	-
NGC 708	$01^{\rm h}52^{\rm m}46.46^{\rm s}$	36°09'06.49"	Extended	139.4	A†	62.8	0.0162	6.87	222 ± 8	$0.49^{+0.07\,\ddagger}_{-0.07}$	-
NGC 1316	$03^{\rm h}22^{\rm m}41.71^{\rm s}$	-37°12'28.56"	Extended	228.4	A	22.7	0.0059	2.11	223 ± 3	$0.17^{+0.03}_{-0.03}$	[2]
NGC 1399	$03^{\rm h}38^{\rm m}29.02^{\rm s}$	-35°27'01.51"	No	204.5	A (B)	20.9	0.0048	1.39	332 ± 5	$1.26^{+0.52}_{-0.63}$	[2]
NGC 1407	$03^{\rm h}40^{\rm m}11.79^{\rm s}$ *	-18°34'48.90" *	No	44.5	A	25.4	0.0059	4.94	266 ± 5	$4.65^{+0.73}_{-0.41}$	[2]
NGC 1600	$04^{\rm h}31^{\rm m}39.85^{\rm s}$ *	-05°05'10.48" *	No	243.6	A	63.7	0.0156	3.19	331 ± 7	$17.0^{+1.5}_{-1.5}$	[3]
NGC 4261	$12^{\rm h}19^{\rm m}23.24^{\rm s}$	05°49'29.65"	Nuclear	135.3	C	32.4	0.0074	1.65	297 ± 4	$1.67^{+0.39}_{-0.24}$	[4]
NGC 4374	$12^{\rm h}25^{\rm m}3.74^{\rm s}$	12°53'13.14"	Nuclear	882.4	B	18.5	0.0034	2.85	278 ± 2	$0.93^{+0.10}_{-0.09}$	[2]
NGC 4472	$12^{\rm h}29^{\rm m}46.76^{\rm s}$	08°00'01.71"	No	367.0	A (C)	16.7	0.0033	1.56	282 ± 3	$2.54^{+0.58}_{-0.10}$	[2]
NGC 4486	$12^{\rm h}30^{\rm m}49.42^{\rm s}$	12°23'28.04"	Extended	370.7/135.4 [e]	A	16.7	0.0043	1.23	323 ± 4	$6.5^{+0.7}_{-0.7}$	[5]
NGC 4552	$12^{\rm h}35^{\rm m}39.81^{\rm s}$	12°33'22.73"	Extended [d]	201.4	C	16.0	0.0011	2.72	250 ± 3	$0.50^{+0.06}_{-0.06}$	[1]
NGC 4636	$12^{\rm h}42^{\rm m}49.83^{\rm s}$	02°41'15.99"	Nuclear	197.4	A	14.7	0.0031	1.82	200 ± 3	$0.33^{+0.04\,\ddagger}_{-0.04}$	-
NGC 4649	$12^{\rm h}43^{\rm m}39.99^{\rm s}$	11°33'09.86"	No	293.8	B	16.5	0.0037	2.02	330 ± 5	$4.72^{+1.04}_{-1.05}$	[2]
NGC 4696	$12^{\rm h}48^{\rm m}49.28^{\rm s}$ *	-41°18'39.53" *	Extended	711.1	A	42.5	0.0099	7.78	243 ± 6	$0.89^{+0.18\,\ddagger}_{-0.15}$	-
NGC 4778	$12^{\rm h}53^{\rm m}05.70^{\rm s}$ *	-09°12'14.68" *	Nuclear	167.0	B/A	66.2	0.0147	3.86	251 ± 21	$0.84^{+0.17\,\ddagger}_{-0.14}$	-
NGC 5044	$13^{\rm h}15^{\rm m}23.97^{\rm s}$ *	-16°23'07.78" *	Extended	563.7	A	32.2	0.0093	4.92	225 ± 9	$0.22^{+0.12}_{-0.07}$	[6]
NGC 5813	$15^{\rm h}01^{\rm m}11.24^{\rm s}$ *	01°42'07.24" *	Extended	638.2	B	32.2	0.0065	4.29	236 ± 3	$0.71^{+0.10}_{-0.09}$	[1]
NGC 5846	$15^{\rm h}06^{\rm m}29.28^{\rm s}$ *	01°36'20.25" *	Extended	113.4	A	24.9	0.0057	4.31	237 ± 4	$1.10^{+0.16}_{-0.14}$	[1]
NGC 6166	$16^{\rm h}28^{\rm m}38.25^{\rm s}$	39°33'04.23"	Extended	158.3	A†	125.0	0.0304	0.79	301 ± 6	$2.11^{+0.57\,\ddagger}_{-0.45}$	-

[a] Coordinates marked with * represent SMBH positions derived from the hard X-ray (3 – 7 keV) central peak, for the rest of the galaxies the positions are based on radio observations and they were either derived from VLBI data or taken from the literature (NGC 4636, NGC 5846; ALMA; Temi et al., 2018).

[b] VLA array configurations marked with † were taken from the NRAO VLA Archive Survey (NVAS). Array configurations in parentheses represent shorter baselines capturing more extended radio emission.

[c] SMBH masses marked with ‡ were calculated from the velocity dispersion σ_v using the $M_\bullet - \sigma_v$ scaling relation. Masses for all other galaxies were taken from direct measurements of gas or star kinematics from within the sphere of influence of the SMBH.

[d] In the case of NGC 4552, the Hα+[NII] morphology was taken from Boselli et al. (2021).

[e] The first number represents the total exposure time for 1/8th subarray observations (OBSIDs 18232-21458) and the second number is the total exposure time for full-array observations, which are strongly affected by pile-up effects (OBSIDs 352, 2707).

References: [1] Saglia et al. (2016) [2] Kormendy and Ho (2013) [3] Thomas et al. (2016) [4] Boizelle et al. (2021) [5] Event Horizon Telescope Collaboration (2019) [6] Schellenberger et al. (2021)

Spectral analysis

Spectral files were produced for each observation separately using the `specextract` script in the 0.5 – 7.0 keV energy band[2]. The spectra were extracted from concentric annuli with increasing radii centred at the SMBH positions stated in Table 1.1. The radii of individual annuli were chosen to maximize the central spatial resolution while still obtaining a reasonable number of counts required to constrain the electron density with a relative uncertainty smaller than 25 per cent.

In the case of the galaxy NGC 4486 (M87), the bright central AGN and jet emission leads to very strong pile-up effects within the central few arcsec of *Chandra* ACIS-S observations obtained in the classical full-array 3.2 s exptime mode. Following the analysis of Wilson and Yang (2002), Di Matteo et al. (2003) and Russell et al. (2015), we also utilized archival observations in the 1/8th subarray 0.4 s exptime mode. Spectral files for the short frame-time observations were extracted from circular annuli starting at 2 arcsec and up to 30 arcsec from the centre, whereas for observations in the full-frame 3.2 s exptime mode the spectra were extracted in the 15 – 230 arcsec range.

For each galaxy, spectra for all annuli and OBSIDs were fitted simultaneously using PyXspec v2.0.5 (XSPEC v12.12.0; Arnaud, 1996) and ATOMDB v3.0.9 (Foster et al., 2012). The deprojection was performed within PyXspec using the *projct* model, which was applied only to the thermal component (*apec*) that describes the extended emission of the galactic atmosphere. For the deprojection, spherical symmetry and constant temperatures and electron number densities within individual annuli are assumed.

To account for the single-phase collisionally ionised diffuse gas, we used a single *apec* model component, which describes the state of the gas by its temperature kT, metallicity Z, redshift z and normalization Y, which is directly proportional to the emission measure of the X-ray emitting gas

$$Y = \frac{10^{-14} \int n_{\rm e} n_{\rm i} {\rm d}V}{4\pi D_{\rm A}^2 (1+z)^2}, \tag{1.2}$$

where $D_{\rm A}$ is the angular diameter distance and $n_{\rm e}$ and $n_{\rm p}$ are electron and ion concentrations, respectively, where for fully ionised medium with Solar abundances $n_{\rm e} = 1.18\, n_{\rm p}$. The redshift for all objects was fixed to values stated in Table 1.1. Temperatures and abundances were allowed to vary during the fitting, however, for most galaxies, these were tied for two or more neighbouring shells in order to constrain these parameters with a relative uncertainty smaller than 10 and 25 per cent, respectively. The abundances were measured with respect to the proto-solar abundances reported by Lodders (2003).

For some of the galaxies, we also included an absorbed power-law component *zphabs (powerlaw)* in the innermost annulus to account for the obscured emission of the active galactic nucleus. The redshifted absorbing hydrogen column density $n_{{\rm H},z}$, as well as the photon index Γ, were freed during fitting. However, for galaxies for which the fitted values were not significant, we eventually fixed the parameters to $n_{{\rm H},z} = 0$ and $\Gamma = 1.9$ (following Russell et al., 2013), where $\Gamma = 1.9$ represents a mean value of the photon index for nearby AGNs (Gilli et al., 2007). For galaxies, for which even the normalization of the non-thermal power-law component was insignificant, this component was eventually excluded from the model.

For the remaining outer annuli, we added a bremsstrahlung component (*bremss*) with the temperature fixed to 7.3 keV (Irwin et al., 2003), which should well describe the hard X-ray contribution of unresolved low-mass X-ray binaries, cataclysmic variables, and coronally active binaries.

The Galactic absorption was modelled using the *phabs* model with the *bcmc* cross-section (Balucinska-Church and McCammon, 1992). The hydrogen column densities $n_{\rm H}$ were fixed to the values obtained from the *HEASARC*[3] database which uses the values reported by HI4PI Collaboration et al. (2016).

The best-fit parameters were found using the Levenberg-Marquardt minimization method and cash statistics (Cash, 1979). The final values of parameters and their uncertainties were obtained using Markov

[2] For low-energy limit of 0.6 keV, consistent results were obtained.

[3] https://heasarc.gsfc.nasa.gov/cgi-bin/Tools/w3nh/w3nh.pl

Chain Monte Carlo (MCMC) simulations, where we used Gaussian priors centred at the best-fit values. Unless stated otherwise, all uncertainties are expressed in the 1σ credible interval (for asymmetric distributions, this corresponds to distances of 15.9 % and 84.1 % quantiles from the median value). During the fitting, we assumed the standard ΛCDM cosmology with $H_0 = 70\,\mathrm{km\,s^{-1}\,Mpc^{-1}}$, $\Lambda_0 = 0.73$ and $q_0 = 0$.

In addition to the spectral analysis used for determining electron number densities, the fitting was also performed using a *cflux* model component and the fluxes of thermal *apec* components for individual annuli were derived. Each *apec* component was multiplied by a convolutional *cflux* component with an energy range of 0.01 − 100 keV (bolometric X-ray flux). Total X-ray luminosities were calculated from the derived fluxes and distances stated in Table 1.1.

1.2.2 VLA observations

We used VLA observations in A, B, C, or D configurations centred at around 1.4 GHz, which were calibrated and 'imaged' using the NRAO Common Astronomy Software Applications pipeline (CASA, McMullin et al., 2007) version 4.7.2 and 5.6.1. Two categories of data were analysed depending on the year of their observation including both 'historical' data observed before the major upgrade in 2011 (Perley et al., 2009, 2011) and 'Karl G. Jansky VLA/EVLA' data obtained after this upgrade. Three galaxies, NGC 4552, NGC 4636 and NGC 4649, were observed by the upgraded Karl G. Jansky VLA and calibrated using the automatic CASA pipeline version 1.3.11. Reduction and 'imaging' follows standard procedures described in Grossová et al. (2019, 2022). The historical observations were manually calibrated using the NRAO pre-upgrade calibration methods[4]. For galaxies NGC 708 and NGC 6166, reduced images were obtained from the NRAO VLA Archive Survey (NVAS)[5].

The mechanical jet powers were estimated from the sizes of radio lobes that were identified using processed VLA images. For observations showing extended radio emission, we produced radio contours and estimated the sizes of radio lobes manually by overlaying the radio contours with ellipse regions using the *SAOImageDS9* software (Joye and Mandel, 2003). The minimum level of radio contours was set to be 5 times the root mean square error (RMSE) of the surrounding background.

In order to probe the most recent radio-mechanical AGN activity, we used L-band (1 − 2 GHz) images with the best available angular resolution, which for the A configuration data is comparable to our *Chandra* images. However, for some objects in our sample, no A configuration data were available or they did not capture the extended emission fully. For these objects, we used the more compact array configurations (B, C, or D), always aiming for the best possible spatial resolution (see Table 1.1). For NGC 1399 and NGC 4472 it is not entirely clear whether the smaller scale radio emission seen in the A-configuration data, which also appears to be associated with surface brightness depressions in the *Chandra* residual images, corresponds to the most recent radio lobes or to a channel feeding the more extended lobes. For these galaxies, we show the jet power estimates and the resulting correlations based on both the more compact and the larger scale structures.

1.2.3 VLBI observations

Observations from the VLBI were retrieved from the *Astrogeo VLBI FITS image database*[6]. All utilized observations were observed in the X-band (8 − 8.8 GHz) under the *VLBI 2MASS Survey* (V2M) or *Wide-Field VLBA Calibration Survey* (WFCS) and were all analysed by Leonid Petrov (Condon et al., 2013; Petrov, 2021; Petrov & Kovalev in prep.). The exact positions of SMBHs were determined from the peak of the small scale VLBI radio emission.

[4] https://casaguides.nrao.edu/index.php/Jupiter
[5] https://archive.nrao.edu/nvas/
[6] http://astrogeo.org/vlbi_images/

1.3 Results

The deprojected radial profiles of temperature, kT, metallicity, Z, and electron number density, n_e, were determined from spatially resolved spectral analysis of galaxies. During the spectral fitting, the metallicities were derived using a single-temperature *apec* component, but due to the fact that the central parts of early-type galaxies are often multiphase, we checked the metallicity estimates also using a multi-temperature model. Nevertheless, fixing the central abundances to those obtained from the multi-temperature model introduced only minor changes to the final values of thermodynamic properties and the derived Bondi powers.

For some of the galaxies, especially those for which the temperatures and abundances of neighbouring annuli were tied, we observed strong degeneracy (mostly two-peak) in the posterior distributions of some of these parameters. However, for all galaxies with strong temperature and abundance degeneracy, the posterior peaks were relatively nearby and the differences were maximally of the order of 0.05 keV and 0.1 $Z_\odot$, respectively.

For most of the galaxies, the spatial resolution of *Chandra* was not sufficient to constrain the thermodynamic properties at the Bondi radius and, therefore, extrapolations were necessary. The central temperature and metallicity were assumed to be constant within the innermost radial bin, but the electron number density had to be extrapolated (see Figs. A.1.1, A.1.2 and A.1.3). For the extrapolation, we used 3 different profiles (similarly as Russell et al., 2013): a power-law model, a β-model (Cavaliere and Fusco-Femiano, 1976) and a Sersic profile (Sérsic, 1963). The mean of these three profiles was then taken as the final value of the electron number density and the scatter was accounted in the uncertainty[7]. In the case of the power-law model, we only used the inner 3 to 4 radial bins in order to properly fit the innermost substructure. When fitting the β-model and the Sersic profile, we included more radial bins up to the point where the profile slope changes significantly or starts flattening again. To account for uncertainties in both axes, the profile fitting was carried out using the Orthogonal Distance Regression (Scipy v1.4.1; Boggs and Rogers, 1990).

The inferred temperatures and electron number densities were used to calculate the values of central specific entropy $K = kTn_e^{-2/3}$ and also profiles of other thermodynamic quantities such as thermal pressure $p = nkT$, free fall time t_{ff}, and cooling time t_{cool} of the X-ray emitting gas (see Table 1.2). The cooling time is defined as the timescale needed for a gas of certain density, temperature and metallicity to thermally emit all of its energy via bremsstrahlung, recombination and line emission

$$t_{cool} = \frac{3}{2}\frac{nkT}{n_e n_i \Lambda(T,Z)}, \tag{1.3}$$

where n is the total particle density $n = n_e + n_i$ and $\Lambda(T,Z)$ is the temperature and abundance-dependent cooling function, values of which were taken from Schure et al. (2009). The free-fall time resembles a dynamical timescale required for a condensed clump with zero momentum to fall into the centre of the galaxy and is given by $t_{ff} = \sqrt{2r/g}$, where the local gravitational acceleration g was calculated from the velocity dispersion σ and the galactocentric distance r using the assumption of an isothermal sphere $g = 2\sigma^2/r$ (Binney and Tremaine, 1987).

To probe how susceptible the galactic atmospheres are to thermal instabilities, we calculated the profiles of cooling time to free-fall time ratios. Formerly, the atmospheres of galaxies were expected both from analytical (Nulsen, 1986) and numerical computations (McCourt et al., 2012) to become thermally unstable when the cooling time falls below the free-fall time. However, the most up-to-date observations (e.g. Voit and Donahue, 2015; Hogan et al., 2017) and simulations (Sharma et al., 2012; Gaspari et al., 2012) have shown that atmospheres of realistic galaxies may become thermally unstable even when the

[7] We also tried extrapolating the electron number densities only by the power-law model, which resulted in systematically higher densities. The final conclusions were, however, consistent with the results obtained by averaging.

cooling time to free-fall time ratio falls below $t_{\rm cool}/t_{\rm ff} \lessapprox 10$, which is often referred to as the *precipitation limit* (we note that it resembles an approximate division line rather than a strict limit). The susceptibility of galactic atmospheres to thermal instabilities was, therefore, assessed from the minimal values in the $t_{\rm cool}/t_{\rm ff}$ profiles (Fig. A.1.6).

Total power outputs of hot galactic atmospheres were approximated by the total X-ray luminosities within a defined radius such as the cooling radius (*cooling luminosity*). The cooling radius is defined as the radius at which the cooling time profile (Equation 1.3) reaches a certain value. Commonly used are the values of 3 Gyr (Panagoulia et al., 2014) and 7.7 Gyr (lookback time of $z = 1$; Rafferty et al., 2006; Nulsen et al., 2009). However, since most galaxies in our sample are relatively nearby, such radii would often be outside of ACIS chip's edges. Instead, we used the radius where the cooling time profile reaches the value of 1 Gyr (see Fig. A.1.5). The energetic balance of galactic atmospheres was then probed by comparing the cooling luminosities to the mechanical powers of the jets (Table 1.3).

Table 1.2: Summary of parameters derived from *Chandra* observations. Listed quantities: temperature kT, electron number density $n_{\rm e}$, metallicity Z, and specific entropy K at the Bondi radius, minimum of the cooling time over free fall time ratio $t_{\rm cool}$ / $t_{\rm ff}$, sound speed $c_{\rm sound}$, Bondi radius $r_{\rm Bondi}$, Bondi accretion rate $\dot{m}_{\rm Bondi}$, Bondi accretion power $P_{\rm Bondi}$, and mechanical jet power $P_{\rm jet}$.

Galaxy[a]	kT (keV)	$n_{\rm e}$ ($\rm cm^{-3}$)	Z ($Z_\odot$)	K (keV $\rm cm^{-2/3}$)	min $t_{\rm cool}/t_{\rm ff}$	$c_{\rm sound}$ (km / s)	$r_{\rm Bondi}$ (pc)	$\dot{m}_{\rm Bondi}$ ($10^{-3}\,M_\odot$ / yr)	$P_{\rm Bondi}$ (10^{43} erg / s)	$P_{\rm jet}$ (10^{43} erg / s)
IC 4296	$0.69^{+0.05}_{-0.06}$	$1.56^{+0.28}_{-0.24}$	$0.87^{+0.15}_{-0.11}$	$0.47^{+0.39}_{-0.14}$	5.4 ± 0.5	421^{+15}_{-17}	63^{+13}_{-11}	48^{+44}_{-30}	27^{+25}_{-17}	$4.2^{+3.0}_{-1.5}$
NGC 507 *	$0.82^{+0.04}_{-0.05}$	$0.72^{+0.17}_{-0.13}$	$0.65^{+0.16}_{-0.15}$	$1.0^{+0.8}_{-0.3}$	8.7 ± 0.8	460^{+12}_{-15}	87^{+24}_{-20}	44^{+48}_{-28}	25^{+27}_{-16}	$6.8^{+4.6}_{-2.3}$
NGC 708	1.03 ± 0.04	0.081 ± 0.006	$0.88^{+0.06}_{-0.05}$	$5.0^{+4.4}_{-1.5}$	$6.1^{+0.3}_{-0.2}$	514 ± 11	16^{+3}_{-2}	$0.4^{+0.36}_{-0.25}$	$0.23^{+0.20}_{-0.14}$	$0.06^{+0.041}_{-0.021}$
NGC 1316	0.77 ± 0.02	$0.74^{+0.09}_{-0.07}$	0.42 ± 0.02	$0.85^{+0.73}_{-0.25}$	6.9 ± 0.3	444^{+6}_{-7}	$7.4^{+1.2}_{-1.3}$	$0.32^{+0.31}_{-0.20}$	$0.18^{+0.17}_{-0.11}$	$0.012^{+0.008}_{-0.004}$
NGC 1399 *	1.16 ± 0.05	$0.84^{+0.32}_{-0.13}$	1.07 ± 0.06	$1.2^{+1.0}_{-0.3}$	10.8 ± 0.3	545^{+12}_{-11}	37^{+15}_{-17}	$9.1^{+15.2}_{-7.2}$	$5.1^{+8.6}_{-4.1}$	$0.037^{+0.026}$ [b]
NGC 1407	0.94 ± 0.04	0.13 ± 0.01	$1.36^{+0.20}_{-0.16}$	$3.3^{+2.8}_{-1.0}$	$19.9^{+1.2}_{-0.9}$	493^{+9}_{-10}	170^{+30}_{-20}	35^{+29}_{-21}	20^{+17}_{-12}	$0.12^{+0.08}_{-0.04}$
NGC 1600	0.96 ± 0.02	$0.059^{+0.007}_{-0.006}$	1.25 ± 0.10	$5.8^{+5.0}_{-1.8}$	18.8 ± 0.7	498 ± 6	590 ± 50	190^{+150}_{-120}	110^{+90}_{-70}	$0.13^{+0.10}_{-0.05}$
NGC 4261	$0.7^{+0.02}_{-0.03}$	$1.17^{+0.18}_{-0.19}$	$0.57^{+0.06}_{-0.04}$	$0.58^{+0.48}_{-0.18}$	5.9 ± 0.3	424^{+7}_{-8}	80^{+19}_{-12}	60^{+58}_{-37}	34^{+33}_{-21}	$1.2^{+0.81}_{-0.41}$
NGC 4374	0.73 ± 0.02	0.16 ± 0.02	$0.86^{+0.11}_{-0.09}$	$2.2^{+1.9}_{-0.7}$	6.0 ± 0.3	434 ± 6	42 ± 4	$2.4^{+1.9}_{-1.5}$	$1.35^{+1.06}_{-0.82}$	$0.2^{+0.15}_{-0.07}$
NGC 4472	$0.85^{+0.04}_{-0.03}$	$0.37^{+0.02}_{-0.03}$	0.81 ± 0.02	$1.5^{+1.3}_{-0.5}$	10.4 ± 0.2	469^{+10}_{-9}	100^{+18}_{-10}	36^{+32}_{-22}	20^{+18}_{-13}	$0.05^{+0.034}$ [b]
NGC 4486	0.79 ± 0.05	$0.21^{+0.03}_{-0.02}$	0.64 ± 0.05	$2.1^{+1.8}_{-0.6}$	8.4 ± 0.3	451 ± 13	270 ± 30	130^{+110}_{-80}	75^{+60}_{-46}	$1.31^{+0.97}_{-0.49}$
NGC 4552	$1.12^{+0.14}_{-0.12}$	$2.01^{+0.34}_{-0.31}$	$0.47^{+0.04}_{-0.03}$	$0.65^{+0.56}_{-0.20}$	$7.3^{+0.8}_{-0.7}$	537^{+34}_{-29}	15^{+3}_{-2}	$4.4^{+3.7}_{-2.7}$	$2.5^{+2.1}_{-1.5}$	$0.11^{+0.07}_{-0.04}$
NGC 4636	0.3 ± 0.02	0.14 ± 0.04	$0.91^{+0.04}_{-0.03}$	$1.1^{+0.8}_{-0.3}$	$4.9^{+0.5}_{-0.4}$	278 ± 10	37 ± 5	$0.93^{+0.73}_{-0.55}$	$0.53^{+0.41}_{-0.31}$	$0.016^{+0.011}_{-0.006}$
NGC 4649 *	1.46 ± 0.07	$0.43^{+0.06}_{-0.05}$	$1.21^{+0.05}_{-0.07}$	$2.3^{+2.0}_{-0.7}$	13.9 ± 0.3	613^{+14}_{-16}	111 ± 19	54^{+58}_{-35}	31^{+33}_{-20}	$0.024^{+0.018}_{-0.009}$
NGC 4696	0.88 ± 0.02	0.54 ± 0.06	0.51 ± 0.01	$1.2^{+1.0}_{-0.4}$	3.5 ± 0.1	475 ± 5	34^{+7}_{-6}	$5.5^{+5.3}_{-3.5}$	$3.1^{+3.0}_{-2.0}$	$0.42^{+0.29}_{-0.14}$
NGC 4778 *	0.76 ± 0.03	0.26 ± 0.02	$0.99^{+0.08}_{-0.06}$	$1.7^{+1.5}_{-0.5}$	7.3 ± 0.6	443 ± 10	37^{+8}_{-6}	$2.9^{+2.8}_{-1.8}$	$1.6^{+1.6}_{-1.0}$	$0.071^{+0.049}_{-0.024}$
NGC 5044	$0.75^{+0.02}_{-0.03}$	0.10 ± 0.05	$0.43^{+0.03}_{-0.02}$	$3.3^{+2.0}_{-0.8}$	4.7 ± 0.2	440^{+6}_{-8}	$9.9^{+5.3}_{-3.2}$	$0.073^{+0.117}_{-0.049}$	$0.041^{+0.066}_{-0.028}$	$0.016^{+0.011}_{-0.006}$
NGC 5813	0.8 ± 0.01	0.12 ± 0.01	0.82 ± 0.02	$3.0^{+2.5}_{-0.9}$	5.5 ± 0.2	454 ± 2	30 ± 4	$0.92^{+0.78}_{-0.56}$	$0.52^{+0.44}_{-0.32}$	$0.065^{+0.046}_{-0.023}$
NGC 5846	0.77 ± 0.02	0.20 ± 0.01	$0.58^{+0.04}_{-0.03}$	$2.0^{+1.8}_{-0.6}$	7.0 ± 0.3	445 ± 6	48^{+7}_{-6}	$3.9^{+3.4}_{-2.4}$	$2.2^{+1.9}_{-1.4}$	$0.14^{+0.10}_{-0.05}$
NGC 6166	$1.6^{+0.20}_{-0.17}$	$0.37^{+0.06}_{-0.05}$	$1.53^{+0.12}_{-0.09}$	$2.9^{+2.5}_{-0.9}$	11.5 ± 0.4	641^{+39}_{-34}	44^{+13}_{-10}	$8.3^{+9.5}_{-5.4}$	$4.7^{+5.4}_{-3.1}$	$0.68^{+0.47}_{-0.23}$

[a] For galaxies marked with *, the absorbed power-law component describing the non-thermal central AGN emission was not significant and therefore it was not included in the final fit.

[b] For NGC 1399 and NGC 4472, the jet power estimates based on the potentially older, larger scale lobes are $0.29^{+0.18}_{-0.09} \times 10^{43}$ $\rm erg\,s^{-1}$ and $0.27^{+0.21}_{-0.10} \times 10^{43}$ $\rm erg\,s^{-1}$, respectively.

1.3.1 Bondi power

The total power input that the supermassive black hole acquires by accreting the surrounding material was estimated under the assumption of the spherical Bondi accretion model (Bondi, 1952). Bondi accretion assumes steady spherical accretion from the circumnuclear medium, which most likely rarely happens in realistic galactic nuclei due to the presence of angular momentum, outflows, and magnetic fields. However, since the precise geometry of the accretion flow is typically not known, it still provides an order-of-magnitude estimate of the total accretion power (Churazov et al., 2002; Allen et al., 2006) and is parameterizable only by the temperature and density of the ambient gas and the mass of the SMBH.

The radius for which the gravitational influence of the SMBH is dominant over the thermal energy of the gas is the Bondi radius $r_{\rm Bondi} = GM_\bullet c_{\rm s}^{-2}$, where $M_\bullet$ is the SMBH mass and $c_{\rm s} = \sqrt{\gamma kT/\mu m_{\rm p}}$ is the speed of sound in the surrounding medium, where $\mu \approx 0.62$ is the mean atomic weight for fully ionised gas and $\gamma = 5/3$ is the adiabatic index of the X-ray emitting plasma. The accretion rate can be expressed as a flux of matter through a spherical shell of Bondi radius

$$\dot{m}_{\rm Bondi} = 4\pi\lambda\rho(GM_\bullet)^2 c_{\rm s}^{-3} = \pi\lambda\rho c_{\rm s} r_{\rm Bondi}^2, \tag{1.4}$$

with a numerical coefficient for adiabatic gas $\lambda = 0.25$. The accreted matter is then with an efficiency η turned into energy $P_{\rm Bondi} = \eta\dot{m}_{\rm Bondi}c^2$, which can be expelled in the form of relativistic jets. Throughout this analysis, we assume an efficiency of 10 per cent.

The parameters of the Bondi accretion were derived from the spectral properties of the X-ray emitting gas surrounding the supermassive black hole (see Table 1.1 for the black hole masses). The results are listed in Table 1.2.

1.3.2 Mechanical jet power

The mechanical power of a relativistic jet emanating from the vicinity of a supermassive black hole can be estimated either from the size of the extended radio emission (radio lobes) or from the corresponding X-ray cavities inflated in the ambient medium. Throughout this analysis, we estimated the jet powers from the approximate volumes of radio lobes assuming that the same volume of thermal plasma was displaced by the jet producing X-ray cavities.

The total kinetic energy needed to inflate a cavity of volume V into the circumgalactic medium with pressure p is equal to its total enthalpy H, which is the sum of the internal energy of the relativistic plasma and the work done on the ambient gas

$$H = \frac{1}{\gamma - 1} pV + pV, \tag{1.5}$$

where γ is the adiabatic index (ratio of specific heats) of plasma filling the cavity. The value of the adiabatic index depends on whether the gas pressure support is caused by nonrelativistic ($\gamma = 5/3$) or relativistic particles ($\gamma = 4/3$). Modern observations of massive clusters of galaxies via the Sunyaev-Zeldovich effect (Abdulla et al., 2019) have indicated that the X-ray cavities are filled mainly with relativistic gas ($\gamma = 4/3$) and the total enthalpy is therefore given by $H = 4pV$, which is also in a good agreement with magnetohydrodynamical simulations (Mendygral et al., 2011; McNamara and Nulsen, 2012).

The total enthalpy was numerically integrated on a linearly scaled Cartesian 3D grid of pressure, which was interpolated from the pressure profile using linear interpolation in log-log space (see Fig. A.1.4) and under the assumption of spherical symmetry. In the case of IC 4296, the thermal pressure of the gas at the position of the cavity was taken from Grossová et al. (2019), which is based on *XMM-Newton* measurements. Compared to the commonly used method based on estimating the $4pV$ work by using only the exact value of the pressure in the centre of the cavity and its total volume, this approach introduces

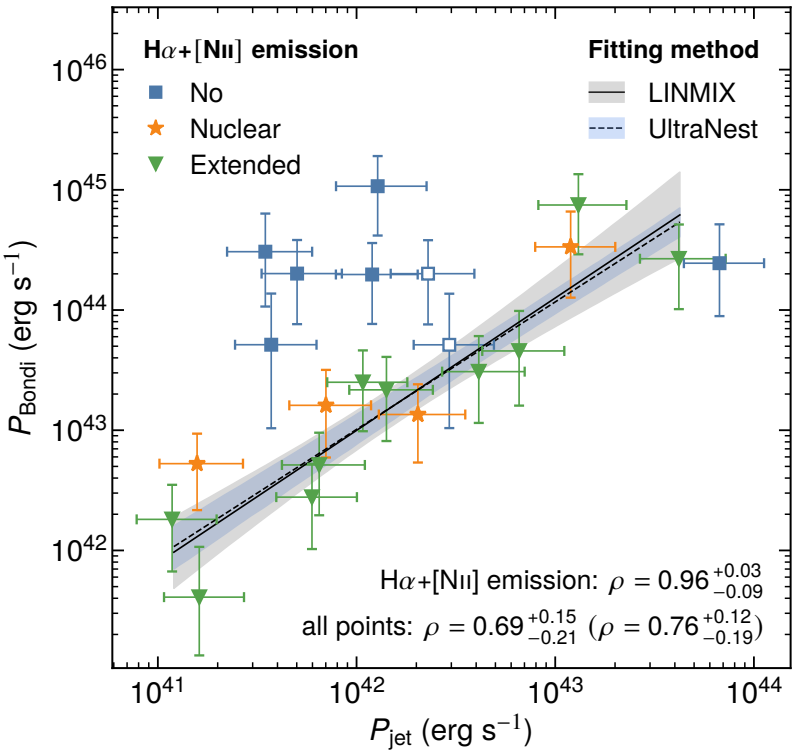

Figure 1.1: Correlation between Bondi accretion power and mechanical jet power. The solid line is the LINMIX power-law fit for the subsample of galaxies containing cold gas (either extended or nuclear Hα+[NII] emission), while the grey area represents its 1 σ confidence band. For comparison, we show also UltraNest fit (dashed line) with its confidence band (blue area). Correlation coefficients for the Hα+[NII] emitting sub-sample and the full sample are shown in the lower right corner. The larger scale radio lobes for NGC 1399 and NGC 4472 (blue empty squares) and the corresponding correlation coefficient (stated in parentheses) are also shown.

for most prolate cavities and galaxies with a non-smooth pressure profile relative changes of up to 25 per cent.

The geometry of cavities was assumed to be prolate or oblate ellipsoids with rotational symmetry along the semi-axis closer to the direction towards the centre of the galaxy. The volume of the ellipsoid is in general given by $V = 4\pi/3\, r_\mathrm{l}\, r_\mathrm{w}\, r_\mathrm{d}$, where r_w (width) is the semi-axis of the ellipsoid which is perpendicular to the direction of the jet, r_l (length) is the semi-axis along that direction and r_d is the unknown depth of the cavity. For the calculations, we assumed the depth of the cavity to be equal to its width. To account for uncertainties caused by the unknown depths of cavities, by the potential irregularities of their shapes and also by projection effects, we introduced an additional factor of 2 uncertainty for their volumes.

The total mechanical power required for inflating a cavity with internal energy E is given by $P_\mathrm{jet} = \frac{E}{t_\mathrm{age}}$, where t_age is the age of the cavity. The ages of individual cavities were calculated from their galactocentric distances, R, and their inflation velocities, v, as $t_\mathrm{age} = R/v$. The velocity of the inflation was assumed to be equal to the average speed of sound in the hot medium, c_s, along the path of the cavity. When integrating the surrounding pressure and estimating the age of the cavities, the galactocentric distances of cavities were calculated based on their angular distances.

Table 1.3: Derived quantities describing the power output of galactic atmospheres: cooling radius $r_{\rm cool}$ in units of kpc and arcsec (radius at which the cooling time profile reaches the value of 1 Gyr), cooling luminosity $L_{\rm cool}$ in the 0.01 − 100 keV range (luminosity of thermal emission within the cooling radius), and the ratio of cooling luminosity to mechanical jet power $L_{\rm cool}/P_{\rm jet}$.

Galaxy	$r_{\rm cool}$ (kpc)	$r_{\rm cool}$ (arcsec)	$L_{\rm cool}$ (erg s^{-1})	$L_{\rm cool}/P_{\rm jet}$
IC 4296	5.4	22.1	$1.7^{+0.1}_{-0.2} \times 10^{41}$	$0.0041^{+0.0022}_{-0.0017}$
NGC 507	8.4	26.8	$2.02^{+0.08}_{-0.07} \times 10^{41}$	$0.003^{+0.0014}_{-0.0012}$
NGC 708	13.0	45.9	$1.427^{+0.014}_{-0.013} \times 10^{42}$	$2.38^{+1.22}_{-0.95}$
NGC 1316	8.7	85.4	$5.3^{+0.1}_{-0.3} \times 10^{40}$	$0.43^{+0.21}_{-0.16}$
NGC 1399	5.2	51.2	$1.24^{+0.02}_{-0.03} \times 10^{41}$	$0.33^{+0.16}_{-0.13}$
NGC 1407	5.8	47.5	$5.5^{+0.2}_{-0.5} \times 10^{40}$	$0.044^{+0.024}_{-0.017}$
NGC 1600	5.5	18.0	$1.216^{+0.016}_{-0.012} \times 10^{41}$	$0.094^{+0.06}_{-0.04}$
NGC 4261	5.5	35.3	$7.4^{+0.3}_{-0.2} \times 10^{40}$	$0.0061^{+0.0034}_{-0.0025}$
NGC 4374	5.4	60.4	$4.035^{+0.003}_{-0.002} \times 10^{40}$	$0.0199^{+0.0095}_{-0.0089}$
NGC 4472	6.1	75.5	$9.72^{+0.15}_{-0.11} \times 10^{40}$	$0.189^{+0.101}_{-0.074}$
NGC 4486	12.0	148.7	$2.35^{+0.01}_{-0.02} \times 10^{41}$	$0.0178^{+0.0103}_{-0.0075}$
NGC 4552	6.3	81.7	$2.47^{+0.01}_{-0.02} \times 10^{40}$	$0.0213^{+0.0125}_{-0.0083}$
NGC 4636	9.3	131.0	$1.539^{+0.021}_{-0.016} \times 10^{41}$	$0.98^{+0.46}_{-0.4}$
NGC 4649	5.9	73.5	$8.5^{+0.3}_{-0.2} \times 10^{40}$	$0.35^{+0.21}_{-0.16}$
NGC 4696	11.7	60.4	$3.13^{+0.03}_{-0.02} \times 10^{42}$	$0.76^{+0.42}_{-0.31}$
NGC 4778	15.8	52.2	$9.4^{+0.2}_{-0.3} \times 10^{41}$	$1.32^{+0.72}_{-0.52}$
NGC 5044	23.0	147.6	$2.40^{+0.09}_{-0.10} \times 10^{42}$	$14.43^{+8.05}_{-5.61}$
NGC 5813	17.6	112.9	$6.675^{+0.015}_{-0.017} \times 10^{41}$	$1.04^{+0.58}_{-0.43}$
NGC 5846	14.2	117.6	$2.76^{+0.04}_{-0.05} \times 10^{41}$	$0.193^{+0.107}_{-0.077}$
NGC 6166	17.9	29.5	$8.72^{+0.12}_{-0.09} \times 10^{42}$	$1.29^{+0.68}_{-0.51}$

The derived properties of each radio lobe, such as its volume, galactocentric distance, approximate age, and derived mechanical jet power can be found in the Appendix (Table A.1.1), while sums of the mechanical powers for both radio lobes are stated in Table 1.2.

1.3.3 Correlations

The relationships between mechanical jet power, Bondi accretion power, SMBH mass, and specific entropy were fitted using a power-law model and the corresponding correlations between the quantity pairs were probed. Since the fit was performed using a linearized power-law model, the uncertainties of all the fitted quantities were recomputed either based on laws of error propagation or using random sampling. For fitting purposes, we approximated asymmetric distributions of all quantities by a normal distribution.

The fitting was performed using a hierarchical Bayesian approach to linear regression included in the LINMIX package[8] (Kelly, 2007). For verification purposes, we performed the linear fit also using MLFriends algorithm (Buchner, 2016, 2019) within the UltraNest 3.3.2 package[9] (Buchner, 2021), which enables incorporating asymmetric and non-gaussian uncertainties of individual data points by randomly sampling from a given distribution.

The correlations were probed via the LINMIX linear correlation coefficient between the latent variables (ρ) and the significance of the correlation was verified by the Bayes factor for the two-sided correlation test $\mathrm{BF}_{10}(\rho \neq 0)$ (Savage-Dickey density ratio[10]; Dickey and Lientz, 1970), where for ρ we assumed a flat prior. For comparison, we also state the classical Pearson product-moment correlation coefficient (Fisher, 1944) between the observed variables calculated without accounting for measurement errors, and the corresponding significance test (two-tailed p-value).

During the fitting, we distinguished between galaxies that do contain signs of cool gas tracers (extended or nuclear Hα+[NII] emission) and galaxies that do not. We, therefore, fitted the whole sample of galaxies and the Hα+[NII] subsample separately and compared the result. Obtained linear correlation coefficients for individual pairs of quantities and subsamples can be found in Table 1.4. For significantly correlated quantity pairs ($P_{\mathrm{Bondi}} - P_{\mathrm{jet}}$, and $P_{\mathrm{jet}} - M_{\bullet}$), we also state the fitted intercept and slope parameters and we show their best-fit power-law models together with $1\,\sigma$ confidence bands (see Fig. 1.1 and Fig. 1.2). For the full sample, we also provide the correlation coefficients when for NGC 1399 and NGC 4472 the jet powers were determined from larger scale radio lobes.

1.4 Discussion

In our sample of 20 nearby massive early-type galaxies, we have found a correlation between the Bondi accretion rate and mechanical jet power (Fig. 1.1). The correlation for the whole sample shows moderate significance ($\rho = 0.69^{+0.15}_{-0.21}$, $\mathrm{BF}_{10} = 13$). However, a strong correlation with extreme evidence ($\rho = 0.96^{+0.03}_{-0.09}$, $\mathrm{BF}_{10} > 100$) is detected for galaxies with thermally unstable atmospheres containing signs of cool gas tracers (Hα+[NII] line emission).

The obtained relation between the Bondi accretion power and the mechanical jet power is for the Hα+[NII] subsample well described by a power-law model

$$\log \frac{P_{\mathrm{Bondi}}}{10^{43}\,\mathrm{erg\,s^{-1}}} = \alpha + \beta \log \frac{P_{\mathrm{jet}}}{10^{43}\,\mathrm{erg\,s^{-1}}}, \tag{1.6}$$

where $\alpha = 1.10 \pm 0.25$ and $\beta = 1.10 \pm 0.24$ with an intrinsic scatter $\sigma = 0.08^{+0.14}_{-0.06}$ dex. We note that the relation is remarkably close to linear, which yields the jet-to-Bondi power ratio to be practically constant (11^{+6}_{-3} per cent) with increasing jet power. Assuming that the accretion is Bondi-like and accounting for the previously presumed ten per cent efficiency, for galaxies with Hα+[NII] emission, we obtain a $1.1^{+0.6}_{-0.3}$ per cent efficiency of converting the rest mass of the accreted material into the energy of relativistic outflows.

Although the accretion, which is also affected by angular momentum of the infalling gas, outflows and magnetic fields, is most probably not spherical nor Bondi-like, the Bondi formula appears to provide a useful parametrization for estimating the total accretion power.

As already discussed by Allen et al. (2006), the positive correlation between P_{jet} and P_{Bondi} is not a result of the Bondi accretion rates and mechanical jet powers being a function of galactic distances.

[8] https://github.com/jmeyers314/linmix

[9] https://github.com/JohannesBuchner/UltraNest

[10] The Bayes factor (BF_{10}), as a Bayesian alternative to classical hypothesis test, expresses the ratio of marginal likelihoods of the alternative and null hypothesis. For the alternative hypothesis, we assume that the data are correlated ($\rho \neq 0$), while the null hypothesis assumes no correlation ($\rho = 0$). For equality constrained models, one can obtain the Bayes factor by directly comparing posterior and prior probabilities evaluated at a given point ($\rho = 0$) (Savage-Dickey density ratio).

Table 1.4: Parameters obtained by fitting the linearized power-law model ($\log y = \alpha + \beta \log x$): fitted quantities, fitted subsample, Pearson correlation coefficient r and the corresponding $p-$value; LINMIX parameters: intercept α, slope β, intrinsic scatter σ, correlation coefficient ρ, Bayes factor $\mathrm{BF}_{10}(\rho \neq 0)$; and the UltraNest parameters: intercept α and slope β. During the fitting, the Bondi and jet powers were expressed in units of $10^{43}\,\mathrm{erg\,s^{-1}}$, black hole masses in units of $10^9\,M_\odot$, specific entropy in units of $\mathrm{keV\,cm^2}$ and cooling luminosities in units of $10^{43}\,\mathrm{erg\,s^{-1}}$. In the case of uncorrelated or non-significantly correlated pairs of quantities the fitted slope and intercept parameters were not stated. All stated uncertainties correspond to 68.3 per cent credible intervals and were either symmetrized or are expressed asymmetrically.

		Pearson		LINMIX					UltraNest	
Quantities[a]	Subsample	r	$p-$value	α	β	σ	ρ	BF_{10}	α	β
$P_{\mathrm{Bondi}} - P_{\mathrm{jet}}$	all	0.61	0.004	1.17 ± 0.29	0.80 ± 0.28	$0.46^{+0.32}_{-0.19}$	$0.69^{+0.15}_{-0.21}$	13	1.18 ± 0.28	0.65 ± 0.22
	all (larger)	0.67	0.0013	1.19 ± 0.27	0.89 ± 0.27	$0.38^{+0.28}_{-0.18}$	$0.76^{+0.12}_{-0.19}$	25	1.19 ± 0.27	0.64 ± 0.22
	Hα+[NII]	0.91	< 0.001	1.10 ± 0.25	1.10 ± 0.24	$0.08^{+0.14}_{-0.06}$	$0.96^{+0.03}_{-0.09}$	> 100	1.08 ± 0.23	1.05 ± 0.20
$P_{\mathrm{jet}} - M_\bullet$	all	0.45	0.046	-	-	-	$0.47^{+0.20}_{-0.24}$	1.8	-	-
	all (larger)	0.48	0.030	-	-	-	$0.50^{+0.18}_{-0.23}$	2.5	-	-
	Hα+[NII]	0.88	< 0.001	-0.62 ± 0.14	1.79 ± 0.36	$0.15^{+0.14}_{-0.07}$	$0.91^{+0.06}_{-0.11}$	> 100	-0.71 ± 0.07	1.57 ± 0.15
$P_{\mathrm{jet}} - K$	all	-0.32	0.17	-	-	-	$-0.49^{+0.57}_{-0.34}$	1.2	-	-
	all (larger)	-0.36	0.12	-	-	-	$-0.57^{+0.52}_{-0.31}$	1.7	-	-
	Hα+[NII]	-0.31	0.29	-	-	-	$-0.47^{+0.60}_{-0.37}$	1.1	-	-
$P_{\mathrm{jet}} - L_{\mathrm{cool}}$	all	0.07	0.76	-	-	-	$0.07^{+0.25}_{-0.26}$	0.33	-	-
	all (larger)	0.02	0.93	-	-	-	$0.02^{+0.25}_{-0.26}$	0.32	-	-
	Hα+[NII]	0.01	0.96	-	-	-	$0.01^{+0.32}_{-0.32}$	0.38	-	-

Firstly, measured distances of all galaxies (except for NGC6166) are within an order of magnitude similar. And more importantly, while the Bondi accretion rates depend on distance approximately as $P_{\mathrm{Bondi}} \propto d^{-0.5}$ (without accounting for the distance dependence of the SMBH mass estimates), the mechanical jet powers are proportional to distance as $P_{\mathrm{jet}} \propto d^{1.5}$.

Instead, based on our results, we suggest that the observed $P_{\mathrm{jet}} - P_{\mathrm{Bondi}}$ correlation originates mainly from the positive correlation between the mechanical jet power and SMBH mass (Fig. 1.2). The Bondi accretion rate is by definition proportional to the square of SMBH mass ($P_{\mathrm{Bondi}} \propto M_\bullet^2$), while, based on our measurements, the mechanical jet power depends on SMBH mass as $P_{\mathrm{jet}} \propto M_\bullet^{1.79\pm0.36}$. The Bondi accretion rate is also proportional to thermodynamic properties of gas inside the Bondi radius (as $\propto K^{-3/2}$), but the central specific entropy appears to correlate with mechanical jet power only mildly and with a much larger scatter (see Fig. 1.3), although the data are rather uninformative ($\mathrm{BF}_{10} = 1.1$). The thermodynamic properties at the Bondi radius were fairly resolved (innermost radius $\lesssim 2\,r_{\mathrm{Bondi}}$) only for 8 out of 20 galaxies, 4 of which contain no Hα+[NII] emission. For the rest of the galaxies, the central parts were only poorly resolved and the extrapolations do not necessarily reflect the real thermodynamic state of the gas at the Bondi radius. A possible strong correlation between mechanical jet power and specific entropy could have therefore been lost in the scatter.

Similarly as for the Bondi power, a tight correlation between SMBH mass and jet power ($\rho = 0.91^{+0.06}_{-0.11}$; $\mathrm{BF}_{10} > 100$) is only observed for the Hα+[NII] emitting subsample, while for the whole sample the correlation is relatively weak and poorly constrained ($\rho = 0.47^{+0.20}_{-0.24}$; $\mathrm{BF}_{10} = 1.8$). Based on our results, when the

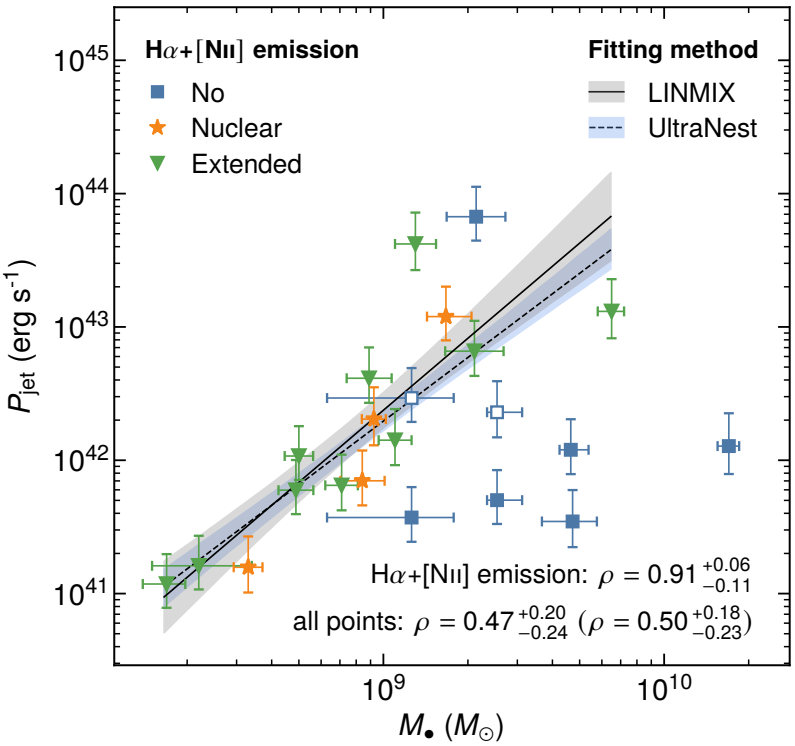

Figure 1.2: Mechanical jet power versus the mass of SMBH. The solid line is the LINMIX power-law fit for the subsample of galaxies containing cold gas (either extended or nuclear Hα+[NII] emission), while the grey area represents its 1σ confidence band. For comparison, we also show the UltraNest fit (dashed line) with its confidence band (blue area). Correlation coefficients for the Hα+[NII] emitting sub-sample and for the full sample are shown in the lower right corner. The larger scale radio lobes for NGC 1399 and NGC 4472 (blue empty squares) and the corresponding correlation coefficient (stated in parentheses) are also shown.

galactic atmospheres are thermally unstable, the jet power will scale with the SMBH mass as described by the power-law model

$$\log \frac{P_{\rm jet}}{10^{43}\ {\rm erg/s}} = \alpha + \beta \log \frac{M_\bullet}{10^9\ M_\odot}, \tag{1.7}$$

where $\alpha = -0.62 \pm 0.14$ and $\beta = 1.79 \pm 0.36$ with an intrinsic scatter of $\sigma = 0.15^{+0.14}_{-0.07}$, while for thermally stable atmospheres the jet power will be unaffected by SMBH mass and remain approximately constant ($10^{41} - 10^{42}$ erg s^{-1}). A similar relation between SMBH mass and jet power, although with a much larger scatter, was reported by McNamara et al. (2011) and also by McDonald et al. (2021) using data from Russell et al. (2013).

For one of the most powerful jets ever recorded with jet power of $1.7^{+0.6}_{-0.5} \times 10^{46}$ erg s^{-1} (MS 0735.6+7421; Vantyghem et al., 2014), the extrapolation of our relation (Eq. 1.7) yields a SMBH mass of $8.0^{+14.1}_{-3.9} \times 10^{10}$ M$_\odot$, which is actually consistent with the most up-to-date mass estimate obtained using the break radius scaling relation (5.1×10^{10} M$_\odot$; Dullo et al., 2021).

1.4.1 Comparison to previous studies

The relation between Bondi accretion power and mechanical jet power has been previously studied for 9 early-type galaxies by Allen et al. (2006) and for 13 sources by Russell et al. (2013). In this work, we

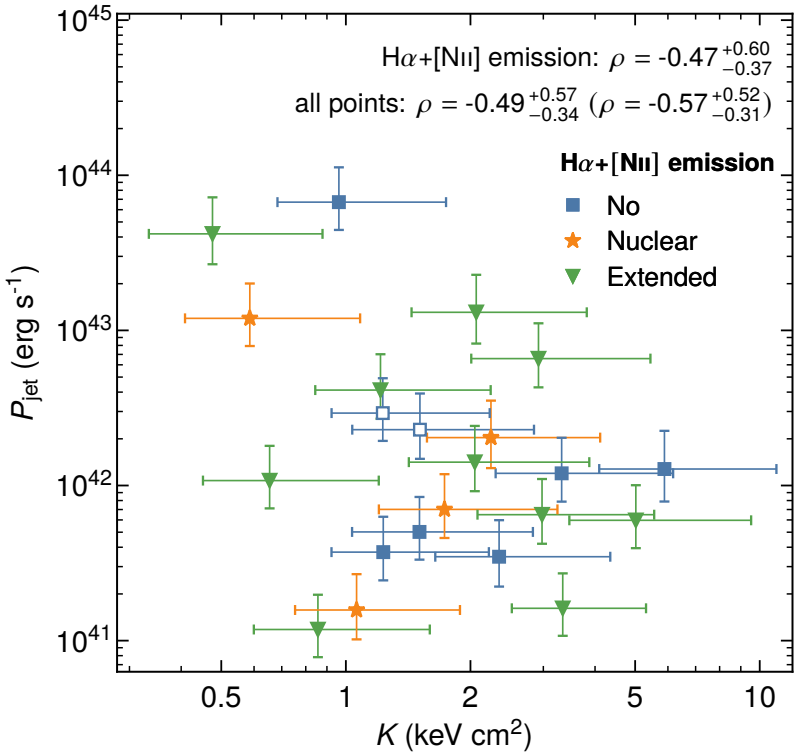

Figure 1.3: Mechanical jet power versus central specific entropy of the X-ray emitting gas. Correlation coefficients for the Hα+[NII] emitting sub-sample and the full sample are shown in the upper right corner. The larger scale radio lobes for NGC 1399 and NGC 4472 (blue empty squares) and the corresponding correlation coefficient (stated in parentheses) are also shown.

analysed data for 20 galaxies, including all sources used in these previous studies and adding 7 new systems. Despite obtaining comparable results for most sources, in several cases order-of-magnitude discrepancies are observed.

One of the most significant sources of potential discrepancies are the assumed black hole masses, which have a significant influence on the Bondi accretion power estimation. In this work, for most objects, we were able to collect recent, direct SMBH mass estimates from within their sphere of influence (Table 1.1). We only had to utilise scaling relations in 6 systems (see Section 1.1.1).

Compared to Allen et al. (2006), in this work, we estimated the jet power of NGC 4472 to be approximately 16 times lower because we used a newer generation of radio lobes (with corresponding X-ray cavities present). Nevertheless, in all our results, we also report the jet powers determined using the older generation of radio lobes, which are comparable to Allen et al. (2006). With respect to the results of Russell et al. (2013), most discrepant results for both Bondi power and jet power were obtained for NGC 1316 and NGC 5044. For the jet power, we also see large discrepancies in NGC 4778. Mechanical jet powers estimated in our work are almost an order-of-magnitude lower, which is in all of these cases most probably due to the use of younger generations of lobes and cavities. The discrepancy in Bondi power is in both NGC 1316 and NGC 5044 caused by different electron densities at the Bondi radius. In this work, a combination of increased spatial resolution and a different extrapolation method, based on fitting the innermost substructure, resulted in almost an order of magnitude lower electron density estimates.

Significant differences between our measurements and the results of Allen et al. (2006) and Russell et al. (2013) were also obtained for the central densities in NGC 4374 and NGC 4486. In the case of NGC 4374, we analysed significantly deeper *Chandra* observations (~ 890 ks) than in the previous stud-

ies (~ 120 ks). In the latter case, the discrepancy can be caused by several reasons, however, we speculate that the main cause is the use of additional short frametime observations observed in 2016, which allowed us to avoid pile-up effects and thus better study the gas properties at smaller radii.

Except for the most distinct cases, modest differences in mechanical jet powers compared to the results of Allen et al. (2006) are most probably a result of using VLA radio observations with slightly different S/N ratio (e.g. NGC 4374). The resulting parameters of the jet-to-Bondi power correlation are, however, consistent within uncertainties with those reported by Allen et al. (2006) ($\alpha = 0.65 \pm 0.16$ and $\beta = 0.77 \pm 0.20$). The differences between our mechanical jet powers and those of Russell et al. (2013) are primarily due to differently defined cavity volumes, with our study using combined X-ray and radio imaging data.

1.4.2 Feeding from thermally unstable atmospheres

The thermal stability of atmospheres was, besides the presence or absence of Hα+[NII] line emission, also probed using the minimum value of the cooling time to free-fall time ratio. Fig. 1.4 shows that, for galaxies with $\min(t_{\rm cool}/t_{\rm ff})$ lower than or close to the precipitation limit, the jet-to-Bondi power efficiency is approximately constant ($\approx$ 10 per cent), while for higher values of $\min(t_{\rm cool}/t_{\rm ff})$ the efficiency appears to decrease. Interestingly, the presence of the Hα+[NII] emission correlates well with the minimal value of $t_{\rm cool}/t_{\rm ff}$ ratio, which supports the idea of galaxies with $\min(t_{\rm cool}/t_{\rm ff}) \lesssim 10$ hosting thermally unstable atmospheres.

The fact that we only see a strong correlation for thermally unstable atmospheres with a lower value of $\min(t_{\rm cool}/t_{\rm ff})$ suggests that the black holes producing the jets and lobes are fed by thermally unstable gas from the galactic atmospheres. The ratios of jet powers and Bondi powers inferred for the given black hole masses are within an order of magnitude similar for all these systems (of the order of 10^{-1} of the Bondi power) and the scatter in the inferred ratio is remarkably small. It appears that once the atmosphere becomes thermally unstable, the cooling gas feeds the black hole in the centres of all galaxies at a similar jet-to-Bondi power ratio, possibly indicating a key universal property of black hole accretion in early-type galaxies. The fact that all 14 thermally unstable atmospheres have similar jet powers relative to the inferred Bondi powers, indicates that the accretion in early-type galaxies is stable and the accreted cooling gas is relatively uniform and not particularly clumpy.

Interestingly, for 5/6 galaxies with no detected Hα+[NII] emission and thus most likely hosting thermally stable atmospheres, the jet power is of the order $10^{41}-10^{42}$ erg s^{-1} and does not appear to trace the black hole mass. All these galaxies have within the order of magnitude similar stellar populations, and similar stellar masses. Given our interpretation, we expect that the hot atmosphere of NGC507 is thermally unstable and future, more sensitive observations should detect multi-phase gas in this system. We speculate that in these thermally stable atmospheres the stellar mass loss material provides a similar amount of fuel in all these systems (Matthews and Reid, 2007; Voit and Donahue, 2011), resulting in a similar 'floor' jet power. But once the atmospheres become thermally unstable, the amount of additional fuel that reaches the black hole and results in jet production will scale with the black hole mass.

1.4.3 Lack of 'true AGN feedback'?

The obtained ratios of cooling luminosities to jet powers are lower than in studies, which include more massive galaxy clusters (Rafferty et al., 2006; Panagoulia et al., 2014; Hlavacek-Larrondo et al., 2015). On the other hand, our results are consistent with the findings of Nulsen et al. (2009), that for lower luminosity early-type galaxies the atmospheres are in general not precisely energetically balanced. The energy balance of our galactic atmospheres appears systematically inclined in favour of radio-mechanical heating. In other words, most of the galactic atmospheres seem to acquire more energy than they emit

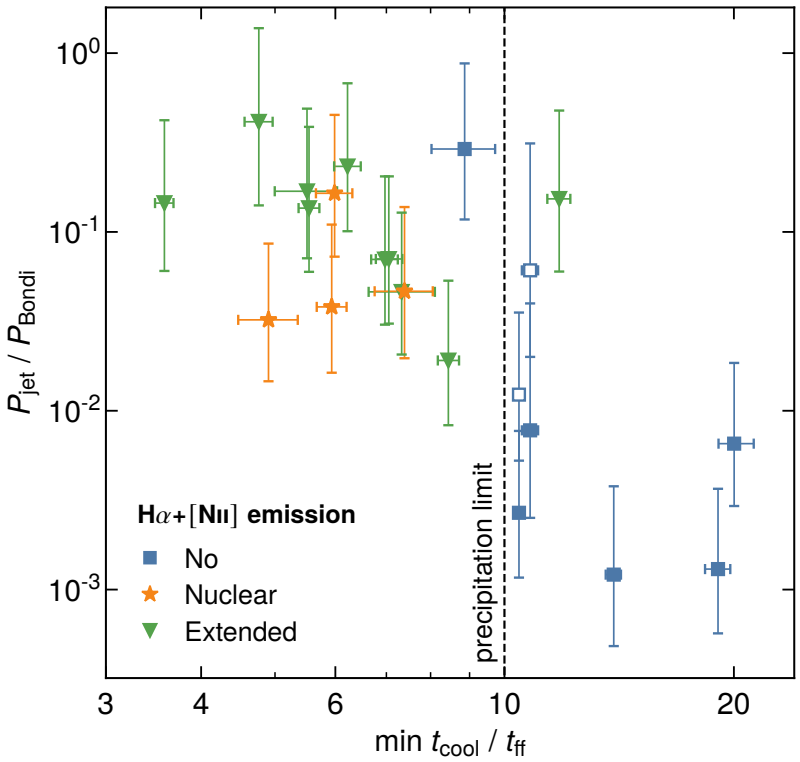

Figure 1.4: Dependence of jet power to Bondi power efficiency on the susceptibility to thermal instabilities expressed by the minimum of the cooling time to free-fall time ratio. The vertical dashed line represents the precipitation limit $t_{cool}/t_{ff} \approx 10$. The larger scale radio lobes for NGC 1399 and NGC 4472 (blue empty squares) are also shown.

(Fig. 1.5). Partially, it may be due to our choice of a lower cooling time threshold of 1 Gyr (compared to 3 or 7.7 Gyr) resulting in smaller cooling radii.

Interestingly, we observe no correlation between the cooling luminosity and the mechanical jet power (Table 1.4, see Fig. 1.5), which is most likely a result of the relatively small range of cooling luminosities and jet powers in our study. Similarly, for X-ray luminosities extracted from within a predefined fixed radius (e.g. 1 or 10 kpc), we observed at most weak correlations. At first glance, these results indicate a lack of fine-tuning between the jet power and the thermodynamic global state of hot atmospheres.

Instead, the atmospheric properties seem to provide an 'on/off switch' - they determine whether the atmosphere will be thermally stable or not. The maximal possible jet power will be primarily set by the black hole mass. For thermally unstable galaxies, the jet power will trace this maximal limit (Eq. 1.7), while for stable atmospheres the jet power will be orders of magnitude smaller.

Heavier dark matter haloes with more massive atmospheres will also host larger black holes (e.g. see Bogdán and Goulding, 2015; Lakhchaura et al., 2019b; Truong et al., 2021). For galaxies with thermally unstable atmospheres (central cooling times shorter than 1 Gyr), heavier haloes will also have more powerful AGNs (Main et al., 2017). These more powerful AGNs powered by heavier black holes will provide more jet heating, compensating for the larger cooling luminosities of more massive systems. We propose that the correlation between the P_{jet} and L_{cool} observed over a relatively large dynamic range from galaxies to clusters of galaxies (e.g. see Hlavacek-Larrondo et al., 2015) is primarily due to the underlying correlation between the black hole mass and halo mass.

Lakhchaura et al. (2019b) showed that the average atmospheric gas temperature in early-type ellipticals correlates with the mass of the central black hole (see also Gaspari et al., 2019). By comparing

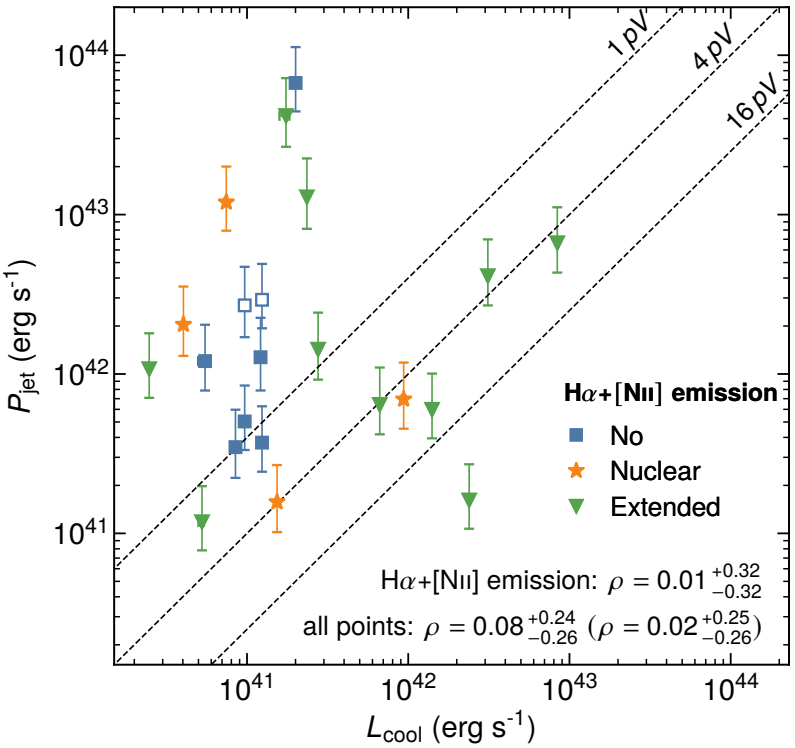

Figure 1.5: Relation between mechanical jet power and bolometric X-ray luminosity of the galactic atmosphere from within the cooling radius (*cooling luminosity*), which is the radius where the cooling time profile reaches the value of 1 Gyr. The diagonal dashed lines represent power input-output equalities for various values of cavity enthalpy (1pV, 4pV and 16pV). Correlation coefficients for the Hα+[NII] emitting sub-sample and the full sample are shown in the upper right corner. The larger scale radio lobes for NGC 1399 and NGC 4472 (blue empty squares) and the corresponding correlation coefficient (stated in parentheses) are also shown.

observations and state-of-the-art numerical simulations (Illustris TNG), Truong et al. (2021) shows that this is primarily due to an underlying correlation between the halo mass and the mass of the central supermassive black hole and jet heating will have a secondary effect. Our results show that more massive black holes will provide more heat to galactic atmospheres (see also Martín-Navarro et al., 2020), which could also contribute to the correlation between black hole mass and atmospheric gas temperature.

1.5 Conclusions

We have confirmed the presence of a correlation between the Bondi accretion power and the mechanical jet power in early-type galaxies previously reported by Allen et al. (2006). We show that a particularly strong correlation holds for galaxies with thermally unstable atmospheres, as indicated by the presence of cool gas traced by Hα+[NII] emission and with $\min(t_{\rm cool}/t_{\rm ff}) \lesssim 10$, while for the whole sample of galaxies the correlation is weaker.

Interestingly, according to the power-law fit for the Hα+[NII] subsample, the Bondi power scales with jet power as $\propto P_{\rm jet}{}^{1.10\pm0.25}$ with correlation coefficient of $\rho = 0.96^{+0.03}_{-0.09}$. We note that the exponent is remarkably close to unity, which yields a constant jet-to-Bondi power efficiency (11^{+6}_{-3} per cent).

Importantly, we find a strong correlation between the mechanical jet power ($P_{\rm jet}$) and the mass of the central supermassive black hole ($M_\bullet$) and, although poorly constrained, a hint of an anti-correlation

with the specific entropy (K) of the ambient gas inside the Bondi radius. The mechanical jet power for the galaxies with Hα+[NII] emission scales with the supermassive black holes mass as

$$\log \frac{P_{\rm jet}}{10^{43}\,{\rm erg\,s^{-1}}} = \alpha + \beta \log \frac{M_\bullet}{10^9\,M_\odot}, \tag{1.8}$$

where $\alpha = -0.62 \pm 0.14$ and $\beta = 1.79 \pm 0.36$ with a correlation coefficient of $\rho = 0.91^{+0.06}_{-0.11}$, while for the full sample the correlation is weaker.

The results indicate that at least for thermally unstable systems, the jet power is set primarily by the supermassive black hole mass. Since the central black hole mass of X-ray luminous early-type galaxies correlates with the total mass of the host halo (see Lakhchaura et al., 2019b; Truong et al., 2021), more massive systems undergoing thermally unstable cooling will naturally have larger jet powers.

Acknowledgements

This research was supported by the GACR grant 21-13491X. A.S. is supported by the Women In Science Excel (WISE) programme of the Netherlands Organisation for Scientific Research (NWO), and acknowledges the World Premier Research Center Initiative (WPI) and the Kavli IPMU for the continued hospitality. SRON Netherlands Institute for Space Research is supported financially by NWO. We acknowledge support from the U.S. Department of Energy under contract number DE-AC02-76SF00515. This research has made use of the NASA/IPAC Extragalactic Database (NED), which is funded by the National Aeronautics and Space Administration and operated by the California Institute of Technology. We acknowledge the usage of the HyperLeda database (http://leda.univ-lyon1.fr). The use of Very Long Baseline Array (VLBA) data is acknowledged. VLBA is operated by the National Radio Astronomy Observatory, which is a facility of the National Science Foundation, and operated under cooperative agreement by Associated Universities, Inc.

Annex 2

CAvity DEtection Tool (CADET): Pipeline for detection of X-ray cavities in hot galactic and cluster atmospheres

T. Plšek[1], N. Werner[1], M. Topinka[1,2] and A. Simionescu[3,4,5]

[1] Department of Theoretical Physics and Astrophysics, Masaryk University, Brno, Czech Republic
[2] INAF-Istituto di Astrofisica Spaziale e Fisica Cosmica, Via A. Corti 12, I-20133 Milano, Italy
[3] SRON Netherlands Institute for Space Research, Niels Bohrweg 4, 2333 CA Leiden, The Netherlands
[4] Leiden Observatory, Leiden University, PO Box 9513, 2300 RA Leiden, The Netherlands
[5] Kavli Institute for the Physics and Mathematics of the Universe, The University of Tokyo, Chiba 277-8583, Japan

Abstract: The study of jet-inflated X-ray cavities provides a powerful insight into the energetics of hot galactic atmospheres and radio-mechanical AGN feedback. By estimating the volumes of X-ray cavities, the total energy and thus also the corresponding mechanical jet power required for their inflation can be derived. Properly estimating their total extent is, however, non-trivial, prone to biases, nearly impossible for poor-quality data, and so far has been done manually by scientists. We present a novel machine-learning pipeline called *Cavity Detection Tool* (CADET), developed as an assistive tool that detects and estimates the sizes of X-ray cavities from raw *Chandra* images. The pipeline consists of a convolutional neural network trained for producing pixel-wise cavity predictions and a DBSCAN clustering algorithm, which decomposes the predictions into individual cavities. The convolutional network was trained using mock observations of early-type galaxies simulated to resemble real noisy *Chandra*-like images. The network's performance has been tested on simulated data obtaining an average cavity volume error of 14% at an 89% true-positive rate. For simulated images without any X-ray cavities inserted, we obtain a 5% false-positive rate. When applied to real *Chandra* images, the pipeline recovered 93 out of 97 previously known X-ray cavities in nearby early-type galaxies and all 14 cavities in chosen galaxy clusters. Besides that, the CADET pipeline discovered 7 new cavity pairs in atmospheres of early-type galaxies (IC 4765, NGC 533, NGC 2300, NGC 3091, NGC 4073, NGC 4125, NGC 5129) and a number of potential cavity candidates.

Keywords: methods: data analysis – techniques: image processing – software: data analysis – galaxies: active – galaxies: haloes – X-rays: galaxies

Published in Monthly Notices of Royal Astronomical Society (MNRAS), Volume 527, Issue 2, January 2024, Pages 3315–3346.

2.1 Introduction

Studies of hot atmospheres of galaxies, groups and clusters of galaxies underwent substantial progress at the turn of the millennium mainly due to the launch of three X-ray telescopes: *ROSAT*, *Chandra X-ray Observatory*, and *XMM-Newton*. Among many other important discoveries, their observations have revealed the existence of prominent surface brightness depressions, so-called *X-ray cavities*, in the hot atmospheres of clusters, groups, and massive early-type galaxies (Boehringer et al., 1993; Huang and Sarazin, 1998; McNamara et al., 2000a; Fabian et al., 2000; Blanton et al., 2001). Subsequent radio observations (McNamara et al., 2001; Fabian et al., 2002; Bîrzan et al., 2004) of these systems have shown that the cavities are filled with nonthermal relativistic electrons producing radio emission via synchrotron radiation. In the following two decades, several comprehensive studies of X-ray cavities and radio lobes in the atmospheres of nearby giant ellipticals (Dunn et al., 2010), distant galaxy clusters (Hlavacek-Larrondo et al., 2012, 2015) or both nearby and distant systems (Bîrzan et al., 2004; Rafferty et al., 2006; Diehl et al., 2008; Dong et al., 2010; McNamara et al., 2011; Panagoulia et al., 2014; Shin et al., 2016) were performed, tens of new cavities were discovered, and their underlying attributes were inferred.

The presence of extended radio emission suggests that the cavities are products of the interaction between the relativistic jets emanating from the active galactic nucleus (AGN) and the hot intergalactic medium (McNamara et al., 2000a). Signs of previous AGN activity can thus be observed either in the radio band as extended radio lobes or in the X-ray band as brightness depressions (X-ray cavities). For some of the cavities and especially for older cavity generations, however, the extended radio emission might be significantly misaligned (Gitti et al., 2006) or it can be completely missing ('ghost' cavities; McNamara et al., 2000b; Bîrzan et al., 2004). In such cases, X-ray cavities represent the only remnant of the previous AGN activity. The latest radio observations at MHz frequencies (GMRT, Giacintucci et al., 2011; LOFAR, Bîrzan et al., 2020; Capetti et al., 2022) have, however, revealed the existence of extended radio emission filling some of the X-ray cavities previously classified as 'ghost'.

The process of cavity inflation is expected to involve a significant amount of energy released by the central supermassive black hole (SMBH) and therefore play an important role in the energetics of the whole galactic atmosphere and the AGN feedback. For nearby radio galaxies, this type of radio-mechanical feedback is believed to be dominant over the energy expelled by electromagnetic radiation. Furthermore, the mechanical power of the AGN jet is, for radio-mechanical feedback, within an order of magnitude consistent with the expected accretion power (Allen et al., 2006; Plšek et al., 2022). The enormous amount of energy deposited in cavities and in the relativistic plasma is then on timescales of $10^7 - 10^8$ years being dissipated back into the hot atmosphere through shocks, sound waves and turbulent flows (Churazov et al., 2002; Werner et al., 2019). A detailed description of such processes is therefore crucial for understanding the evolution and energetic balance of the entire galaxy.

The comparison of basic cavity parameters and their corresponding mechanical jet powers with other underlying properties of their host galaxies has shown interesting implications. Bîrzan et al. (2004) reported that mechanical jet powers derived from the X-ray cavities correlate with the radio luminosity at 1.4 GHz and the X-ray luminosity of the host atmospheres. Similarly, Rafferty et al. (2006) found a relation between the mechanical jet powers and luminosity of the X-ray emitting gas from within a cooling radius (cooling luminosity). Allen et al. (2006) found a tight correlation between the mechanical jet powers determined from the combination of observations of radio lobes and X-ray cavities and approximate SMBH accretion powers estimated from the assumption of the spherical Bondi accretion, which has been confirmed by Plšek et al. (2022).

2.1.1 Properties of X-ray cavities

X-ray cavities, just like radio lobes, typically come in pairs and originate in a single relativistic outflow. Their observations show that cavities are discrete, separate bubbles rather than continuous funnel-

like structures, and for many galactic systems, even multiple generations of cavities are observed (e.g. NGC 5813; Randall et al., 2015). However, to this day it is not clear whether the discrete nature of X-ray cavities is a result of occasional episodic outbursts or whether they are caused by the fragmentation of relatively continuous outflows.

Many X-ray cavities are surrounded by shell-like or arm-like features of enhanced brightness. These bright rims correspond to regions of shocked or piled-up gas created by the inflation of cavities. Although shock fronts caused by the highly supersonic motion of material were expected, no significant temperature jumps connected with strong shocks were detected and some of the bright rims were even observed to be cooler than the surrounding gas (Fabian et al., 2000). Instead, mostly only mildly supersonic weak shock fronts are observed with Mach numbers between 1.2 and 1.7 (NGC 4636, Jones et al., 2002; NGC 5813, Randall et al., 2015), which are close to being in pressure balance with the ambient medium (McNamara and Nulsen, 2007). Nonetheless, these weak shocks, when present, can also deposit a significant amount of energy in the X-ray gas (e.g. NGC 5813, Randall et al., 2015).

As long as the inflation of cavities is ongoing, cavities are marked as 'attached' and due to the weak nature of the surrounding shocks, they are assumed to be inflated approximately at the speed of sound (Bîrzan et al., 2004). Once they detach from the central AGN, they rise buoyantly into the thinner lower-pressure environment and they increase their volumes to maintain pressure equilibrium with the surrounding medium. As a result, we can observe a correlation between cavity areas (or radii) and distances (Diehl et al., 2008; Dong et al., 2010; Shin et al., 2016). As they rise, part of their energy is extracted and, for an M87-like pressure profile (Böhringer et al., 2001), after reaching a 20 kpc distance, nearly half of the original energy is lost (Churazov et al., 2002). Moreover, rising cavities can drag the central low entropy gas, uplift it and thus dilute the hot atmospheres of host galaxies (e.g. M87, Werner et al., 2010).

Although X-ray cavities come in various shapes, they are most commonly approximated as prolate or oblate spheroids with rotational symmetry along the semi-axis closer to the direction towards the centre of the galaxy (see Bîrzan et al., 2004; Allen et al., 2006). X-ray cavities tend to have their semi-major axis either aligned or perpendicular to the galactocentric direction (Shin et al., 2016). Furthermore, cavities are preferentially elongated towards the centre for attached or recently detached outflows and flattened for formerly separated cavities (Churazov et al., 2001; Guo, 2020). We note, however, that many real cavities are far from being ideally ellipsoidal and their structure is much more complex, which is supported also by current idealized simulations of radio-mechanical AGN feedback (Brüggen et al., 2009; Mendygral et al., 2011, 2012; Guo, 2015).

Individual cavities vary significantly in their size and also in the amount of displaced material ranging from 0.5 kpc and 10^8 $M_\odot$ for NGC 4636 up to hundreds of kiloparsecs and more than 10^{12} $M_\odot$ for Hydra A (McNamara and Nulsen, 2007). The mechanical jet powers required to inflate typical X-ray cavities are of the order of $10^{41} - 10^{44}$ erg s^{-1}, however, for the largest X-ray cavities typically found in brightest cluster galaxies in massive clusters (Hercules A, Nulsen et al., 2005; MS0735.6+7421, Vantyghem et al., 2014) it can be up to 10^{46} erg s^{-1}, which is comparable to the power output of a typical powerful quasar.

2.1.2 Motivation

The total energy deposited in X-ray cavities and the corresponding mechanical jet power required for their inflation can be measured by estimating the volumes of X-ray cavities (e.g. Bîrzan et al., 2004). The accurate identification of X-ray cavities and estimation of their total extent is, however, non-trivial, prone to biases and nearly impossible for poor-quality data. Additionally, most of the current detection and size-estimation methods (unsharp masking, β-modelling), widely used in the previous studies of X-ray cavities (e.g. Bîrzan et al., 2004; Diehl et al., 2008; Dong et al., 2010; Panagoulia et al., 2014; Hlavacek-Larrondo et al., 2015; Shin et al., 2016), are all ultimately based on visual inspection and manual estimation of cavity sizes. The total extent of thereby identified and size-estimated cavities is, also

due to over-simplifying assumptions (ellipsoidal shape, rotational symmetry, projection effects), rather uncertain and difficult to reproduce among different studies performed by different teams.

The utilization of machine learning techniques has registered significant progress in the field of observational astronomy and astrophysics. It has great potential in the automation of tasks that would otherwise require human or even expert insight into the problematics. Neural networks and other machine learning techniques are already being widely used in various astronomical fields for classification tasks: point source vs extended source classification (Alhassan et al., 2018), galaxy morphology classification (Dieleman et al., 2015; Hausen and Robertson, 2020), radio galaxy morphology classification (Wu et al., 2019), detection of galaxy clusters using multiwavelength observations (Kosiba et al., 2020), distinguishing between astrophysical gamma-ray photons and cosmic-ray induced events in satellite observations (Shilon et al., 2019; Wilkins et al., 2022) or for distinguishing between single and multi-temperature plasma from X-ray spectra (Ichinohe and Yamada, 2019); for regression tasks: photometric redshift estimation (D'Isanto and Polsterer, 2018) and pre-fitting of X-ray spectral properties (Ichinohe et al., 2018); and also for more complex problems: predicting the cosmological structure formation (He et al., 2019) or producing hydrodynamical simulations by learning the basic physical laws (Dai and Seljak, 2021). In the past, there were also attempts aiming for cavity detection and size estimation using either granular convolutional neural networks (Ma et al., 2017) or Inception-like convolutional neural networks (Fort, 2017), the latter served as an inspiration for this work.

For these reasons, we have decided to tackle the problem of searching for and estimating the sizes of X-ray cavities on *Chandra* images using the power of machine learning techniques and modern computer technology. Using a set of artificially generated images, we have trained a detection pipeline composed of a convolutional neural network (CNN) and a clustering algorithm, which we have called the *CAvity DEtection Tool*[1] (CADET).

The paper is organised as follows. In Section 2.2, we describe how the set of artificial training images was generated and discuss our main assumptions. The architecture of the CADET pipeline, as well as the process of training and subsequent testing of the pipeline, are described in Section 2.3. In Section 2.4, we present results obtained by applying the CADET pipeline to a sample of 70 nearby early-type galaxies and 7 more distant galaxy clusters. We discuss the precision and accuracy of CADET predictions in Section 2.5 and we conclude in the last Section. In the Supplementary online material, we share the resulting CADET predictions for the whole sample of 70 nearby early-type galaxies and 7 distant galaxy clusters.

2.2 Artificial data

The CADET pipeline was trained on artificially generated mock images processed to resemble real X-ray images as observed by the *Chandra X-ray Observatory*. The real data was not used for the training for two main reasons: the number of known galactic systems with well-defined X-ray cavities is low, and even if the number of real images with cavities was sufficiently larger ($> 10^3 - 10^4$ images), all cavities would need to be manually size-estimated, which would bring a systematical human bias into the training process.

We, therefore, produced a large set of simplified 3D models of early-type galaxies and randomly inserted pairs of ellipsoidal cavities into them. The 3D models were then reprojected onto the 2D plane by simply summing the values across one axis – we used this approximation assuming that atmospheres of early-type galaxies are optically thin. Thereby obtained brightness maps were noised using Poisson statistics to resemble real low-count X-ray images.

The gas distribution of the 3D galaxy models was generated based on observed surface brightness profiles of nearby early-type galaxies. To approximate the gas distribution in both real and simulated

[1] `https://github.com/tomasplsek/CADET`

galaxies, we used either single or double β-models (Cavaliere and Fusco-Femiano, 1976):

$$\rho_{\rm gas}(r) = \rho_0 \left[1 + \left(\frac{r}{r_0}\right)^2\right]^{-3\beta/2}, \tag{2.1}$$

where r_0 is the core radius, ρ_0 is the central density and β is the beta parameter, which describes the logarithmic slope of the distribution at larger radii. The resulting surface brightness of the simulated images was obtained as an emissivity of the gas $\epsilon(r) = \Lambda(T)\, n_{\rm p}^2(r)$, where $n_{\rm p} = \rho_{\rm gas}/(2.21\, m_{\rm p})$, and $\Lambda(T)$ is the cooling function of the X-ray emitting gas (see Schure et al., 2009).

We note that the gas distribution in real galaxies is often not ideally smooth and symmetric but is disrupted by sloshing effects and cold fronts due to past mergers (NGC 1275, Fabian et al., 2006; NGC 4696, Sanders et al., 2016), ram pressure striping (NGC 1404, Machacek et al., 2005; NGC 4552, Kraft et al., 2017), shock fronts (NGC 4552, Machacek et al., 2006; NGC 5813, Randall et al., 2015), and also by a low entropy gas uplifted by the inflation of X-ray cavities (e.g. NGC 4486, NGC 4696; see also Churazov et al., 2001; Simionescu et al., 2008; Werner et al., 2010). However, realistically simulating such inner structure is beyond the scope of this work and it would be reachable only using detailed hydrodynamical simulations of radio-mechanical feedback in early-type galaxies. Instead, we tried to reproduce these irregularities by generating simple geometrical features tailored to resemble real observed structures on a purely empirical basis.

To imitate the non-spherical perturbation of gas distribution brought on by gas sloshing, we generated a 2D grid with an anti-symmetric spiral-like pattern and, before applying Poisson noise, we multiplied the surface brightness maps with this grid. Basic parameters of the spiral pattern (e.g. periodicity and depth) were generated according to real galaxies with prominent sloshing patterns (e.g. NGC 507, NGC 1275, NGC 4696, NGC 7618) and are based on basic assumptions further discussed in Section 2.2.2.

Real images of galaxies also contain bright point sources such as background AGNs, distant galaxies, and stellar sources located in the host galaxy: Low Mass X-ray Binaries (LMXB), Coronally Active Binaries (CAB) or Cataclysmic Variables (CV) (Irwin et al., 2003). Besides that, the central parts of many galaxies are often dominated by point-like non-thermal emission of their AGNs, and some of them might even contain prominent jets (e.g. NGC 315, NGC 383, NGC 4261, NGC 4486). However, we did not take the point sources and jets into account while generating the artificial dataset. Instead, before applying the CADET pipeline to real *Chandra* images, we detected all point sources except for the central one and replaced them with their average surrounding background (see Section 2.2.1).

To account for X-ray cavities, we randomly generated pairs of ellipsoidal masks and cut off the corresponding regions from our 3D models. The gas inside cavity regions has been removed completely assuming that they are filled purely with relativistic plasma not producing any X-ray emission (McNamara and Nulsen, 2012), which is supported also by Sunyaev-Zeldovich observations (e.g. MS0735, Abdulla et al., 2019, Orlowski-Scherer et al., 2022). X-ray cavities were generated at various galactocentric distances, radii and shapes (ellipticities) – their parameters were sampled from distributions based on measurements of real X-ray cavities (Section 2.2.2). When generating the cavities, we tried to both entirely remove the gas from the corresponding regions as well as displace part of it to the edges of cavities to resemble bright rims caused by shocks. The rims were generated as ellipsoidal shells of the same ellipticity as the corresponding cavities (see Section 2.2.2).

2.2.1 Data analysis

When generating 3D β-models of artificial galaxies, their parameters were sampled from distributions derived from β-modelling analysis of real X-ray observations. For this purpose, we fitted a sample of 70 nearby early-type galaxies with a single or double β-model and determined the parameters and uncertainties describing the best-fitting models.

Observations of all galaxies were processed using standard CIAO 4.14 procedures (Fruscione et al., 2006) and current calibration files (CALDB 4.9.8). For galaxies with multiple *Chandra* observations, individual OBSIDs were reprojected and merged. All observations were deflared using the `lc_clean` algorithm within the `deflare` routine. Most objects were observed using the ACIS-S chip, however, for some galaxies, we included also ACIS-I observations. All the OBSIDs are listed in Table A.2.3.

The images were generated from reprojected and cleaned observations using the `flux_obs` procedure with a bin size of 1 pixel (0.492 arcsec) in the broad energy band (0.5 – 7.0 keV). Point sources were found using the `wavdetect` tool and filled with an average surrounding background using the `dmfilth` procedure. Before applying the `dmfilth` script, the exposure-corrected flux images were converted back to units of counts (scaled by the lowest non-zero pixel value) to enable the use of Poisson statistics.

Individual processed and source-filled images were, based on the scale of interest of each galaxy, cropped to the size of an integer multiple of 128 *Chandra* pixels, mostly to 512 pixels or 640 pixels. For galaxies with prominent cavities, the scale of interest was chosen to encompass the outer edge of cavities (oldest cavities if more were present). For galaxies without any visible cavities, the scale of interest was visually chosen to enclose most of the galactic emission or set to the edge of the chip for very extended sources (e.g. NGC 4406).

The resulting cropped images were fitted with a 2D representation of a single or double β-model – for the purpose of modelling the surface brightness distribution of X-ray images, a classical 3D β-model (Cavaliere and Fusco-Femiano, 1976) has been projected onto a 2D plane under the assumption of isothermality and thus constant emissivity (Ettori, 2000):

$$S(r) = n_0^2 \, \Lambda(T) \, r_0 \, B(3\beta - 0.5, 0.5) \left[1 + \left(\frac{r}{r_0} \right)^2 \right]^{0.5-3\beta}, \tag{2.2}$$

where n_0 is the central particle concentration, $\Lambda(T)$[2] is the cooling function, B is the beta function, r_0 is the core radius and β is the beta parameter of the β-model. When using composite β-models, individual β-components were simply summed together. For all galaxies, we also added a constant background model (c_0).

The fitting was performed in the SHERPA 4.14 package (Freeman et al., 2001) using Cash statistics (Cash, 1979) and Levenberg-Marquardt optimization method (Levenberg, 1944). Within the SHERPA 4.14 package, each β-model is described by a set of 7 parameters: centre coordinates x_0 and y_0, amplitude A, core radius r_0, power-law slope α, ellipticity e and rotational angle φ; and following equations[3]:

$$r^2 = \frac{(x_0 - x)^2 (1 - e)^2 + (y_0 - y)^2}{r_0^2 (1 - e)^2}, \tag{2.3}$$

$$S(r) = A \left(1 + r^2 \right)^{-\alpha}. \tag{2.4}$$

For simplifying the fitting process, an interactive Python tool[4] based on Jupyter Ipywidgets was developed. Using this tool, the galaxies were first fitted using a single β-model and for galaxies for which it introduced a significant improvement in the fit statistics, we included an additional beta component. For double β-models, both ellipticities and, for most objects, also the central coordinates of individual components were linked together during the fitting. In several cases (mainly for images with a low

[2] For simplicity, the temperature and thus also the cooling function was assumed to be the same for all the analyzed as well as generated galaxies and the cooling function was therefore omitted from further calculations. We instead accounted for a scatter of 0.3 dex in the distribution of the β-model amplitudes, which corresponds to the difference of cooling functions at 0.5 and 2.5 keV at solar abundance.

[3] For simplicity, rotations of the XY grid by the angle φ were omitted.

[4] `https://github.com/tomasplsek/Beta-modelling`

number of counts but a complex radial profile), we even tied the β parameters of individual beta components in order to reduce the number of free parameters. After finding the best-fitting β-models, median values and uncertainties of individual parameters were derived from their posterior distributions obtained from Markov-Chain-Monte-Carlo (MCMC) simulations (pyBLoCXS algorithm; Siemiginowska et al., 2011). The fitted parameters with their uncertainties are listed in Table A.2.2. Plots with distributions of parameters for the whole sample of galaxies and correlations between them can also be found in Figures A.2.4, A.2.5.

The best-fitting β-models were subtracted from the original images and smoothed versions of thus obtained residual images were used to visually detect X-ray cavities. Individual detected cavities were size-estimated by manually overlaying ellipses using the *SAOImageDS9* software (Joye and Mandel, 2003). Significances of estimated cavities were probed using azimuthal surface brightness profiles (see Hlavacek-Larrondo et al., 2015; Ubertosi et al., 2021) and we only chose cavities with depth lower than or equal to 3σ below the surrounding background. Combining this method with known cavities from the literature (see Table A.2.1 and references therein), we detected in total 97 cavities in 34 galaxies.

To describe a pair of X-ray cavities, we introduced 10 parameters (see Figure 2.1) – parameters describing the first cavity: distance from the galactic centre d, positional angle $\phi_{\rm cav}$, semi-major axis R, ellipticity $e_{\rm cav}$, rotational angle $\varphi_{\rm cav}$, and parameters describing the second cavity with respect to the first one: relative change in distance $r_{d_{\rm cav}}$, difference in positional angle $d\phi_{\rm cav}$, relative change in semi-major axis $r_{R_{\rm cav}}$, relative change in ellipticity $r_{e_{\rm cav}}$, and difference in rotational angle $d\varphi_{\rm cav}$. Properties of all significant cavities were derived and are stated in Table A.2.3 (see also Figures A.2.6, A.2.7).

2.2.2 Parameter distributions

Some of the parameters describing β-models and X-ray cavities can occur according to certain distributions and may even correlate with others (e.g. cavity sizes and distances), while others are naturally totally random (e.g. rotational angle of β-model). In order to properly reproduce real observations, we, therefore, derived the distributions from our β-modelling and cavity analyses and we sampled the parameters of simulated data from approximations of those distributions[5] (further described in Section 2.2.3).

Although most of the parameters were uncorrelated and therefore could have been generated purely from their measured marginal distributions, some of them seem to correlate strongly with others. We tried to uncover these relations and take them into account while generating the artificial dataset. Linear correlations were identified using the Pearson product-moment correlation coefficient (r) (Fisher, 1944). We also investigated monotonous but nonlinear correlations using Kendall's Tau coefficient (τ) (Kendall, 1938). Corresponding correlation coefficients are stated above plots of individual quantity pairs in Figures A.2.4, A.2.5, A.2.6, and A.2.7.

Correlations were found between individual parameters of the primary β-component as well as between primary and secondary β-components. Parameters of secondary β-components were therefore generated with respect to the primary component. Among other key correlations, we found the correlation between β parameters, core radii and amplitudes of the primary β-component especially important because these parameters define the total number of counts of the resulting images (see Figure 2.2). It is, therefore, necessary to simulate these parameters according to the correlated distributions, because populating uniformly the whole parameter space would result in generating a big number of images with either an extremely low ($< 10^3$) or unrealistically high ($> 10^7$) number of counts, both of which are not suitable for training the network.

[5]We note that the measured distributions may suffer from systematic effects and biases and are representative only of the given sample of galaxies. For the purpose of this work, however, we sampled the parameters of simulated galaxies directly from measured distributions and thus we 'optimized' the CADET pipeline for the given sample of 70 early-type galaxies.

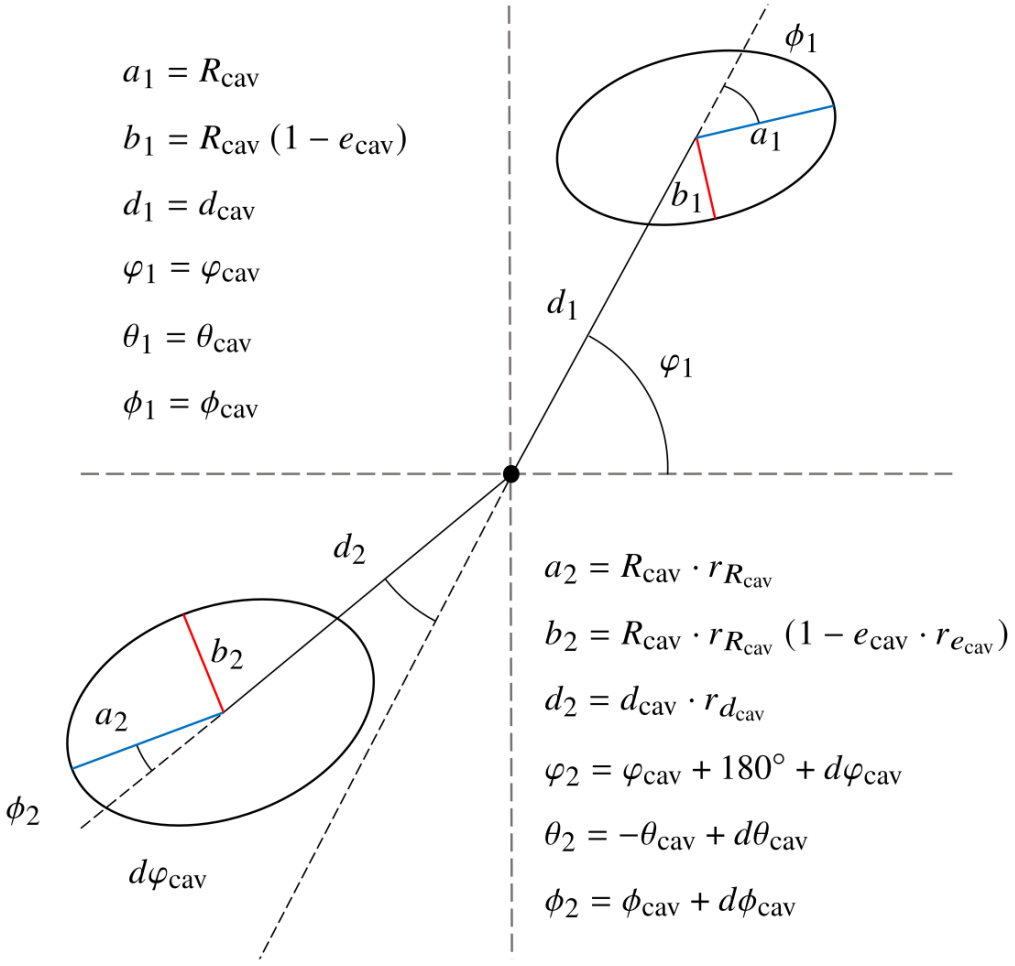

Figure 2.1: Parametric model of a pair of X-ray cavities – each cavity is described by a set of 6 parameters: distance from the galactic centre d, semi-major axis R_{cav}, ellipticity e_{cav}, positional angle φ_{cav}, positional angle with respect to the line-of-sight θ_{cav}, and rotational angle ϕ_{cav}. Due to the parameters of both cavities being closely correlated, parameters of the secondary cavity (d_2, a_2, b_2, φ_2, θ_2, ϕ_2) were expressed with respect to the primary cavity using relative ($r_{d_{\mathrm{cav}}}$, $r_{R_{\mathrm{cav}}}$, $r_{e_{\mathrm{cav}}}$) and differential factors ($d\varphi_{\mathrm{cav}}$, $d\theta_{\mathrm{cav}}$, $d\phi_{\mathrm{cav}}$.) Positional angles with respect to the line-of-sight direction were for simplicity omitted from the scheme.

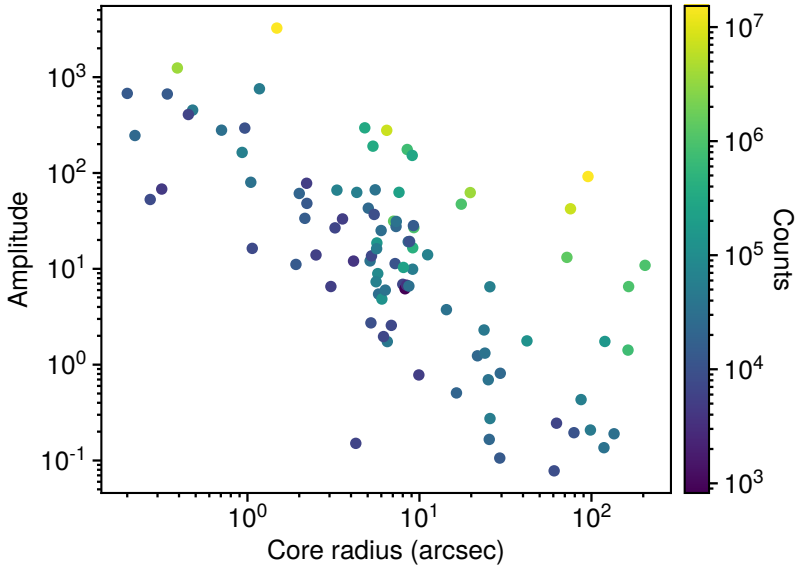

Figure 2.2: Colour-coded number of counts in 512 × 512 images for a sample of 70 nearby early-type galaxies as a function of the core radius and amplitude of the primary β-model. The plot shows that the number of counts is, with certain scatter given by different values of β parameter and level of background (c_0), proportional to the product of core radius and amplitude of their best-fitting β-model.

Parameters of individual cavities within the cavity pair were expected to be correlated from the beginning of the analysis and parameters of secondary cavities were therefore expressed directly via relative and differential coefficients with respect to primary cavities (see Figure 2.1). Among other correlated primary cavity parameters, a very strong correlation ($r = 0.94$) is observed between galactocentric distances of cavities and their radii[6]. One of the consequences of sampling from these correlated distributions is that simulated cavities will not have bigger radii than their separation from the centre and therefore they will not intersect each other or the galactic centre. Sampling from such a correlated distribution will also not produce hardly detectable, very small cavities located far from the centre.

2.2.3 Dataset generation

For generating artificial images, we used single and double β-models. Their relative frequencies were estimated from our β-modelling analysis described in Section 2.2.1 to be nearly 50 % and 50 % for single and double β-models, respectively. Into each galaxy model, we inserted either one or zero cavity pairs in order for the network to learn the possibility that there can also be no cavities present in the image. Other features (bright cavity rims, sloshing effects) were generated based on their probabilities stated in Table 2.1 and randomly combined.

Central coordinates of β-models were set to be equal to the centre of the image with random Gaussian variation in both axes with a 1-pixel standard deviation. For double β-models, the central coordinates of individual components were not linked together but generated independently from the same distribution. Positions of X-ray cavities were generated with respect to the coordinates of the centre of the β-model (the most compact one for multiple beta components).

Except for ellipticities, which are for most galaxies clustered at zero and follow an approximately exponential distribution, and rotational angles, which by nature should be distributed uniformly randomly

[6]The existence of this correlation is probably a combination of physical (cavities grow as they rise into decreasing pressure) and selection effects (detectability of small cavities drastically decreases with their distance).

Table 2.1: Parameter ranges and distributions used for sampling parameters of training and testing data. For positional angles of β-models (φ, φ_2) and X-ray cavities ($\varphi_{\rm cav}$), a uniform distribution between 0 and 360 degrees was used since both should emerge at random orientations. Distributions of parameters describing bright rims and sloshing effect were generated uniformly randomly and are based on basic assumptions further discussed in Section 2.2.2. The rest of the parameters that could have been determined from observed properties of real galaxies (from data) were derived from β-modelling or cavity analyses.

Parameter	Distribution	Range
primary beta model (100 %)		
dx_0	from data	±1 pixels
dy_0	from data	±1 pixels
r_0	from data	$0.1-20$ pixels
α	from data	$0.45-1.40$
A	from data	$1-1000$
e	from data	$0-0.3$
φ	uniform	$0^\circ-360^\circ$
c_0	from data	$0.001-5$
secondary beta model (50 %)		
$r_{c,2}$ / r_c	from data	$5-55$
A_2 / A	from data	$0.005-1$
α_2 / α	from data	$1-6$
φ_2	uniform	$0^\circ-360^\circ$
primary cavity parameters (50, 90 or 100 %)		
$d_{\rm cav}$	from data	$5-60$ pixels
$R_{\rm cav}$	from data	$5-30$ pixels
$e_{\rm cav}$	from data	$0-0.65$
$\varphi_{\rm cav}$	uniform	$0^\circ-360^\circ$
$\phi_{\rm cav}$	from data	$\pm90^\circ$
$\theta_{\rm cav}$	normal	$\pm25^\circ$
secondary cavity parameters		
$r_{d_{\rm cav}}$	from data	$0.4-1$
$r_{R_{\rm cav}}$	from data	$0.5-1$
$r_{e_{\rm cav}}$	from data	$0-1$
$d\varphi_{\rm cav}$	from data	$\pm65^\circ$
$d\phi_{\rm cav}$	from data	$\pm90^\circ$
$d\theta_{\rm cav}$	normal	$\pm10^\circ$
cavity rims (20 % of cavities)		
width	uniform	$0.05-0.6$
height	uniform	$0-0.25$
type	binary	{I, II}
sloshing effect (33 %)		
periodicity	uniform	$0.5-2.5$
depth	uniform	$0-0.15$
angle	uniform	$0^\circ-360^\circ$
direction	binary	{-1, +1}

between 0 and 360 degrees, marginal distributions of all other parameters were close to normal (Gaussian). All other parameters of single β-models were therefore randomly sampled from approximations of their measured distributions. For double β-models, parameters (r_0, β and A) of secondary components were generated with respect to the parameters of the primary component. Rotational angles of individual beta components were generated independently and their ellipticities were all tied with respect to the primary component.

Similarly, as for β-models, plane-of-the-sky positional angles of primary cavities were expected to be uniformly random in the range from 0 to 360 degrees. All other cavity parameters were generated based on their measured distributions. Among all the distributions, strong deviations from normality are observed only in the distribution of rotational angles (angle between cavity semi-major axis and galactocentric direction) – cavities tend to have their semi-major axis either aligned ($\phi_{\rm cav} \approx 0°$; prolate shape) or perpendicular ($\phi_{\rm cav} \approx 90°$; oblate shape) to the galactocentric direction, which is in a good agreement with results of Shin et al. (2016). Although positional angles along the line-of-sight should also be naturally random, it is not possible to estimate them from X-ray observations and usually X-ray cavities are assumed to lie directly in the plane of the sky. As discussed later (see Section 2.5.2), this assumption is good enough for most cavities, since their detectability decreases steeply at higher launching angles. When generating artificial images we have, however, varied the line-of-sight positional angles by drawing them from a normal distribution with zero mean and standard deviation of 20 degrees[7]. Rotational angles along the line of sight were for simplicity omitted.

Since the CADET pipeline can only input 128 × 128 images, real images will usually be probed on multiple scales by binning variously cropped images into 128 × 128 pixels (see Section 2.4). For most of the galaxies, images will maximally be cropped to 512 pixels (4 binning) and minimally to 64 pixels (0.5 binning). When simulating artificial galaxy models, core radii of β-models are, however, generated in units of arcsec based on the measured distribution of core radii in real images (later transformed to *Chandra* pixels; 1 pixel ≈ 0.4928 arcsec). In order to sufficiently adapt the training data for the possibility of probing images on different scales, before generating 3D models of galaxies, we rescaled core radii[8] by a random factor in the range from 1 (512 pixels) to 8 (64 pixels). Radii and distances of X-ray cavities have also been rescaled to always be located within the simulated 128 × 128 image.

When sampling parameters of simulated β-models and X-ray cavities, the parameters were drawn from an approximation of measured distributions (see Figures A.2.4, A.2.5, A.2.6, and A.2.7). For approximating the measured distributions, we used a Gaussian kernel density estimation (KDE) truncated at data margins[9] taking into account also multidimensional correlations. For a single β-model with a pair of cavities, the parameters were therefore drawn from a 19-dimensional correlated parameter space (7 for the β-model, 12 for a pair of cavities) and additional 7 parameters describing bright rims and gas sloshing were generated uniformly randomly.

The bright rims around cavities representing shocked or entrained regions were produced for approximately one-fifth of generated cavities. The rims were generated as ellipsoidal shells of the same ellipticity as corresponding cavities and they can be in general described by many various parameters. For simplicity, we linked the parameters of individual rims within a cavity pair together and assumed only 3 basic parameters: *width*, *height* and *type* of the rim. Values of the *width* of the rim were drawn from a uniform distribution ranging from 0.05 to 0.6 times the radius of the cavity. For the *height* of the rim, we assumed a uniform distribution from 0 to 0.25 times the local surface brightness at the position of the rim. The actual height of the rim was set to be linearly decreasing from its maximal value (*height*) at the inner side of the rim to zero at the outer side, so a sharp boundary of the rim is only produced at its

[7] In the preliminary training phase, we also tried other standard deviations (0°, 10°, 30°, 40°), however, the best performance was obtained using the standard deviation of 20 degrees.

[8] Based on Eq. 2.2, we also rescaled amplitudes of β-models accordingly.

[9] Distributions of all parameters were not truncated directly at data margins, but instead, we used a 10 per cent overlay where possible in order to properly populate the parameter space even around extreme values.

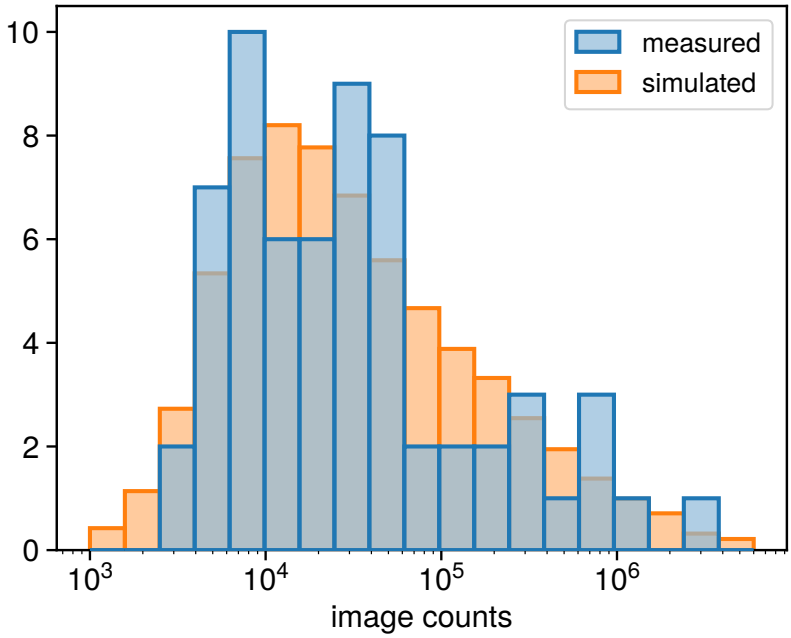

Figure 2.3: Number-of-counts distributions for real *Chandra* images (blue) and simulated data (orange). The distribution of a number of counts for simulated images was obtained by simulating 14000 images, the parameters of which were sampled from identical distributions as used for training of the network.

inner edge. Bright rims were produced in two different realizations (Figure A.2.8) – type I: the height of the rim decreases with angular distance from the minor axis, and type II: the height of the rim decreases with the physical distance from the centre of the cavity. The relative frequency of each rim type is 50 %.

The effects of gas sloshing were simulated for approximately one-third of galaxies by multiplying the original surface brightness map with a grid of spiral-like pattern (see Figure A.2.8). The values in the grid are axially anti-symmetric with a mean value of 1, and the whole pattern can be described by four parameters: *periodicity* describing the number of angular periods within the image, *depth* which represents a maximal / minimal value of the whole pattern, *starting angle* of the 'overdensity / under-density' boundary, and *direction* that sets if the pattern is clockwise or anti-clockwise. The possible values of the *periodicity* were taken from a uniform distribution from 0.5 to 2.5, the *depth* of the 'overdensity / under-density' field was drawn from a uniform distribution between 0 and 0.15, the *starting angle* of the spiral pattern was generated uniformly randomly (0 to 360 degrees) and the *direction* was either clockwise (+1) or anti-clockwise (-1).

Before the training process, a large number ($\approx 10^6$) of simulated parameters was generated and saved into a CSV file. By comparing generated parameters to their measured distributions, we can see a good agreement between the distributions. We also tested an agreement for numbers of counts (Figure 2.3) between simulated and real images by simulating a set of 14000 mock images which later served as validation and testing images.

2.3 Cavity Detection Tool

The *CAvity DEtection Tool* (CADET) consists of a convolutional neural network (CNN) composed of a series of Inception-like convolutional blocks (Szegedy et al., 2015) and a density-based spatial clustering algorithm (DBSCAN; Ester et al., 1996). The CNN part of the pipeline is trained for finding pairs of elliptical surface brightness depressions (X-ray cavities) on noisy *Chandra*-like images of early-type galaxies

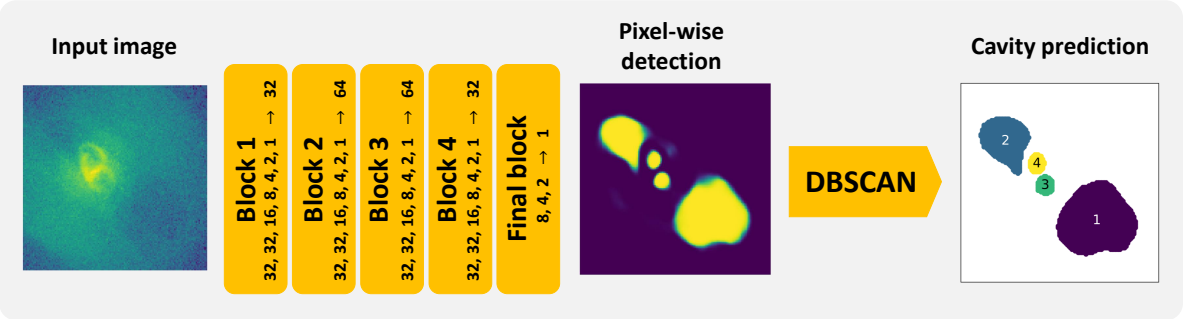

Figure 2.4: The architecture of the CADET pipeline consisting of a convolutional neural network (composed of five Inception-like convolutional blocks) producing a pixel-wise cavity prediction and a clustering algorithm `DBSCAN`, which decomposes the prediction into individual cavities. The number of individual filters within the Inception layers and subsequent dimensionality-reducing layers is stated alongside individual blocks. The scheme is inspired by Fig. 3 in Fort (2017).

and for producing pixel-wise predictions of their position and total extent. The clustering algorithm is used for the decomposition of thereby obtained predictions into individual cavities (Figure 2.4). The creation of the pipeline was inspired by the work of Fort (2017) and Secká (2018), although we made several changes in the network and mainly also in the process of generating the artificial dataset.

The convolutional neural network (CNN) was implemented using a high-level Python *Keras* library (Chollet et al., 2015) with *Tensorflow* back-end (Abadi et al., 2015). The CNN was written using a functional *Keras* API which enables saving and loading the model into the Hierarchical Data Format (HDF5) without the need to re-define the model when loading. For the clustering task, we used the DBSCAN implementation in the *Scikit-Learn* library (Pedregosa et al., 2011). For monitoring learning curves, comparing final test statistics and selecting optimal hyper-parameters, we used the *Tensorboard* dashboarding tool (Abadi et al., 2015). The final model as well as training and data generating scripts can be found on CADET Github page[10].

Elliptical β-models and ellipsoidal cavities were generated with the use of the *JAX* library[11] (version 0.2.26; Bradbury et al., 2018). Thanks to the Graphical Processing Unit (GPU) support of the *JAX* library, training images were generated 'on the fly' in a vectorized way using the same GPU as was used for training of the network. This dramatically improved the data generation time compared to generating the data using a CPU and also enabled additional tweaking of the parameters of training images between individual training runs (e.g. the fraction of images containing X-ray cavities). To enable the comparison of CADET performance for various values of network hyper-parameters, a fixed set of testing images with X-ray cavities (10^4 images), testing images without X-ray cavities (2000 images) and validation images (2000 images) were generated before the entire training process.

2.3.1 Network architecture

On the input of the CNN, there is a single channel 128×128 image. Since radial profiles of β-models in both real and simulated images are rather exponential, we transform the input images by a decimal

[10] `https://github.com/tomasplsek/CADET`
[11] `https://github.com/google/jax`

logarithm[12] (the value of each pixel was raised by one to avoid calculating the logarithm of zero). Before the images are processed by the first Inception-like convolutional block, they are further normalized in mini-batches by a batch-normalization layer within the convolutional neural network.

The architecture of the convolutional neural network is similar to that developed by Fort (2017) and is composed of a series of 5 convolutional blocks (Figure 2.4). Each block resembles an Inception-like layer (Szegedy et al., 2015) as it applies a set of multiple parallel 2D convolutional layers with various kernel sizes and concatenates their outputs (Figure A.2.9). Inception layers within the first 4 blocks consist of convolutional layers with 32 of 1×1 filters, 32 of 3×3 filters, 16 of 5×5 filters, 8 of 7×7 filters, 4 of 9×9 filters, 2 of 11×11 filters, and one 13×13 filter. The output of each convolutional layer within the Inception-like layer is activated by Rectified Linear Unit (ReLU; Fukushima, 1975) activation function, and then normalized by batch normalization (Ioffe and Szegedy, 2015). As opposed to the original Inception block (Szegedy et al., 2015), we omitted the max-pooling layer because it did not bring any performance improvement. Each Inception layer is then followed by a 2D convolutional layer with 32 or 64 of 1×1 filters, which is introduced mainly due to dimensionality reduction. The output of this convolutional layer is also activated using the ReLU activation function and batch-normalized. The 1×1 convolutional layers are, in order to prevent overfitting, followed by a dropout layer, where the dropout rate was varied as a hyper-parameter.

The convolutional neural network is ended by a final block, which is also composed as an Inception-like layer but differs from the previous blocks by the numbers and sizes of individual 2D convolutional filters (8 of 8×8 filters, 4 of 16×16 filters, 2 of 32×32 filters, and one 64×64 filter) and also by the activation function of the last 1×1 convolutional filter. Since the output of the network is intended to be a prediction of whether a corresponding pixel belongs to a cavity (value 1) or not (value 0), the activation function of the final layer was set to be the *sigmoid* function, which outputs real numbers in the range between 0 and 1.

Initial weights of individual 2D convolutional layers were generated using He initialization (He et al., 2015) and biases were initialized with low but non-zero values (0.01). In total, the network has 563 146 trainable parameters and the size of the model, when saved in the HDF5 format, is 7.4 MB.

On the output of the CNN, there is a pixel-wise prediction of the same shape as the input image with a value in each pixel ranging from 0 to 1, which expresses whether that pixel corresponds to a cavity or not. The pixel-wise prediction is then decomposed into individual cavities using the DBSCAN clustering algorithm. Before the decomposition, a pair of discrimination thresholds are applied for the pixel-wise prediction excluding low-significance regions and keeping only solid cavity predictions while properly estimating their areas and volumes (see Appendix A.2.2).

2.3.2 Training

During the training, the convolutional neural network was given a set of 128×128 training images on the input, and as ground truth images on the output, we used cavity masks projected into 128×128 images and binned to contain either ones (inside the cavity) or zeros (outside of it)[13]. For galaxies with no inserted cavities, the ground truth output image was represented by a zero matrix.

The loss function of the network was calculated as the binary cross-entropy of the pixel-wise prediction with respect to the ground truth image:

$$\mathscr{L} = -\frac{1}{N}\sum_{i}^{N} y_{\mathrm{true},i} \cdot \log y_{\mathrm{pred},i} + (1 - y_{\mathrm{true},i}) \cdot \log(1 - y_{\mathrm{pred},i}), \tag{2.5}$$

[12] We tested various approaches to input image normalization including widely used techniques incorporated in *Scikit-Learn* or *Keras* libraries (e.g. zero mean, unit variance), however, the best results were obtained for the above-stated approach.

[13] We also tried not binning label masks to express depths of cavities (with MSE as loss function and ReLU as last layer activation function). However, this drastically worsened the performance of the network.

Table 2.2: Hyper-parameters and test statistics for individual training runs: fraction of cavities in training data, learning rate, dropout, test loss function, average absolute volume error, false-positive (FP) rate, true-positive (TP) rate, real data performance. The loss function, average cavity volume error and true-positive rate were calculated using the set of testing images with X-ray cavities (10000 images), while the false-positive rate correspond to the dataset of images without any X-ray cavities (2000 images). Optimal hyper-parameters are marked in boldface.

Cavities (%)	Learning rate	Dropout	Loss function	Average error (%)	TP rate	FP rate	Real data performance
50	0.0005	0.0	0.056	14^{+11}_{-9}	0.78	0.03	6/6
50	0.0005	0.2	0.057	15^{+13}_{-8}	0.79	0.02	4/6
90	0.0005	0.0	0.051	14^{+13}_{-7}	0.81	0.04	2/6
90	0.0005	0.2	0.049	14^{+14}_{-8}	0.83	0.07	2/6
100	0.0005	0.0	0.041	16^{+15}_{-8}	0.87	0.08	5/6
100	**0.0005**	**0.2**	0.042	14^{+13}_{-8}	0.89	0.05	6/6
50	0.001	0.0	0.052	14^{+12}_{-7}	0.80	0.01	2/6
50	0.001	0.2	0.057	14^{+12}_{-7}	0.76	0.02	3/6
90	0.001	0.0	0.044	15^{+12}_{-8}	0.84	0.04	5/6
90	0.001	0.2	0.048	15^{+12}_{-8}	0.84	0.07	4/6
100	0.001	0.0	0.051	16^{+14}_{-9}	0.86	0.19	1/6
100	0.001	0.2	0.040	15^{+13}_{-8}	0.86	0.07	2/6
50	0.002	0.0	0.061	15^{+11}_{-8}	0.75	0.02	2/6
50	0.002	0.2	0.063	16^{+15}_{-8}	0.78	0.08	3/6
90	0.002	0.0	0.052	15^{+12}_{-8}	0.82	0.07	1/6
90	0.002	0.2	0.073	19^{+18}_{-10}	0.80	0.11	3/6
100	0.002	0.0	0.044	15^{+13}_{-8}	0.86	0.12	1/6
100	0.002	0.2	0.042	15^{+12}_{-8}	0.86	0.07	1/6

where $y_{\text{true},i}$ is the value in the i-th pixel of the binary cavity mask (ground truth), $y_{\text{pred},i}$ is the value in the i-th pixel of the pixel-wise prediction, and N is the total number of pixels in each image. The minimization of the loss function was realized using the *Adaptive Moment Estimation* (ADAM) optimizer (Kingma and Ba, 2014). The learning rate of the ADAM optimizer was varied as a hyper-parameter and the decay of the learning rate was for all runs set to zero.

During the training, we examined various sets of hyper-parameters describing the data and also the network itself: the fraction of images containing X-ray cavities (50 %, 90 % or 100 %), learning rate (0.0005, 0.001, 0.002), and dropout rate (0.0, 0.2). The batch size was not varied as a hyper-parameter, and for all networks, it was set to 24 images per mini-batch, which corresponds to the maximal possible batch size due to large GPU memory consumption caused by on-the-fly data generation. We tested all combinations of hyper-parameters and produced 18 trained networks in total (see Table 2.2).

All networks were first trained for 32 epochs, wherein each epoch the network was given 12288 images. Nevertheless, instead of using the same images every epoch, we continuously generated new data by sampling their parameters from identical distributions. During the training, the network was therefore given 393 216 different images in total. After every epoch, the performance of the network was validated using a fixed set of 2000 validation images. For controlling the learning rate, in order for the network to prevent overfitting, we utilized the `ReduceLROnPLateau` *Tensorflow* callback, which reduces the learning rate when the validation loss (loss function calculated for the validation dataset) stops im-

proving in a given number of epochs. The training of all networks including on-the-fly data generation was performed on NVIDIA GPU type GeForce RTX 3080 (10 GiB) and lasted approximately 8 hours per single network. The network with the best performance was trained for additional 32 epochs and further tested using the testing dataset.

2.3.3 Testing

To compare the performance of individual networks, we calculated the cross-entropy loss function for the whole testing dataset, true-positive (TP) rate for testing images with X-ray cavities (10^4 images) and false-positive (FP) rate for testing images without X-ray cavities (2000 images). For correctly recovered X-ray cavities (true-positives), we also compared inferred cavity volumes to their real values known from the simulations and calculated their average differences. We note, however, that the accuracy of CADET predictions depends strongly on the total number of counts of the given images (further discussed in Section 2.5.1). For this reason, individual testing statistics were also computed as a function of the number of counts and corresponding dependencies were logged and compared using *Tensorboard* callback.

For qualitative comparison, we picked 3 real images with well-defined and obvious cavities (NGC 4649, NGC 4778 and NGC 5813), and 3 images with hardly detectable cavities due to more complex features (NGC 1600, NGC 4552, NGC 6166) and we visually compared CADET predictions with presumed cavity extent estimated manually. Real-data performance was based upon visual inspection of CADET predictions for individual galaxies evaluated as sufficient (1 point) or insufficient (0 points). Each network could therefore get between 0 and 6 data points for real-data performance.

For the final testing (see Section 2.5) and application of the network, we chose the combination of hyper-parameters with the best possible test score (lowest possible loss function), lowest FP rate, highest TP rate, best volume prediction accuracy, and best real-data performance. Hyper-parameters of the best-performing network are: 100 % of training images containing cavities, a learning rate of 0.0005 and a dropout of 0.2. The architecture and saved weights of the best-performing network can be found on the CADET GitHub page[14] (`CADET.hdf5`).

2.4 Application on real data

The CADET network with the best testing score was further applied to real *Chandra* images of early-type galaxies, groups and clusters of galaxies. Firstly, we applied the CADET pipeline to images of 70 nearby early-type galaxies, the parameters of which were used to generate the training dataset. For galaxies known to contain X-ray cavities (34 systems with confirmed cavities and 4 systems with candidate cavities), we tested whether the CADET pipeline is able to recover all previously detected X-ray cavities and for the rest of the galaxies (32 sources with non-detections or no mention in the literature), we looked for new cavity candidates. To test the performance on out-of-distribution sources, the CADET pipeline was also applied to a sample of 7 more distant galaxy clusters with known X-ray cavities.

Due to the fact that the underlying presence or absence of cavities identified by CADET is unknown, we were not able to adopt similar metrics as for simulated images and thus express true positive and false positive rates for real data. Instead, we report positive detections of previously known X-ray cavities and, for the previously unknown detections, we distinguish between new cavities, new candidates, and rather spurious detections based on visual assessment of the residual images and using azimuthal and radial photon count statistics (see Appendix A.2.3).

Before being processed by the CADET pipeline, real *Chandra* images were cropped on various different scales (multiples of 128 pixels) and binned to 128 × 128 pixels. For most galaxies, we used 6 different

[14] `https://github.com/tomasplsek/CADET`

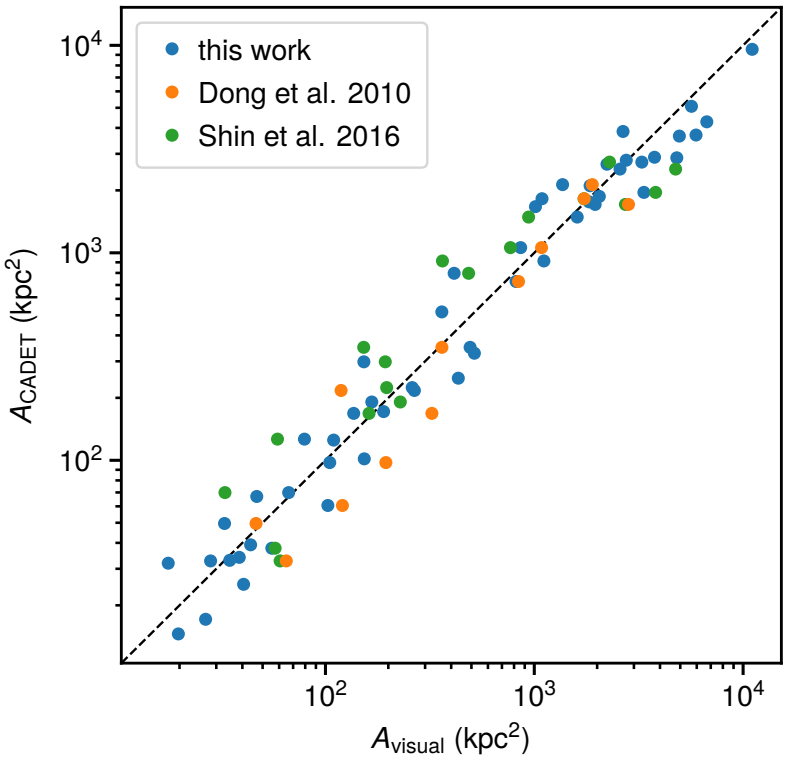

Figure 2.5: Areas of CADET predictions compared with manually derived cavity sizes for the sample of 33 early-type galaxies with known X-ray cavities estimated in our work and for 12 sources estimated by Dong et al. (2010) and 16 sources by Shin et al. (2016).

scales: 64×64 pixels (0.5 binning[15]), 128×128 pixels (no binning), 196×196 pixels (1.5 binning), 256×256 pixels (2 binning), 384 × 384 pixels (3 binning), 512 × 512 pixels (4 binning). For very extended or nearby sources, also larger scales were used (e.g. 640, 728 pixels). The binning of images was performed using the `dmregrid` routine within the CIAO pipeline.

To partly mitigate possible systematical uncertainties due to different positional angles of X-ray cavities, in the final version of the CADET pipeline, the resulting prediction is averaged over predictions produced for 4 different rotation angles (0°, 90°, 180°, 270°). To suppress systematic effects connected with improper centring of the input image, CADET predictions are additionally averaged for 25 possible shifts of the central pixel (maximally by ±2 pixels in both coordinates). Both of these approaches are combined, so the final prediction represents an average of 100 possible combinations.

2.4.1 Recovering known X-ray cavities

The CADET pipeline was applied on 34 systems previously known to harbour X-ray cavities in their hot atmospheres and 4 cavity candidates (see Table D1 and references therein). The resulting CADET predictions were examined and cavities of interest that were spatially co-aligned (visually verified) with previously known X-ray cavities were selected and their estimated areas were compared (Figure 2.5)[16].

The CADET pipeline was able to detect 93 out of 97 X-ray cavities in 34 galaxies that are known to have experienced single or multiple outbursts that produced these cavities. Besides that, CADET detected

[15] For 0.5 binning, we used *Chandra* sub-pixel resolution images.

[16] Estimates from other comprehensive studies focusing on radio lobes (Dunn et al., 2010; Giacintucci et al., 2011; Bîrzan et al., 2020) were not used for comparison because a discrepancy between sizes of X-ray cavities and radio lobe sizes has been observed, which will be thoroughly studied in a forthcoming publication (Plšek et al. in prep.).

a number of potential cavity candidates (Section 2.4.2) as well as rather spurious detections (further discussed in Section 2.5).

A comparison between predictions produced by the CADET pipeline and human-made predictions shows a good agreement (see Figure 2.5) of estimated cavity areas with an average difference of $-0.09^{+0.29}_{-0.17}$ dex, $-0.08^{+0.14}_{-0.30}$ dex, and $-0.16^{+0.36}_{-0.37}$ dex for this work, Dong et al. (2010), and Shin et al. (2016), respectively. The differences between areas of individual cavities estimated manually in this study and by Dong et al. (2010) and Shin et al. (2016) are maximally within a factor of 2 and are most probably resulting from uncertainties and biases associated with estimating the sizes of X-ray cavities by eye from smoothed original or residual images.

For systems with previously reported cavity candidates, the CADET pipeline was able to recover both inner (Panagoulia et al., 2014) and outer (Kim et al., 2019) cavities in NGC 499, and one cavity in NGC 1407 (Dong et al., 2010). For the rest of the systems (NGC 2300, NGC 6868), cavity candidates reported in the literature were not detected by CADET.

2.4.2 New cavity candidates

In addition, we applied the CADET pipeline to all the images of early-type galaxies, both with and without previously detected X-ray cavities, and searched for new cavity candidates. For this purpose, we increased the discrimination threshold (~ 0.8) to reduce the possibility of obtaining a false positive detection and to only obtain high-significance brightness drops. Moreover, the predictions were only taken as valid if present on at least two different size scales (verified visually). For subsequent significance testing, we usually used the smaller size scale with better spatial resolution.

Based on the combination of CADET predictions, visual inspection of analyzed images, radial and azimuthal photon count statistics, and simulated images with similar properties (see Appendix A.2.3), we claim the discovery of several new pairs of X-ray cavities (Table 2.3) in the following systems: IC 4765, NGC 533, NGC 2300, NGC 3091, NGC 4073, NGC 4125, NGC 5129 (see Figure 2.6). For the following galaxies, we report the detection of new cavity candidates for which further confirmation is needed: IC 1860, NGC 1521, NGC 1700, NGC 3091, NGC 3923, NGC 4526, NGC 6482 (see Figure 2.7). For the rest of the galaxies, CADET positive predictions are most likely spurious false positive detections – mainly for the below-discussed reasons (see Section 2.5).

2.4.3 Cavities in distant clusters

Besides the sample of 70 nearby early-type galaxies for which the CADET pipeline was optimized, we also aimed to test CADET predictions for sources whose parameters lie outside the distributions used to generate our training images. We, therefore, applied CADET to a sample of well-probed but more distant ($z > 0.05$) galaxy clusters. X-ray cavities in distant galaxy clusters are generally harder to detect compared to nearby early-type galaxies and galaxy groups because observations of galaxy clusters are characterised by lower S/N ratio, higher background contribution, and they often have substantial and complicated sloshing patterns and cold fronts due to more frequent merger activity.

For the testing, we selected 7 clusters of galaxies known to harbour X-ray cavities in their hot atmospheres: Abell 2597 (McNamara et al., 2001), Abell 3017 (Parekh et al., 2017; Pandge et al., 2021), Hydra A (Kirkpatrick et al., 2009), RBS 797 (Cavagnolo et al., 2011; Ubertosi et al., 2021), MS0735.6+7421 (McNamara et al., 2005), SPT-CLJ0509-5342 (Hlavacek-Larrondo et al., 2015), and SPT-CLJ0616-5227 (Hlavacek-Larrondo et al., 2015). Despite being trained mostly based on parameters of nearby giant elliptical galaxies, for all of the selected galaxy clusters, CADET was able to detect all 14 cavities from the previously known cavity pairs (see Figure 2 in the Supplementary material). For galaxy cluster Abell 3017, we discovered a possible additional outer pair of X-ray cavities. In the central parts of MS0735.6+7421, CADET detected also low-significance inner cavities previously proposed by Biava et al. (2022).

Table 2.3: Significances of newly detected X-ray cavities (upper part) and potential cavity candidates (lower part): galaxy name, cavity side and generation, maximal azimuthal significance, maximal radial significance, false positive rate (fraction of non-cavity images with positive cavity prediction with similar properties as given cavities), true positive rate (fraction of images with properly recovered cavities), volume error (relative cavity volume error estimated for true positive cases). For cavities with TP rates smaller than 25%, average volume errors were omitted.

Galaxy	Cavity	Azimuthal (σ)	Radial (σ)	FP rate	TP rate	Volume error (%)
IC 4765	S1	6.7	4.1	0.02	0.72	2^{+11}_{-13}
IC 4765	N1	5	5.6	0.1	0.94	-4^{+19}_{-17}
NGC 533	SE2	6.8	8	0.02	0.96	2^{+15}_{-15}
NGC 533	W2	7.4	9.8	0.04	0.97	15^{+21}_{-17}
NGC 2300	SE1	5.9	3.8	0.01	0.99	-10^{+13}_{-12}
NGC 2300	NW1	5.3	5.9	0.01	0.68	-14^{+18}_{-16}
NGC 3091	W2	3.4	5.7	0.03	0.93	-0^{+16}_{-12}
NGC 3091	NE2	7.3	4.7	0.02	0.92	-2^{+13}_{-13}
NGC 4073	SW1	6.4	4.6	0.01	0.91	-0^{+18}_{-14}
NGC 4073	SE1	2	3	0.01	0.87	-17^{+11}_{-12}
NGC 4125	S1	9.6	8.9	0.06	0.97	9^{+17}_{-15}
NGC 4125	N1	5.1	6.3	0.08	0.87	25^{+27}_{-20}
NGC 5129	SE1	3.1	4.5	0.01	0.76	-0^{+21}_{-15}
NGC 5129	NW1	4.1	5.2	0.01	0.96	-6^{+13}_{-10}
IC 1860	W1	3.9	4.6	0.1	0.12	-
IC 1860	NE1	0	2.3	0.06	0.17	-
NGC 1521	SE1	5.2	8.5	0.08	0.71	66^{+157}_{-59}
NGC 1521	NW1	6	3.3	0.11	0.45	18^{+82}_{-33}
NGC 1700	SE1	3.4	4.3	0.26	0.45	52^{+93}_{-62}
NGC 1700	N1	3	2.4	0.24	0.46	50^{+77}_{-59}
NGC 3091	SW1	3.6	4.1	0.1	0.74	27^{+47}_{-35}
NGC 3091	N1	2.7	2.4	0.12	0.25	-
NGC 3923	E1	3.7	3.8	0.1	0.03	-
NGC 3923	W1	2.1	4.5	0.08	0.01	-
NGC 4526	SW1	8.1	9.9	0.02	0.62	-22^{+20}_{-21}
NGC 4526	N1	8	13	0.02	0.69	22^{+83}_{-35}
NGC 6482	S1	3.6	2.6	0	0.03	-
NGC 6482	N1	2.9	4.1	0	0.22	-
NGC 6482	SW2	2.8	3.9	0	0.69	9^{+16}_{-17}
NGC 6482	NE2	1.8	3.7	0.01	0.88	25^{+23}_{-18}

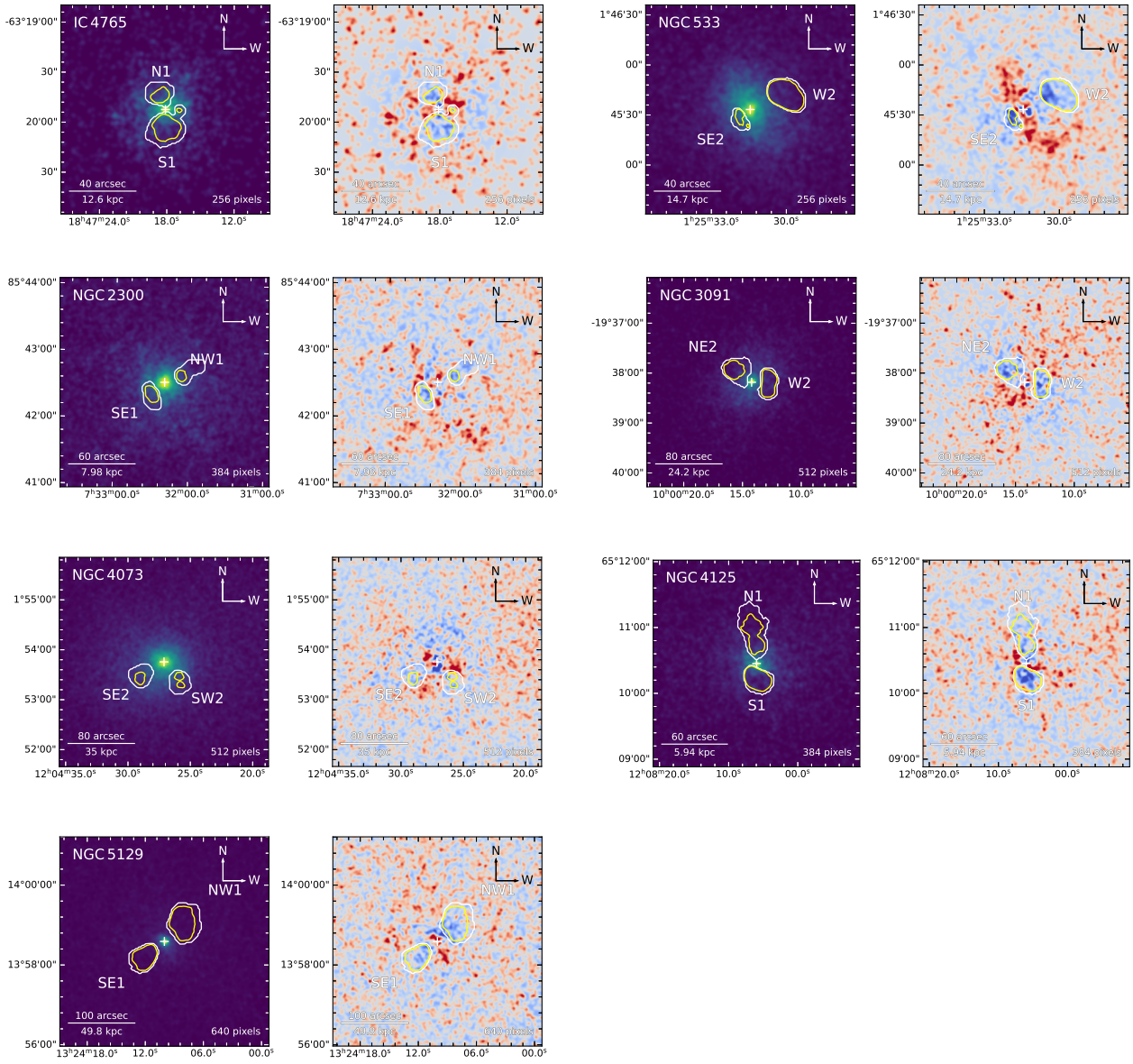

Figure 2.6: Newly detected and confirmed X-ray cavities: IC 4765, NGC 533, NGC 2300, NGC 3091, NGC 4073, NGC 4125, NGC 5129. *Left subplots*: original X-ray images with filled point sources overlaid by CADET prediction contours, *right subplots*: smoothed residual images, obtained by subtracting the best-fit β-model from the original image, overlaid by the CADET prediction contours.

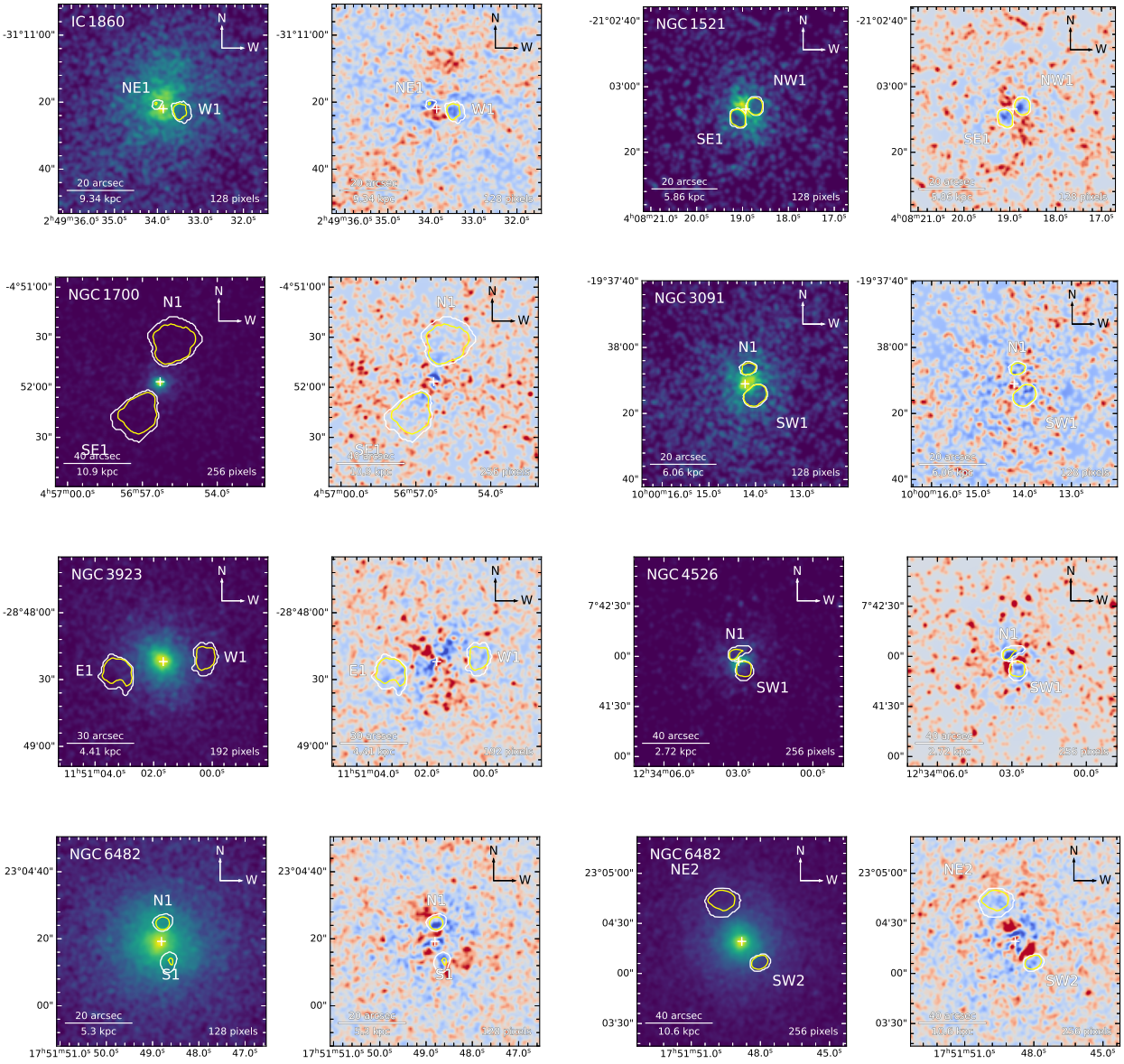

Figure 2.7: Newly detected X-ray cavity candidates: IC 1860, NGC 1521, NGC 1700, NGC 3091, NGC 3923, NGC 4526, NGC 6482. *Left subplots*: original X-ray images with filled point sources overlaid by CADET prediction contours, *right subplots*: smoothed residual images, obtained by subtracting the best-fit β-model from the original image, overlaid by the CADET prediction contours.

2.5 Discussion

We have shown that the utilization of machine learning techniques (convolutional neural networks) for the detection and size estimation of X-ray cavities on noisy *Chandra* images provides satisfactory results. Despite being trained on idealised simulated data, the convolutional neural network performed well when applied to real *Chandra* images of early-type galaxies. Although the simulated X-ray cavities only had elliptical shapes, the network is able to produce cavity predictions of any shape. This property can be utilized in a more accurate determination of their total volume and therefore also the corresponding energy required for their inflation ($4pV$). Furthermore, even though we only generated images with zero or one pair of cavities for the training dataset, the network is able to find an arbitrary number (also a non-even number) of surface brightness depressions. The advantage of this behaviour is that, for multi-cavity systems, all cavities can be recorded at once and larger cavities are not prioritized over smaller ones. On the other hand, for many systems, in addition to true high-significance cavities, low-significance brightness drops and possibly spurious predictions can be obtained. In the current state, the output of the network requires further visual analysis and the cavities of interest need to be selected by the user (see Appendix A.2.3).

We note that the CADET pipeline has problems with detecting cavities in galaxies with more complex spiral-like structures (IC 1262, NGC 1553, NGC 4636) as well as very bright rims around X-ray cavities or shocks (NGC 4374, NGC 5813). The network is also unable to properly handle X-ray jets or similar elongated structures and tends to predict cavities to be located on either one or both sides of such structures (e.g. NGC 315, NGC 383, NGC 4261). Another type of hardly analyzable images are, as expected, very faint sources with an extremely low number of counts (e.g. NGC 57, NGC 777, NGC 2305) and due to spaces between the chips also galaxies observed only by the ACIS-I chip (NGC 1387, NGC 2563). Proper detection and estimation of cavity extent are nearly impossible also for galaxies that are currently undergoing a noticeable merging event (e.g. NGC 507, NGC 741, NGC 1132, NGC 4406, NGC 7618) or ram pressure stripping (NGC 1404, NGC 4342, NGC 4552).

2.5.1 Reliability of CADET predictions

The convolutional part of the CADET pipeline produces pixel-wise prediction maps (128×128 pixels) with values in each pixel ranging from 0 to 1. The values are typically highest (close to 1) in cavity centres and decrease towards their edges. By discarding pixels with values lower than a given threshold (discrimination threshold), cavity predictions can be trimmed to obtain only the most 'significant' central parts. By setting a pair of discrimination thresholds (see Section A.2.2), the CADET pipeline can be simultaneously calibrated to produce not overestimated nor underestimated cavity predictions while maintaining a reasonable level of true-positive and false-positive rates (Figure A.2.2).

We note, however, that although such a pair of discrimination thresholds optimises the errors, TP and FP rates averaged out over the whole range of possible β-model and cavity parameters, it may still lead to overestimating some of the cavities while underestimating others. For each galaxy, a well-calibrated prediction is, therefore, reached using a slightly different value of the discrimination threshold. In order to investigate how the value of the optimal discrimination threshold depends on the parameters of given images, we binned the testing images into groups with a distinct number of counts, parameters of β-models (core radius r_0, slope parameter β), or parameters of inserted cavities (cavity sizes r_{cav}; see Figure 2.8).

Considerably strong dependence was, however, found only for the number of counts of the given images (Figure 2.9). We have therefore binned testing images by the number of counts into 2 bins and estimated optimal discrimination thresholds for both bins separately: for images with the number of counts lower than 50 000 the optimal thresholds are 0.4 and 0.6, and for images with more than 50 000 counts 0.45 and 0.3, respectively. Since for images with more than 50 000 counts, the discrimination

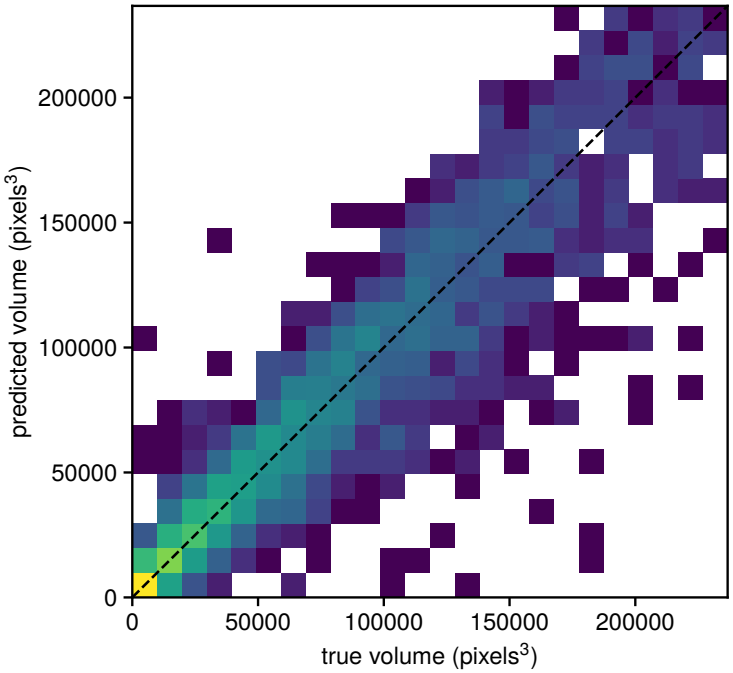

Figure 2.8: Predicted vs true cavity volumes for a sample of 10^4 testing images with X-ray cavities obtained for the optimized discrimination thresholds. The black dashed line represents the perfect recovery, the colour indicates the total number of points inside the corresponding bin.

threshold optimizing TP and FP rates is lower than the threshold optimizing cavity volumes, we only apply the double-threshold approach for images less than 50 000 counts.

2.5.2 Angular dependence

Although jets and X-ray cavities are expected to emerge at random orientations with respect to the observer, when estimating their properties, it is usually assumed that all cavities are located in the plane of the sky. We note, however, that this simplification leads, for many systems, to the underestimation of cavity distances and ages, and when calculating total cavity energy also to the overestimation of surrounding pressures.

Nevertheless, for X-ray cavities launched at higher angles with respect to the plane of the sky, their contrast decreases rapidly with increasing distance from the galactic centre. According to Enßlin and Heinz (2002), for a spherical cavity launched at the angle of 0 degrees with respect to the plane of the sky, the detectability declines with distance as $d^{-0.3}$, at 45 degrees as d^{-1}, and at the angle of 90 degrees as d^{-3}. For the detected cavities, there is therefore a much higher chance that they are located closer to the plane of the sky. This idea is supported also by the observed correlation and small scatter between cavity sizes and their distances from the galactic centre (see Figure A.2.6).

Using simulated images, we tested the angular dependence of cavity detectability for the CADET pipeline (see Figure 2.10). We generated images with parameter distributions identical to testing images and we varied the plane-of-the-sky positional angle θ of the primary cavity in a uniform range from 0 to 90 degrees[17]. Up to an angle of $\sim$ 45 degrees, the detectability (TP rate) and prediction accuracy (cavity volume error) only weakly depend on the plane-of-the-sky positional angle of X-ray cavities. For higher launching angles (45 – 90 degrees), the detectability steeply decreases and reconstructed volumes

[17]The secondary cavity was launched in an opposite angle $-\theta$ with random gaussian variation ($\mu = 0$, $\sigma = 10°$).

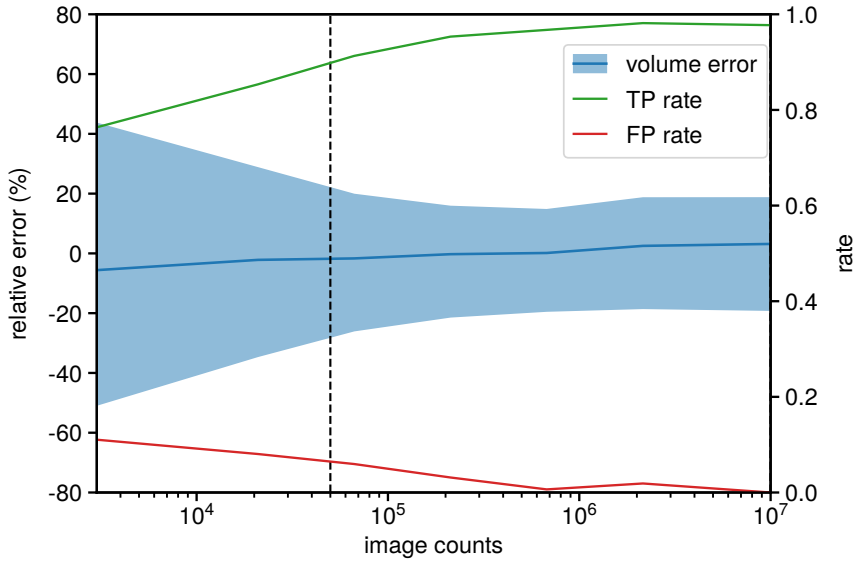

Figure 2.9: Relative volume error (blue), true-positive (TP) rate (green), and false-positive (FP) rate (red) of CADET predictions as a function of the number of counts in the input images. Volume errors and true-positive rates were estimated for a sample of 10^4 testing images each containing a single pair of X-ray cavities and false-positive rates were derived from a sample of 2000 testing images without any X-ray cavities. Parameter distributions used to generate testing images are identical to the parameter distributions of training images. The vertical dashed line corresponds to the division line between low-count images (less than 50 000 counts) and high-count images.

of true-positive X-ray cavities launched are heavily underestimated. For the angle of 90 degrees, the TP rate only reaches 25 %. However, we note that this behaviour is also affected by the fact that most of the cavities in the training data were generated close to the plane of the sky.

Cumulatively, the CADET pipeline was able to detect 66 % of X-ray cavities compared to 89 % for testing images with most X-ray cavities close to the plane of the sky. Assuming that the vast majority of early-type galaxies harbour X-ray cavities, with current data quality and methods they can only be detected for approximately 2 out of 3 galaxies. We note that this is consistent with the fraction of previously known X-ray cavities (34 sources) combined with confirmed cavity candidates (2 unique sources), new CADET detections (6 unique sources), and new CADET candidates (6 unique sources)[18] for our sample of 70 nearby early-type galaxies (48/70 = 68.5 %).

2.5.3 New detections and candidates

IC 1860

For the galaxy IC 1860, the CADET pipeline detected a pair of rather low-significance central X-ray cavities, which was marked as a cavity candidate. While Grossová et al. (2022) detected only a central point source in the radio band, VLA observations of Dunn et al. (2010) show extended radio emission that is spatially co-aligned with the cavities detected by the CADET pipeline.

[18] For newly detected cavities and candidates, some sources were already known to contain cavities, and the cavities detected by the CADET pipeline correspond to older generations detected on top of the younger ones.

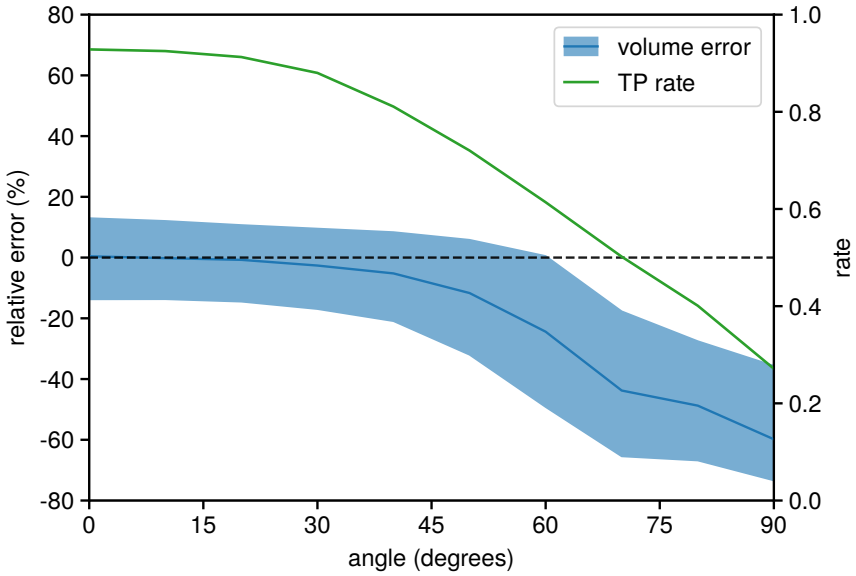

Figure 2.10: Average reconstructed cavity volume errors and TP rates as a function of cavity launching angle. Parameters of the images were generated from the identical distribution as used to generate the testing images.

IC 4765

X-ray cavities in the atmosphere of IC 4765 have not been previously detected, and the galaxy has not been reported to contain point-like or extended radio emission indicating the presence of radio-mechanical AGN feedback. The CADET pipeline has detected several cavities, two of which have been marked as significant brightness drops.

NGC 499

For the galaxy NGC 499, the CADET pipeline detected two pairs of X-ray cavities. The inner pair of cavities was previously detected by Panagoulia et al. (2014) and marked as a possible cavity candidate. The inner cavity pair did not meet our significance criteria and therefore it cannot be declared a confirmed cavity candidate. On the other hand, the outer pair of X-ray cavities previously reported by Kim et al. (2019) as a possible 'ghost' cavity candidate represent significant brightness drops with respect to the surrounding background and they are also well visible in the residual and even the original *Chandra* image. The outer cavities were therefore marked as a confirmed cavity candidate. All the publications studying this galaxy in the radio band (Dunn et al., 2010; Bîrzan et al., 2020; Grossová et al., 2022) have reported only a point-like radio emission.

NGC 533

The inner pair of X-ray cavities in NGC 533, which was detected by Dong et al. (2010) and Shin et al. (2016) while Panagoulia et al. (2014) reported a non-detection, has been successfully recovered by the CADET pipeline. According to Grossová et al. (2022), there is also a co-aligned radio emission in the GHz energy range (L-band A-conf VLA). In addition, the CADET pipeline detected a previously unreported outer pair of X-ray cavities (W2, SE2), which lacks a co-aligned extended radio emission, but due to its significance and visibility in the residual image (Figure 2.6) we have marked it as a newly detected cavity pair.

NGC 1407

For the galaxy NGC 1407, Dong et al. (2010) reported a possible cavity candidate that is spatially co-aligned with the extended radio emission detected by Giacintucci et al. (2011) and Grossová et al. (2022). The cavity has also been successfully detected by the CADET pipeline and was therefore marked as a confirmed cavity candidate.

NGC 1521

No X-ray cavities or extended radio emission have been reported in the literature for NGC 1521. However, the CADET pipeline has detected a pair of low-significance X-ray cavities in the centre of the galaxy, which has been marked as a new cavity candidate.

NGC 1700

Similarly, the galaxy NGC 1700 has not been previously reported to contain X-ray cavities or extended radio emission in the form of radio lobes. The CADET pipeline detected a pair of X-ray cavities, which were marked as cavity candidates due to their low significance.

NGC 2300

For the galaxy NGC 2300, the X-ray cavities detected by CADET do not correspond to the cavity candidate reported by Dong et al. (2010), which was not even detected by our pipeline. In addition, both Bîrzan et al. (2020) and Grossová et al. (2022) found only point-like radio emission comparable to the beam size of the telescope ($\sim 5-10$ arcsec). The cavity pair detected by the CADET pipeline has passed all of our significance tests and the cavities are therefore reported as newly discovered.

NGC 3091

Dong et al. (2010) reported a non-detection of X-ray cavities in NGC 3091 while Grossová et al. (2022) detected only a point-like radio emission. The CADET pipeline has detected two pairs of X-ray cavities in this galaxy. The inner detected cavities are rather low-significance cavity candidates, while the outer ones are high-significance brightness drops, which are also well visible in the original and residual images (Figure 2.6).

NGC 3923

For the galaxy NGC 3923, the presence of X-ray cavities has not been previously reported in the literature and VLA observations (Grossová et al., 2022) only show a point-like radio emission consistent with the beam size of the observation. The CADET pipeline was able to detect a single pair of low-significance X-ray cavities, which was marked as a new cavity candidate.

NGC 4073

X-ray cavities in NGC 4073 discovered by the CADET pipeline were previously not detected by Dong et al. (2010), Panagoulia et al. (2014), and Shin et al. (2016). Furthermore, Grossová et al. (2022) only reported a radio emission in the form of a central point source. X-ray cavities detected by the CADET pipeline have passed all significance tests and are therefore marked as newly detected cavities.

NGC 4125

For the galaxy NGC 4125, (Dong et al., 2010) reported a non-detection of X-ray cavities and Grossová et al. (2022) found no extended emission co-aligned with the X-ray cavities detected by the CADET pipeline. The detected X-ray cavities are, however, significant brightness drops and are also visually apparent in both the original and residual image (Figure 2.6).

NGC 4526

Although the galaxy NGC 4526 has not been previously reported to contain X-ray cavities or extended radio emission, the CADET pipeline has detected a possible pair of X-ray cavities in the centre of the galaxy. The detected cavities are not significant brightness drops and thus they were marked as a new cavity candidate.

NGC 5129

The X-ray cavities detected by the CADET pipeline in NGC 5129 were previously unreported. Dong et al. (2010) actually reported a non-detection in their analysis of *Chandra* X-ray data. On the other hand, at a smaller size scale than the detected cavities (~5 arcsec), Grossová et al. (2022) observed an extended radio emission at 1.5 GHz (L-band A-conf VLA), and the direction of the radio jets agrees with the position of the X-ray cavities detected by CADET.

NGC 6482

X-ray cavities in the atmosphere of NGC 6482 have not been detected by several X-ray studies (Panagoulia et al., 2014; Shin et al., 2016). In the radio bands (610 MHz and 1.4 GHz), Miraghaei et al. (2014) detected a rather featureless extended radio emission peaking at the position of the galaxy. However, the CADET pipeline detected two pairs of X-ray cavities, both of which are marked as low-significance cavity candidates, but are quite visible in the residual image. We speculate that the non-detection of Panagoulia et al. (2014) and Shin et al. (2016) may be caused by the rather short exposure time (~ 20 ks) compared to our analysis, which includes also the latest observations with a total exposure time of ~ 215 ks.

2.6 Conclusions

We have developed a machine learning pipeline called the *Cavity Detection Tool* (CADET), which we have trained for detecting and estimating sizes of surface brightness depressions (X-ray cavities) on *Chandra* images of early-type galaxies and galaxy clusters. We have shown that the brute force of modern computing, combined with the state-of-the-art algorithms represented by convolutional neural networks, is capable of handling more complex astronomical tasks, such as detecting elliptical brightness drops in noisy X-ray data.

The CADET network was trained on a large set ($\approx 10^6$) of artificial images generated to imitate real X-ray data of early-type galaxies as observed by the *Chandra X-ray Observatory*. The gas density distribution of the simulated galaxies was approximated by an ellipsoidal 3D β-model (single or double) from which we cut out a pair of ellipsoidal cavities. Parameters of both simulated galaxy models and inserted cavities were generated based on an analysis of 70 nearby early-type galaxies, 34 of which contained one or more pairs of X-ray cavities (97 cavities in total).

By varying the hyper-parameters of the network (fraction of cavities in training images, learning rate, dropout rate) and training all networks for 32 epochs, we found the optimal combination of parameters with the best performance on the testing dataset of mock and real images. For the best-performing network, we further tested the accuracy of its predictions as well as true-positive (TP) and false-positive (FP)

rates on simulated images. Moreover, the best-performing network was calibrated (see Appendix A.2.2) not to produce overestimated or underestimated predictions (discrimination threshold ≈ 0.4) while maintaining a plausible level of FP and TP rates (discrimination threshold ≈ 0.6). After the calibration, we obtain the resulting average absolute volume reconstruction error of 14^{+13}_{-8} per cent and true-positive rate of 89 per cent for the testing dataset of 10^4 simulated images with X-ray cavities, and a false positive rate of 5 per cent for the testing dataset of 2000 images without any X-ray cavities.

For the sample of 34 real images of galaxies known to harbour one or more pairs of X-ray cavities, the CADET pipeline recovered 93 out of 97 cavities. The comparison between predictions produced by the CADET pipeline and human-made predictions shows a good agreement (see Figure 2.5) between estimated cavity volumes with an average difference of $-0.09^{+0.29}_{-0.17}$ dex, $-0.08^{+0.14}_{-0.30}$ dex, and $-0.16^{+0.36}_{-0.37}$ dex for this work, Dong et al. (2010), and Shin et al. (2016), respectively. For previously known cavity candidates, the CADET pipeline confirmed X-ray cavities in two systems (NGC 499, NGC 1407), and the same number of candidate cavity pairs was not recovered (NGC 2300, NGC 6868).

Furthermore, the CADET network led to the discovery of 7 new pairs of X-ray cavities in nearby early-type galaxies (IC 4765, NGC 533, NGC 2300, NGC 3091, NGC 4073, NGC 4125, NGC 5129), that were further confirmed using azimuthal and radial photon count statistics as well as by simulating mock images with similar properties. The CADET pipeline also discovered another 8 potential cavity pair candidates in 7 sources (IC 1860, NGC 1521, NGC 1700, NGC 3091, NGC 3923, NGC 4526, NGC 6482), that need further confirmation in the form of deeper X-ray observations or detection of co-aligned extended radio emission. When applied to images of 7 galaxy clusters harbouring X-ray cavities, the CADET pipeline was able to recover all known X-ray cavities, confirm a possible cavity pair candidate (MS 0735.6+7421; Biava et al., 2022), and detect a new cavity candidate (Abell 3017).

Acknowledgements

This research was supported by GACR grant 21-13491X. A.S. is supported by the Women In Science Excel (WISE) programme of the Netherlands Organisation for Scientific Research (NWO), and acknowledges the Kavli IPMU for the continued hospitality. SRON Netherlands Institute for Space Research is supported financially by NWO. This research has made use of the NASA/IPAC Extragalactic Database (NED), which is funded by the National Aeronautics and Space Administration and operated by the California Institute of Technology. We thank Laurence Perreault-Levasseur, Yashar Hezavez, Carter Rhea, and Matej Kosiba for valuable advice in the field of convolutional neural networks and machine learning in general. We thank Steve W. Allen for his comments and feedback on the manuscript, and Tony Mroczkowski for discussing the potential application to galaxy clusters.

Annex 3

The infalling elliptical galaxy M89: Chemical composition of the AGN disturbed hot atmosphere

S. Kara[1], T. Plšek[2], K. Protušová[2], J.P. Breuer[2], N. Werner[2], F. Mernier[3,4] and E. N. Ercan[1]

[1] Department of Physics, Boğaziçi University, Bebek, 34342 Istanbul, Turkey
[2] DTPA, Faculty of Science, Kotlářská 2, Masaryk University, Brno, 611 37, Czech Republic
[3] NASA Goddard Space Flight Center, 8800 Greenbelt Rd, Greenbelt, MD 20771, USA
[4] Department of Astronomy, University of Maryland, College Park, MD 20742, USA

Abstract: The chemical enrichment of X-ray-emitting hot atmospheres has hitherto been primarily studied in galaxy clusters. These studies revealed relative abundances of heavy elements that are remarkably similar to Solar. Here, we present measurements of the metal content of M89 (NGC 4552), an elliptical galaxy infalling into the Virgo cluster with a ~10 kpc ram-pressure stripped X-ray tail. We take advantage of deep *Chandra* and *XMM-Newton* observations, and with particular attention to carefully modelling the spectra, we measure the O/Fe, Ne/Fe, Mg/Fe, Si/Fe and S/Fe ratios. Contrary to previous measurements in galaxy clusters, our results for the hot atmosphere of M89 suggest super-Solar abundance ratios with respect to iron (i.e. α/Fe > 1), similar to its stellar components. Our analysis of the active galactic nucleus (AGN) activity in this system indicates that the AGN-induced outflow could have facilitated the stripping of the original galactic atmosphere, which has been replaced with fresh stellar mass loss material with super-Solar α/Fe abundance ratios. Additionally, we report a new fitting bias in the RGS data of low-temperature plasma. The measured O/Fe ratios are >1σ lower in multi-temperature models than a single temperature fit, leading to discrepancies in the calculations of supernova fractions derived from the metal abundances.

Keywords: galaxies: abundances - galaxies: clusters: intracluster medium - X-rays: galaxies - galaxies: active - galaxies: individual (M89)

Published in Monthly Notices of Royal Astronomical Society (MNRAS), Volume 528, Issue 2, February 2024, Pages 1500–151.

3.1 Introduction

Massive galaxies, galaxy groups and galaxy clusters are pervaded by hot, X-ray-emitting diffuse gas, which contains 80% of the total baryonic matter of the Universe (for a recent review, see e.g. Werner and Mernier, 2020). Since the ~7 keV K-shell Fe emission lines were discovered in intracluster medium (ICM) X-ray spectra in the late 1970s (Mitchell et al., 1976; Serlemitsos et al., 1977), the hot plasma pervading the Universe is known to be enriched with heavy elements.

Through decades, it has been debated if the main enrichment mechanisms of the hot atmospheres in such systems are internal (e.g. stellar winds at galactic scale) or external (gas inflows from the intergalactic medium). Measurements of heavy elements play a crucial role in answering this question. The observations show that the spatial metal distribution does not follow the galaxy distribution, and the metal distribution in cluster outskirts is remarkably uniform (Werner et al., 2013; Urban et al., 2017), indicating significantly homogeneous gas formation. Furthermore, there is no apparent dependency of metal abundances on the mass of the galaxy cluster (de Plaa et al., 2017; Mernier et al., 2018b; Truong et al., 2019). In line with the observations, simulations indicate (Biffi et al., 2017) that the enrichment of the ICM was completed at $z \sim 2-3$ ($10-12$ billion years ago), which is the epoch of peak star formation and active galactic nuclei (AGN) activity (Madau and Dickinson, 2014; Hickox and Alexander, 2018).

The chemical enrichment of the Universe on the largest scales occurred at early times when energetic AGN feedback outflows expelled the metals to the intergalactic medium. Later, the enriched and mixed atmosphere gas was externally accreted and heated by clusters, galaxy groups, and galaxies to form the present atmospheres (for a recent review, see e.g. Mernier and Biffi, 2022).

Measurements of abundance ratios of light α elements (e.g. O, Ne, Mg, Si, and S), mostly produced by core-collapse supernovae (SNcc), and heavy Fe-peak elements (e.g. Ca, Cr, Mn, Fe and, Ni), mainly produced by Type Ia supernovae (SNIa), can be used to understand the chemical enrichment histories of different systems. Mernier et al. (2016) analysed central chemical composition of 44 systems using *XMM-Newton* EPIC and RGS observations. They found the chemical composition in their samples to be very similar to our Solar system (i.e. α/Fe ratio is ~1 Solar). Similarly, by utilising the high-resolution *Hitomi* SXS and *XMM-Newton* RGS observations, Simionescu et al. (2019) found Solar abundance ratios in the Perseus cluster. These and other studies (e.g. Hitomi Collaboration, 2017; de Grandi and Molendi, 2009) indicate that the relative abundances of supernova products have Solar ratios from cores to the outskirts. These remarkable discoveries strongly suggest that the hot plasma pervading our Universe has become chemically well-mixed, achieving Solar composition through continuous inflows and outflows.

In cluster galaxies, the chemical composition of hot atmospheres and the stellar population are considered to be decoupled. The externally accreted hot gas has Solar abundance ratios (i.e. $\alpha/\mathrm{Fe} \approx 1$), while the stars have super-Solar abundance ratios (i.e. $\alpha/\mathrm{Fe} > 1$) (Conroy et al., 2013). The origin of the decoupling is that the elliptical (i.e. early-type) galaxies are considered to have had rapid and intense star formation very early in cosmic history, with a star formation peak around $z \sim 3$ (Thomas et al., 2010). As a result, considering SNcc products formed earlier in the cosmic time, SNcc products have been locked in stars before the star-forming gas in such a galaxy has been polluted by SNIa products that are dominantly produced later in the cosmic time.

Although the hot galaxy atmospheres consist mainly of externally accreted and heated gas, internal sources also produce a large amount of hot gas. Internal sources of hot gas in elliptical galaxies are the thermalised stellar mass loss products (Mathews, 1990; Mathews and Brighenti, 2003). In a case without any external inflow of Solar gas, stellar wind-originated gas with super-Solar abundance ratios might dominate the galaxy's atmosphere over time. However, Mernier et al. (2022) recently showed that NGC 1404, an infalling elliptical galaxy experiencing such an accretion cut-off, has Solar abundance ratios, which means internally produced hot gas has not dominated the overall composition in that system. Still, in the current picture of hot gas replenishment in elliptical galaxies, enrichment processes have not

been tested in a system that might also undergo a significant loss of its original atmosphere due to internal mechanisms like AGN activity.

M89 (a.k.a. NGC 4552) is an excellent target to examine the hot gas replenishment processes due to stellar mass loss products. M89 is a massive elliptical galaxy experiencing AGN activity, oscillating inside the gravitational potential well of the Virgo cluster. Because of its motion, any gas inflow with Solar abundance ratios onto the galaxy is stopped (Gunn and Gott, 1972). Moreover, due to the AGN activity, it is possible that the galaxy might have lost a portion of its original atmosphere with Solar abundance ratios. Therefore, due to its exceptional dynamics, a dedicated enrichment study on M89 has the potential to provide new constraints on the chemical enrichment of the Universe. The galaxy is located 350 kpc (72 arcmin) east of the central dominant galaxy of the cluster (NGC 4486, a.k.a. M87). *Chandra* images in the 0.5-2.0 keV band (Figure 3.1) show two ring-like structures approximately ~1.3 kpc away from the centre of the galaxy, which is associated with the LINER type AGN in its centre (Machacek et al., 2006). Moreover, it shows a ~10 kpc X-ray tail at its south, along the motion direction, associated with the ram-pressure stripping of the galaxy's hot atmosphere (Machacek et al., 2006). Notably, the α/Fe ratios in the stellar content of M89 are higher than the average ratios in ellipticals with similar mass. Lonoce et al. (2021) measured the abundance values within $0.975r_e$ with 10 symmetric galactocentric bands, where the 1D extraction corresponds to ~38.4 arcsec. From this study, stars in M89 have O/Fe ratios of $3.02^{+0.15}_{-0.17}$ and Mg/Fe ratios of $1.92^{+0.16}_{-0.15}$.

The origin of the hot atmosphere of M89 can be investigated via the abundance ratios in the system. Previous abundance ratio measurements of M89 were first conducted by Ji et al. (2009). They analysed M89 within a sample of 10 elliptical galaxies and found Solar abundance ratios for Mg/Fe and Si/Fe and sub-Solar for O/Fe in a circular region of 1 arcmin radius. However, their measurement assumes only a single-temperature model, which is known to result in unreliable measurements in cool systems ($kT \lesssim 2-3$ keV) due to the so-called 'Fe bias' (Buote and Fabian, 1998; Buote, 2000; Gastaldello et al., 2021). The 'Fe bias' is an underestimation of Fe abundance when a spectrum containing multiple temperature components is estimated with a single-temperature model. Given that multi-temperature components are inevitable in the spectrum of a galaxy's atmosphere due to issues such as projection effects and cooling in the galaxy's core, we can assume that such measurements need to be revisited. Furthermore, Ji et al. (2009) reported unusually high abundances in M89, findings that were not corroborated by the CHEERS (the CHEmical Evolution RGS Sample) catalogue (de Plaa et al., 2017; Mernier et al., 2016). In the CHEERS study, they found super-Solar O/Fe and Si/Fe ratios and Solar Ne/Fe using single-temperature models. Although necessary to understand chemical enrichment processes as a whole, studies based on a sample of several systems at once are, by nature, much less suited to investigate individual outliers.

In this paper, we revisit this elliptical galaxy with a detailed and comprehensive analysis. In particular, taking advantage of *XMM-Newton* and *Chandra* observations, we investigate the chemical enrichment of M89 for the first time by presenting the O/Fe, Ne/Fe, Mg/Fe, Si/Fe and S/Fe abundance ratios in the core and the tail of M89. Moreover, to comprehensively explore how the dynamical processes within M89 may influence its chemical enrichment history, we analyse the shock properties exhibited by the "hourglass" structure within M89, which is caused by the nuclear activity of the central AGN.

The structure of this paper is as follows. Section 3.2 describes the data reduction and region selection. The spectral modelling is described in Section 3.3. Section 3.4 presents the abundance ratio results, supernova contribution fractions derived from the ratios, the systematic uncertainties in the measurement, and the properties of AGN-induced nuclear outburst. We discuss the possible chemical enrichment history of M89 in Section 3.5. Finally, Section 3.6 summarises the results and conclusions. Throughout the paper we assume the standard ΛCDM cosmology with $H_0 = 70\,\mathrm{km\,s^{-1}\,Mpc^{-1}}$, $\Lambda_0 = 0.73$ and $q_0 = 0$. All the abundances are expressed using the proto-Solar values of Lodders et al. (2009), and for simplicity,

Figure 3.1: (*Left*) Exposure corrected, *Chandra*/ACIS-S mosaic image of the core of M89 in 0.5 – 2.0 keV band. Two ring-shaped AGN-induced shock rims are present. The point sources are left for visualisation purposes. (*Middle*) Point source removed *Chandra*/ACIS-S mosaic image of M89 and the Ram-pressure associated tail in the 0.7 – 1.1 keV band, with the corresponding white contours of X-ray surface brightness. (*Right*) Exposure corrected *XMM-Newton*/EPIC image of M89 in 0.7 – 1.1 keV band.

Table 3.1: *Chandra* and *XMM-Newton* observations of M89. Both *XMM-Newton* RGS and EPIC data are taken from the same single *XMM-Newton* observation.

Observatory	ObsID	Observation Date	Instrument	Total Exposure (ks)	Clean Exposure (ks)
Chandra	2072	2001-04-22	ACIS-S	54.4	54.2
	13985	2012-04-22		49.4	49.4
	14358	2012-08-10		49.4	49.4
	14359	2012-04-23		48.1	48.1
XMM-Newton	0141570101	2003-07-10	EPIC MOS 1	42.7	24.0
			EPIC MOS 2	42.7	24.1
			EPIC pn	39.5	17.1
			RGS	43.7	24.3

the values are referred to as 'Solar' throughout the paper. Unless stated otherwise, all uncertainties are expressed in the 1σ credible interval[1].

3.2 Data Reduction and Region Selection

3.2.1 Chandra X-ray observatory

For our study, we used all available archival *Chandra* observations of M89 with a total cleaned exposure of 201 ks (see Table 3.1). All observations were performed using the Advanced CCD Imaging Spectrometer array with ACIS-S (chip S3) in the aim point. Since the desired area of M89 does not overlap with other chips, we limited the analysis to the S3 chip. All observations were processed using standard `CIAO` 4.15.1 (Fruscione et al., 2006) procedures and current calibration files (CALDB 4.10.4).

Chandra observations were reprocessed and filtered for VFAINT events using the `chandra_repro` script and deflared using the `lc_clean` algorithm within the `deflare` routine. Individual OBSIDs were further reprojected to the same tangent point. These reprojected event files were then merged. The images were extracted in the 0.7 – 1.1 keV and 0.5 – 2.0 keV bands and exposure-corrected using weighted exposure maps (the weighting was computed using `make_instmap_weights`[2] procedure assuming an absorbed `vgadem` model with $kT \approx 0.64$ keV; see Table 3.2).

Chandra X-ray images of M89 in the 0.7 – 1.1 keV and 0.5 – 2.0 keV bands are shown in Figure 3.1. The ram-pressure stripped tail of ~10 kpc is clearly visible. In the central region, we can see the diffuse emission from the galaxy along with two ring-like structures associated with AGN-driven weak shocks.

Chandra spectral files were extracted using the `specextract` script. When extracting spectra, we used stowed spectral files obtained using the `blanksky` script for background subtraction for all extraction regions. The reason for choosing stowed spectral files rather than the blank-sky data set is because stowed files only account for the instrumental background and thus allow for more accurate modelling of the sky background components. This is particularly crucial for low-temperature background compo-

[1] This corresponds to distances of 15.9% and 84.1% quantiles from the median value.

[2] https://cxc.cfa.harvard.edu/ciao/ahelp/make_instmap_weights.html

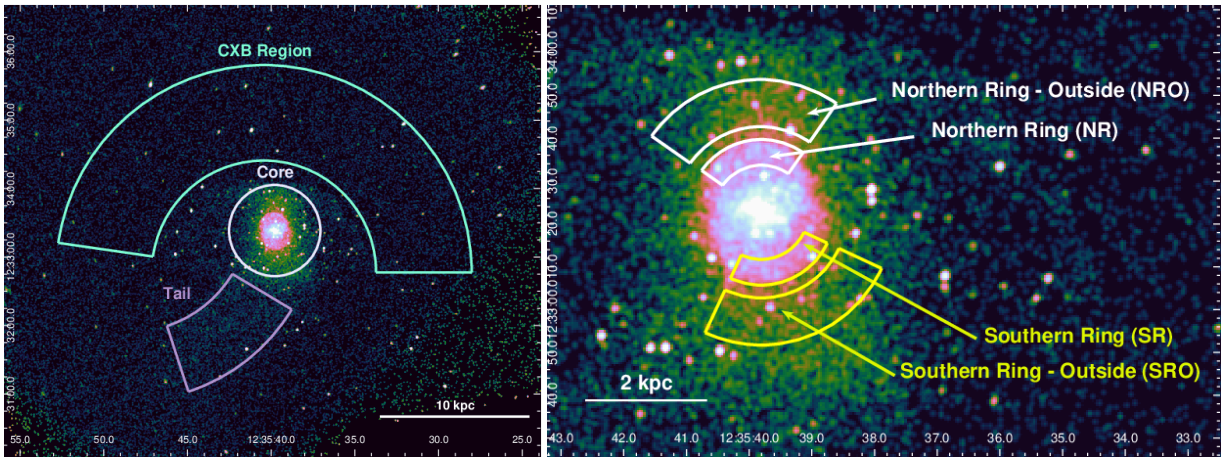

Figure 3.2: *(Top)* Background subtracted *Chandra*/ACIS-S image of M89 with highlighted regions used for our abundance study: Cosmic X-ray Background (CXB) region, Core region, and Tail region. *(Bottom)* Zoom onto the centre of the galaxy with highlighted extraction regions used for estimating parameters of the shock.

nents that are comparable to the temperature structure of M89. Robustly constraining the background components is essential for accurate abundance measurements, as further explained in Section 3.3.2. In Section 3.4, we compare our results obtained from the stowed spectral files and blank-sky data set. The background files were reprojected onto the observations, filtered for VFAINT events, and the background spectra were scaled to match the particle background of the observations in the 9 – 12 keV energy range.

3.2.2 XMM-Newton

We used the single *XMM-Newton* observation listed in Table 3.1. Reduction of the EPIC and RGS data is done by using the *XMM-Newton* Science Analysis System (`SAS` v20.0.0), along with the integrated Extended Source Analysis Software (`ESAS` v9.0[3]) package.

EPIC

Following the standard procedure, the calibrated photon event files of MOS and pn data were created using `emchain` and `epchain`, respectively. Then, in order to exclude the soft proton (SP) contamination, we used `mos-filter` and `pn-filter`, which call the task `espfilt` to create good time intervals (GTI). We kept the single, double, triple, and quadruple events in the MOS data (`pattern`≤12). Due to the charge transfer inefficiency problems for double events of pn, we kept the single events only (`pattern`=0). After the filtering, the exposure time has decreased from 44.3 ks to a net 24.3 ks due to the heavy contamination by flares. A combined, exposure-corrected image is merged with the `combimage` task and presented in Figure 3.1. Point sources were detected and removed by the `CIAO` algorithm `wavdetect`. The Point-Spread Function (PSF) map of EPIC was created using the `dmimgcalc` tool for the purpose of the `wavdetect` algorithm. We generated corresponding PSF maps with a size of 9 arcsec, roughly equivalent to a 0.50 Encircled Energy Fraction (ECF) on-axis. After performing the point source detection, we see that the only resolved and detected point sources are located outside the central region of the galaxy. In Section 3.4, we discuss variations in results obtained from background spectra with different sizes of removed point sources.

[3]https://www.cosmos.esa.int/web/xmm-newton/xmm-esas

We processed the *XMM-Newton*-EPIC data by using `mos-spectra` and `pn-spectra` tasks, which call the `evselect`, `rmfgen` and `arfgen` tasks to extract the spectra and generate RMFs and ARFs, respectively.

RGS

We used the `SAS` task `rgsproc` to process the RGS data. The RGS1 and RGS2 data were filtered with the same GTI file for MOS1. To reduce the instrumental line broadening due to the slit-less nature of the gratings, we included 90% of the PSF along the cross-dispersion direction (`xpsfincl=90`), which corresponds to a spatial width of ~0.8 arcmin. We combined the RGS1 and RGS2 spectra with `rgsproc` task and fitted the first-order and second-order data simultaneously.

3.2.3 Region Selection

The emission of the hot atmosphere of M89 is, apart from the cosmic X-ray background, highly contaminated also by the ICM emission of the Virgo cluster. In order to properly estimate the abundance of chemical elements in M89, it is critical to describe this background emission well. Furthermore, the central active galactic nucleus (AGN) can also contribute to the observed spectrum and can only be properly spatially excluded using *Chandra* data. For these reasons, we adopted the following approach and extracted spectra from multiple regions.

First, to investigate the chemical composition of the disturbed hot gas of M89, we extracted a spectrum from a circular region at its centre with a 40 arcsec radius (Core region), presented in Figure 3.2. The size of this region is selected to correspond to the galaxy core and also, considering the relatively short clean exposure time of *XMM-Newton*, to be large enough to have a sufficient number of counts so that the abundances can be constrained robustly. For *Chandra* data, the circular region with a 1.5 arcsec radius corresponding to the central AGN was excluded. In order to investigate the elemental structure of the escaped gas, we also created a Tail region enclosing the galaxy's X-ray tail.

In order to model the Virgo ICM and the cosmic X-ray background (CXB) robustly, we created an arc-shaped region (CXB Region) in front of the galaxy along the direction of the motion of M89. The CXB region (see Figure 3.2) and the Core or Tail region are modelled simultaneously by linking the joint background parameters. The modelling procedure is further explained in Section 3.3.

To describe the time-variability and spectral properties of the central AGN, we extracted *Chandra* spectra from a circular region with a 1.5 arcsec radius centred at the bright central point source (AGN Region).

Additionally, in order to examine the dynamics of the AGN-induced shock, we created region pairs encompassing each shock ring individually in annular sections with the inner and outer radii of 11 and 17 arcsec, respectively, while the outside regions of the rings are present in annular sections of inner and outer radii of 30 and 31 arcsec centred around the central AGN. For the northern ring, the annular sections Northern Ring (NR) and Northern Ring - Outside (NRO) regions extend from 55° to 145°. The Southern Ring (SR) and Southern Ring - Outside (SRO) regions extend from 245° to 335° (see Figure 3.2). These regions are used to investigate the temperature discrepancy present across the rim of the shock, which enables us to determine the shock Mach number.

3.3 Spectral analysis

Modelling of *Chandra* and *XMM-Newton* data is done separately. However, data from individual *Chandra* observations as well as individual *XMM-Newton*-EPIC detector (MOS1, MOS2 and pn) data are fitted simultaneously. Both EPIC and ACIS-S data are fitted within the $0.55-7$ keV energy range. The 0.55 keV limit is chosen to avoid biases caused by the oxygen K-edge. In the case of RGS data, we chose the interval $8-27$ Å. We used optimal binning by Kaastra and Bleeker (2016) for ACIS-S, EPIC, and RGS data.

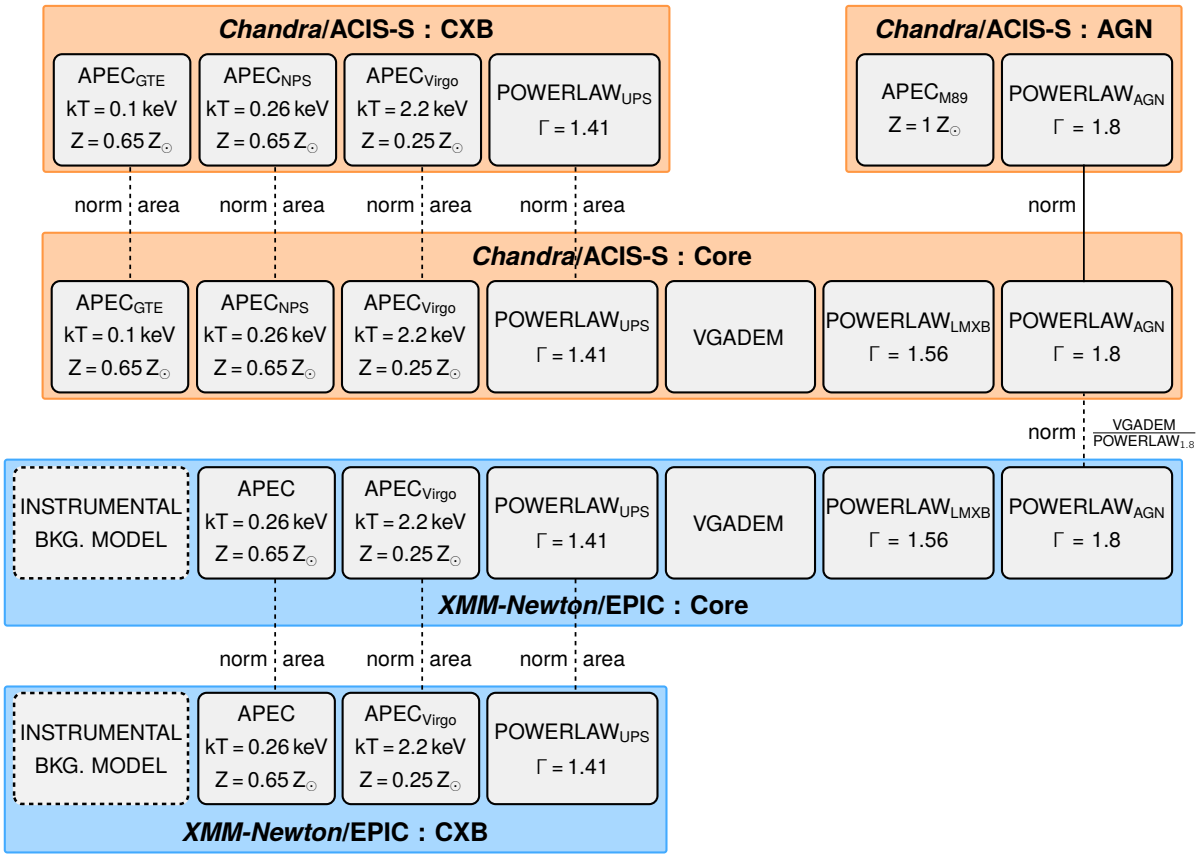

Figure 3.3: Modelling scheme of M89. The orange-coloured part represents the model for the *Chandra* data extracted from the CXB, AGN and Core regions; while the blue-coloured part represents the *XMM-Newton* model. The shared model components of the CXB and Core regions are tied with a scaling parameter obtained as a fraction of the areas of the two regions. A similar scaling parameter between the AGN `powerlaw` normalisation and the core `vgadem` normalisation was applied from the obtained ratio from the *Chandra* fit into the *XMM-Newton* model. All the other parameters for *Chandra* and *XMM-Newton* data are fitted separately.

The spectral modelling was performed using the Levenberg-Marquardt algorithm and Cash statistics (Cash, 1979) within `PyXspec v2.1.0` (Xspec 12.12.1; Arnaud, 1996). After finding the best-fit values, parameter uncertainties were estimated from posterior distributions obtained from an MCMC simulation.

3.3.1 Emission from galaxy core and tail

There are three main sources of X-ray emission that originate inside M89. Therefore the following components are present in the Core and Tail regions exclusively: the first is the hot atmosphere that we are probing, which is assumed to be a thermal plasma in collisional ionisation equilibrium (CIE). The other two are the AGN component and the emission from Low-Mass X-ray Binaries (LMXBs).

The AGN component is represented by a `powerlaw` model with a photon index Γ of ~ 1.8, derived from the *Chandra*/ACIS-S spectrum (further described in Section 3.3.3). The integrated LMXB emission is reproduced by a `powerlaw` with a photon index fixed to 1.56 (Irwin et al., 2003; Su et al., 2017). As for the hot atmosphere, we tested three different models to represent the thermal emission component: single temperature (1T vapec), double temperature (2T vapec), and finally, multi-temperature, using the

Gaussian distribution of emission measure (vgadem). All the above-mentioned emission components are absorbed by the interstellar medium of our Galaxy, which is represented by the `phabs` model with a fixed value of $N_H \approx 1.36 \times 10^{20}\,\mathrm{cm}^{-2}$ (HI4PI Collaboration et al., 2016) and our model is corrected for the redshift value of $z = 0.000113$, taken from the *Nasa Extragalactic Database*. The total model representing the X-ray emission from the Core and Tail regions is as follows

$$\texttt{phabs * (vgadem + powerlaw}_{\texttt{AGN}}\texttt{+ powerlaw}_{\texttt{LMXB}}\texttt{).}$$

vgadem

As discussed in previous studies (see e.g. Mernier et al., 2015a, Werner et al., 2006), a model employing the Gaussian distribution of temperatures improves statistics significantly for cluster cores. For the galaxy core, especially for our region that encircles a relatively wide area with presumably different temperatures, we employ the same model. In this analysis, we also tried single-temperature (1T) and double-temperature (2T) models to represent the thermal emission, and the results are presented in Table 3.2.

3.3.2 Background modelling for EPIC and ACIS-S

Unlike some of the previous abundance measurements of M89 (Ji et al., 2009), which subtracted background spectra, we carefully applied customised modelling for all of the background components. This approach has been shown to provide more reliable measurements compared to subtracting a local background spectrum (see relevant discussions in e.g. Mernier et al. (2015b); Zhang et al. (2020); Zhang et al. (2018)). In particular, de Plaa et al. (2007) reported that any small inaccuracies in the background spectra, which are highly probable when extracting spectra from a rigid background, can lead to inaccuracies in the temperature profile of an extended source. Therefore, because line emissivities depend on the temperature of the plasma at fixed abundances, the assumed temperature significantly affects the abundance determination. To avoid such inaccuracies in our abundance measurements, we chose to model the background components for both EPIC and ACIS-S.

Background effects that are not galaxy-originated are modelled by linking the parameters of the region of interest (Core or Tail region) and CXB region for the shared background emission components. The background components that are shared with the region of interest and CXB regions are the Virgo ICM, Unresolved Point Sources (UPS), Galactic Thermal Emission (GTE) and North Polar Spur (NPS) emissions. NPS is a structure in the Milky Way that emits both X-ray and radio emission, which is argued to be originated from a nearby supernova explosion (e.g. Berkhuijsen, 1971), or that it is a remnant of an explosion or a starburst at the galactic centre (e.g. Sofue, 1994). It is located at the northeastern edge of the Galactic bubble, with the brightest ridge at $(l, b) \sim (30^\circ, 20^\circ)$. As the Virgo cluster is in the vicinity of the NPS, we expect our observation to be affected by this emission. To model the background emission present in both the Core and CXB regions, we used the following model:

$$\texttt{phabs * (apec}_{\texttt{NPS}}\texttt{) + phabs * (apec}_{\texttt{Virgo}}\texttt{+ powerlaw}_{\texttt{UPS}}\texttt{).}$$

The NPS was modelled with an absorbed `apec` component ($kT_{\mathrm{NPS}} = 0.26\,\mathrm{keV}$, $Z_{\mathrm{NPS}} = 0.65\,\mathrm{Solar}$; Willingale et al., 2003), where the absorption hydrogen density column was set to the half of the value measured by HI4PI Collaboration et al. (2016) because the NPS emission is expected to lie behind at least 50 per cent of the line-of-sight Galactic column density (Willingale et al., 2003). The ICM emission from the Virgo cluster is represented by an absorbed `apec` component ($kT_{\mathrm{Virgo}} = 2.2\,\mathrm{keV}$, $Z_{\mathrm{Virgo}} = 0.25\,\mathrm{Solar}$) taken from Machacek et al. (2006) and checked independently for the CXB region by a separate ICM emission model. To account for the hard X-ray emission produced by UPS, we used a `powerlaw` component with photon index frozen to $\Gamma = 1.41$ (De Luca and Molendi, 2004), which represents well the contribution of background AGNs. The other two conventionally modelled background components of

Local Hot Bubble (LHB) and the Galactic Thermal Emission (GTE) were also added, however, LHB could not have been constrained in both EPIC and ACIS-S, while the GTE could have been constrained only in the ACIS-S data. This is expected as we only included data above 0.55 keV, the contribution of LHB and GTE is expected to be sub-dominant, and the NPS and Virgo ICM are significantly dominant in M89 spectra. Moreover, the `apec` model ($kT_{\rm NPS} = 0.26\,$keV) that reproduces the NPS is expected to represent the LHB and GTE emission components which have a similar temperature structure. Soft GTE emission in ACIS-S data is modelled with an `apec` component with the same abundance value and absorption hydrogen density column with the NPS component ($kT_{\rm GTE} = 0.1\,$keV, $Z_{\rm GTE} = 0.65\,$Solar).

For testing purposes, we also tried removing the NPS component and instead having LHB and GTE components solely. However, this representation gave a significantly poorer fit.

Spectra from the regions of interest (Core and Tail regions) and the CXB region were fitted simultaneously, and normalizations of all of their common components (NPS, Virgo and UPS) were tied by a scaling factor compensating the differences in effective areas between those regions, assuming that the Virgo ICM and NPS emission do not vary between the two regions. This approach was applied separately to *XMM-Newton*/EPIC and *Chandra*/ACIS-S data.

For *XMM-Newton*-EPIC data, there are also non-X-ray background components which should be modelled. HP background creates fluorescence emission lines in the spectra, even when the filter wheel is closed. The instrumental HP background is represented by a series of Gaussian lines and one broken powerlaw, unconvolved by the auxiliary response file, with values obtained by fitting the filter wheel closed (FWC) data, taken from Breuer et al. (in preparation). Because the HP background varies differently across the instrument, its modelling is done for the Core and CXB regions separately with different normalization values.

The instrumental background model is further combined with the source model using a constant factor, which is allowed to vary during the fitting[4]. Instrumental background modelling is done separately for the Core and CXB region spectra.

3.3.3 AGN treatment approach

Due to the spatial resolution of the *XMM-Newton* observation, we were not able to detect and remove the central AGN region from our spectra for the *XMM-Newton*-EPIC data. Therefore, we were required to reproduce the AGN emission in our model. Thanks to the excellent spatial resolution of the *Chandra* X-ray observatory, we were able to extract a 1.5 arcsec circular region covering the AGN from the *Chandra*/ACIS-S data. By fitting the spectra of this region alone, we estimated the photon index of the `powerlaw` model that is to reproduce the central AGN emission. We use this model in the *XMM-Newton*/EPIC and *Chandra*/ACIS-S fittings for the Core region.

Using the central AGN region (1.5 arcsec), we investigated the emission from the central AGN and its variability within four individual *Chandra* observations. All observations were simultaneously fitted with an absorbed `powerlaw` model with an additional thermal component, `apec`, representing the CIE emission from this region:

```
phabs * (powerlaw + apec).
```

The `apec` abundance was fixed to Solar and the temperatures and normalizations were for all observations tied with respect to the first one. All other parameters (`powerlaw` photon index and normalization) were untied within observations and left free during the fitting.

Photon indices of the `powerlaw` component for individual *Chandra* observations were consistent within uncertainties (Figure 3.4) so we stacked their posterior distributions resulting in a final value of

[4]We also tried unfreezing the normalization of individual instrumental lines to decrease the residuals, however, consistent results were obtained.

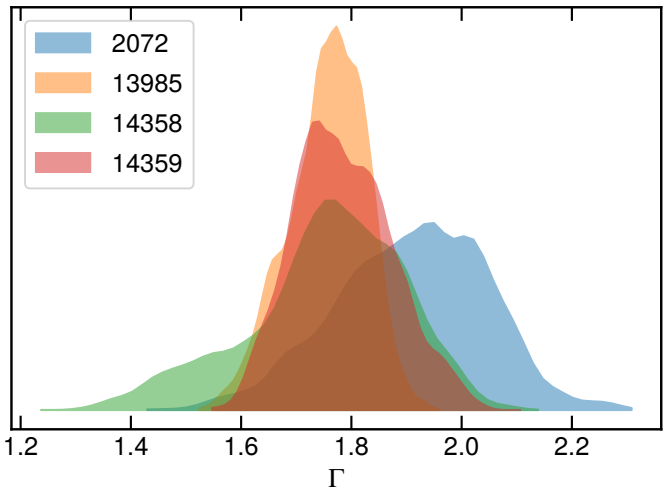

Figure 3.4: Posterior distributions of the powerlaw photon index Γ for the central 1.5 arcsec region (AGN region) for individual *Chandra* OBSIDs. All distributions are consistent within uncertainties and therefore were combined resulting in the final value of $\Gamma = 1.79^{+0.13}_{-0.11}$.

$1.79^{+0.13}_{-0.11}$. The normalizations of the `powerlaw` component varied slightly within individual observations, but the differences between individual OBSIDs were of a factor of ~ 2 at most. The total unabsorbed powerlaw flux averaged over individual OBSIDs was estimated to $F_{2-10\,\mathrm{keV}} = (1.7 \pm 0.1) \times 10^{-14}\,\mathrm{erg\,cm^{-2}\,s^{-1}}$. Assuming the distance of 15.9 Mpc (Tully et al., 2013), this corresponds to a resulting AGN luminosity of $L_{2-10\,\mathrm{keV}} = (5.5 \pm 0.3) \times 10^{38}\,\mathrm{erg\,s^{-1}}$.

As the central AGN emission can not be spatially resolved and excluded with *XMM-Newton*, we instead constrain the contribution of the central AGN emission. For *Chandra* data, we fitted the central Core region (in this case, including the central point source) simultaneously with the AGN region, and we tied the normalizations of their `powerlaw` components, assuming that all emission of the AGN lies within the central 1.5 arcsec region[5]. For the Core region, we then expressed the `powerlaw` normalization as a constant ratio with respect to the normalization of the main thermal emission component (`vgadem`), which was allowed to vary. This ratio was then assumed to be the same for *XMM-Newton* data, and the uncertainty was propagated by fitting the *Chandra* spectra simultaneously with that of *XMM-Newton*. We note that, in general, the contribution of the AGN can be time-variable and the ratio of thermal to AGN components can vary from observation to observation. Still, we believe that this represents a better approach than fitting the AGN `powerlaw` component from *XMM-Newton* data alone. For comparison, we performed the spectral fitting for *XMM-Newton* data also without the AGN `powerlaw` component. In this case, statistical uncertainties were larger. In Figure 3.5, we present MOS spectra of the Core and CXB regions with all emission components.

3.3.4 RGS Analysis

The RGS data is expected to contain very limited background contamination after the standard background template derived from CCD9 was subtracted, which registers the least source events. Therefore, we fitted RGS data without any background components.

We tried several fitting combinations of 1) including the second order spectra or restricting to the first order exclusively; 2) testing 1T, 2T, Gaussian temperature distribution (`vgadem`). The complete results are presented in Table 3.2 and further demonstrated in Appendix A.3.1.

[5] For the core region, we assumed similar model as in Section 3.3.1.

3.4 Results

Abundance ratios in the Core region were obtained by separate modelling of *XMM-Newton*/EPIC, *XMM-Newton*/RGS and *Chandra*/ACIS-S spectra. In addition to the iron (Fe), the magnesium (Mg), silicon (Si) and sulphur (S) abundances were allowed to be free in the EPIC CCDs. The neon (Ne) abundance was initially left free to vary for both the EPIC and ACIS-S models, but it could only be constrained using ACIS-S data, so ultimately neon was set free in the ACIS-S model and fixed relative to iron (Fe) in the EPIC model. For RGS, the oxygen (O), neon (Ne), magnesium (Mg) and iron (Fe) were the free abundance parameters. First, we see that fitting with the addition of second-order RGS spectra gives better statistics, also making the results from the different temperature models more consistent with each other. In each of these fits, all the other elements were tied to Fe except He, which was fixed to be Solar.

After performing our multi-temperature modelling, we measured indications for possible super-Solar abundance ratios (i.e. α/Fe > 1) of Ne/Fe, Mg/Fe, Si/Fe and S/Fe in ACIS-S and EPIC data. As for RGS measurements, Mg/Fe is also super-Solar, however, the O/Fe and Ne/Fe ratios are found to be sub-Solar and Solar, respectively, within uncertainties.

Additionally, we performed tests on the removal of point sources from the CXB region spectra of EPIC using PSF maps with sizes of 20 arcsec, approximately corresponding to a 0.75 ECF. We see that the elemental abundance and abundance ratio results remain consistent even with the application of larger point source masks.

We also tested the differences obtained from the blank-sky data set instead of stowed spectral files. After performing the spectral fit, we observed that the results are comparable, although uncertainties increase with the background-removed blank-sky spectra.

EPIC studies of M89 were previously conducted by Ji et al. (2009), as also stated in Section 3.1. They utilized a single-temperature model, i.e. `wabs × (vapec + powerlaw)`, and subtracted a local background spectrum. Although they investigated a region with a similar size (1 arcmin), we observe that none of our individual abundances from multi-temperature models agree with their single-temperature results. This is expected, because of the 'Fe bias' as explained in Section 3.1. Similarly, although we found super-Solar Mg/Fe, Si/Fe, and S/Fe, they reported Solar ratios.

When we also conducted a single-temperature modelling, we observed that only our individual Mg and Si abundance measurements agree with their results, which were $0.46^{+0.11}_{-0.10}$ and $0.44^{+0.13}_{-0.12}$ Solar, respectively. We also note that the previous versions of AtomDB (Smith et al., 2001; Foster et al., 2012) before the update of AtomDB 3.0.9 in 2020 suffered from the interpolation issue[6]. This issue involved discrepancies caused by the interpolation of `(v)apec` between its pre-calculated spectra (Mernier et al., 2020), which has now been fixed. Therefore, the possible reasons for the discrepancy, even in the single-temperature model, are (i) the use of outdated spectral codes and databases by Ji et al. (2009), (ii) differences in the subtraction of background spectra, which could create biases in abundance measurements (see de Plaa et al., 2007), and (iii) differences in modelling the AGN and LMXB components, which might not be well-described by the single `powerlaw` model in Ji et al. (2009).

Moreover, their RGS analysis suggests individual abundances around $4-5$ Solar. These values are highly unusual considering the highest recurrently and robustly reported elemental abundances are around ~ 2 Solar (e.g. Centaurus Cluster; (Matsushita et al., 2007; Sanders et al., 2016; Fukushima et al., 2022)).

In the CHEERS catalogue, de Plaa et al. (2017) showed that M89 has an O/Fe ratio of 2.0 ± 0.6, which is the highest O/Fe ratio observed in the whole sample. They also showed Ne/Fe = 1.1 ± 0.7, and subsequent work by Mernier et al. (2016) indicates Si/Fe = $1.4^{+5.3}_{-0.7}$. The main difference between our sub-Solar O/Fe ratio and their super-Solar measurement is the choice of the model: we used a multi-temperature model with Gaussian distribution of emission measure while de Plaa et al. (2017) assumed single-temperature

[6] `http://www.atomdb.org/interpolation/index.php`

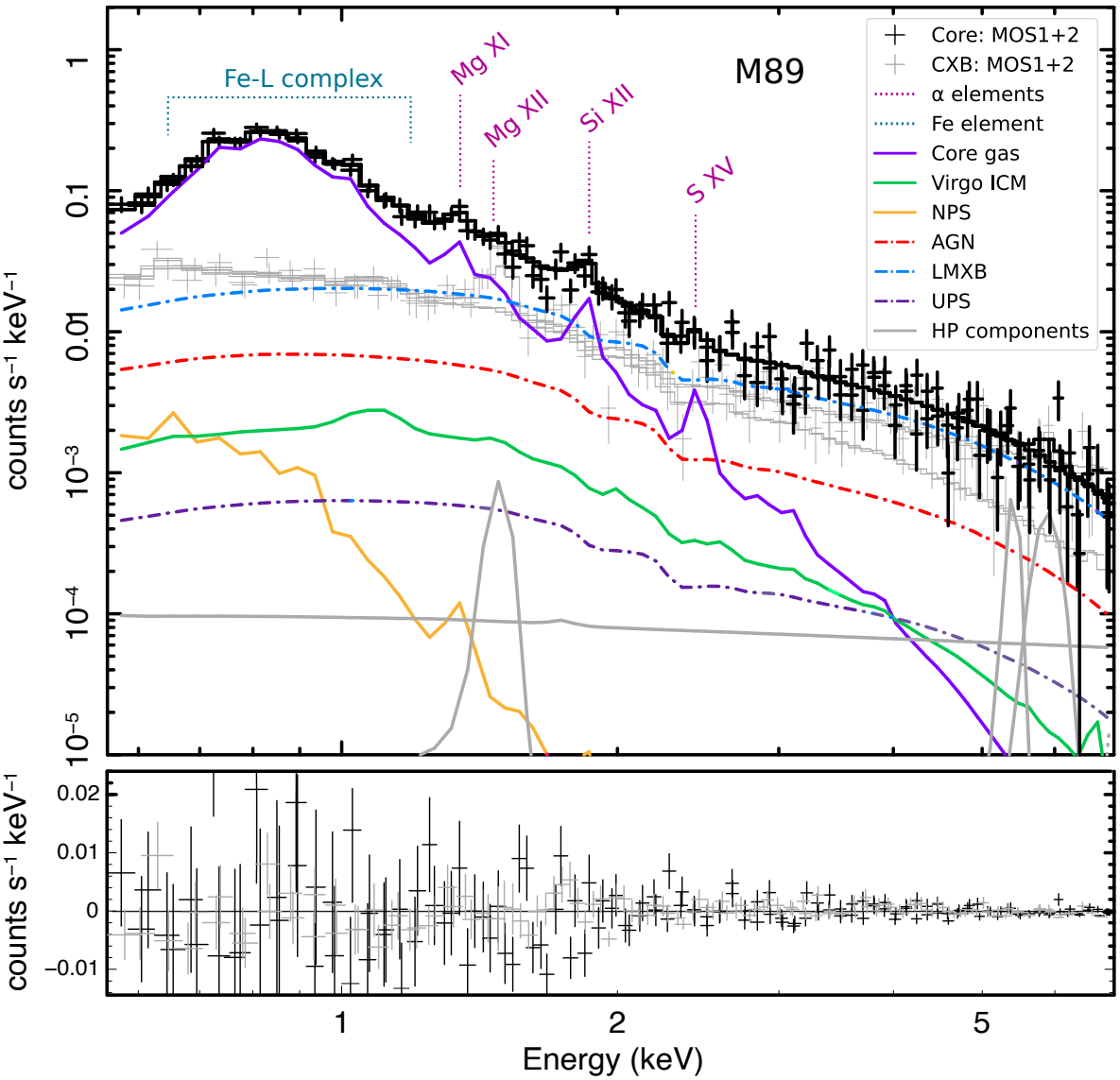

Figure 3.5: *XMM-Newton*-EPIC MOS 1 and MOS 2 combined fit of the core of M89. The CXB region data, which is fitted simultaneously with the Core by tying the parameters of common components after scaling, is also shown (light grey). The best-fit models of the M89 core gas (purple), Virgo ICM (green), NPS (yellow), AGN (dashed-red), LMXB (dashed-blue), UPS (dashed-dark purple) and HP (for MOS 1 and MOS 2) components (grey) are also presented.

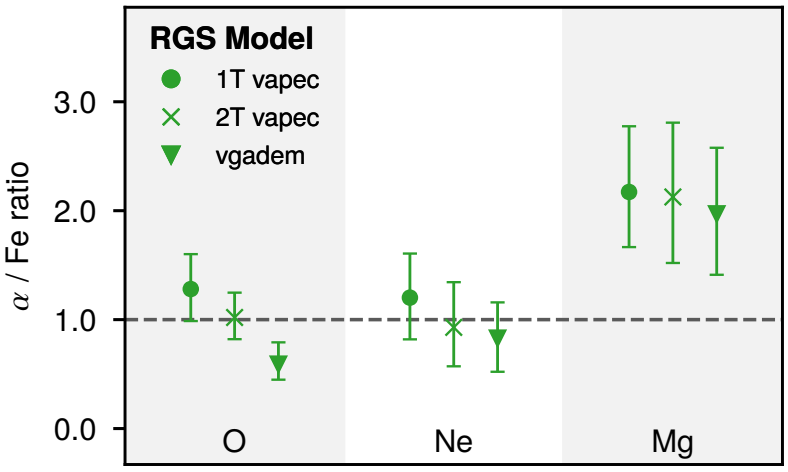

Figure 3.6: O/Fe bias in the *XMM-Newton*-RGS data of the low temperature plasma. The O/Fe ratios differ significantly between multi-temperature models.

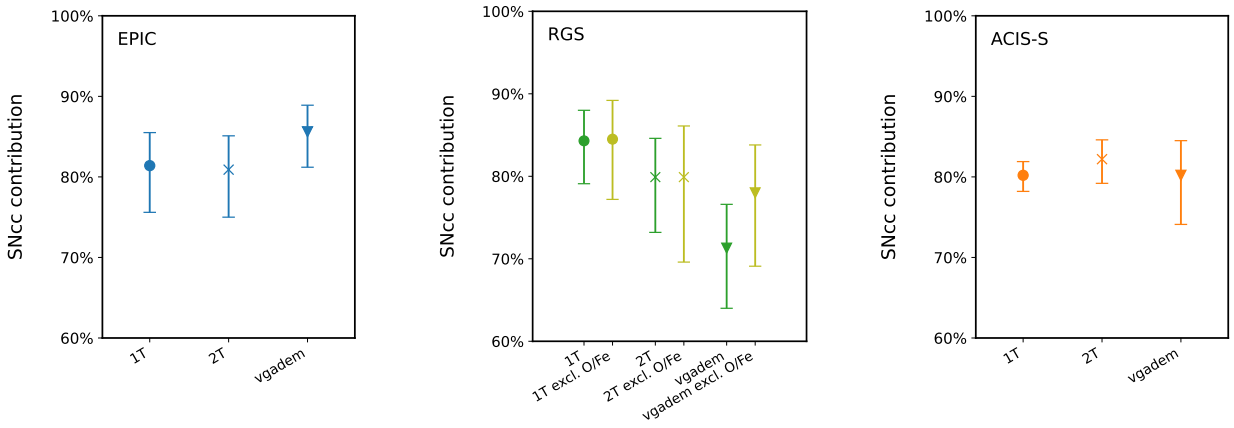

Figure 3.7: SNcc contribution of each instrument with different temperature models. (*Left*) The EPIC calculation used Mg/Fe, Si/Fe and S/Fe ratios. (*Middle*) The RGS calculation used O/Fe, Ne/Fe and Mg/Fe ratios. (*Right*) The ACIS-S calculation used Ne/Fe, Mg/Fe, Si/Fe and S/Fe ratios.

plasma. Therefore, we suspect that in the analysis of low-temperature M89 RGS spectra, the choice of modelling (single-T vs. multi-T) may have a considerable impact on the O/Fe ratio and its interpretation. In our results, we see that the O/Fe ratio changes $> 1\sigma$ between single temperature to `vgadem` model, which is presented in Figure 3.6. The differences between the CHEERS results and ours may also be attributed to the use of the AtomDB database and `vgadem`/`vapec` plasma codes in our study, whereas they employed the SPEXACT database and `cie` plasma code.

The complete list of parameters for EPIC, RGS and ACIS-S obtained from different multi-temperature models is presented in Table 3.2. In the following sections, we first describe the fitting biases. Then, we present the chemical composition results within the Core and Tail regions.

3.4.1 Systematic uncertainties

In order to investigate the differences in abundance estimates between single and multi-temperature models, we refit our data from all three instruments with the same modelling scheme, changing only the

Table 3.2: The parameters derived from different temperature models for *XMM-Newton*/EPIC, *XMM-Newton*/RGS and *Chandra*/ACIS-S observations of M89. Elemental abundances are in the Solar units. The background modelling is the same for each temperature model.

	XMM-Newton EPIC			*XMM-Newton* RGS			*Chandra* ACIS-S		
Parameter	vapec	2 × vapec	vgadem	vapec	2 x vapec	vgadem	vapec	2 x vapec	vgadem
kT_1 (keV)	0.71 ± 0.01	0.62 ± 0.01	–	$0.61^{+0.02}_{-0.03}$	0.84 ± 0.09	–	0.65 ± 0.06	0.35 ± 0.02	–
kT_2 (keV)	–	0.83 ± 0.03	–	–	$0.53^{+0.02}_{-0.03}$	–	–	0.70 ± 0.04	–
kT_μ (keV)	–	–	0.64 ± 0.02	–	–	$0.49^{+0.08}_{-0.10}$	–	–	0.49 ± 0.03
kT_σ (keV)	–	–	0.26 ± 0.04	–	–	$0.41^{+0.19}_{-0.14}$	–	–	0.33 ± 0.04
O	–	–	–	0.29 ± 0.08	0.29 ± 0.08	$0.21^{+0.06}_{-0.05}$	–	–	–
Ne	–	–	–	$0.27^{+0.10}_{-0.09}$	0.26 ± 0.11	$0.30^{+0.09}_{-0.11}$	$0.99^{+0.09}_{-0.11}$	$0.94^{+0.25}_{-0.15}$	$1.51^{+0.30}_{-0.26}$
Mg	0.67 ± 0.14	$1.21^{+0.23}_{-0.27}$	$0.71^{+0.14}_{-0.15}$	$0.50^{+0.15}_{-0.14}$	0.60 ± 0.19	$0.69^{+0.20}_{-0.12}$	0.64 ± 0.07	$0.99^{+0.14}_{-0.11}$	$1.58^{+0.41}_{-0.25}$
Si	$0.55^{+0.14}_{-0.12}$	$1.07^{+0.18}_{-0.19}$	0.73 ± 0.13	–	–	–	0.46 ± 0.05	$0.73^{+0.11}_{-0.10}$	$1.18^{+0.31}_{-0.22}$
S	1.36 ± 0.46	$1.92^{+0.79}_{-0.71}$	1.07 ± 0.48	–	–	–	$0.76^{+0.25}_{-0.21}$	$1.04^{+0.30}_{-0.27}$	$1.57^{+0.70}_{-0.48}$
Fe	$0.62^{+0.08}_{-0.07}$	$1.05^{+0.13}_{-0.14}$	0.58 ± 0.07	0.23 ± 0.04	0.28 ± 0.06	$0.35^{+0.09}_{-0.08}$	0.54 ± 0.03	0.60 ± 0.04	$1.04^{+0.30}_{-0.27}$
C-stat / d.o.f.	437 / 382	420 / 380	414 / 381	649 / 534	642 / 533	638 / 533	759 / 513	659 / 511	672 / 512
SNcc contribution	$81.4\%^{+4.1}_{-5.8}$	$80.9\%^{+4.2}_{-5.9}$	$85.6\%^{+3.3}_{-4.4}$	$84.3\%^{+3.7}_{-5.2}$	$79.9\%^{+4.7}_{-6.7}$	$71.3\%^{+5.3}_{-7.3}$	$82.4\%^{+1.8}_{-2.0}$	$85.4\%^{+2.2}_{-2.7}$	$85.7\%^{+3.7}_{-5.3}$
χ^2 / d.o.f.	4.9 / 2	3.3 / 2	0.7 / 2	2.7 / 2	2.8 / 2	4.6 / 2	24.0 / 3	1.7 / 3	1.1 / 3

M89 hot gas emission component: the single-temperature (`vapec`), double-temperature (`vapec+vapec`) and multi-temperature with Gaussian distribution of emission measure (`vgadem`). The resulting temperatures and abundances derived using individual models (1T, 2T, vgadem) and instruments (ACIS-S, EPIC, RGS) are presented in Table 3.2 and the abundance estimates are graphically compared in Figure A.3.1.

O/Fe bias in the RGS data of low-temperature plasma

The most prominent discrepancy is that the O/Fe ratio is ∼ 2 times lower in `vgadem` compared to 1T `vapec` model, as presented in Figure 3.6. Although not formally significant in our case, we note that this decreasing trend between 1T `vapec` and `vgadem` is also present in Ne/Fe and not in Mg/Fe ratios.

We caution the reader that in the `vgadem` model, kT_μ and σ_{kT} values are $0.49^{+0.08}_{-0.10}$ keV and $0.41^{+0.14}_{-0.19}$ keV respectively. As the dispersion of the Gaussian distribution is comparable to the mean, the imperfections in constraining the multi-temperature nature may cause additional measurement bias.

As we have different abundance results for each instrument and model, we further check the SNe ratios derived from these values. Our aim is to investigate the bias more extensively.

The relative SNcc contribution

In this section, we calculate the relative supernova contributions to the enrichment via the α/Fe ratios. Considering various approaches to model M89's hot atmosphere, we fit the abundance ratios obtained from each instrument to a number of SNcc and SNIa nucleosynthesis yield models available from the literature. Our strategy is to compare the obtained best-fitting SNcc yields, checking for any discrepancy between different temperature models. We note that, for the calculation of SNcc fractions, the input elements and their abundance values differ for each instrument. Therefore, when comparing the relative contributions of SNcc between models, it is important to restrict the comparison within each instrument separately.

We aim to recover the total SNcc/(SNcc + SNIa) fraction contributing to the enrichment. For the calculation, we used `SNeratio`[7] code developed by Erdim et al. (2021), used by recent enrichment studies

[7] `https://github.com/kiyami/sneratio`

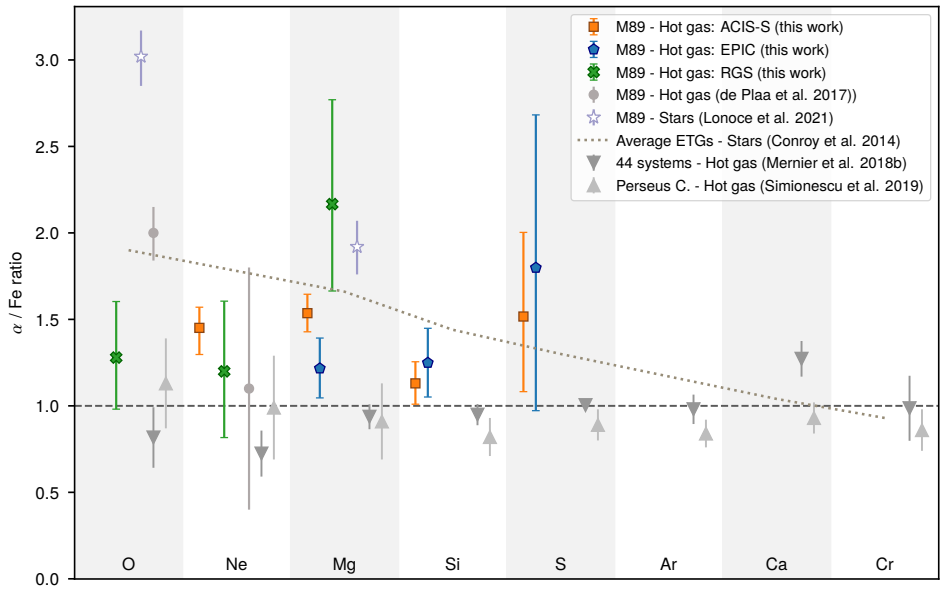

Figure 3.8: α/Fe ratios in the core of the galaxy. For ACIS-S (orange); Ne/Fe, Mg/Fe, Si/Fe and S/Fe ratios are derived via `vgadem` model. For EPIC (blue), `vgadem` model is used to derive Mg/Fe, Si/Fe and S/Fe ratios. In the RGS results (green); O/Fe, Ne/Fe and Mg/Fe are measured with a 1T `vapec` model.

(e.g. Gatuzz et al., 2023). The `SNeratio` code provides the relative SNe contribution for the observed abundance data for selected yield tables and models.

For SNIa yields, we applied 3D models of near Chandrasekhar-mass with delayed detonation from Seitenzahl et al. (2013) and a pure deflagration model from Fink et al. (2014). For the SNcc yields, we used a model from Nomoto et al. (2013). For the yield calculation of the latter, we assume a Salpeter initial mass function (IMF) (Salpeter, 1955). The lower zero-age main sequence mass of stars is adopted with $10M_{\odot}$ and $50M_{\odot}$ as the lower and upper limit, respectively. We integrate the yields using the equation,

$$M_i = \frac{\int_{10M_{\odot}}^{50M_{\odot}} M_i(m) m^{\alpha} dm}{\int_{10M_{\odot}}^{50M_{\odot}} m^{\alpha} dm}, \tag{3.1}$$

where M_i is the total yield (also denoted as Y_i) of the i-th element, $M_i(m)$ is the i-th element mass produced in a star of mass m, and α is the slope of the IMF. For the parameter α, we adopted the value of -2.35 corresponding to the Salpeter IMF.

Furthermore, the number of atoms of element X is given by

$$N_X = aN_{X,\mathrm{SNIa}} + bN_{X,\mathrm{SNcc}}, \tag{3.2}$$

where $N_{X,\mathrm{SNIa}}$ and $N_{X,\mathrm{SNcc}}$ are the number of atoms produced in a single SNIa and SNcc event, respectively, and a and b are the multiplicative factors.

When calculating the SNe fraction with the `SNeratio` code, we used different initial metallicity values for the SNcc yields of Z = 0.0, 0.0001, 0.004, 0.008, 0.02, 0.05. The results are presented in Table 3.2 and Figure 3.7.

For EPIC calculations, we used the Mg/Fe, Si/Fe and S/Fe ratios and found that the SNcc contribution results from different temperature models agree with each other. In this sample, the `vgadem` result is the largest ($85.6^{+3.3}_{-4.4}$ %), while the 1T `vapec` is the smallest ($81.4^{+4.1}_{-5.8}$ %).

As for the SNe contributions estimated from RGS data, we used O/Fe, Ne/Fe and Mg/Fe ratios. From these ratios, the obtained results for 1T `vapec` and 2T `vapec` are comparable within uncertainties. However, we observe $> 1\sigma$ discrepancy between `vgadem` and 1T `vapec` results for SNcc contributions. We

also performed the calculation by excluding the biased O/Fe ratio as input. In this case, we observe that all SNcc contributions agree within uncertainties. We also note that, although the results are consistent when excluding the O/Fe ratios, the same aforementioned trend persists, where the 1T `vapec` and `vgadem` are, respectively, the largest and smallest.

The ACIS-S calculation used Ne/Fe, Mg/Fe, Si/Fe and S/Fe ratios. Using these ratios, we again derived comparable SNcc contributions between temperature models. In this case, the 2T `vapec + vapec` model gave the highest percentage ($85.4^{+2.2}_{-2.7}$ %). Nevertheless, we found that SNcc contribution is > 70% for all detectors and temperature models.

Summary on systematic uncertainties

The discussion on systematic uncertainties can be summarised as follows:

- The O/Fe ratio changes significantly (> 1σ) in the RGS data between different multi-temperature models.
- We observe a systematic change in the SNcc ratios, with or without the O/Fe ratio.
- The SNcc ratios obtained from RGS data differ by more than 1σ between different temperature models. However, excluding the O/Fe ratio makes the results comparable.
- The SNcc contribution cannot be well constrained with the accessible abundance ratios.
- Due to the relatively low clean exposure time of *XMM-Newton*, we observe rather high statistical uncertainties that mask out the true nature of the systematic uncertainties.
- With deeper observations and consequently less statistical error, it would be possible to understand the systematic differences between temperature models more accurately. However, measuring abundance ratios and constraining SNe ratios robustly would still be difficult even if we have deeper observations with the current spectral resolution available.

Consequently, because of the systematic biases and the fact that the σ_{kT} of the `vgadem` model ($0.41^{+0.14}_{-0.19}$ keV) is comparable to the kT_{μ} value ($0.49^{+0.08}_{-0.10}$ keV), we conclude that, for RGS, the `vgadem` model is not adequate to constrain the temperature structure. Therefore, for further analysis in this paper, we use the 1T model for the RGS data, which is also used in de Plaa et al. (2017) for M89.

3.4.2 Summary on α/Fe ratios

Core

In Figure 3.8, we present the best-fit values of the abundance ratios that are previously discussed. In the plot, the results for EPIC and ACIS data correspond to `vgadem` model, while for RGS a single-temperature (1T vapec) fit was presented.

We find the overall abundance ratios to be super-Solar. S/Fe and Si/Fe ratios from ACIS-S and EPIC are 1σ larger than the Solar values. Similarly, Mg/Fe for EPIC and RGS are also 1σ larger while the ACIS ratio of Mg/Fe is 5σ greater. The Ne/Fe ratio is again super-Solar for both ACIS-S and RGS. Likewise, the O/Fe ratio is 1σ higher than its Solar value in RGS.

The super-Solar O/Fe and Ne/Fe ratios, also presented in Figure 3.8, agree with the results of de Plaa et al. (2017). Moreover, Mernier et al. (2016) showed that Si/Fe is also super-Solar with a value of $1.4^{+5.3}_{-0.7}$; however, due to a large positive uncertainty, we exclude it from the plot for visualisation purposes. In fact, M89 is the only sample in the CHEERS measurements having super-Solar values for all ratios.

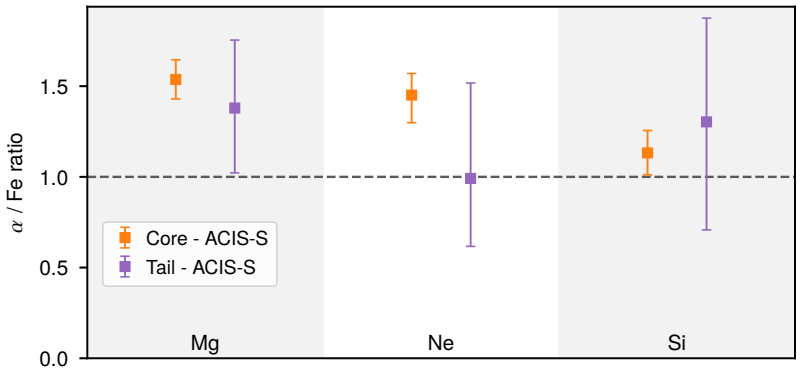

Figure 3.9: α/Fe ratios in the Tail region obtained from the *Chandra*/ACIS-S data.

This result differs from the global Solar composition in the elliptical galaxy atmospheres (Mernier et al., 2018). The results indicate that the composition in M89 hot gas is more similar to the stellar components.

The physical interpretation of these results and the possible scenarios explaining the atmosphere with super-Solar abundance ratios are presented and discussed in the Discussion section.

Tail

For the striped tail of the galaxy, the chemical abundances could only be constrained with the deep *Chandra*/ACIS-S observation. We found that absolute abundances are lower than in the Core region and thus less than Solar. The ratios, on the other hand, are super-Solar for Mg/Fe and Si/Fe, all comparable with the Core region within uncertainties, presented in Figure 3.9. Ne/Fe ratio, on the other hand, is Solar but still comparable with that of the Core region. Regrettably, the uncertainties in the tail region are so large that a robust physical interpretation is not possible.

The chemical abundance ratios in the two gas regions are found to be comparable. These results are further discussed in the Discussion section.

3.4.3 AGN activity

The AGN-driven shock front

One of the prominent features of M89 is an 'hourglass' structure first noted by Filho et al. (2004) in the inner region of the galaxy. This hourglass shape is composed of two rings of approximately circular shape where each inner edge reaches ~ 0.85 kpc while the outer edge reaches ~ 1.30 kpc from the centre. These rings of shocked gas have been attributed by past research to the nuclear activity of the central AGN of this galaxy (Machacek et al., 2006).

To determine the temperature jump across the rim of the shock, we utilised all four *Chandra* observations with a total observation time of 201.3 ks, in contrast to Machacek et al. (2006) who used a single 54.4 ks observation. Unlike other studies, we investigate the Northern and Southern Rings separately for the first time. We fit the spectra of the regions NR, NRO, SR, and SRO described in Section 3.2.3 with a single-temperature (1T `vapec`) model with abundances fixed to Solar values, focusing only on the hot atmosphere component as described in Section 3.3. We also tried spectral fitting using the single temperature Fe abundance result obtained by 1T `vapec` fitting of the *Chandra* Core region data, which is approximately half of the Solar value. However, we see that changing the abundance value affects the temperature value by less than 0.5%, and we ultimately decided to use the Solar abundances. The result-

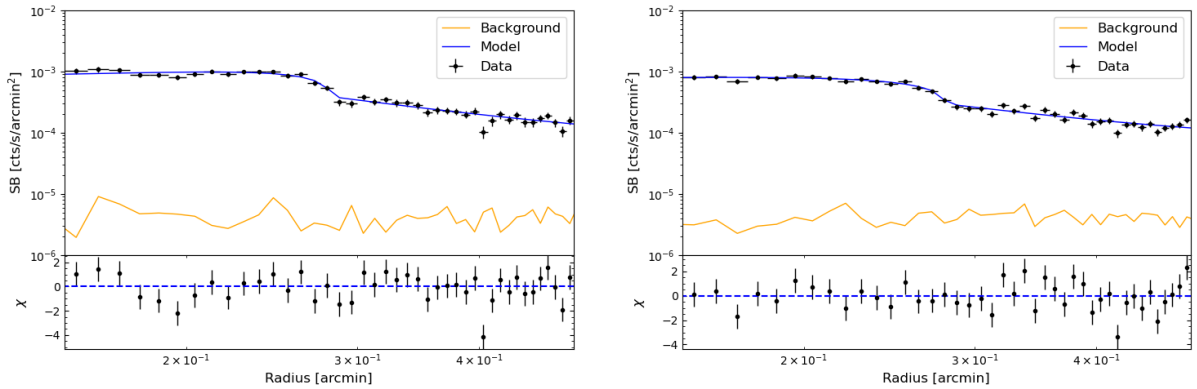

Figure 3.10: *(Left)* The best fit broken powerlaw model fitted to the surface brightness profile of the northern ring, extracted from an annular section spanning from 55° to 145° with inner and outer radii of 11 and 31 arcsec. *(Right)* The best fit broken powerlaw model fitted to the surface brightness profile of the southern ring, extracted from an annular section spanning from 245° to 335° with inner and outer radii of 11 and 31 arcsec.

ing temperatures are 0.73 ± 0.01 keV at the rim of the northern ring (NR), with the temperature decreasing to 0.43 ± 0.02 keV on the outside of the northern ring (NRO). For the southern part, the temperature reaches 0.76 ± 0.01 keV at the edge of the shock (SR) and declines to 0.43 ± 0.03 keV on the outside of the rim (SRO).

The change in electron density across the edge of the shock can be gauged from the surface brightness profile across these rings. Therefore, we extract the surface brightness profile from the exposure-corrected, background-subtracted image in the energy band of $0.5 - 2.0$ keV and analyse each ring in annular sections encompassing both the NR (SR) and NRO (SRO) regions. For each brightness discontinuity, we model the surface brightness profile using an MCMC analysis and we assume a spherically symmetric broken powerlaw distribution projected along the line of sight for the electron density of

$$n_e = \begin{cases} n_{\rm rim} \left(\frac{r}{r_{\rm rim}}\right)^{-\alpha_1} & r < r_{\rm rim} \\ \frac{1}{J} n_{\rm out} \left(\frac{r}{r_{\rm out}}\right)^{-\alpha_2} & r \geq r_{\rm rim} \,, \end{cases} \tag{3.3}$$

where $r_{\rm rim}$ is the outer radius of the shock ring, $r_{\rm out} = 3.1$ kpc and marks the unshocked region outside of the rim, $n_{\rm rim}$, $n_{\rm out}$ are the normalisation inside and outside the rim of the shock, α_1, α_2 are the power law indices for each region, while J is the discontinuity parameter. The discontinuity parameter is given by

$$J = \frac{\Lambda_{\rm rim} n_{\rm rim}^2}{\Lambda_{\rm out} n_{\rm out}^2} \,, \tag{3.4}$$

where Λ and n represent the emissivity and electron density of each region.

We find the best-fit position for the outer rim of the shock to be $r_{\rm rim} = 1.31^{+0.01}_{-0.01}$ kpc for the northern ring and $r_{\rm rim} = 1.29^{+0.01}_{-0.02}$ kpc for the southern ring. The inferred electron density ratio $n_{\rm rim}/n_{\rm out}$ across each ring is $1.46^{+0.09}_{-0.09}$ (NR) and $1.41^{+0.09}_{-0.08}$ (SR). By fitting the region inside and outside of the shock rim with a simple powerlaw, we calculate the densities in these regions for the northern (southern) ring to be $n_{\rm rim} = 0.06^{+0.01}_{-0.01}$ ($0.07^{+0.01}_{-0.01}$) cm^{-3} and $n_{\rm out} = 0.04^{+0.01}_{-0.01}$ ($0.04^{+0.01}_{-0.01}$) cm^{-3}. The best-fit models of the surface brightness profiles can be found in Figure 3.10.

The temperature and density inside the brighter region are higher than those of the fainter surroundings. This confirms the nature of the discrepancy at $r_{\rm rim} \sim 1.3$ kpc as a shock driven by a nuclear outflow

as mentioned by Machacek et al. (2006). Utilising the $T_{\rm rim}/T_{\rm out}$ and $n_{\rm rim}/n_{\rm out}$ ratios in the Rankine-Hugoniot (e.g. Landau and Lifshitz, 1959) shock conditions for a monatomic ideal gas with adiabatic index $\gamma = 5/3$ allows to estimate the speed of the shock's propagation.

Using the measured temperature discrepancies across each ring, we find the propagation speed of the shock for the northern (southern) ring to be $M_1 = 1.67 \pm 0.09$ ($M_1 = 1.74 \pm 0.09$), while the inferred density discrepancy measured through the change in surface brightness suggests a speed of $M_1 = 1.31 \pm 0.24$ ($M_1 = 1.28 \pm 0.23$). As stated in Machacek et al. (2006), due to the narrowness of the shock front, the measured surface brightness discontinuity will underestimate the real density discrepancy. Therefore, this method infers the lower limits of the shock speed.

The total energy of the outburst

The speed of the shock front allows us to calculate its age and the power of the outburst that created it. For a mean radius of $R \sim 0.81$ kpc estimated from the surface brightness profile, and the lower limit on the speed estimated from the density discontinuity, the age of the shock is ~ 1.8 Myr, while the temperature change indicates a somewhat younger age of ~ 1.4 Myr. The outburst energy can be expressed as $E_{\rm shock} \sim p_{\rm rim} V (p_{\rm rim}/p_{\rm out} - 1) \sim 7.7 \times 10^{54}$ erg, where $p_{\rm rim}$ and $p_{\rm out}$ represent the pressure of the shocked and unshocked gas.

By combining the X-ray cavity volumes determined by Plšek et al. (2024) with the thermal pressure profiles from Plšek et al. (2022), we estimated the total radio-mechanical energy released by the central AGN to $E_{\rm cav} = 1.37^{+0.02}_{-0.03} \times 10^{55}$ erg. The total mechanical energy of the nuclear outburst is $E_{\rm tot} = E_{\rm shock} + E_{\rm cav} \sim 2.14 \times 10^{55}$ erg.

3.5 Discussion

Super-Solar α/Fe abundance ratios in the hot atmosphere of M89 would suggest that this galaxy is a rare case where the abundance ratios of the hot gas deviate from the Solar value, and are closer to the average stellar abundance ratios. Considering that this is potentially the first atmosphere with reported super-Solar abundance ratios and that M89 is a particularly dynamic system, our result requires careful investigation.

The stellar age of M89 is calculated to be $8.9^{+3.4}_{-2.5}$ Gyr (McDermid et al., 2006), which corresponds to a formation time of $z \sim 0.7 - 4.3$. The early enrichment scenario, which is briefly explained in Section 3.1, suggests that the ICM gas has mostly completed its enrichment around $z \sim 2 - 3$. Assuming that the galaxy accumulated most of its hot X-ray emitting gas after the enrichment (i.e. after $z \sim 2 - 3$), M89 should have a hot atmosphere composed of 'universal' gas. So far, other similar ellipticals have been found to host hot gas with Solar abundance ratios (e.g. Mernier et al., 2022; Mernier et al., 2016), therefore it is critical to constrain the possible scenarios.

Observational indications for the super-Solar abundance ratios might be explained by the depletion of the original atmosphere due to AGN activity and ram-pressure stripping. M89 may have lost a significant part of the hot gas through turbulent mechanisms, replacing it with accumulated thermalised stellar wind wind material with super-Solar α/Fe abundance ratios.

3.5.1 Ram-pressure stripping and accretion cut-off

The tailored simulation studies of M89 by Roediger et al. (2015a,b) show that the observable X-ray tail itself is not the subject of stripping. Instead, it is a morphologically deformed atmosphere, shielded from the ICM and preserved by the galaxy up to or beyond pericenter passage. In more general terms, if the ambient medium of an infalling galaxy has sufficient viscosity and/or magnetic field, the Kelvin-Helmholtz instabilities that cause turbulent mixing are suppressed (Chandrasekhar, 1961). Therefore,

in an ICM that is viscous and has a strong enough magnetic field, the downstream hot atmosphere (i.e. the 'tail') is unmixed, dense and therefore X-ray bright, which is believed to be the case of M89. This is confirmed by our measurements, as the elemental ratios of the Tail and Core regions are compatible, and the overall gas content in the tail is similar to that in the core. The less-dense Solar gas, which was once in the outskirts of the galaxy's original atmosphere, has been relocated at the edges of the tail due to the flow. As the simulations of M89 suggest, this less dense Solar gas at the edges of the tail is the subject of peeling. Consequently, as the motion continues, the Solar gas at the periphery constantly depletes. Moreover, the gas from the surrounding environment is no longer able to fall onto the galaxy because of the large velocity differences between the ICM and the galaxy (Gunn and Gott, 1972).

Before the infall, M89 experienced gas inflows and outflows simultaneously. At this unperturbed stage, the galaxy continuously accreted gas with Solar abundance ratios from the surrounding intergalactic medium, while part of its initial atmosphere was lost due to supernova-driven and AGN-induced outflows (for a review on the topic, see e.g. Werner et al., 2019). However, once the galaxy encounters the Virgo ICM, the accretion of external material stops, and the atmosphere begins to be stripped. During its oscillation inside the Virgo cluster, the thermalised stellar mass loss products, which have super-Solar abundance ratios are accumulated in the galaxy's atmosphere. As a result, the stellar mass loss products may become dominant in the hot atmosphere of M89.

We caution the reader that our proposed scenario is not compatible with a similar infalling galaxy NGC 1404 which is also exhibiting an X-ray tail. Mernier et al. (2022) showed that NGC 1404, a satellite galaxy in the Fornax cluster, has Solar chemical composition. It is possible that the difference between the two stripped galaxies is a result of the AGN feedback in M89. Unlike M89 with AGN-induced X-ray cavities, NGC 1404 does not exhibit any AGN activity. Therefore, the initial atmosphere of NGC 1404 might not be uplifted and stripped as effectively.

3.5.2 Gas displacement by the AGN

The outflow of the initial hot gas with Solar abundance ratios in M89 might be facilitated because of the AGN activity. In Section 3.4.3, we showed that the mechanical energy to evacuate both cavities is greater than 1.5×10^{55} erg. The total mechanical energy of the nuclear outburst is $\sim 2.14\times10^{55}$ erg, and the mechanical power of the nuclear outburst is $1.3-1.7\times10^{41}$ erg s^{-1}. For comparison, the gravitational binding energy of the galaxy is calculated as $E_{\rm bind} =\sim 3.97\times10^{56}$ erg within a half-light radius ($r_{\rm e}$), using the total mass from Cappellari et al. (2013) and X-ray gas mass from Plšek et al. (2022).

Based on these results, the energy released into the galaxy atmosphere from the AGN-induced outflows in M89 is significant. As the atmospheric gas is uplifted to higher altitudes, ram-pressure stripping becomes more effective, facilitating the loss of the original galactic atmosphere.

3.5.3 Replenishment due to the stellar mass loss

Internal sources of hot gas in elliptical galaxies are the thermalised stellar mass loss products (Mathews, 1990; Mathews and Brighenti, 2003). When the red giant stars orbit supersonically relative to the hot ambient gas, simulations suggest that approximately 75% of the ejected gas is shock-heated and becomes part of the hot atmosphere (Parriott and Bregman, 2008). Planetary nebulae are another source of hot gas, although the interaction between the hot ambient medium and a planetary nebula shells thermalizes only a small fraction of the material (Bregman and Parriott, 2009).

In the core of M89, due to the lack of ongoing Solar gas accretion, the internal sources of hot gas can dominate the overall chemical composition. The presence of higher-than-average SNcc products in the stars of the galaxy (Lonoce et al., 2021) supports this scenario. In this section, we focus on the ejected wind material of evolving stars and compare it to the metal masses in the hot gas based on our measured metal abundances.

Table 3.3: Masses of the gas-phase metals inside M89 at $2\,r_e$ obtained from the abundance values from the Core region.

Element	EPIC ($10^5 M_\odot$)	RGS ($10^5 M_\odot$)	ACIS-S ($10^5 M_\odot$)
O	–	3.71 ± 1.02	–
Ne	–	$1.10^{+0.40}_{-0.36}$	$6.16^{+1.22}_{-1.06}$
Mg	0.85 ± 0.18	0.64 ± 0.20	$2.01^{+0.52}_{-0.32}$
Si	$0.78^{+0.20}_{-0.17}$	–	$1.69^{+0.44}_{-0.31}$
S	0.93 ± 0.31	–	$1.07^{+0.48}_{-0.33}$
Fe	$1.50^{+0.19}_{-0.17}$	0.55 ± 0.09	$2.51^{+0.72}_{-0.65}$

Total mass budget of metals

We find the individual metal budget in the hot gas phase. The total X-ray emitting hot gas in M89 is derived as $\sim 1.8 \times 10^8\,M_\odot$ for 2 r_e region (Su et al., 2015). The elemental metal mass in a hot gas region enclosed with radius R can be calculated as

$$M_X(R) = X_\odot X(R) \frac{A_X}{A_H} \chi_H M_{\rm gas}(R), \tag{3.5}$$

where $X_\odot$ and $X(R)$ are the Solar abundance of element X, taken from Lodders et al. (2009), and the measured abundance of that element, respectively. Their product, $(N_{X\odot}/N_{H\odot}) \times (N_X/N_H)/(N_{X\odot}/N_{H\odot})$, gives the ratio of number of X atoms over H atoms in the medium. A_X and A_H are the atomic weights of X and H respectively. The obtained mass fraction of element X with respect to H is then multiplied by the χ_H, the H mass fraction adopted as 0.735, which gives the ratio of X mass over the total mass. $M_{\rm gas}(R)$ is the total mass in the enclosed volume, consequently, their product gives the mass of element X. Finally, the calculated hot-gas phase metals in the centre of M89 are presented in Table 3.3.

Stellar wind contribution to the hot gas

The stellar mass loss rate in an elliptical galaxy with a Salpeter initial mass function (Salpeter, 1955) in a given time t, can be approximated according to (Ciotti et al., 1991) as following:

$$\dot{M}_*(t) = 1.5 \times 10^{-11} L_{\rm B} (t/t_H)^{-1.3} \tag{3.6}$$

where L_B is the present B band luminosity and t_H is the Hubble time. From Ellis and O'Sullivan (2006), we adopt the $L_B = 1.95 \times 10^{10} L_\odot$ for M89. As for determining the time interval for the integral, we investigate the star formation of the galaxy. Using MegaCam observations, Boselli, A. et al. (2022) showed that the Hα[NII] distribution in M89 mostly comes from the diffuse filamentary structures rather than any apparent star-forming region. Moreover, HST observations of the galaxy do not show significant Hα[NII] emission (Temi et al., 2022). Therefore, similar to other elliptical galaxies, we assume that the galaxy experienced a short and brief star formation peak around $z \approx 3$ (Thomas et al., 2010). As a result, we integrate the mass-loss equation from $z = 3$ to $z = 0$ ($t = t_H$), and find a total mass of $10.6 \times 10^9\,M_\odot$. Notice that this approximation is very rough and should be taken as an order-of-magnitude estimation for further analysis.

For the next step, we take the average ranges of stellar abundances in M89 from Lonoce et al. (2021) and calculate the individual metal masses. Using Equation 3.5, the ejected masses via stellar wind are found to be $(1.2-1.6) \times 10^7\,M_\odot$ for Fe, $(1.1-1.7) \times 10^7\,M_\odot$ for Mg and $(1.6-2.1) \times 10^7\,M_\odot$ for O.

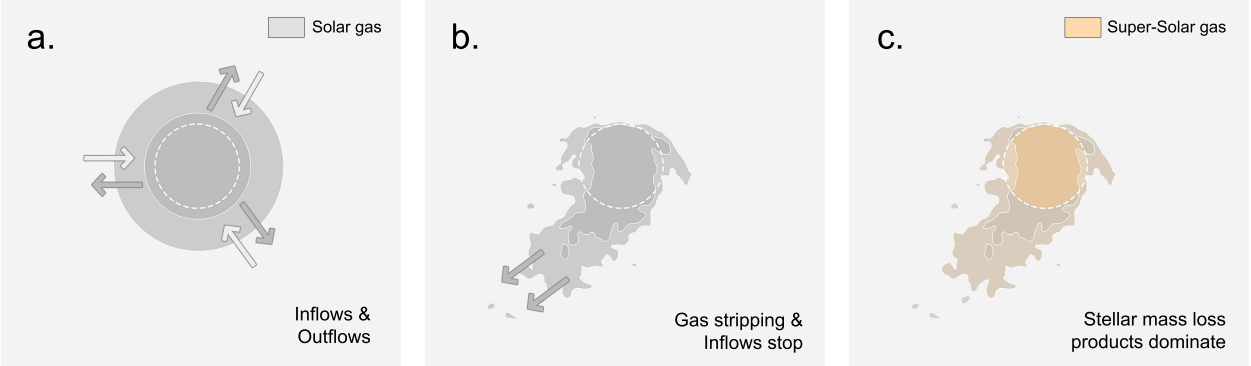

Figure 3.11: Illustration of the proposed chemical enrichment scenario of M89. The colour shade changes in the illustrative sketch are arbitrary and present density changes in a simplified approach, where the lighter outskirts have high entropy and darker inner regions have low entropy. The initial size of the hot atmosphere is again arbitrary, while the dashed circle corresponds to the Core region. (**a.**) Continuous inflows and outflows occur between the M89 and the intergalactic medium. The X-ray gas in both mediums has Solar abundance ratios. (**b.**) Once the galaxy falls into the Virgo cluster, because of the ram pressure and AGN activity, its original atmosphere begins to be stripped. Due to the accretion cut-off, the galaxy is not able to accrete new gas from the surrounding ICM. (**c.**) As the inflow of gas is prevented and the stellar content of the galaxy ejects fresh gas with super-Solar abundance ratios via the stellar winds, the super-Solar gas becomes dominant.

Note that the above calculations are rough predictions for order of magnitude comparison between the observed and theoretically ejected metal masses. Nonetheless, we find 1–2 orders of magnitude more mass is ejected through stellar winds compared to the total observed mass of O, Mg and Fe. Therefore it is possible to say that the hot gas with super-Solar ratios could originate from the super-Solar stellar content present in M89.

In this scenario, gas outflows and inflows existed simultaneously before the infall (see (a.) in Figure 3.11). After the infall, the original Solar gas content of M89 begins to be depleted because of the ram-pressure stripping and AGN-induced outflows. Furthermore, during the infall, accretion of the Solar gas from surroundings is restrained (see (b.) in Figure 3.11). The stars in M89, which have a higher α/Fe ratio than the average elliptical galaxies, eject hot gas into the galaxy via stellar winds. As a result, we argue that the freshly ejected gas is mixed with the remaining original atmosphere and creates a new generation of hot gas with super-Solar abundance ratios (see (c.) in Figure 3.11).

We note that Mernier et al. (2022) showed that the metal mass produced and ejected through stars in NGC 1404 also exceeds the observed mass: ~20 and ~40 times more mass is produced for Fe and Mg, respectively. Interestingly, the hot atmosphere of NGC 1404 is found to be Solar by that study. Therefore, any metal excess caused by stellar winds does not necessarily indicate a super-Solar composition in an X-ray gas. By studying the differences between two ram-pressure stripped galaxies NGC 1404 (which does not harbour an active nucleus) and M89 (which harbours a prominent AGN with bubbles and shocks), we can attempt to derive constraints on the chemical enrichment and the origin of galactic atmospheres. We can address questions such as: (i) is a stellar-like chemical composition in a hot gas a universal feature in galaxies with an accretion cut-off? (ii) Why does NGC 1404 have Solar ratios while M89 has super-Solar ratios? More generally, (iii) is it enough to experience an accretion cut-off to have a stellar-like atmosphere, or is it necessary to undergo a significant loss of original gas? We conclude that, in M89, AGN-induced outflows could have facilitated the stripping of the original galactic atmosphere, which has been replaced with fresh stellar mass loss material with super-Solar α/Fe abundance ratios, producing the observed difference between M89 and NGC 1404.

Moreover, the metal budget in the ICM gas is measured to be 2 to 10 times larger than what their stars could have produced (e.g. Renzini and Andreon, 2014). Similar to the Mernier et al. (2022), we observe an 'inverse metal conundrum' in M89 where the metals in the hot gas are $1-2$ orders of magnitude less than the stars could have ejected. The two conundra might be comparable. It is possible that the excess metals that are ejected by the stars of elliptical galaxies are mixed with the ICM during the enrichment.

3.6 Conclusions

In this paper, we investigated the chemical composition of the infalling elliptical galaxy M89 (NGC 4552), which hosts X-ray cavities and a prominent shock front due to radio mechanical AGN activity. During its voyage into the Virgo cluster, the hot galaxy atmosphere experiences ram-pressure stripping caused by the interaction with the intracluster medium. Due to the stripping, M89 hosts a bright X-ray tail.

Using *XMM-Newton* and *Chandra* archival observations, we investigated the chemical composition in the core and the tail of the galaxy. With particular attention to the modelling, we derived O/Fe, Ne/Fe, Mg/Fe, Si/Fe and S/Fe ratios from EPIC MOS, EPIC pn, RGS and ACIS-S. Our results can be summarised as follows.

- Our measurements suggest a super-Solar abundance ratios (i.e. $\alpha/\mathrm{Fe} > 1$) in the core. Such a gas content is chemically closer to the stellar population of the galaxy (Lonoce et al., 2021) rather than the rest of the gaseous content in the universe, which is closer to our Solar system (i.e. $\alpha/\mathrm{Fe} \sim 1$). In the tail, the results are comparable with the core, however, it is less certain due to large uncertainties.

- We report a fitting bias in the *XMM-Newton*/RGS data. In low-temperature plasma, the O/Fe ratio changes significantly ($> 1\sigma$) between different multi-temperature models. Because of the bias, we were unable to robustly constrain the SNcc contribution fraction as there is a systematic change in the SNcc ratios. Nevertheless, we found that the SNcc contribution to the hot atmosphere of M89 is greater than 70% for all multi-temperature models and instruments.

- We argue that the potential super-Solar abundance ratios might be produced mainly by the stellar population of the galaxy via stellar winds after the infall. During the infall, the low-density Solar gas is stripped from the edges of the tail. Moreover, because of the motion of the galaxy, the continual infall of gas with Solar abundance ratios from the surrounding ICM is stopped. Therefore, a new generation of hot atmosphere with super-Solar abundance ratios might be produced due to the stellar mass loss products in M89.

- In order to test the stellar contribution to the observed chemical composition, we calculated the mass of the observed hot gas metals and compared them to the metal content that stellar winds possibly eject since $z = 3$. We showed that the stellar winds alone could possibly produce ~ 2 orders of magnitude more metal mass than the metal budget of the hot gas in M89.

- In the AGN activity analysis, we showed that the AGN-induced nuclear outburst energy is $\sim 2.14 \times 10^{55}$ erg; while the gravitational binding energy is $\sim 3.97 \times 10^{56}$ erg. We conclude that the comparable energies suggest that AGN significantly facilitates the stripping of the original galaxy atmosphere.

- We state that the chemical enrichment history of galaxies is still a matter of debate. Based on our results, we argue a possible scenario that would explain the potential super-Solar abundance ratios. However, this scenario does not explain such a composition universally. For instance, an atmosphere of similar infalling galaxy NGC 1404 exhibits Solar abundance ratios. We show that in

M89 the AGN activity might facilitate ram-pressure stripping, possibly clarifying the differences between the two galaxies.

This work shows the importance of studying low-mass systems in various dynamical states to improve our understanding of the chemical enrichment of the universe. Due to the relatively short exposure time of *XMM-Newton*, we were unable to investigate the spatial distribution of metals. In order to fully understand the metal mixing between the X-ray tail and the Virgo ICM, as well as the AGN-induced metal distribution in the galaxy core, a deeper observation by *XMM-Newton* is required. Future missions with higher spectral resolution, such as *XRISM* and *Athena*, will help us to significantly improve the systematic uncertainties in the measurements of the abundances of SN_{CC} products such as O, Ne, and Mg.

Acknowledgements

The authors thank the anonymous referee for constructive feedback that helped improve this paper. S.K. and E.N.E. would like to thank TUBITAK for the financial support under the 1002 project with code number 121F436. The research leading to these results has received funding from the European Union's Horizon 2020 Programme under the AHEAD2020 project (grant agreement n. 871158). T.P., N.W. and J-P.B. were supported by GACR grant 21-13491X. The material is based upon work supported by NASA under award number 80GSFC21M0002. E.N.E. would like to thank Bogazici University for their support through BAP project number 13760. This work is based on observations obtained with *XMM-Newton*, an ESA science mission with instruments and contributions directly funded by ESA member states and the USA (NASA). The scientific results reported in this article are based in part on data obtained from the *Chandra* Data Archive.

Annex 4

Missing metals in the core of the Centaurus cluster's ICM

T. Plšek[1], N. Werner[1], F. Mernier[2], A. Majumder[3], A. Simionescu[4] and L. Stofanova[1]

[1] Department of Theoretical Physics and Astrophysics, Masaryk University, Brno, Czech Republic
[2] IRAP, CNRS, Université de Toulouse, CNES, UT3-UPS, Toulouse, France
[3] Centre for Astrophysics, University of Waterloo, 200 University Avenue West, Waterloo, Ontario N2L 3G1, Canada
[4] SRON Netherlands Institute for Space Research, Niels Bohrweg 4, 2333 CA Leiden, The Netherlands

Abstract: We revisit archival *Chandra* ACIS-S and *XMM-Newton* EPIC observations of the Centaurus cluster to study the Fe abundance profile in its cool core and to compare deprojected CCD results with recent XRISM Resolve measurements. We model the spectra with deprojected thermal plasma models, examine the eastern and western sectors separately, and test whether the hot and cool phases can have different Fe abundances. A strong off-centre Fe peak at $r \approx 14$–19 kpc is recovered robustly in both *Chandra* and *XMM-Newton* data and on both sides of the core, reaching about $3\,Z_{\odot}$. When the core is described with a deprojected two-temperature model and current atomic data, the central Fe abundance increases to values broadly consistent with XRISM, showing that much of the classical deep central dip is caused by unresolved multi-phase structure. However, a residual decline from the Fe peak toward the innermost few kpc remains. The sector-resolved profiles show that the metal distribution is asymmetric: the eastern side has a broader metal-rich region and a stronger cool component, whereas the western profile begins to rise at larger radii. Allowing the hot and cool phases to have different Fe abundances yields a metal-rich hot phase in the centre, $Z_{\rm Fe,hot} \approx 1.6$–$1.7\,Z_{\odot}$, and a much lower-abundance cool phase, $Z_{\rm Fe,cold} = 0.52 \pm 0.06\,Z_{\odot}$. These results suggest that the remaining central Fe drop is produced by a combination of a true decrease in the hot-phase abundance toward the centre and residual fitting biases, with contributions of resonance scattering and possibly dust depletion.

Keywords: galaxies: abundances - galaxies: clusters: intracluster medium - X-rays: galaxies - galaxies: active - galaxies: individual (NGC4696)

Publication in preparation – will be submitted to Monthly Notices of Royal Astronomical Society (MNRAS) in the following months. The publication will likely be expanded with estimates of the effect of resonance scattering on measured metallicity profiles.

4.1 Introduction

Early X-ray observations of galaxy clusters provided the first evidence that the intracluster medium (ICM) is enriched with heavy elements. The initial detections were limited to the iron K-shell emission line, observed in cluster spectra obtained with proportional counters, which demonstrated the presence of Fe in the hot plasma (Mitchell et al., 1976; Serlemitsos et al., 1977). Using a sample of nearby clusters, Mushotzky et al. (1978) showed that the ICM is significantly enriched, with typical iron abundances of about 0.3 – 0.5 times the Solar metallicity. Subsequent observations with the *Einstein Observatory* led to the detection of emission lines from additional elements, including O, Mg, Si, and S (Canizares et al., 1979; Mushotzky et al., 1981; Lea et al., 1982), establishing that the ICM contains a broader range of metals synthesised by stellar and supernova activity. X-ray observations extending to high redshift showed that the mean metal abundance of the ICM exhibits little to no evolution with redshift, indicating that most of the enrichment must have taken place at early epochs (Mushotzky and Loewenstein, 1997; Finoguenov et al., 2000). This early enrichment scenario is further supported by studies of cluster outskirts, which indicate that metals are widely distributed throughout the ICM, with metallicities of 0.2 – 0.3 Solar observed out to the virial radius (Fujita et al., 2008; Urban et al., 2017).

Spatially resolved X-ray studies of cluster cores revealed a pronounced increase in metallicity toward the centres of non-cool-core systems, where the metal abundance rises monotonically and reaches Solar or even super-Solar values (Fukazawa et al., 1994; De Grandi and Molendi, 2001). Nonetheless, X-ray observations at the turn of the millennium using detectors with high spatial resolution (*Chandra* and *XMM-Newton*) revealed that, for nearby systems such as Abell 2199 (Johnstone et al., 2002), Centaurus cluster (Sanders and Fabian, 2002), and Perseus cluster (Schmidt et al., 2002; Churazov et al., 2003), the measured metallicity profiles drop back to sub-Solar values when the innermost tens of kpc are resolved. This central abundance dip is not present in all systems, but has been later observed in a wide variety of them, including giant elliptical galaxies (NGC 4636, Mernier et al., 2017), galaxy groups (NGC 5044 and NGC 5813, Mernier et al., 2017; HCG62, Rafferty et al., 2013), as well as other galaxy clusters (Abell 262 and Abell 1991, Panagoulia et al., 2015; Ophiuchus cluster, Million et al., 2010). Mernier et al. (2017) have observed the abundance to drop in the centre for about 30 per cent of the studied sample of 44 nearby cool-core galaxy clusters, groups, and ellipticals, while Liu et al. (2019) have detected a central Fe abundance dip for 10 out of 12 studied galaxy groups and clusters.

Several physical mechanisms have been proposed to explain the distribution of metals in the ICM and also their deficiency in cluster cores. Heavy elements are believed to be introduced into the intracluster medium through various channels: galactic winds from star-forming galaxies and supernovae, ram pressure stripping of satellite galaxies as they move through the ICM (Schindler et al., 2005; Cui et al., 2010), and AGN-driven outflows that can expel metal-enriched gas from the central galaxy (Sanders et al., 2005; Simionescu et al., 2008, 2009). Once metals are present in the ICM, different processes may contribute to their redistribution and to the observed central abundance depressions. AGN feedback can redistribute metals within cluster cores through powerful jets and outflows, and deposit them at larger distances from the cluster core, potentially creating regions of higher metallicity with respect to the centre and thus producing an observed central metallicity drop (Panagoulia et al., 2015; Liu et al., 2019).

Gravitational sedimentation and diffusion may physically separate heavy elements from lighter ones over cosmic timescales, though these processes operate relatively slowly in dynamically active environments. Observations of central abundance peaks in cool-core clusters showed the necessity for long enrichment times of ≥ 5 Gyr to build up and maintain steep metal gradients, implying that neither major mergers nor strong convective disruption by AGN bubbles have been frequent enough to fully mix these metals (Böhringer et al., 2004). Additionally, helium sedimentation and thermal diffusion can also be responsible for apparent abundance drops – enhanced helium abundance in cluster cores leads to overestimated continuum emission and artificially suppressed metal content estimates (Ettori and Fabian,

2006). Increasing the assumed central helium abundance by 50% can eliminate the observed iron drop in some systems (Mernier et al., 2017). However, recent models suggest that helium-related processes may be less important and that AGN feedback is dominant in shaping abundance profiles, particularly in galaxy groups where most iron drops occur (Panagoulia et al., 2015; Mernier et al., 2017).

Another physically motivated explanation is dust depletion, whereby a fraction of heavy elements condense into dust grains and are removed from the X-ray-emitting phase. In this scenario, reactive elements such as Fe, Si, S, Mg, and Ca are preferentially depleted, while noble elements remain in the gas phase, potentially producing element-dependent central abundance drops. Dust-bearing cold filaments and clouds are commonly observed in cool-core cluster centres, often co-spatial with Hα emission and infrared dust lanes, suggesting that metals released by the central galaxy can be temporarily hidden from X-ray view before being redistributed by AGN activity (Panagoulia et al., 2015; Sanders et al., 2016). Furthermore, the presence of cold, dusty gas in cluster cores can lead to intrinsic soft X-ray absorption, suppressing metal line emission and biasing abundance measurements if not properly accounted for. Such absorption has been inferred in several cool-core systems (Fabian et al., 2022, 2024).

Observational and systematic effects also play a significant role in the apparent abundance drops. Projection effects, arising from the superposition of gas with different thermodynamic properties along the line of sight, can bias both the inferred temperatures and metallicities (Sanders and Fabian, 2007). Employing techniques that account for projection effects either using direct spectral deprojection or via spectral modelling, such as `dsdeproj` (Sanders and Fabian, 2007) or `projct` (Xspec; Arnaud, 1996) respectively, are therefore crucial for spatially resolved abundance studies and especially important for systems with pronounced temperature gradients such as cool-core clusters. In addition, spectral fitting can be affected by the so-called 'Fe bias', a systematic underestimation of the iron abundance that occurs when an intrinsically multi-temperature plasma emission is modelled with an overly simplified single-temperature model (Buote, 2000; Werner et al., 2008). It has been demonstrated that this effect can lower the Fe abundance estimates on average by a factor of 1.5–2 (Buote, 2000; Su and Irwin, 2013).

Additionally, the effect of resonance scattering can suppress the observed flux of the strongest (optically thick) resonance lines in dense cluster cores by scattering line photons out of the line of sight; if not accounted for in spectral modelling, this effect can lower the inferred metal abundances (Gilfanov et al., 1987). The magnitude of the effect depends on the line optical depth and on the velocity broadening (turbulence), and it has been widely explored both as a diagnostic of gas motions and as a potential systematic in core metallicity measurements (Churazov et al., 2004; Werner et al., 2009; Ogorzalek et al., 2017). Recently, Štofanová et al. (2025) introduced and applied the SPEX `clus` model (Kaastra et al., 2024), demonstrating that a combination of multi-temperature plasma structure and resonance scattering can, in some cases, reproduce an apparent central Fe abundance drop in less massive and cooler systems (for example, the giant elliptical galaxy NGC 4636). They also concluded that these effects alone are generally insufficient to explain the abundance drops reported in more massive clusters, and that projection can additionally bias the best-fit temperature profiles in such objects.

4.1.1 Centaurus cluster

The Centaurus cluster (Abell 3526 or NGC 4696) represents an extreme case of metal enrichment and abundance morphology across known galaxy clusters. Previous X-ray studies revealed a steeply peaked metallicity profile, with Fe abundances rising to highly super-Solar values of $Z \sim 2\,Z_\odot$ at radii of ~ 15 kpc, followed by a pronounced drop to sub-Solar levels ($\sim 0.5\,Z_\odot$) within the central $\lesssim 5$ kpc (Sanders and Fabian, 2002). The amplitude of this drop is significantly larger than observed in most other cool-core systems, largely because the metallicity at intermediate radii is exceptionally high. Subsequent studies confirmed that this central decrease is not limited to iron but is also present in other elements such as Si, S, Ca, and Mg, while noble elements like Ar show a much weaker central decline (Lakhchaura et al.,

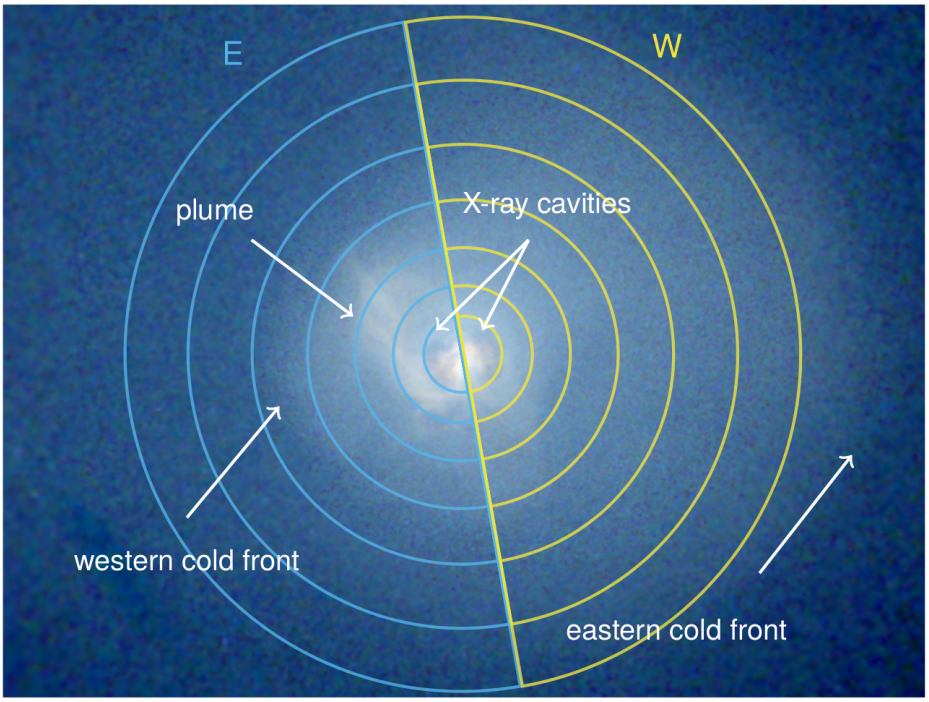

Figure 4.1: False-colour *Chandra* image of the Centaurus cluster with marked position of the western and eastern cold fronts, the plume, and the central X-ray cavities. Visualised are also the eastern (E) and western (W) semicircles corresponding to the innermost 7 of the radial bins used for side-resolved spectral extraction.

2019a). This element-dependent behaviour has been interpreted as evidence for metal depletion onto dust grains in the densest central regions.

It has also been demonstrated that part of the apparent central abundance drop in Centaurus arises from spectral modelling biases. In particular, Sanders et al. (2016) and Lakhchaura et al. (2019a) showed that the presence of multi-phase gas in the core leads to a significant Fe bias when fitting with single-temperature models. When two-temperature or more complex multi-temperature models are adopted, the inferred central Fe abundance increases substantially, reaching values of about 1 Solar within the inner ~ 5 kpc. While a residual drop may still be present, its magnitude is considerably reduced compared to single-temperature deprojected profiles, highlighting the importance of properly accounting for thermal structure in the cluster core.

Recent observations with the XRISM Resolve instrument have provided an independent and high-resolution view of the metal content in the core of the Centaurus cluster. Using Resolve spectra in the 1.7–10 keV band and modelling the central region with a two-temperature plasma, Xrism Collaboration (2025) measured a super-Solar Fe abundance of ($Z_{\rm Fe} \approx 1.6\,Z_{\odot}$), significantly higher than previous estimates based on broadband *Chandra* or *XMM-Newton* analyses. A complementary reanalysis of *Chandra* data in the same work demonstrated that the low central Fe abundance ($\sim 0.5\,Z_{\odot}$) is recovered only when fitting the full $0.5-7$ keV band with single-temperature model, whereas restricting the fit to the hard band ($1.7-7$ keV) yields a much higher central abundance, consistent with the XRISM results.

Beyond iron, XRISM has enabled precise measurements of abundance ratios for a wide range of elements in the Centaurus core. Using Resolve data, Mernier et al. (2025) measured Si/Fe, S/Fe, Ar/Fe, Ca/Fe, Ni/Fe and other ratios, finding that the majority are consistent with Solar values within uncertainties. Similar conclusions are reached by Fukushima et al. (in prep.), who report that the spatial distributions of Si, S, Ar, Ca, Fe, and Ni broadly track each other and show no strong differential trends in

the hot ICM. These results indicate that, at least for the volume-filling hot phase, the chemical composition of the Centaurus core is close to Solar, with no strong evidence for element-selective depletion in the gas phase itself.

The Centaurus cluster also hosts multiple generations of AGN-driven X-ray cavities, indicative of repeated feedback episodes. Sanders et al. (2016) identified up to three distinct generations of cavities in deep *Chandra* data within the central 10 kpc, a picture that has been reinforced by recent XRISM analyses (Xrism Collaboration, 2025) who used an image segmentation tool CADET (Plšek et al., 2024) to detect the cavities in broad-band *Chandra* images. Despite this prolonged AGN activity, XRISM measurements reveal only modest levels of turbulence in the core, with velocity dispersions of order $\sim 100-120$ km s^{-1}. Such low turbulence implies that resonant scattering effects may not be substantially suppressed. Indeed, modelling by Kondo et al. in prep shows that for turbulence levels of ~ 100 km s^{-1}, the optical depth of the Fe XXV Heα line reaches $\tau \sim 0.7$ within ~ 10 kpc, leading to a suppression of the line flux by $\sim 20\%$. Resonant scattering may therefore contribute, alongside multi-temperature structure and dust depletion, to the apparent central abundance drops inferred from CCD-resolution spectra.

This paper is organised as follows. In Section 4.2, we explain the data reduction and spectral extraction process for both *Chandra* and *XMM-Newton* data. Section 4.3 describes the spectral modelling with emphasis on the deprojection approach. In Section 4.4, we show the obtained temperature and Iron metallicity radial profiles. In the Discussion section, we compare the central abundances from individual methods and detectors as well as discuss the effects of fitting biases on the measured central metallicity.

4.2 Data processing

4.2.1 *Chandra X-ray Observatory*

For this study of abundance morphology in the Centaurus cluster's ICM, we have revisited 13 archival non-grating *Chandra* observations with the ACIS-S3 chip aimed at the central galaxy NGC 4696, with a total cleaned exposure time of 709.1 ks. All *Chandra* observations were processed using the latest CIAO 4.18 pipeline (Fruscione et al., 2006) and current calibration files (CalDB 4.12.3). The point sources were detected using the `wavdetect` script and omitted from further analysis. The background light curves were extracted in the 0.5–7.0 keV band and used to deflare the observations using the `deflare` routine. Blank-sky background event files were obtained using the `blanksky` script.

For the spatially resolved deprojected spectral analysis, we produced spectra from 13 concentric annuli centred at the X-ray surface brightness peak, with the outermost annulus of 500 arcsec (≈ 91.5 kpc). To match the extent of the ACIS-S chip, spectra for annuli 10,11,12, and 13 were extracted from circular sectors with widths of 120°, 90°, 70°, and 60° on each side[1] and varying rotational angle to match the roll angle of each observation. All spectra were extracted using the `specextract` command and binned using `ftgrouppha` (Kaastra and Bleeker, 2016) to at least one count per bin to allow the use of `cstat` statistics (Cash, 1979). Background spectra were extracted from blanksky background files and, during spectral modelling, treated using the `wstat` statistics (modified `cstat`).

To also compare the abundance profiles in various directions, the spectra were further extracted from semicircles in the eastern ($100^\circ - 280^\circ$) and western ($280^\circ - 100^\circ$) directions (see Figure 4.1), corresponding to the eastern and western cold fronts. Furthermore, as can be seen on the false-colour *Chandra* image (Figure 4.1), the contribution of the cold-phase gas is presumably higher in the eastern direction due to the presence of a red-ish plume substructure, which was further motivation for also splitting the spectra-extraction annuli into two semi-circles.

[1] Corresponding angular sizes for these partial annuli were written into spectral headers as *angleNl* and *angleNu* keywords for `projct` and *XFLT0004* and *XFLT0005* keywords for the `dsdeproj` deprojection tools.

4.2.2 *XMM-Newton*

To assess the reliability of the radial trends derived from the *Chandra* data, we also analysed *XMM-Newton* observations of the Centaurus cluster. We restricted the analysis to ObsID 0406200101 (124 ks), which provides the longest exposure with NGC 4696 at the aim point. Spectra were extracted from the EPIC MOS1, MOS2, and pn detectors in the same annuli as adopted for the *Chandra* analysis, enabling a direct comparison between the two data sets.

The EPIC event files were processed following the standard SAS reduction procedure, including the filtering of intervals affected by soft-proton flares. For the spectral analysis, single to quadruple events were retained for MOS and single-pixel events for pn, and response files were generated for each detector and extraction region. Background spectra were extracted from blank-sky files using detector regions identical to the source annuli. The resulting spectra were used to derive deprojected radial profiles and to verify the consistency of the results obtained from the *Chandra* data.

4.3 Spectral modelling

The spectra from each annulus were fitted with the single-temperature `vapec` model or two-temperature `vapec` model. To account for projection effects, especially strong in Centaurus cluster due to the temperature gradient, we have performed a deprojection by fitting spectra from individual annulli simultaneously using the `projct` mixing model component. For comparison, we have also performed a direct spectral deprojection using the `dsdeproj` tool (Sanders and Fabian, 2007; Russell et al., 2008). In addition to the thermal emission, we have included a `powerlaw` model component with a photon index of 1.9 (Gilli et al., 2007) to describe the emission of the central AGN in the innermost annulus, and with a photon index of $\Gamma = 1.56$ (Irwin et al., 2003) in outer annuli to account for unresolved point sources from the host galaxy (LMXBs, CVs, CABs). We note, however, that the powerlaw component was only significant for five innermost annuli up to the radius of ≈ 20 kpc and excluding this component completely only had a minor effect on the obtained abundance profiles. The Galactic absorption was modelled using the `phabs` component assuming the *bcmc* cross-section (Balucinska-Church and McCammon, 1992).

In the case of a two-temperature model, the model expression for each annulus was defined as follows:

$$\texttt{projct(phabs(vapec}_{\texttt{hot}}\texttt{))+phabs(vapec}_{\texttt{cold}}\texttt{ + powerlaw)}$$

We note that only one of the thermal components ($\texttt{vapec}_{\texttt{hot}}$) was multiplied by the `projct` model component, assuming that only the hot component is volume-filling and should thus be deprojected. The cold thermal component ($\texttt{vapec}_{\texttt{cold}}$) was included to correspond to the cold plasma of the plume-like feature (Figure 4.1), which has a complicated non-symmetric structure, is only dominant in the centre of the system, and the temperature of which is assumed to be rather constant (≈ 0.8 keV).

The temperatures and Fe abundances of individual annuli were allowed to vary. However, in order to constrain these parameters with a relative uncertainty smaller than 25 per cent, for some of the neighbouring annuli, we tied together the temperatures and abundances for two or more neighbouring annuli (e.g. in annuli 1 and 2, the temperatures were allowed to vary, but abundances in both annuli were tied together). Emission lines of the following elements Ne, Mg, Si, S, Ar, and Ca were identified and were untied from that of Fe, but remained tied across neighbouring annuli in the same manner as Fe.

Spectral fitting of *Chandra* data was performed in the energy range of 0.7–7.0 keV. For comparison with XRISM estimates, we have also performed single-temperature fits only in the hard X-ray band matching the lower energy limit of XRISM Resolve detector ($1.7 - 7.0$ keV). For *XMM-Newton* data, we have used the energy range of 0.5–7.0 keV for EPIC MOS spectra and 0.7–7.0 keV for MOS pn spectra, respectively.

During the fitting, the redshift was fixed to $z = 0.0104$, and the galactic hydrogen column of both `phabs` components was fixed to the value of $N_H = 1.22 \times 10^{21}$ cm^{-2} (Willingale et al., 2013). The spectral modelling was performed using *PyXspec* 2.1.4 package (*Xspec* 12.14.1; Arnaud, 1996). We assumed the standard flat ΛCDM cosmology, with $H_0 = 70$ km s^{-1} Mpc^{-1}, $q_0 = 0$, $\Omega_{\Lambda,0} = 0.73$. All the abundances are expressed with respect to proto-Solar values reported by Lodders et al. (2009). The uncertainties are expressed in the 1σ credible interval and were estimated from posterior distributions obtained from MCMC simulations using the Goodman-Weare algorithm (Goodman and Weare, 2010) with 28 walkers and a length of $\sim 10^4$ steps. In order to compare the spectral fits obtained with the latest atomic database (AtomDB 3.1.3) to previous versions and also another spectral fitting package (SPEX, Kaastra et al., 2022), we have performed the spectral fitting also using AtomDB v3.0.9 and SPEXACT atomic database v3.08.01 (Kaastra et al., 2024).

4.4 Results

We first compare the deprojected *Chandra* profiles obtained with three different spectral descriptions of the core: a single-temperature fit and a two-temperature fit in the 0.7–7.0 keV energy band, and a single-temperature fit in the hard 1.7–7.0 keV band, matching the lower energy limit of XRISM/Resolve. The resulting temperature and Fe abundance profiles are shown in Figure 4.2, together with the projected XRISM Resolve measurements (Xrism Collaboration, 2025).

The upper panel of Figure 4.2 shows that all three approaches recover the same overall temperature structure. The temperature rises from about 1 keV in the central few kpc to nearly 4 keV in the outermost annulus. The main differences are limited to the central region. The broad-band and hard-band single-temperature fits provide very similar temperature profiles, while the two-temperature model resolves a separate cool phase (≈ 0.8 keV) in the innermost two radial bins, in addition to the hotter volume-filling component (≈ 1.4–1.6 keV).

The Fe profiles in the lower panel show the same general radial trend for all three models: the abundance rises inward from sub-Solar values at large radii, reaches a strong maximum of about $3\,Z_\odot$ at $r \approx 10$–20 kpc, and then decreases again toward the centre, with the hard-band fit having the Fe peak slightly shifted closer to the centre. The largest difference, however, is in the depth of the central drop. The broad-band single-temperature fit gives the strongest drop, with the innermost Fe abundance falling to about $0.6\,Z_\odot$. While the hard-band single-temperature fit gives higher central values, around $2.2\,Z_\odot$, the two-temperature fit raises the central abundance to about $1.7\,Z_\odot$, which is in much better agreement with XRISM (Xrism Collaboration, 2025).

4.4.1 Comparison to *XMM-Newton*

To test whether the Fe profile derived from the *Chandra* ACIS-S data could be affected by instrument-specific systematics, we repeated the same two-temperature deprojected analysis using *XMM-Newton* EPIC data. The fitting setup was kept as similar as possible to the *Chandra* case, including the energy band and the tying of temperatures and abundances across neighbouring annuli. We used all three EPIC detectors, MOS1, MOS2, and pn. Since the MOS1 and MOS2 profiles were consistent within uncertainties, they were combined into a single MOS profile shown in Figure 4.3.

The *XMM-Newton* data recover the same main Fe abundance pattern as the *Chandra* ACIS-S data. In all instruments, the Fe abundance is already elevated in the central bins, rises to a clear maximum of about $3\,Z_\odot$ in the fifth annulus (~ 14–19 kpc), and then declines again toward larger radii. The central Fe abundances are also broadly comparable within uncertainties, although the EPIC pn values are slightly lower than those from *Chandra* ACIS-S and EPIC MOS. At intermediate radii, the EPIC MOS profile remains somewhat higher and broader, while pn is generally lower than MOS. Despite these small offsets,

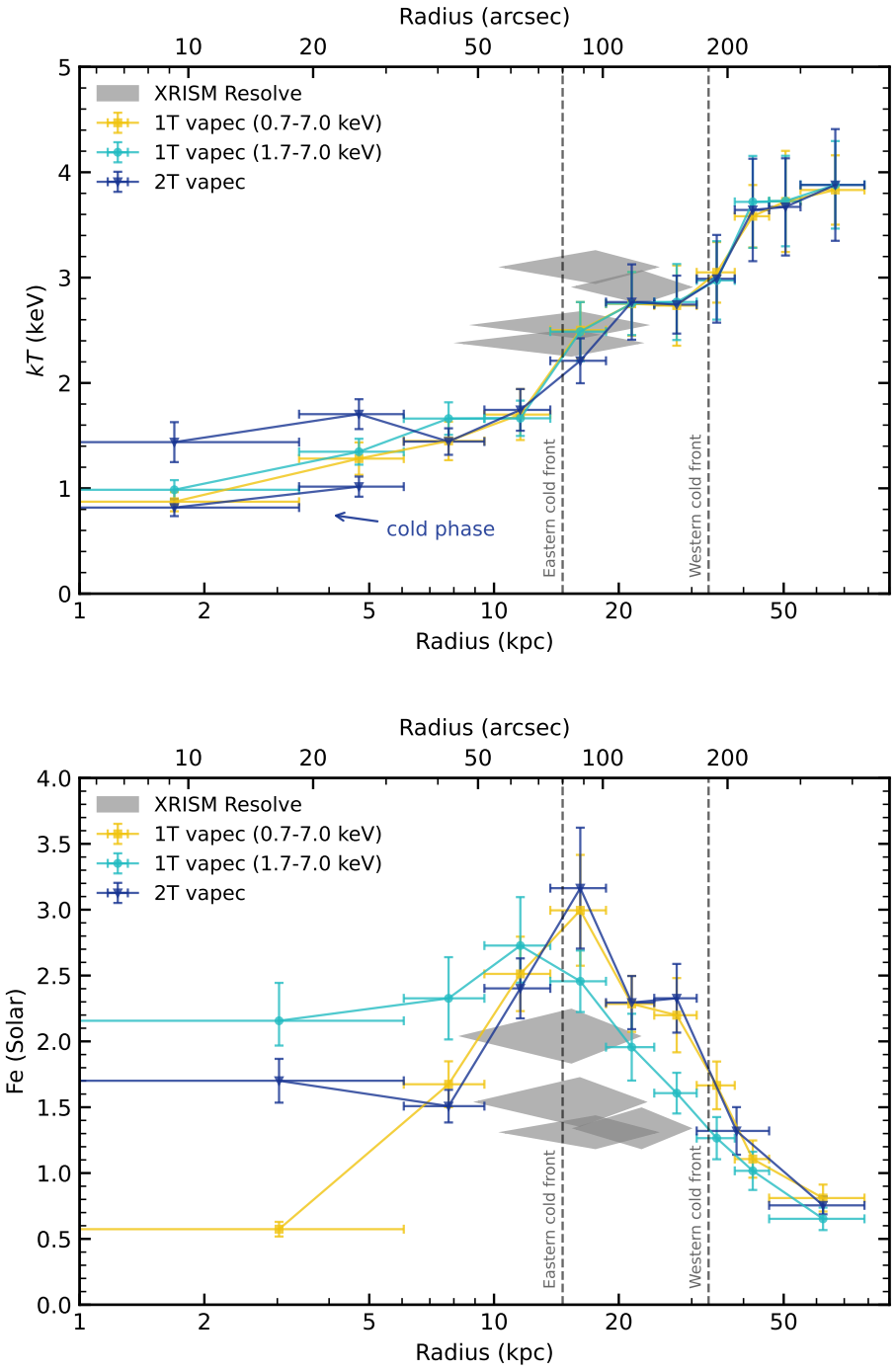

Figure 4.2: Temperature (*upper*) and iron (Fe) abundance (*lower*) deprojected radial profiles obtained from *Chandra* data using a single-temperature `vapec` model fitted in the broad 0.7–7.0 keV band, a single-temperature model fitted in the hard 1.7–7.0 keV band, and a two-temperature `vapec` model fitted in the broad band. Grey shaded regions show the projected XRISM Resolve measurements (Xrism Collaboration, 2025). Vertical dashed lines mark the positions of the eastern and western cold fronts. In the two-temperature fit, the low-temperature points in the innermost bins correspond to the cold phase.

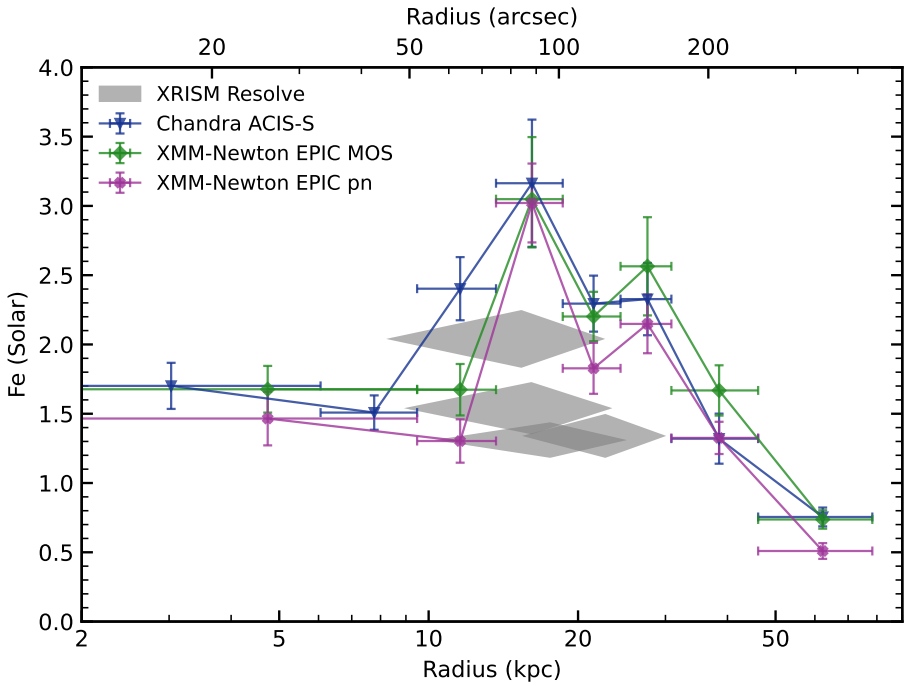

Figure 4.3: Comparison of deprojected Fe abundance profiles obtained with the two-temperature model from *Chandra* ACIS-S and *XMM-Newton* EPIC MOS and pn data. Grey shaded regions show the projected XRISM Resolve measurements (Xrism Collaboration, 2025).

the overall agreement is good and supports the view that the strong Fe peak at 14–19 kpc is not specific to the *Chandra* data.

We also compared the radial profiles of the other fitted elements, namely Mg, Si, S, Ar, and Ca, shown in Figure A.4.3. The Si and S profiles are broadly consistent between *Chandra* and *XMM-Newton*, while Ar and Ca have large uncertainties but remain compatible within those errors. The clearest differences are seen for Mg, where the *XMM-Newton* profiles do not show such a pronounced peak at 14–19 kpc as the *Chandra* data.

The central spectra from the individual instruments, shown in Figure A.4.1, indicate that the temperatures of the hot and cold components and their relative normalisations are comparable across *Chandra*, EPIC MOS, and EPIC pn. The main difference is that the powerlaw component in the EPIC pn fit is weaker than in *Chandra* and MOS. However, removing the powerlaw component has little effect on the derived central Fe abundance and, when it does affect the fit, it increases the central Fe value. We therefore suggest that the lower pn abundances are unlikely to be caused mainly by the treatment of the hard continuum.

4.4.2 Eastern vs Western front

Because the core of the Centaurus cluster is clearly asymmetric, we also extracted spectra separately from the eastern and western semicircles shown in Figure 4.1. Both sides were fitted with the same two-temperature model. The resulting Fe abundance profiles are shown in Figure 4.4.

Both sides exhibit behaviour similar to the azimuthally averaged profile. In both directions, the Fe abundance rises from lower values at large radii to a pronounced peak at $r \approx 14$–19 kpc, and then decreases again toward the centre. The peak value is very similar on both sides, reaching about 2.8–2.9 $Z_{\odot}$, while the azimuthally averaged profile is slightly higher in the same radial bin.

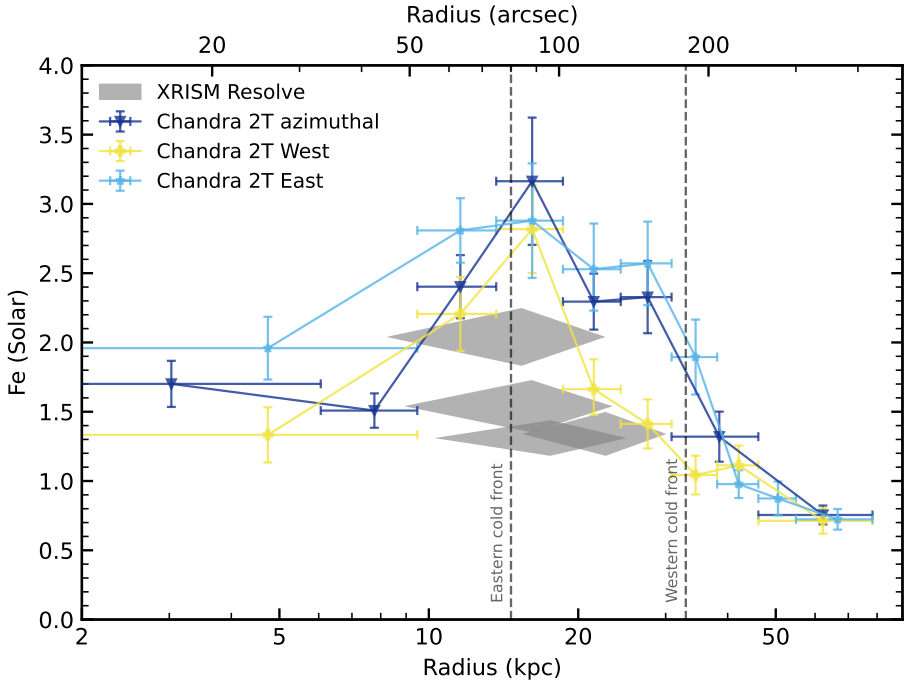

Figure 4.4: Comparison of deprojected Fe abundance profiles obtained from azimuthally averaged *Chandra* data and from the eastern and western semicircles, all fitted with the two-temperature model. Grey shaded regions show the projected XRISM Resolve measurements (Xrism Collaboration, 2025).

The main difference is in the shape of the profile around the peak. On the eastern side, the high-abundance region is broader and remains elevated out to nearly 30 kpc, with Fe still around 2.5–2.6 $Z_\odot$ in the bins just outside the peak. On the western side, the profile declines more rapidly outside the peak and falls to about 1.7 $Z_\odot$ by ~ 20 kpc. In the centre, the eastern profile is also somewhat higher than the western one, although the uncertainties nearly overlap. The azimuthally averaged profile lies between the two sector profiles at nearly all radii.

The two sides also differ in the need for the cool component. On the eastern side, where the plume-like soft structure is present, the cool thermal component can be constrained in the inner two annuli. On the western side, it can only be constrained in the innermost annulus.

4.5 Discussion

Using a deprojected two-temperature model with updated atomic data (AtomDB 3.1.3), we find central Fe abundances that are broadly consistent, within uncertainties, with the projected XRISM Resolve measurements. Compared with earlier CCD studies, this likely reflects a combination of factors rather than a single change: a better description of the multi-phase gas, the updated atomic data, and the use of a `projct`-based deprojection. The somewhat finer radial sampling of the inner region may also help to follow the central temperature structure more closely. In this sense, the present results support the idea that a substantial part of the very deep central dip reported in earlier analyses was related to the difficulty of modelling the complex core with CCD spectra (Sanders et al., 2016; Lakhchaura et al., 2019a; Xrism Collaboration, 2025).

At the same time, the abundance drop is not removed completely. In the azimuthally averaged two-temperature profile, the Fe abundance still decreases from the strong peak at $r \approx 14$–19 kpc toward the innermost few kpc. The same general behaviour is also seen in the eastern and western sector profiles,

although the detailed radial shape differs between the two sides. After reducing the Fe bias, a smaller residual central drop therefore remains.

The present results shift the emphasis from whether the whole drop can be produced by overly simple spectral modelling to how much of the remaining decrease in Fe abundance between the off-centre peak and the cluster centre is physical and how much is due to residual modelling uncertainties. In this respect, our results are broadly consistent with earlier work showing that multi-temperature modelling weakens the drop substantially, even if it does not remove it completely (Sanders et al., 2016; Lakhchaura et al., 2019a).

4.5.1 Possible origin of the central Fe drop

The location of the Fe peak is particularly suggestive because it lies inside the region where several generations of X-ray cavities have been reported, consistent with AGN-driven uplift playing an important role in shaping the metal distribution in the inner core (Sanders et al., 2016; Xrism Collaboration, 2025). In such a picture, part of the enriched gas released by the central galaxy may have been displaced from the nucleus to radii of order 10–20 kpc, producing the observed off-centre maximum.

The east–west differences further suggest that this redistribution is not spherically symmetric. On the western side, the Fe abundance begins to rise somewhat farther out, whereas on the eastern side, the metal-rich region remains broader inside ~ 30 kpc and is accompanied by a stronger cool component. This pattern is consistent with gas sloshing helping to redistribute centrally enriched gas outward, which may contribute to the eastern profile remaining at higher Fe abundance out to larger radii. In this view, the observed behaviour also fits the known asymmetry of the Centaurus core, where the plume, the cold fronts, and repeated AGN activity all affect the thermodynamic structure (Sanders et al., 2016).

Dust depletion may also contribute to this intrinsic central decrease. The core of NGC 4696 contains dusty optical filaments, and previous element-by-element studies of Centaurus have shown that reactive elements such as Fe, Si, and S exhibit stronger central drops than noble elements (Panagoulia et al., 2015; Lakhchaura et al., 2019a). In that case, a fraction of the metals would be temporarily removed from the X-ray-emitting phase and incorporated into cold dust-bearing gas. The present analysis does not test this directly, but the persistence of a residual drop after introducing a second thermal component is consistent with such a contribution.

4.5.2 Residual fitting biases

The remaining central abundance estimates still depend noticeably on the adopted analysis choices and on the data set. This is illustrated in Figure 4.5, which compares Fe profiles obtained using different deprojection approaches, plasma codes, and atomic databases, together with the *XMM-Newton* MOS result (for the corner plot showing confidence level of all parameters of the innermost bin, see Figure A.4.2). All profiles exhibit the same broad behaviour: a pronounced Fe peak at 14–19 kpc and a central drop to about half that value. However, the absolute Fe abundance in the innermost bins varies significantly, especially between `projct` and `dsdeproj`, and to a lesser extent between AtomDB and SPEXACT (see Figure 4.5).

One possible residual bias is resonance scattering. The turbulence measured by XRISM in the Centaurus core is relatively low, so resonance scattering in the strongest Fe lines is not expected to be fully suppressed by velocity broadening. If these lines are scattered out of the line of sight and this effect is not included in the spectral model, the central Fe abundance can be biased low (Xrism Collaboration, 2025). Resonance scattering could therefore deepen the apparent central drop and, at the same time, enhance the contrast of the off-centre Fe peak.

However, resonance scattering is unlikely to account for the entire profile on its own. Earlier work on Centaurus showed that the abundance drop persists even after accounting for projection effects and

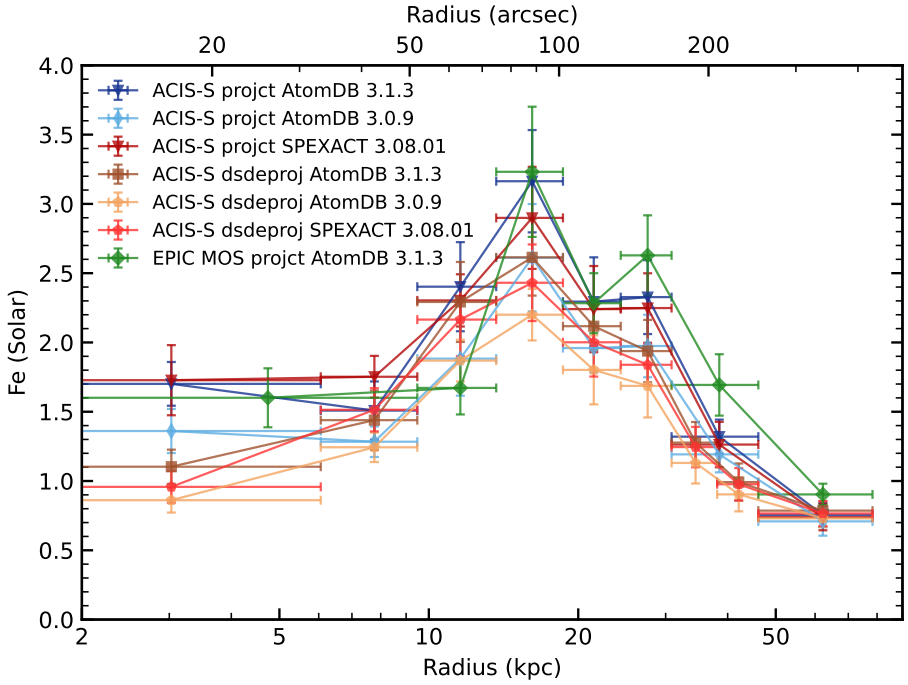

Figure 4.5: Comparison of deprojected Fe abundance profiles illustrating the sensitivity of the innermost metallicity measurements to the adopted analysis method and plasma code. Shown are *Chandra* ACIS-S two-temperature profiles obtained with `projct` and `dsdeproj` using AtomDB v3.1.3, AtomDB v3.0.9, and SPEXACT v3.08.01, together with the *XMM-Newton* EPIC MOS `projct` profile based on AtomDB v3.1.3. While all profiles recover the same strong off-centre Fe peak at ∼ 14–19 kpc, the absolute Fe abundance in the innermost bins varies significantly.

radiative transfer (Sanders and Fabian, 2006). More recent modelling also suggests that, although resonance scattering combined with multi-temperature structure can in some cases reproduce an apparent abundance drop, this mechanism alone is generally insufficient in more massive clusters (Štofanová et al., 2025). It is therefore more likely to act as a secondary effect superimposed on a genuine radial abundance variation.

Additional uncertainty is introduced by the deprojection itself. The inner ∼ 10–20 kpc of Centaurus are strongly asymmetric, and the cool plume is not a volume-filling, spherically distributed component. In a `projct`-based fit, where all annuli are linked simultaneously, small mismatches in the assumed geometry or in the projected emission from outer shells can propagate inward and accumulate in the central bins. The sector-resolved profiles suggest the same: although the eastern and western two-temperature profiles show the same overall behaviour, their innermost Fe abundances are not identical, even if their uncertainties partly overlap. Part of this difference may be physical, but it also suggests that residual systematic effects become increasingly important toward the centre. The exact Fe abundance in the innermost bin should therefore be regarded as less secure than the existence and radial position of the strong peak at 14–19 kpc.

By contrast, the treatment of the hard continuum appears to be less important. Varying or removing the central powerlaw component has only a minor effect on the fitted central Fe abundance, and when a difference is seen, it tends to increase the central Fe value rather than decrease it. The residual drop is therefore unlikely to be driven mainly by contamination from the central AGN or unresolved hard point sources.

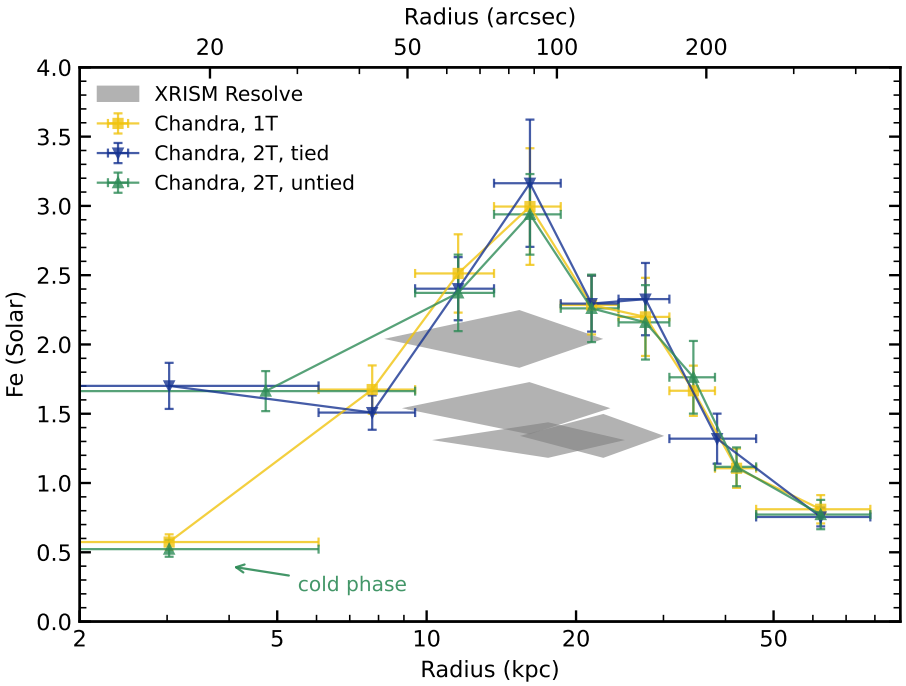

Figure 4.6: Comparison of deprojected Fe abundance profiles obtained from *Chandra* data using a broad-band single-temperature model (shown for reference), a two-temperature model with the Fe abundances tied between the hot and cool components, and a two-temperature model with the Fe abundances allowed to vary independently. In the untied case, the low inner green point marked by the arrow corresponds to the cool component, whereas the remaining green points show the hot phase. Grey shaded regions show the projected XRISM Resolve measurements (Xrism Collaboration, 2025). Vertical dashed lines mark the positions of the eastern and western cold fronts.

4.5.3 The multi-metallicity picture

To examine whether the hot, volume-filling gas and the central cool phase can have different Fe abundances, we repeated the broad-band two-temperature fit, allowing the Fe abundances of the two thermal components to vary independently. The resulting profiles are shown in Figure 4.6. In the untied model, the low inner green point marked by the arrow corresponds to the cool component, whereas the remaining green points show the hot phase.

Outside the central region, the tied and untied two-temperature profiles are nearly identical. Both recover the same strong Fe peak at $r \approx 14$–19 kpc and the same outward decline. The main difference appears in the innermost bins. Once the two components are allowed to have different Fe abundances, the hot phase remains close to the tied two-temperature result, with a central abundance of about 1.6–1.7 $Z_\odot$. By contrast, the cool component has a much lower abundance, $Z_{\mathrm{Fe,cold}} = 0.52 \pm 0.06\, Z_\odot$ within the inner ~ 6 kpc.

This result suggests that the very low central Fe abundance obtained from single-temperature broad-band fits is strongly influenced by the cool X-ray-emitting phase and does not simply reflect the metallicity of the hot, volume-filling gas. The residual central drop is therefore unlikely to be explained solely by mixing gas phases of different temperatures within the same spectral bin, since a smaller decline still appears to remain in the hot component itself.

The low Fe abundance of the cool component should nevertheless be interpreted with caution. This component is constrained only in the innermost bins, it is not deprojected, and it represents an asym-

metric structure associated with the plume rather than a spherical shell. It would therefore be premature to conclude that the coolest X-ray-emitting gas is intrinsically metal-poor. If the low abundance of the cool component is physical, at least two possibilities remain open. The first is that this gas condensed from material with lower metallicity than the gas at the radius of the Fe peak. The second is that part of its metal content has already left the X-ray-emitting phase through further cooling and dust formation. The present data do not allow these scenarios to be distinguished, but they both point to a more complex chemical structure in the central few kpc than can be captured by a single abundance assigned to the entire core.

4.6 Conclusions

We have revisited archival *Chandra* and *XMM-Newton* observations of the Centaurus cluster and compared the resulting deprojected Fe abundance profiles with recent XRISM Resolve measurements. The main conclusions can be summarised as follows.

- Using a deprojected two-temperature model together with updated atomic data and a `projct`-based deprojection, the central Fe abundance increases to values broadly consistent, within uncertainties, with the XRISM Resolve measurements. This suggests that a large part of the classical deep central Fe dip in Centaurus was related to unresolved multi-temperature structure and to the details of the spectral modelling.
- The most robust feature of the metallicity profile is the strong off-centre Fe peak at $r \approx 14$–19 kpc. This peak is recovered in both *Chandra* and *XMM-Newton* data, is present on both the eastern and western sides of the cluster, and appears less sensitive to modelling choices than the absolute Fe abundance in the innermost bin.
- Even after reducing the Fe bias, a residual central Fe drop remains. Allowing the two thermal components to have different Fe abundances suggests that the very low abundance obtained in single-temperature broad-band fits is strongly influenced by the cool X-ray-emitting phase. At the same time, a smaller drop appears to remain in the hot phase itself, so the remaining decline is likely to reflect a combination of true abundance structure and residual modelling effects, with resonance scattering and dust depletion both possible contributors.

Future spatially resolved micro-calorimeter observations, especially those covering the soft X-ray band, will be needed to determine how much of the remaining central decline is due to true abundance structure, how much is caused by resonance scattering and other residual biases, and whether the cool and hot phases in the Centaurus core are genuinely chemically distinct.

Conclusions

In this thesis, I have examined hot X-ray-emitting atmospheres in massive early-type galaxies and galaxy clusters from two connected perspectives: radio-mechanical AGN feedback and chemical enrichment. The four papers combined X-ray spectroscopy, radio and X-ray imaging, and machine-learning methods to address how hot atmospheres feed supermassive black holes, how the impact of jets can be measured, and how feedback, stripping, and multiphase structure shape the observed metal distribution.

AGN feeding and radio-mechanical feedback

Paper I studied the relation between Bondi accretion power and mechanical jet power in nearby, X-ray-bright early-type galaxies. The analysis showed that this relation becomes especially tight in galaxies with thermally unstable atmospheres, as indicated by the presence of cool gas and by low values of $t_{\rm cool}/t_{\rm ff}$. In these systems, the jet-to-Bondi power ratio is approximately constant, suggesting that once thermal instability develops, the cooling atmosphere can feed the central black hole in a relatively regular way. The same work also showed that jet power is strongly linked to black hole mass, indicating that the mass of the central black hole is one of the main parameters setting the scale of radio-mechanical feedback.

These results strengthen the view that AGN feedback in massive early-type galaxies is not a purely stochastic process, but is connected to the thermodynamic state of the surrounding hot gas. They also suggest that thermally unstable atmospheres provide the conditions under which accretion and jet production are most tightly coupled.

Measuring feedback through X-ray cavities

Paper II addressed an important methodological aspect of this problem. Since the mechanical power of AGN jets is commonly inferred from X-ray cavities, the reliability of cavity measurements directly affects the study of feedback. In this paper, the CAvity DEtection Tool (CADET) was developed as a machine-learning pipeline for the detection and size estimation of X-ray cavities in hot atmospheres.

CADET was trained on realistic mock *Chandra* images and then tested on both simulated and real observations. The pipeline recovered the large majority of previously known cavities and also revealed several new cavity systems and candidates. This demonstrated that cavity detection can be made more objective, reproducible, and scalable than in purely manual analyses. In the broader context of this thesis, CADET provides a practical tool for extending cavity-based studies of AGN feedback to larger samples and to lower-quality data, where eye identification becomes difficult.

Chemical enrichment in disturbed hot atmosphere of M89

Paper III investigated the chemical composition of the infalling elliptical galaxy M89, whose hot atmosphere is affected by both AGN activity and ram-pressure stripping in the Virgo cluster. In contrast to the approximately Solar abundance pattern commonly measured in clusters, the hot gas in M89 was

found to have super-Solar abundance ratios with respect to iron, making it chemically closer to the stellar population of the galaxy. This result showed that the chemical composition of hot atmospheres is not necessarily universal, but can depend on the individual history of stripping, gas replacement, and stellar mass loss.

The same paper also identified a fitting bias in low-temperature RGS spectra, where the measured O/Fe ratio changes significantly with the adopted multi-temperature model. This result is important because it shows that conclusions about enrichment channels and supernova contributions can depend sensitively on how the thermal structure of the gas is modelled. In M89, the preferred interpretation was that AGN activity helped ram-pressure stripping remove the original hot atmosphere, which was then replaced by fresh stellar mass-loss material with super-Solar α/Fe abundance ratios.

Metallicity structure in the Centaurus cluster

Paper IV returned to the question of abundance structure in the Centaurus cluster, one of the best known examples of a cool-core system with a central Fe abundance drop. Using deprojected two-temperature models and current atomic data, the analysis showed that the very low central Fe abundance obtained from simpler broad-band CCD fits is largely caused by unresolved multi-temperature structure. Once this effect is reduced, the central Fe abundance rises to values broadly consistent with recent XRISM measurements.

At the same time, the central drop does not disappear completely. The strongest and most robust feature of the Fe profile is a pronounced off-centre peak at roughly 14–19 kpc, which is recovered in both *Chandra* and *XMM-Newton* data and is present on both the eastern and western sides of the core. A weaker residual decline toward the centre remains. The sector-resolved analysis showed that the metal distribution is asymmetric, and the fits allowing different abundances in the hot and cool phases indicated that the very low central abundance from simpler broad-band analyses is driven mainly by the cool component rather than by the hot volume-filling gas. The remaining drop therefore most likely reflects a combination of true abundance structure and residual modelling biases, with resonance scattering and possibly dust depletion being the most plausible additional effects.

Overall perspective

Taken together, the four papers show that hot atmospheres are multiphase and dynamically evolving systems, shaped by cooling, heating, uplift, stripping, and mixing. AGN jets affect not only the thermal state of the gas, but also its spatial distribution and the way its metal content is observed. Likewise, abundance measurements do not reflect nucleosynthesis alone, but also depend on the thermal structure of the plasma and on the assumptions used in spectral modelling.

The thesis therefore contributes in two related ways. On the physical side, it links the fueling of AGN jets to the thermodynamic state of hot atmospheres and shows how AGN activity, stripping, and phase structure influence the chemical composition of hot gas. On the methodological side, it develops and applies tools needed for more reliable measurements, including systematic cavity detection and more careful treatment of spectral fitting biases.

Appendix

This thesis is based on four publications, Annexes 1, 2, 3, and 4. The following pages of the Appendix contain additional material that supports the results presented in these papers and provides additional details for the reader. It includes radial profiles, images of radio lobes, corner plots with parameter distributions, supporting plots, tables of measured quantities, and tables listing the archival observations used in these publications.

A.1 The relation between accretion rate and jet power

A.1.1 Radial profiles

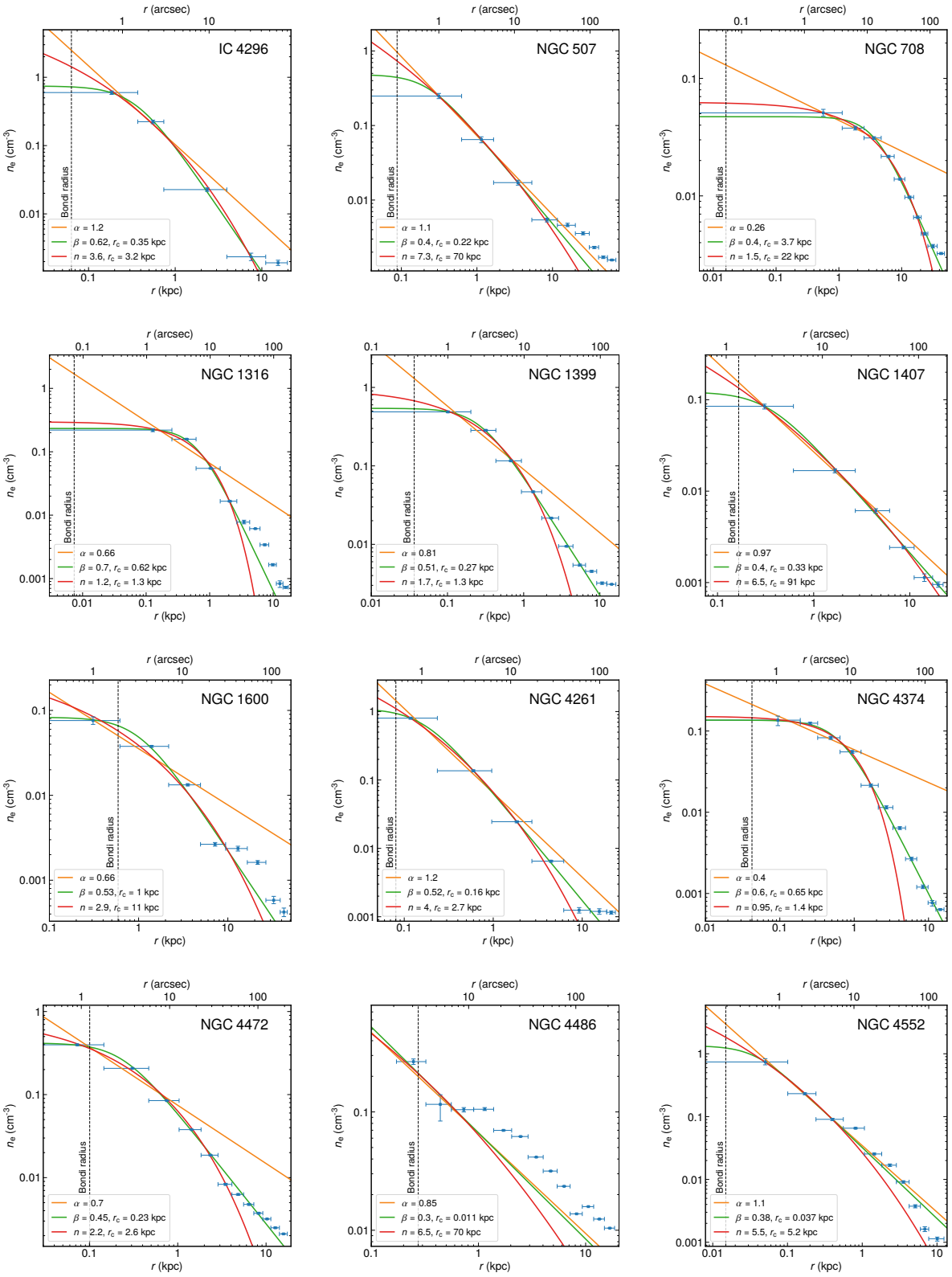

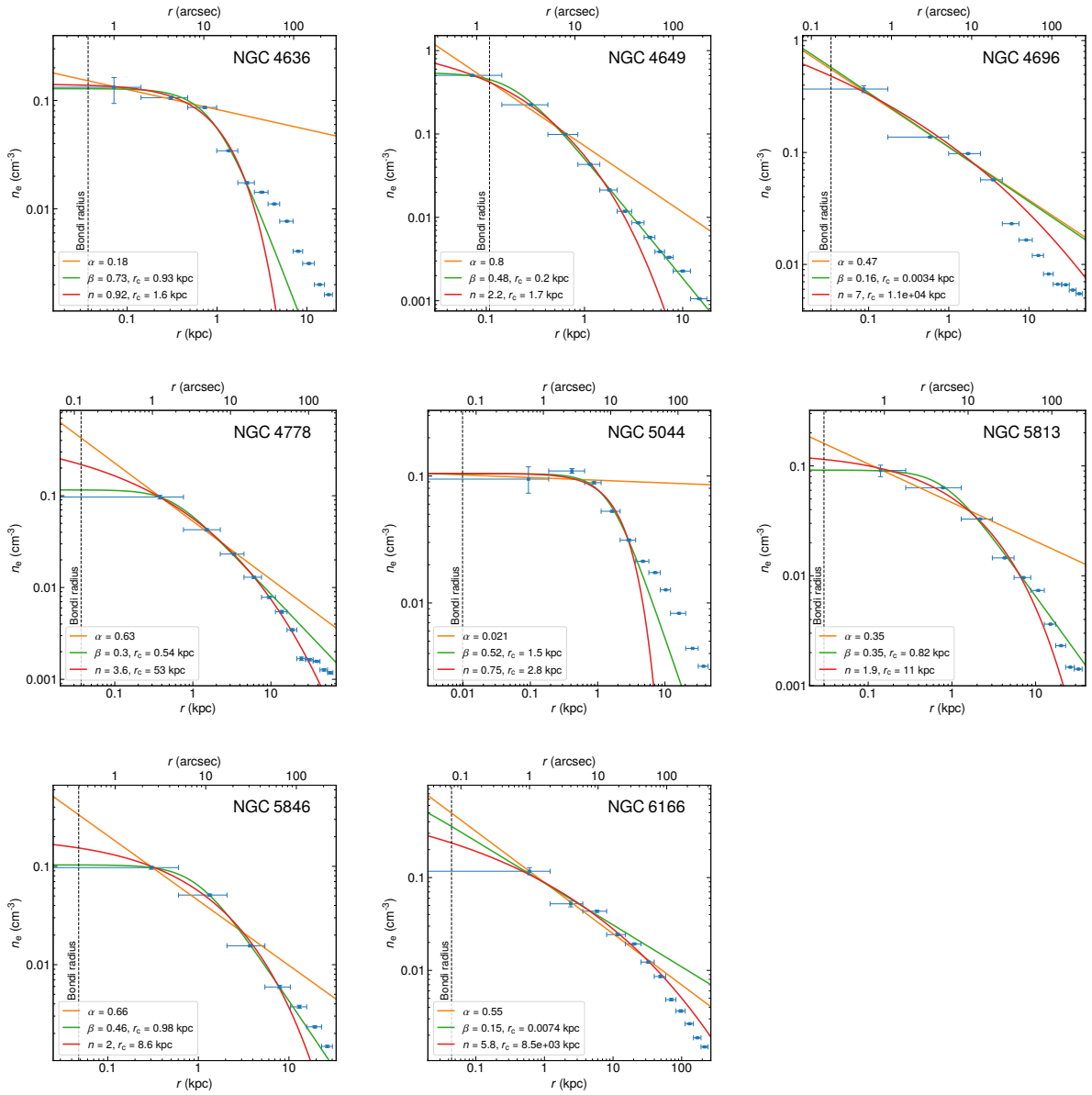

Figure A.1.1: Azimuthally averaged radial profiles of electron number densities n_e. The vertical dashed lines represent the Bondi radius $r_{\rm Bondi}$ to which the electron number densities were extrapolated. For the extrapolation, we used three different profiles: power-law model (*orange*), β-model (*green*) and sersic profile with freed parameter n (*red*). The final value of electron number density at the Bondi radius was calculated as a mean from these three profiles and the scatter was accounted in the uncertainty.

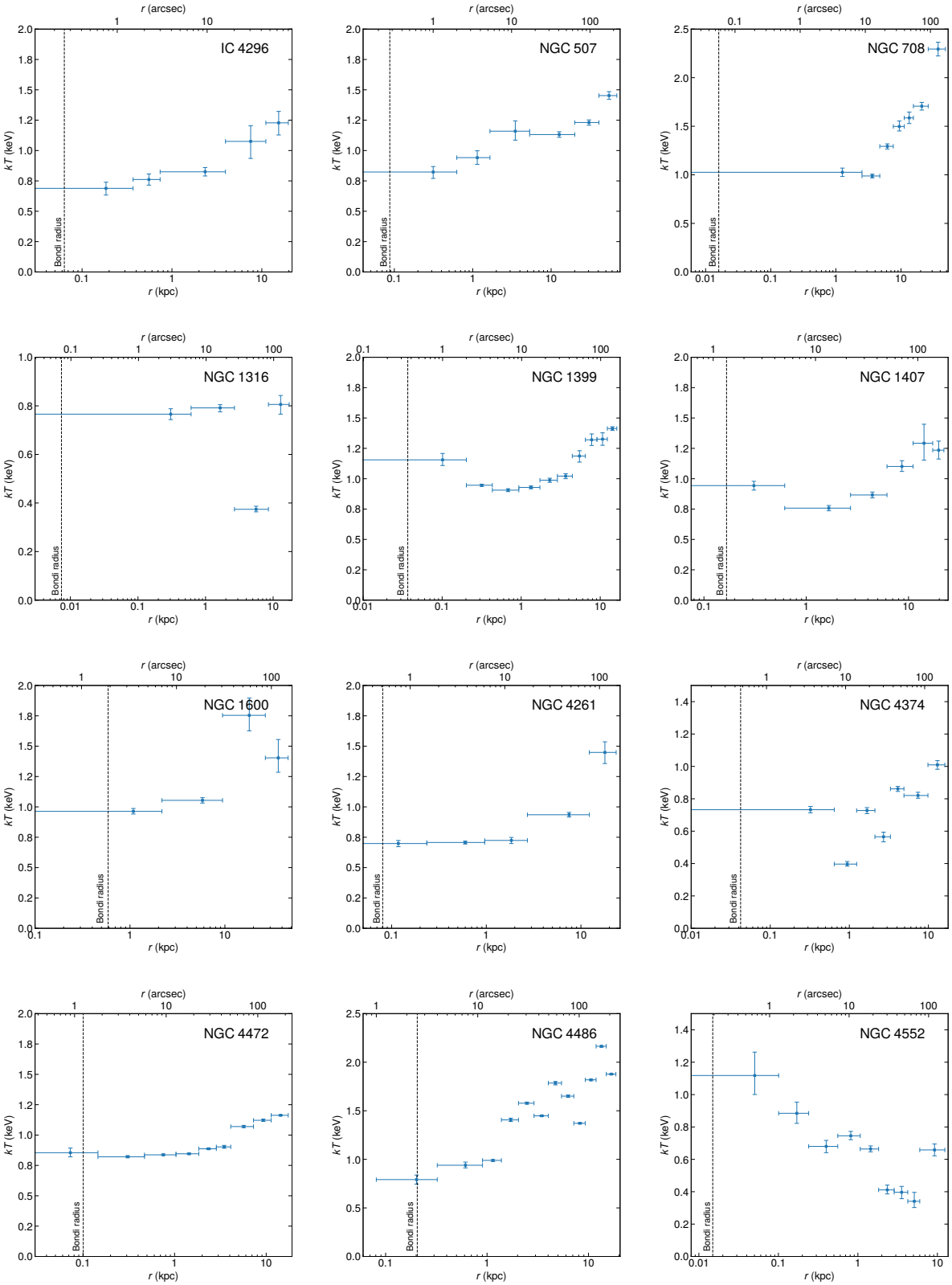
IC 4296
NGC 507
NGC 708
NGC 1316
NGC 1399
NGC 1407
NGC 1600
NGC 4261
NGC 4374
NGC 4472
NGC 4486
NGC 4552
r (arcsec)
r (kpc)
kT (keV)
Bondi radius

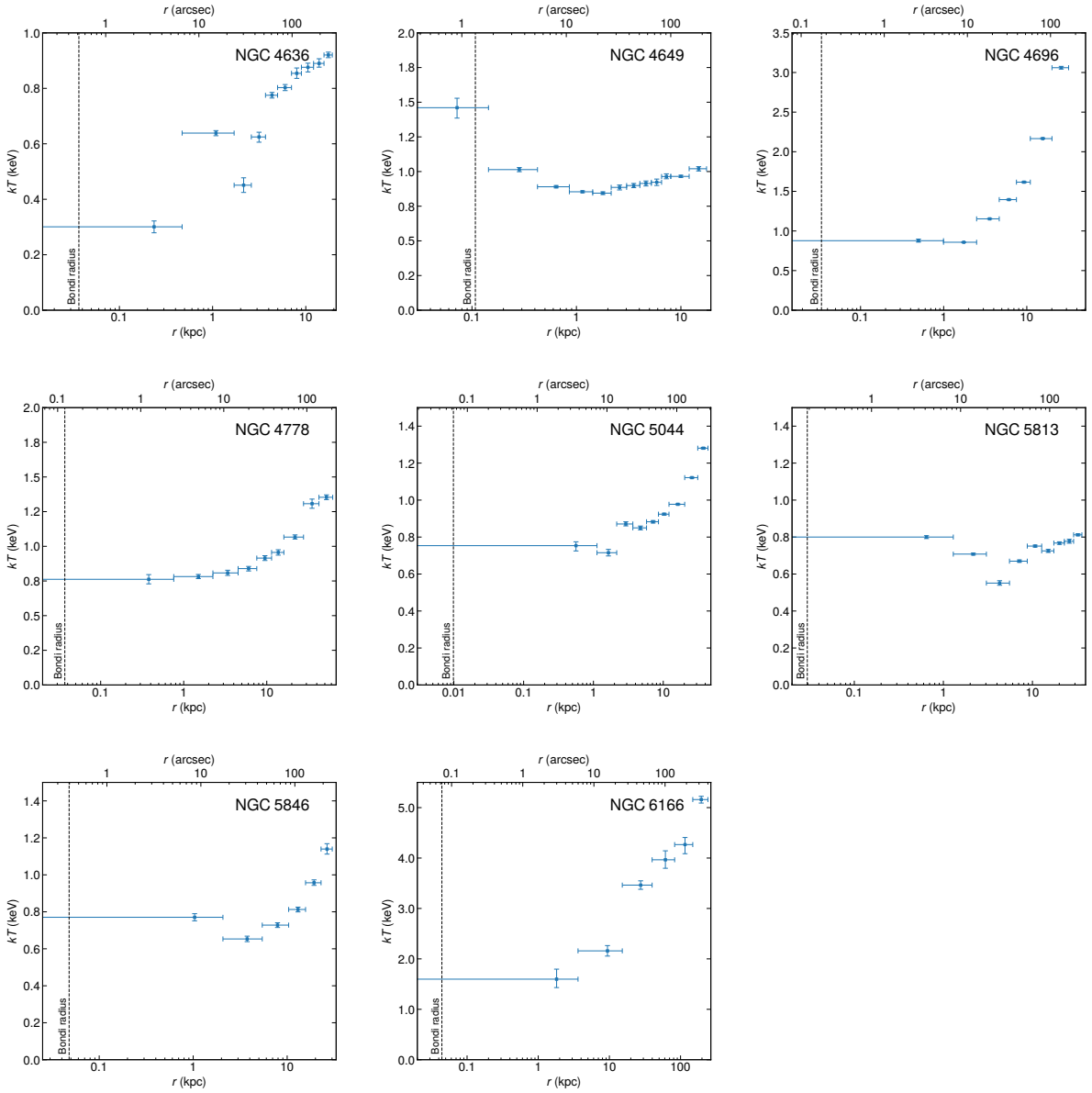

Figure A.1.2: Azimuthally averaged radial profiles of temperature kT. The vertical dashed line represents the Bondi radius $r_{\rm Bondi}$. For most galaxies, the temperatures of two or more neighbouring radial bins were tied together. The temperature of the gas inside the Bondi radius was assumed to be the same as the temperature of the innermost radial bin.

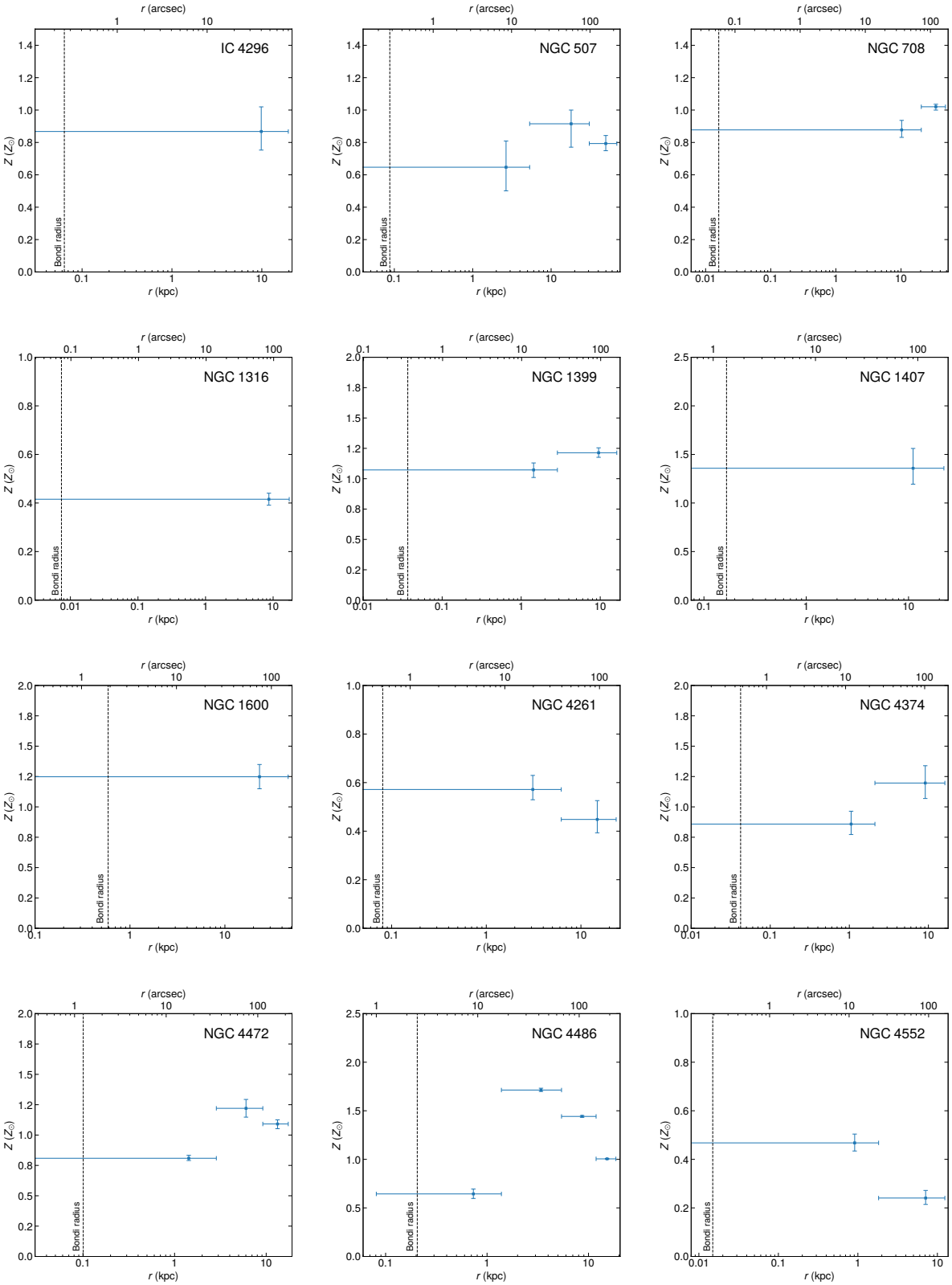
IC 4296
NGC 507
NGC 708
NGC 1316
NGC 1399
NGC 1407
NGC 1600
NGC 4261
NGC 4374
NGC 4472
NGC 4486
NGC 4552
r (arcsec)
r (kpc)
Z (Z⊙)
Bondi radius

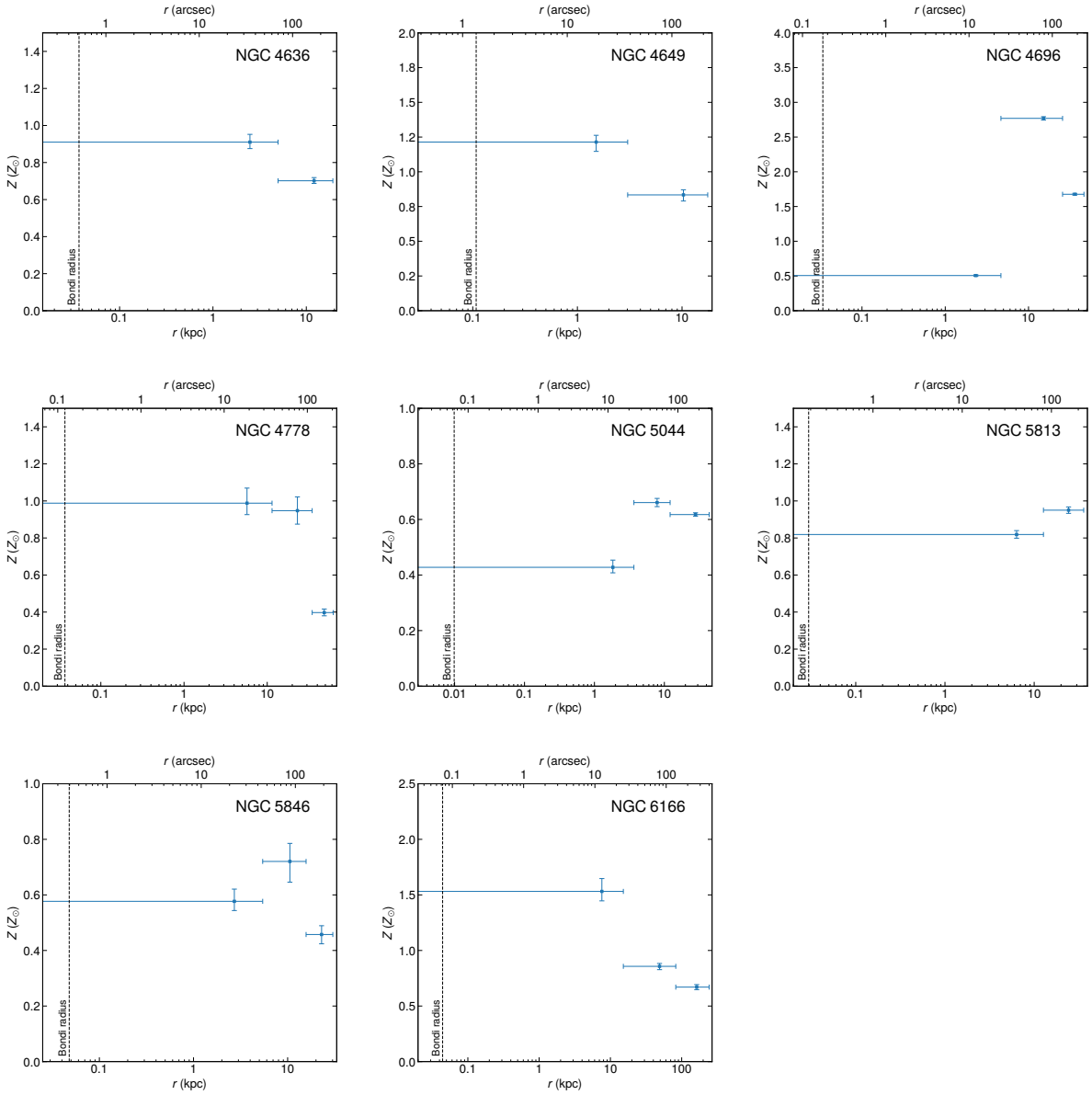

Figure A.1.3: Azimuthally averaged radial profiles of the abundance of heavier elements Z. The vertical dashed line represents the Bondi radius r_{Bondi}. The abundances are expressed relatively with respect to solar abundance measurements reported by Lodders (2003). For most galaxies, the abundances of two or more neighbouring radial bins were tied together. The abundance inside the Bondi radius was assumed to be the same as that of the innermost radial bin.

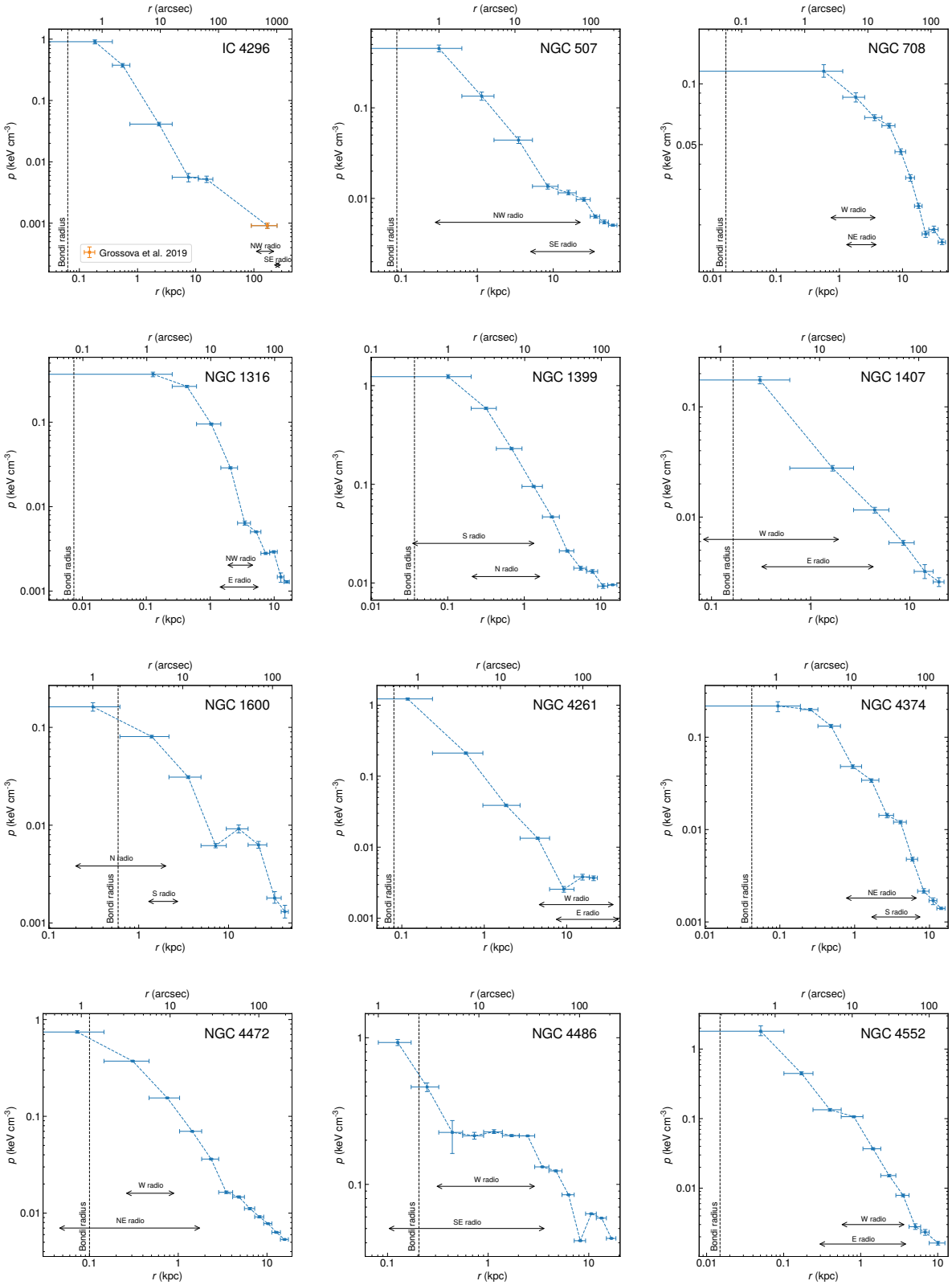
IC 4296
Grossova et al. 2019
NW radio
SE radio
NGC 507
NW radio
SE radio
NGC 708
W radio
NE radio
NGC 1316
NW radio
E radio
NGC 1399
S radio
N radio
NGC 1407
W radio
E radio
NGC 1600
N radio
S radio
NGC 4261
W radio
E radio
NGC 4374
NE radio
S radio
NGC 4472
W radio
NE radio
NGC 4486
W radio
SE radio
NGC 4552
W radio
E radio
Bondi radius
r (arcsec)
r (kpc)
p (keV cm−3)

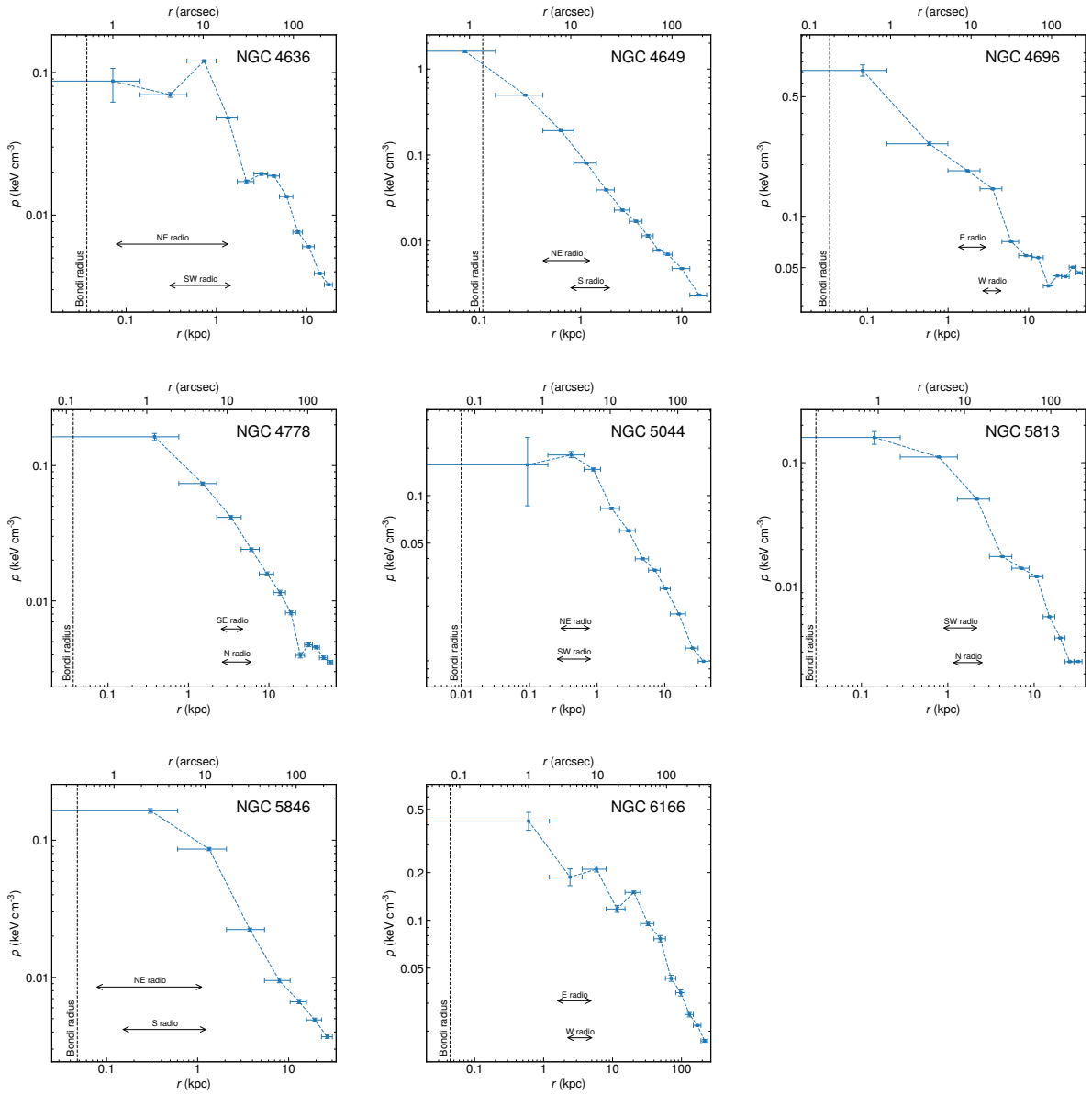

Figure A.1.4: Azimuthally averaged radial profiles of thermal pressure $p = n\,kT$. The vertical dashed line represents the Bondi radius $r_{\rm Bondi}$. The double-sided arrows represent radial ranges of individual radio lobes and the labels express the corresponding position from the galactic centre.

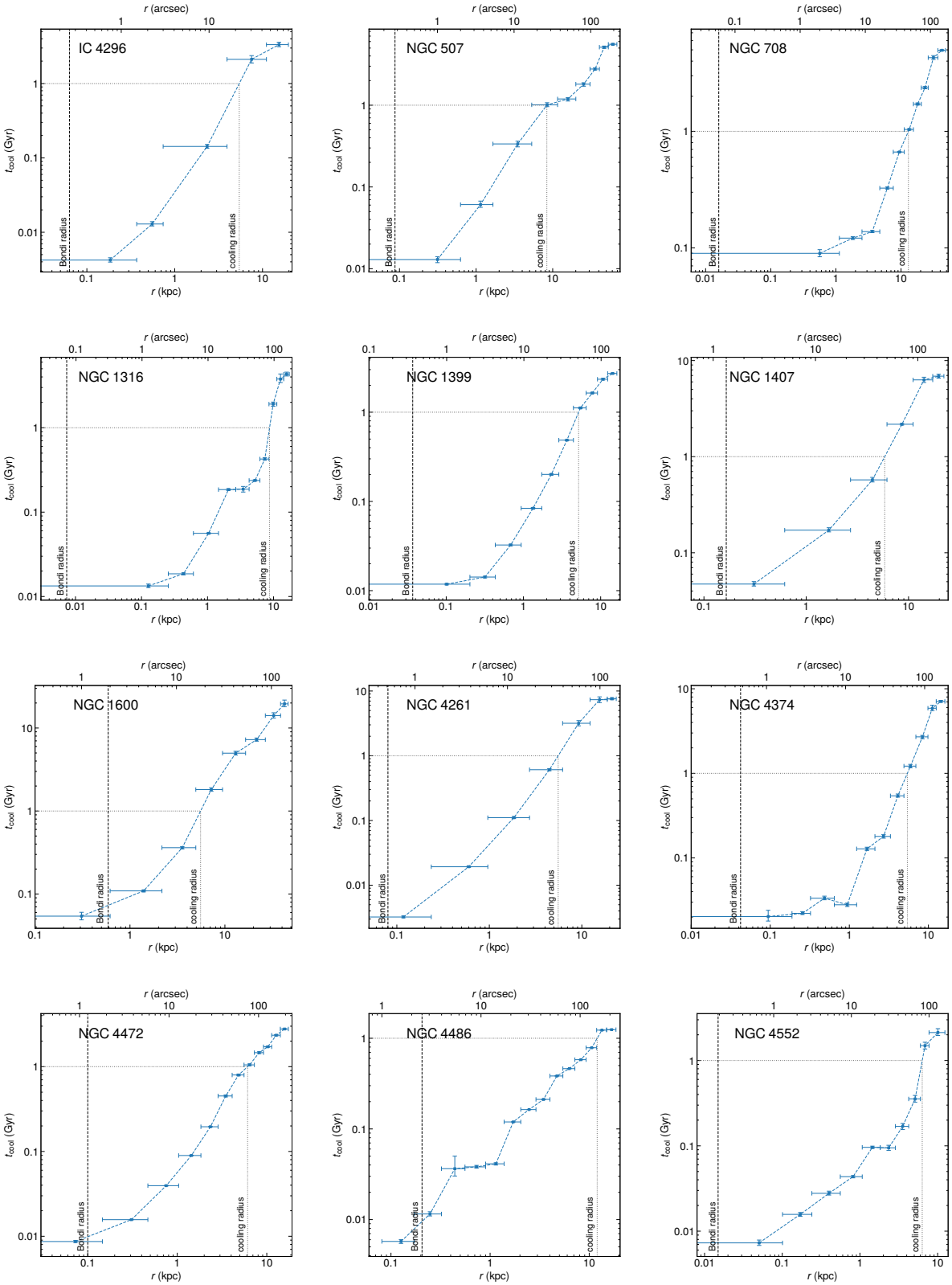
IC 4296
NGC 507
NGC 708
NGC 1316
NGC 1399
NGC 1407
NGC 1600
NGC 4261
NGC 4374
NGC 4472
NGC 4486
NGC 4552
r (arcsec)
r (kpc)
t_cool (Gyr)
Bondi radius
cooling radius

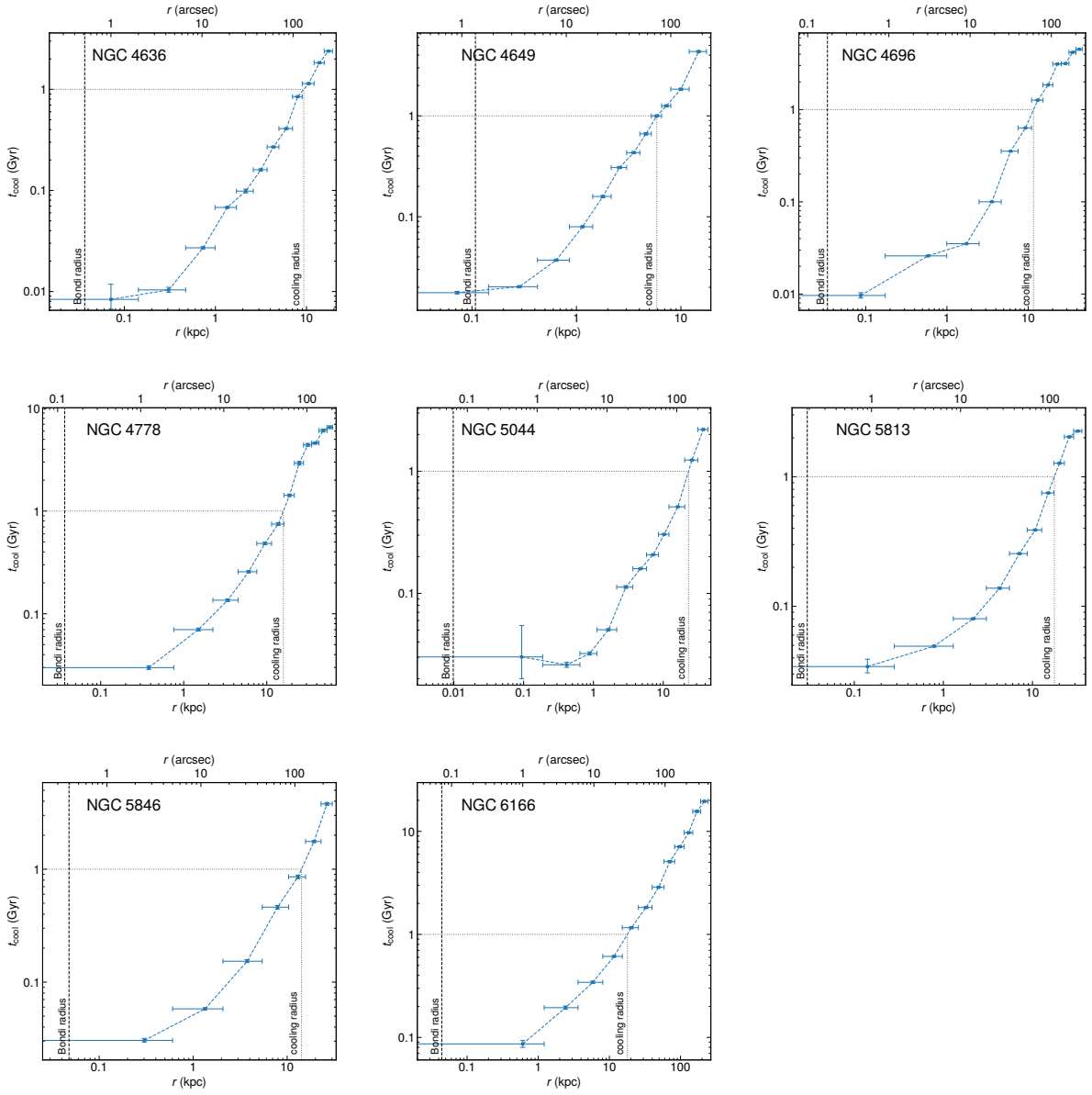

Figure A.1.5: Azimuthally averaged radial profiles of cooling time $t_{\rm cool}$. The vertical dashed line represents the Bondi radius $r_{\rm Bondi}$ while the dotted lines show the 1 Gyr limit and the corresponding cooling radius.

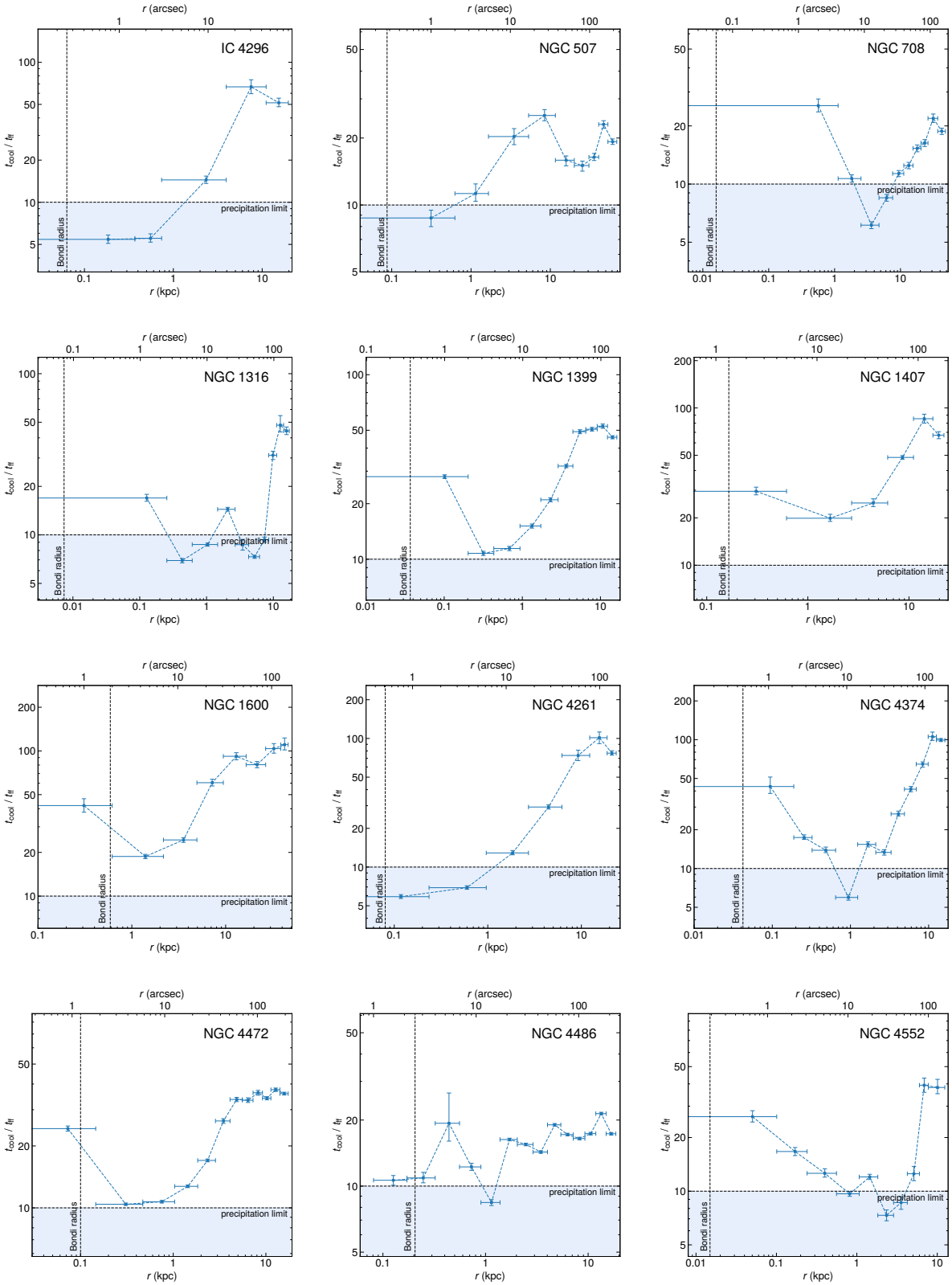
IC 4296
NGC 507
NGC 708
NGC 1316
NGC 1399
NGC 1407
NGC 1600
NGC 4261
NGC 4374
NGC 4472
NGC 4486
NGC 4552
r (arcsec)
r (kpc)
t_cool / t_ff
precipitation limit
Bondi radius

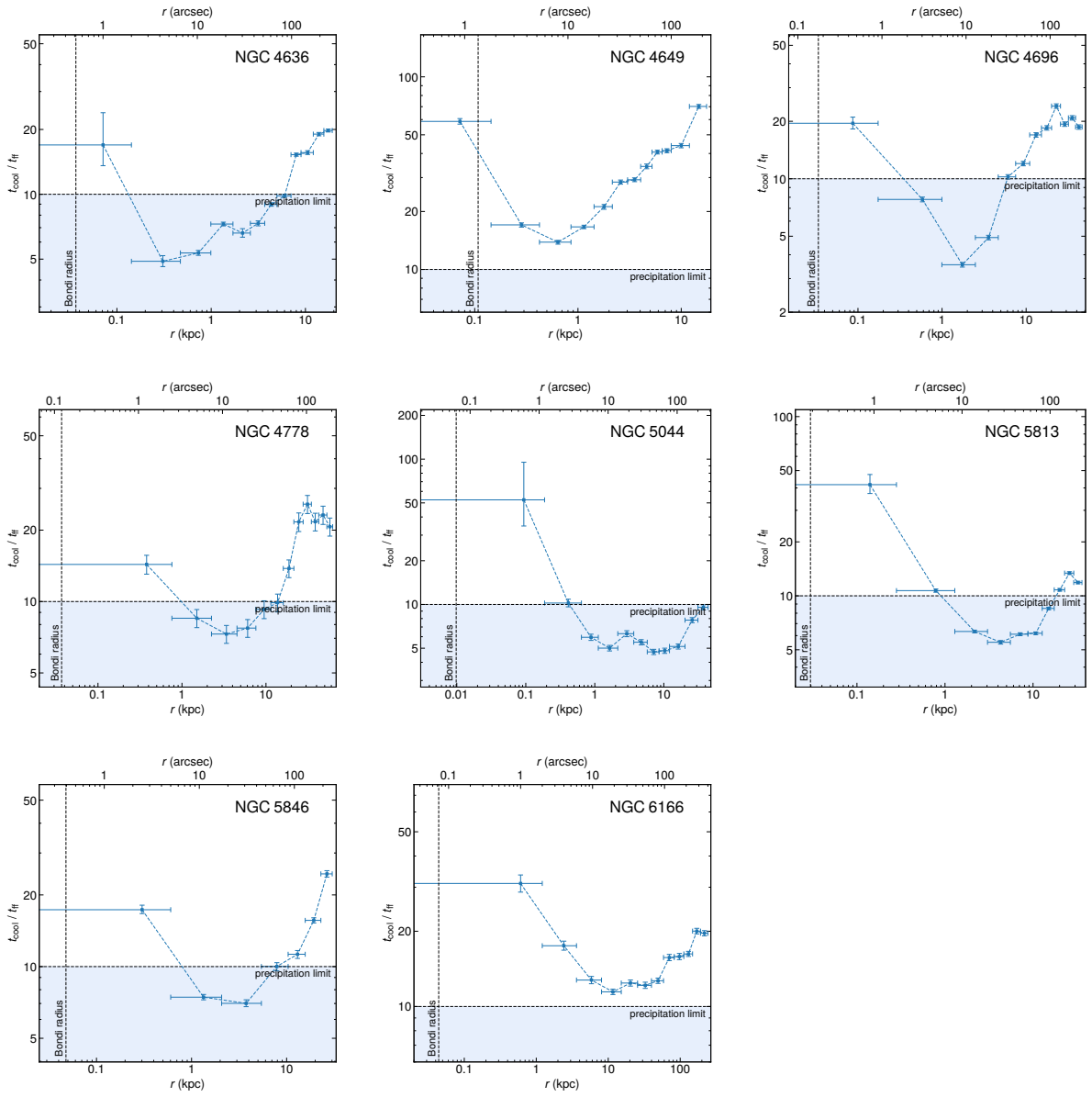

Figure A.1.6: Azimuthally averaged radial profiles of cooling time to free fall time ratio $t_{\rm cool}/t_{\rm ff}$ estimated from the assumption of an isothermal sphere. The vertical dashed line represents the Bondi radius $r_{\rm Bondi}$, while the horizontal dashed line is the precipitation limit $t_{\rm cool}/t_{\rm ff} \approx 10$.

A.1.2 Radio lobes

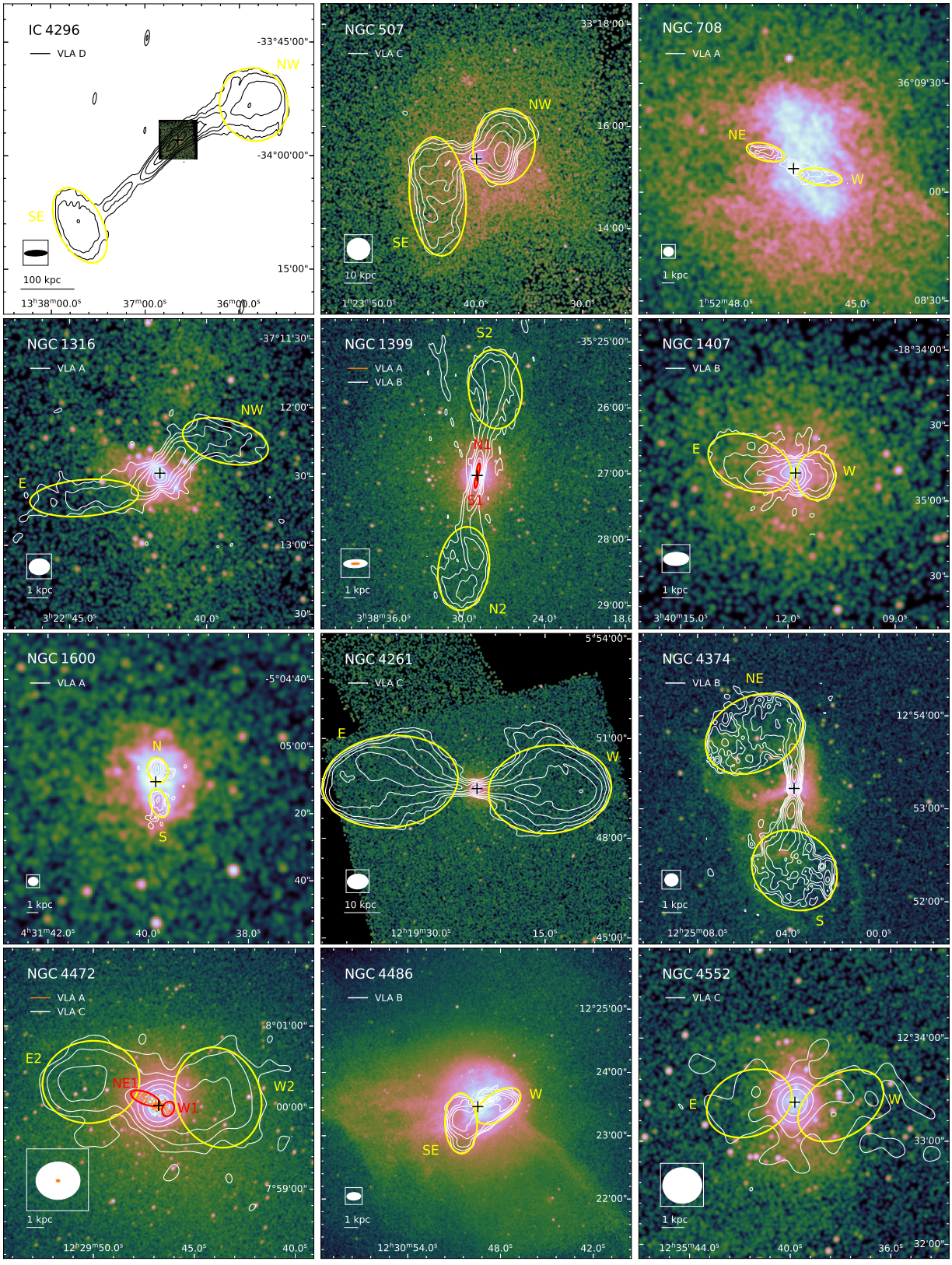

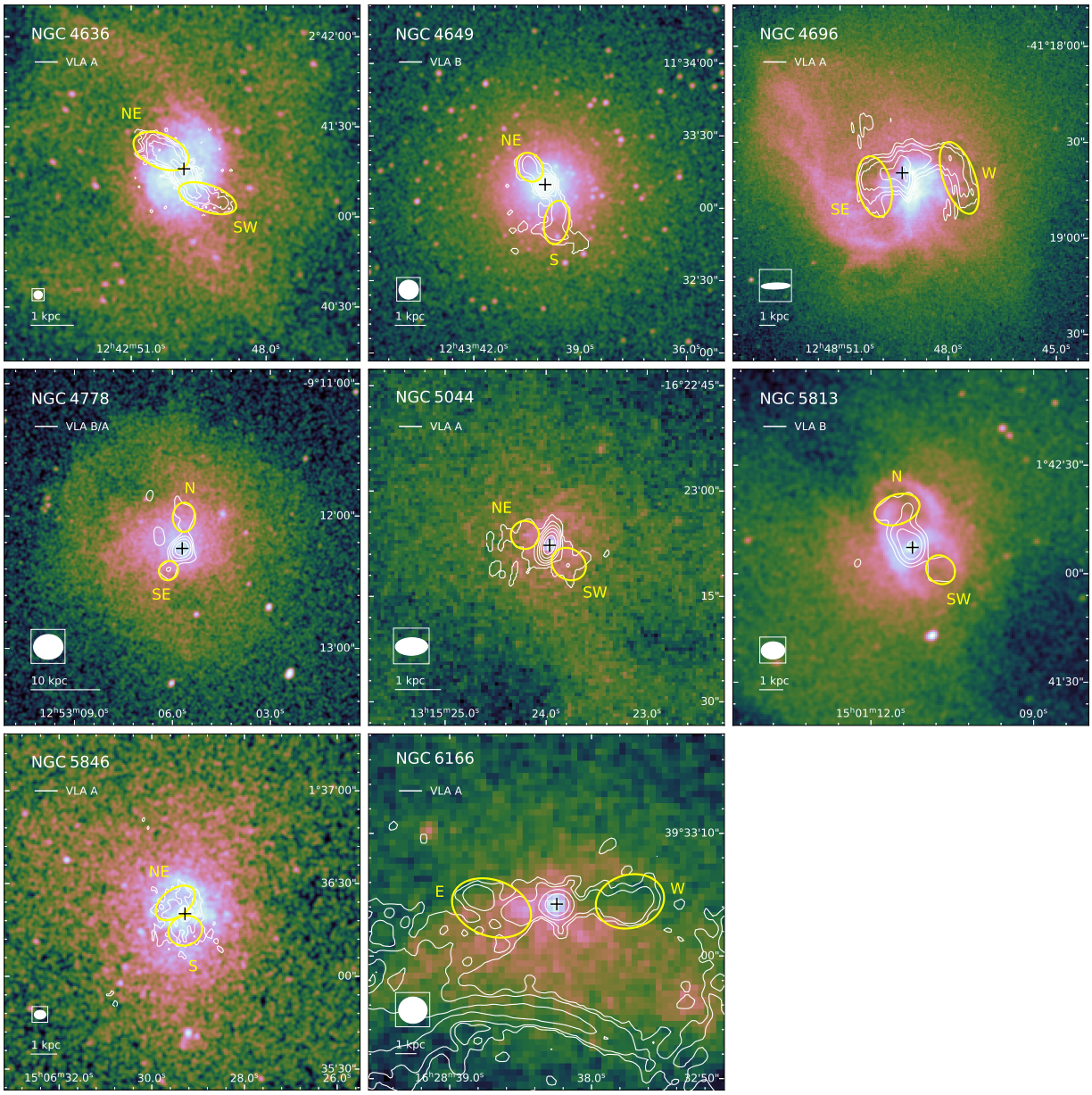

Figure A.1.7: Exposure-corrected *Chandra* (0.5 – 7.0 keV) images overlaid by VLA 1.4 GHz radio contours (*white*) and corresponding ellipse regions (*red*) which were used for size-estimation of radio lobes. VLA array configurations for individual galaxies are stated in the upper left corner of each plot while the corresponding beam sizes are shown in the lower-left corner together with physical scales (1 or 10 kpc). The central black cross represents the exact centre of the galaxy (position of the SMBH).

A.1.3 Cavity powers

Table A.1.1: Properties of individual radio lobes: cavity position with respect to galactic centre, semi-axis along the jet direction (length) $r_{\rm l}$, semi-axis perpendicular to the jet direction (width) $r_{\rm w}$, cavity volume V, galactocentric distance R, age of the cavity assuming inflation at the speed of sound $t_{\rm age}$, total enthalpy of the cavity E, and estimated mechanical power required for its inflation $P_{\rm cav}$.

Galaxy	Side	$r_{\rm w}$ (kpc)	$r_{\rm l}$ (kpc)	V (m^3)	R (kpc)	$t_{\rm age}$ (Myr)	E (erg)	$P_{\rm cav}$ ($erg\,s^{-1}$)
IC4296	SE	78.0	49.0	3.6×10^{64}	250.0	$529.03^{+11.54}_{-10.08}$	$2.1^{+2.1}_{-1.0}\times10^{59}$	$1.3^{+1.2}_{-0.6}\times10^{43}$
	N	78.0	70.0	5.2×10^{64}	160.0	$343.9^{+7.5}_{-6.55}$	$3.0^{+3.0}_{-1.5}\times10^{59}$	$2.9^{+2.8}_{-1.4}\times10^{43}$
NGC507	NW	14.0	11.0	2.7×10^{62}	11.0	$21.25^{+0.18}_{-0.2}$	$2.3^{+2.3}_{-1.1}\times10^{58}$	$3.5^{+3.4}_{-1.7}\times10^{43}$
	SE	22.0	10.0	6.1×10^{62}	20.0	$37.57^{+0.26}_{-0.3}$	$3.7^{+3.7}_{-1.8}\times10^{58}$	$3.2^{+3.1}_{-1.5}\times10^{43}$
NGC708	NE	0.66	1.5	8.2×10^{58}	2.5	4.83 ± 0.1	$4.0^{+4.0}_{-2.0}\times10^{55}$	$2.7^{+2.6}_{-1.3}\times10^{41}$
	W	0.64	1.7	8.3×10^{58}	2.2	4.22 ± 0.09	$4.3^{+4.3}_{-2.1}\times10^{55}$	$3.3^{+3.2}_{-1.6}\times10^{41}$
NGC1316	E	0.81	2.4	2.0×10^{59}	3.5	7.72 ± 0.05	$1.3^{+1.3}_{-0.7}\times10^{55}$	$5.5^{+5.3}_{-2.6}\times10^{40}$
	NW	0.96	1.9	2.2×10^{59}	3.2	7.06 ± 0.05	$1.4^{+1.4}_{-0.7}\times10^{55}$	$6.3^{+6.0}_{-3.0}\times10^{40}$
NGC1399	S1	0.22	0.71	4.2×10^{57}	0.67	$1.26^{+0.01}_{-0.02}$	$8.4^{+8.4}_{-4.2}\times10^{54}$	$2.2^{+2.1}_{-1.0}\times10^{41}$
	N1	0.26	0.76	6.3×10^{57}	0.88	1.7 ± 0.01	$8.0^{+8.0}_{-4.0}\times10^{54}$	$1.5^{+1.5}_{-0.7}\times10^{41}$
	S2	3.2	6.8	8.7×10^{60}	8.5	15.86 ± 0.06	$6.9^{+6.9}_{-3.4}\times10^{56}$	$1.4^{+1.4}_{-0.7}\times10^{42}$
	N2	3.3	6.4	8.4×10^{60}	7.9	$15.04^{+0.06}_{-0.05}$	$7.0^{+7.0}_{-3.5}\times10^{56}$	$1.5^{+1.5}_{-0.7}\times10^{42}$
NGC1407	E	1.3	2.1	4.5×10^{59}	2.3	$4.53^{+0.09}_{-0.08}$	$6.7^{+6.7}_{-3.3}\times10^{55}$	$4.8^{+4.6}_{-2.3}\times10^{41}$
	W	1.2	0.96	1.6×10^{59}	1.0	2.02 ± 0.04	$4.5^{+4.5}_{-2.2}\times10^{55}$	$7.3^{+6.9}_{-3.5}\times10^{41}$
NGC1600	N	0.91	1.2	1.2×10^{59}	1.1	$2.12^{+0.02}_{-0.03}$	$6.3^{+6.3}_{-3.2}\times10^{55}$	$9.8^{+9.3}_{-4.6}\times10^{41}$
	S	0.8	1.3	1.1×10^{59}	2.0	3.93 ± 0.05	$3.6^{+3.6}_{-1.8}\times10^{55}$	$3.0^{+2.9}_{-1.4}\times10^{41}$
NGC4261	E	13.0	19.0	4.0×10^{62}	25.0	$49.89^{+0.43}_{-0.34}$	$9.1^{+9.1}_{-4.6}\times10^{57}$	$6.0^{+5.7}_{-2.9}\times10^{42}$
	W	12.0	17.0	3.3×10^{62}	21.0	$41.78^{+0.36}_{-0.28}$	$7.7^{+7.7}_{-3.8}\times10^{57}$	$6.0^{+5.7}_{-2.9}\times10^{42}$
NGC4374	NE	4.0	3.1	6.2×10^{60}	3.7	8.89 ± 0.08	$3.9^{+3.9}_{-1.9}\times10^{56}$	$1.4^{+1.4}_{-0.7}\times10^{42}$
	S	2.9	3.9	4.0×10^{60}	4.6	10.64 ± 0.09	$2.0^{+2.0}_{-1.0}\times10^{56}$	$6.2^{+6.0}_{-3.0}\times10^{41}$
NGC4472	W1	0.46	0.35	8.9×10^{57}	0.6	1.27 ± 0.01	$1.0^{+1.0}_{-0.5}\times10^{55}$	$2.6^{+2.5}_{-1.2}\times10^{41}$
	NE1	0.36	0.91	1.5×10^{58}	0.9	1.89 ± 0.01	$1.4^{+1.4}_{-0.7}\times10^{55}$	$2.4^{+2.3}_{-1.2}\times10^{41}$
	E2	2.4	2.8	2.0×10^{60}	4.3	8.87 ± 0.03	$2.0^{+2.0}_{-1.0}\times10^{56}$	$7.3^{+7.0}_{-3.5}\times10^{41}$
	W2	3.0	2.5	2.9×10^{60}	3.2	$6.71^{+0.02}_{-0.03}$	$4.1^{+4.1}_{-2.0}\times10^{56}$	$2.0^{+1.9}_{-0.9}\times10^{42}$
NGC4486	SE	2.3	1.2	8.2×10^{59}	1.8	3.55 ± 0.03	$1.0^{+1.0}_{-0.5}\times10^{57}$	$9.3^{+9.0}_{-4.4}\times10^{42}$
	W	1.0	1.9	2.6×10^{59}	1.6	$3.22^{+0.03}_{-0.04}$	$3.5^{+3.5}_{-1.7}\times10^{56}$	$3.5^{+3.4}_{-1.7}\times10^{42}$
NGC4552	E	1.5	2.0	5.2×10^{59}	2.1	$4.38^{+0.06}_{-0.08}$	$8.0^{+8.0}_{-4.0}\times10^{55}$	$6.0^{+5.6}_{-2.8}\times10^{41}$
	W	1.4	2.1	5.0×10^{59}	2.1	$4.43^{+0.07}_{-0.08}$	$6.5^{+6.5}_{-3.2}\times10^{55}$	$4.8^{+4.6}_{-2.3}\times10^{41}$
NGC4636	NE	0.4	0.69	1.3×10^{58}	0.69	$2.41^{+0.09}_{-0.08}$	$7.5^{+7.5}_{-3.8}\times10^{54}$	$1.0^{+1.0}_{-0.5}\times10^{41}$
	SW	0.32	0.71	8.8×10^{57}	0.89	$2.68^{+0.05}_{-0.04}$	$4.6^{+4.6}_{-2.3}\times10^{54}$	$5.6^{+5.4}_{-2.7}\times10^{40}$
NGC4649	NE	0.69	0.38	2.2×10^{58}	1.0	1.81 ± 0.02	$1.3^{+1.3}_{-0.7}\times10^{55}$	$2.4^{+2.3}_{-1.1}\times10^{41}$
	S	0.46	0.75	2.0×10^{58}	1.3	2.4 ± 0.02	$8.1^{+8.1}_{-4.1}\times10^{54}$	$1.1^{+1.1}_{-0.5}\times10^{41}$
NGC4696	E	1.8	0.84	3.2×10^{59}	2.1	4.3 ± 0.03	$3.4^{+3.4}_{-1.7}\times10^{56}$	$2.6^{+2.5}_{-1.2}\times10^{42}$
	W	2.0	0.82	4.1×10^{59}	3.5	7.26 ± 0.05	$3.4^{+3.4}_{-1.7}\times10^{56}$	$1.5^{+1.5}_{-0.7}\times10^{42}$
NGC4778	SE	1.3	1.4	2.7×10^{59}	3.6	7.86 ± 0.08	$6.5^{+6.5}_{-3.3}\times10^{55}$	$2.7^{+2.6}_{-1.3}\times10^{41}$
	N	1.5	2.0	5.9×10^{59}	4.3	9.34 ± 0.07	$1.2^{+1.2}_{-0.6}\times10^{56}$	$4.3^{+4.1}_{-2.0}\times10^{41}$
NGC5044	NE	0.28	0.27	2.7×10^{57}	0.52	1.16 ± 0.02	$2.9^{+2.9}_{-1.4}\times10^{54}$	$8.1^{+7.8}_{-3.9}\times10^{40}$
	SW	0.27	0.31	2.8×10^{57}	0.53	1.18 ± 0.02	$2.9^{+2.9}_{-1.5}\times10^{54}$	$8.0^{+7.8}_{-3.8}\times10^{40}$
NGC5813	SW	0.79	0.74	5.6×10^{58}	1.5	$3.27^{+0.02}_{-0.01}$	$2.3^{+2.3}_{-1.2}\times10^{55}$	$2.3^{+2.3}_{-1.1}\times10^{41}$
	N	1.2	0.77	1.4×10^{59}	1.8	3.81 ± 0.02	$4.8^{+4.8}_{-2.4}\times10^{55}$	$4.1^{+4.0}_{-1.9}\times10^{41}$
NGC5846	NE	0.88	0.52	5.0×10^{58}	0.57	1.24 ± 0.02	$3.5^{+3.5}_{-1.7}\times10^{55}$	$9.2^{+8.8}_{-4.4}\times10^{41}$
	S	0.67	0.57	3.2×10^{58}	0.66	1.46 ± 0.02	$2.2^{+2.2}_{-1.1}\times10^{55}$	$5.0^{+4.8}_{-2.4}\times10^{41}$
NGC6166	W	1.3	1.7	3.6×10^{59}	3.6	5.51 ± 0.31	$4.5^{+4.5}_{-2.2}\times10^{56}$	$2.7^{+2.5}_{-1.3}\times10^{42}$
	E	1.4	2.0	4.7×10^{59}	3.2	4.92 ± 0.28	$5.9^{+5.9}_{-2.9}\times10^{56}$	$3.9^{+3.7}_{-1.9}\times10^{42}$

A.1.4 List of OBSIDs

Table A.1.2: List of individual *Chandra* ACIS observations.

Galaxy	OBSID	Instrument	Date	Exptime (ks)
IC 4926	3394	ACIS-S	2001-12-15	18.6
NGC 507	317	ACIS-S	2000-10-11	26.9
	2882	ACIS-I	2002-01-08	43.6
NGC 708	2215	ACIS-S	2001-08-03	28.7
	7921	ACIS-S	2006-11-20	110.7
NGC 1316	2022	ACIS-S	2001-04-17	28.4
	20340	ACIS-S	2019-04-16	45.0
	20341	ACIS-S	2019-04-22	51.4
	22179	ACIS-S	2019-04-17	39.0
	22180	ACIS-S	2019-04-20	13.6
	22187	ACIS-S	2019-04-25	53.2
NGC 1399	319	ACIS-S	2000-01-18	56.0
	9530	ACIS-S	2008-06-08	59.4
	14527	ACIS-S	2013-07-01	27.8
	14529	ACIS-S	2015-11-06	31.6
	16639	ACIS-S	2014-10-12	29.7
NGC 1407	791	ACIS-S	2000-08-16	44.5
NGC 1600	4283	ACIS-S	2002-09-18	22.7
	4371	ACIS-S	2002-09-20	26.8
	21374	ACIS-S	2018-12-03	25.7
	21375	ACIS-S	2019-11-28	42.2
	21998	ACIS-S	2018-12-03	13.9
	22878	ACIS-S	2019-11-25	45.0
	22911	ACIS-S	2019-11-01	31.0
	22912	ACIS-S	2019-11-02	35.6
NGC 4261	834	ACIS-S	2000-05-06	30.92
	9569	ACIS-S	2008-02-12	100.9
NGC 4374	20539	ACIS-S	2019-04-05	39.5
	20540	ACIS-S	2019-02-26	30.2
	20541	ACIS-S	2019-04-10	11.3
	20542	ACIS-S	2019-03-18	34.6
	20543	ACIS-S	2019-04-27	54.3
	21845	ACIS-S	2019-03-28	27.7
	21852	ACIS-S	2019-02-18	15.6
	21867	ACIS-S	2019-03-13	23.6
	22113	ACIS-S	2019-02-20	21.8
	22126	ACIS-S	2019-02-28	35.1
	22127	ACIS-S	2019-03-02	22.8
	22128	ACIS-S	2019-03-03	23.8
	22142	ACIS-S	2019-03-14	20.8
	22143	ACIS-S	2019-03-16	22.8
	22144	ACIS-S	2019-03-15	31.8
	22153	ACIS-S	2019-03-23	21.1
	22163	ACIS-S	2019-03-29	35.6
	22164	ACIS-S	2019-03-31	32.6
	22166	ACIS-S	2019-04-06	38.6
	22174	ACIS-S	2019-04-11	49.4
	22175	ACIS-S	2019-04-12	27.2
	22176	ACIS-S	2019-04-13	51.4
	22177	ACIS-S	2019-04-14	36.6
	22195	ACIS-S	2019-04-28	38.1
	22196	ACIS-S	2019-05-07	20.6
NGC 4472	321	ACIS-S	2000-06-12	34.5
	11274	ACIS-S	2010-02-27	39.7
	12888	ACIS-S	2011-02-21	159.3
	12889	ACIS-S	2011-02-14	133.5
NGC 4486	352	ACIS-S	2000-07-29	37.7
	2707	ACIS-S	2002-07-06	98.7
	18232	ACIS-S	2016-04-27	18.2
	18233	ACIS-S	2016-02-23	37.2
	18781	ACIS-S	2016-02-24	39.5
	18782	ACIS-S	2016-02-26	34.1
	18783	ACIS-S	2016-04-20	36.1
NGC 4486	18836	ACIS-S	2016-04-28	38.9
	18837	ACIS-S	2016-04-30	13.7
	18838	ACIS-S	2016-05-28	56.3
	18856	ACIS-S	2016-06-12	25.5
	20034	ACIS-S	2017-04-11	13.1
	20035	ACIS-S	2017-04-14	13.1
	21075	ACIS-S	2018-04-22	9.1
	21076	ACIS-S	2018-04-24	9.0
	21457	ACIS-S	2019-03-27	14.1
	21458	ACIS-S	2019-03-28	12.8
NGC 4552	2072	ACIS-S	2001-04-22	54.4
	13985	ACIS-S	2012-04-22	49.4
	14358	ACIS-S	2012-08-10	49.4
	14359	ACIS-S	2012-04-23	48.1
NGC 4636	323	ACIS-S	2000-01-26	45.1
	3926	ACIS-I	2003-02-14	74.7
	4415	ACIS-I	2003-02-15	74.4
NGC 4649	785	ACIS-S	2000-04-20	26.9
	8182	ACIS-S	2007-01-30	49.5
	8507	ACIS-S	2007-02-01	17.5
	12975	ACIS-S	2011-08-08	84.9
	12976	ACIS-S	2011-02-24	101.0
	14328	ACIS-S	2011-08-12	14.0
NGC 4696	504	ACIS-S	2000-05-22	31.8
	505	ACIS-S	2000-06-08	10.0
	4954	ACIS-S	2004-04-01	89.0
	4955	ACIS-S	2004-04-02	44.7
	5310	ACIS-S	2004-04-04	49.3
	16223	ACIS-S	2014-05-26	179.0
	16224	ACIS-S	2014-04-09	42.3
	16225	ACIS-S	2014-04-26	30.1
	16534	ACIS-S	2014-06-05	55.4
	16607	ACIS-S	2014-04-12	45.7
	16608	ACIS-S	2014-04-07	34.1
	16609	ACIS-S	2014-05-04	82.3
	16610	ACIS-S	2014-04-27	17.3
NGC 4778	921	ACIS-S	2000-01-25	48.5
	10462	ACIS-S	2009-03-02	67.2
	10874	ACIS-S	2009-03-03	51.4
NGC 5044	798	ACIS-S	2000-03-19	20.5
	9399	ACIS-S	2008-03-07	82.7
	17195	ACIS-S	2015-06-06	78.0
	17196	ACIS-S	2015-05-11	88.9
	17653	ACIS-S	2015-05-07	35.5
	17654	ACIS-S	2015-05-10	25.0
	17666	ACIS-S	2015-08-23	88.5
NGC 5813	5907	ACIS-S	2005-04-02	48.4
	9517	ACIS-S	2008-06-05	98.8
	12951	ACIS-S	2011-03-28	74.0
	12952	ACIS-S	2011-04-05	143.1
	12953	ACIS-S	2011-04-07	31.8
	13246	ACIS-S	2011-03-30	45.0
	13247	ACIS-S	2011-03-31	35.8
	13253	ACIS-S	2011-04-08	118.0
	13255	ACIS-S	2011-04-10	43.4
NGC 5846	788	ACIS-S	2000-05-24	23.4
	7923	ACIS-I	2007-06-12	90.0
NGC 6166	497	ACIS-S	2000-05-13	19.5
	498	ACIS-S	1999-12-11	17.9
	10748	ACIS-I	2009-11-19	40.6
	10803	ACIS-I	2009-11-17	30.2
	10804	ACIS-I	2009-06-23	18.8
	10805	ACIS-I	2009-11-23	30.3

A.2 Cavity Detection Tool (CADET)

A.2.1 Cavity volume calculation methodology

When estimating cavity volumes from decomposed CADET predictions for testing images, we select the two largest X-ray cavities if more cavities are present. For predictions on real images, volumes are estimated for cavities of interest specified visually by the author. To calculate volumes of thus selected cavities, we use the exact predicted cavity shape obtained after applying both discrimination thresholds and we do not further approximate cavities with an elliptical shape. To estimate the depth of the cavity, we only assume rotational symmetry around the direction towards the centre of the image (coordinate $x = 63.5$, $y = 63.5$) and therefore we assume the depth of the cavity at every point along the galactocentric direction to be equal to its width at that direction.

This is technically realized by splitting the cavity prediction into two 128×128 matrices, each containing a single cavity. Each cavity matrix is then rotated so its centre of mass is at $y = 63.5$. For this 'de-rotated' image, the central pixel and width are derived in each pixel-row along the x-axis and the depth of the cavity in each pixel-row is assumed to be equal to its width (see Figure A.2.1). We note that the code published on the CADET GitHub page is robust also for more complex cavity shapes with a gap in between two cavity parts in the same pixel row (e.g. banana shape).

The resulting 3D representations of cavities in the form of $128 \times 128 \times 128$ cubes are saved into a binary NumPy file format and can be further combined with measured pressure profiles to calculate the energy contained in X-ray cavities. As already tested in Plšek et al. (2022), such an approach provides more accurate total energy estimates compared to calculating the energy solely from central pressure and total cavity volumes.

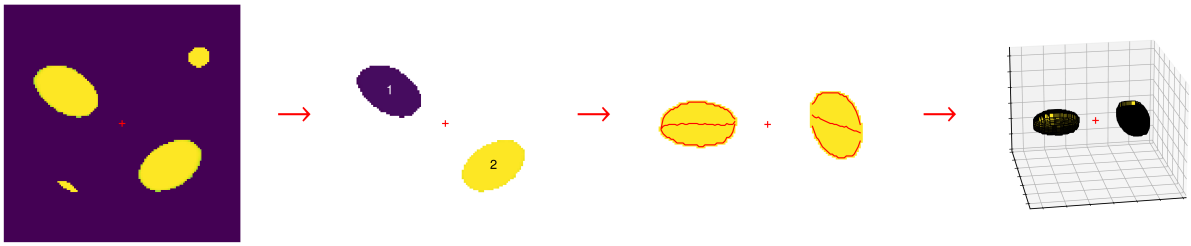

Figure A.2.1: Visualization of the cavity volume estimation process, from left to right: pixel-wise prediction, coordinates of two largest cavities, de-rotated cavities, rotationally symmetric 3D models of both cavities. For visualization purposes, cavity number 1 was de-rotated to the left side of the image while cavity number 2 was to the right side.

A.2.2 Optimization of the discrimination threshold

Pixel-wise predictions obtained from the CNN part of the CADET pipeline are being further decomposed into individual cavities using the DBSCAN algorithm. Nevertheless, before the decomposition, the pixel-wise predictions need to be further trimmed so that only pixels above a given value (discrimination threshold) are accounted for. The choice of this discrimination threshold will, however, strongly affect predicted areas of detected cavities and also the amount of true positive and false positive predictions.

For the testing set of 10^4 images with X-ray cavities, we, therefore, estimated the amount of true positive[2] predictions (TP rate) for 9 different values of the discrimination threshold ($0.1 - 0.9$). For true-

[2] Predictions were accounted as true positive if at least 20% of the original cavity area has been recovered.

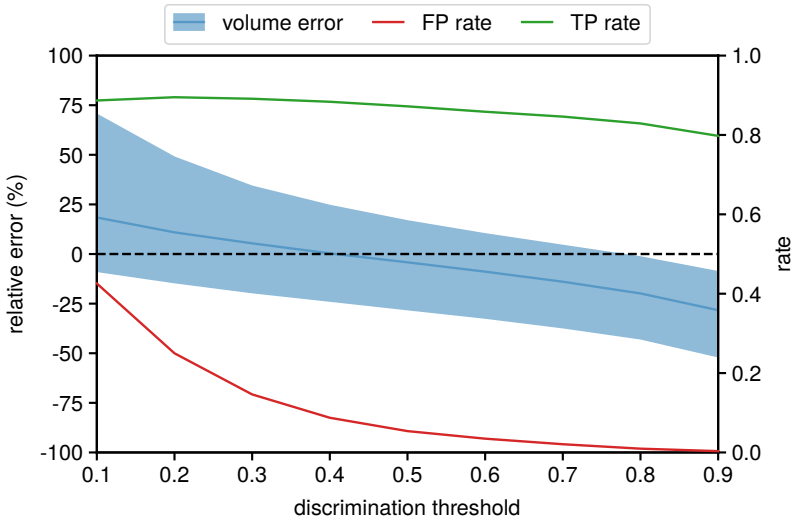

Figure A.2.2: Relative cavity volume error (blue), false positive rate (red) and true positive rate (green) as a function of discrimination threshold. Relative errors and true positive rates were calculated for a sample of 10^4 testing images with a single pair of X-ray cavities and false positive rates were estimated from a sample of 10^3 images without any X-ray cavities. For cavity errors, the blue line is the median value, while the blue area represents the 1σ confidence interval. Meanwhile, area and volume error distributions centre around zero for a discrimination threshold of ≈ 0.4, to obtain optimal FP and TP rates a higher discrimination threshold of ≈ 0.6 is required.

positive cavities, we further expressed their relative area and volume reconstruction errors and using interpolation, we found an optimal value of the discrimination threshold for which the distribution of relative volume errors is clustered around zero (≈ 0.4; see Figure A.2.2).

Nevertheless, setting a relatively low discrimination threshold that properly calibrates reconstructed volumes of true positive cavity detections (≈ 0.4) would, for many networks, result in accounting for plenty of low-significance predictions and thus in producing a lot of false positives (FP rate). For this reason, all trained networks were also applied on a set of 2000 images without any X-ray cavities and the rate of false positive predictions was estimated for the same set of discrimination thresholds as used when estimating the true positive rate. An ideal discrimination threshold that optimizes both FP and TP rates was found (≈ 0.6) by simultaneously minimizing the false positive rate (maximally 5%) and maximizing the true positive rate (minimally 80%).

By applying both thresholds consequently, volumes of detected X-ray cavities can be calibrated by the lower discrimination threshold, and low-significance and hopefully false positive predictions can subsequently be discarded by the higher discrimination threshold[3].

A.2.3 Cavity selection and significance estimation

Although the CADET pipeline automatically detects possible surface brightness drops (X-ray cavities), the specific cavities to be used for further cavity size estimation need to be selected visually by the user. To mitigate spurious detections, we recommend only choosing cavities that are detected on at least two subsequent size scales. Furthermore, one should assess the reliability of obtained cavity predictions in combination with beta-modelling and perform additional tests such as azimuthal and radial photon count statistics. To estimate the sizes of thus selected cavities, we recommend choosing the size scale at which the cavities are fully recovered but at the same time choosing the smallest possible size scale due

[3] In the case of the higher discrimination threshold, the cavity is taken as valid if the mean value is above this threshold.

to better spatial resolution (e.g. for 2-nd generation cavities in NGC3091, one should choose cavities 1 and 2 at the scale of 384 pixels rather than at larger or smaller scales; see Figure A.2.3).

The reliability of detected X-ray cavities can be tested using azimuthal and radial count statistics. To obtain the significance of cavity predictions, we derived azimuthal and radial surface brightness profiles from source-filled images and we expressed the significance of azimuthal and radial bins inside X-ray cavities with respect to the surrounding background (see Hlavacek-Larrondo et al., 2015; Ubertosi et al., 2021). As valid cavity predictions, we only chose cavities with a depth lower than or equal to 3σ below the surrounding background (see Figure A.2.3). We note, however, that such an approach is not robust for highly elliptical β-models or galaxies with strong sloshing patterns and shock fronts, and conversely, due to poor count statistics it can also result in overestimating the significance of random brightness drops.

For these reasons, we have performed additional reliability testing based on simulating images of galaxies with similar properties as the given input images. For each galaxy, we generated 10000 similar images by sampling the parameters of simulated β-models from the results of the beta-modelling analysis (parameter values were varied within estimated uncertainties). Into thus obtained galaxy models, we inserted cavities with the same sizes and properties as derived from CADET predictions. For each cavity, we then expressed the false positive rate (chance of detecting cavity at a similar distance with an area bigger than half of the area of the detected cavity), true positive rate (chance of recovering at least 20% of the original cavity area), and average volume reconstruction error. We note, however, that the estimated false-positive rate represents rather a lower limit and for realistic images, the FP rate can be higher due to the much more complex structure of real galaxies, groups and clusters.

The cavity was marked as successfully confirmed when passing at least 3 out of 4 conditions: radial and azimuthal count statistics is for at least a single bin in each cavity 3σ under the surrounding background, the false positive rate is lower than 5% and the true positive rate is higher than 80%.

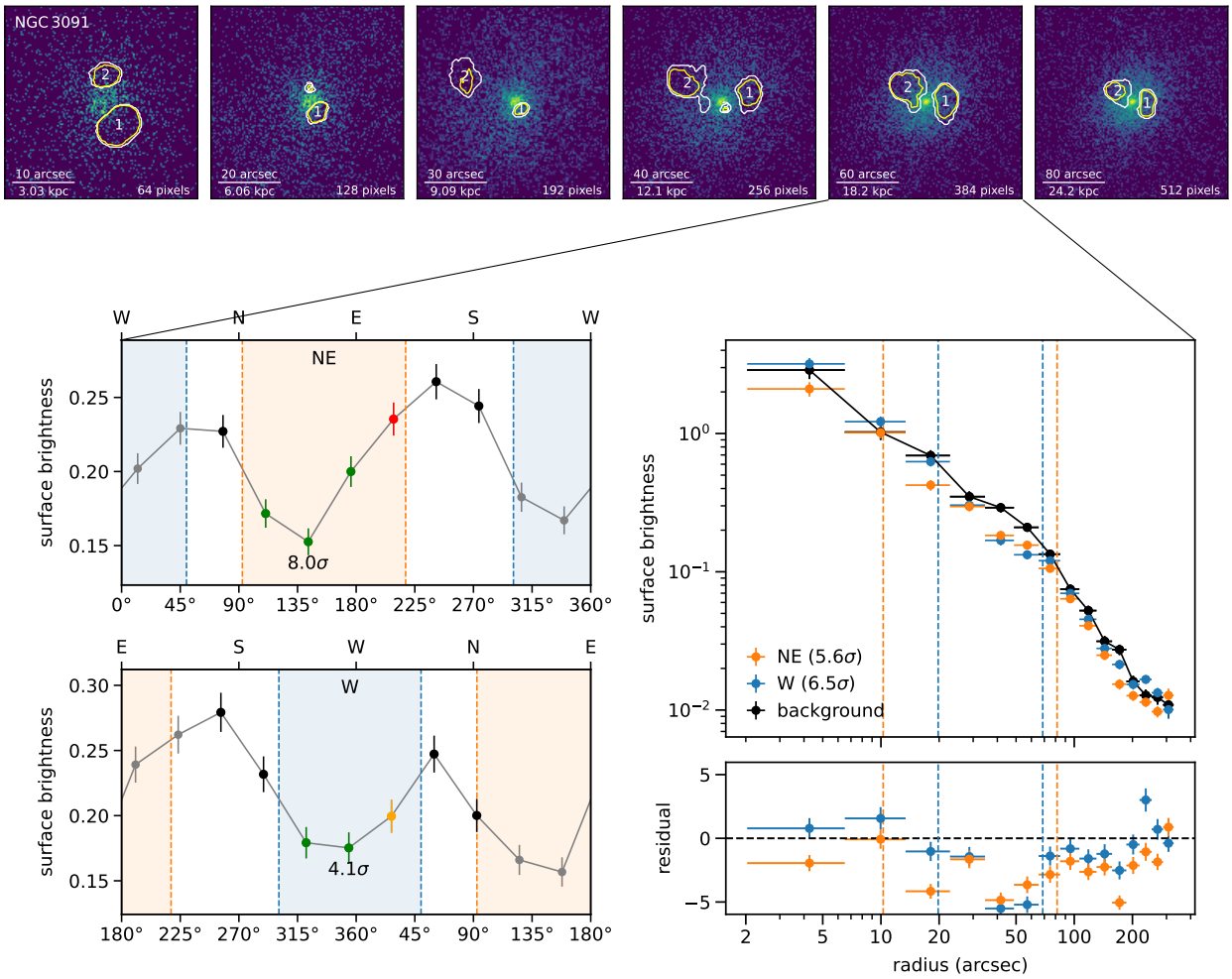

Figure A.2.3: Cavity detection and significance estimation for NGC 3091 in which we detected a new pair of X-ray cavities. *Upper:* Pixel-wise CADET predictions of newly detected X-ray cavities overlaid over X-ray images of NGC 3091. Contours correspond to 0.4 (white) and 0.65 (yellow) levels. Individual subplots show images probed on different size scales, from left to right: 0.5 binning (64 × 64 pixels), 1 binning (128 × 128 pixels), 1.5 binning (196 × 196 pixels), 2 binning (256 × 256 pixels), 3 binning (384 × 384 pixels) and 4 binning (512 × 512 pixels). *Lower left:* azimuthal profiles of detected X-ray cavities. The number of azimuthal bins was chosen so that every cavity is divided into at least 3 bins and another 2 surrounding bins on both sides (black points) were used to estimate the level of background. The significance of individual cavity bins was calculated as in Ubertosi et al. (2021) and is visualized by green (>3σ), yellow (>1σ), and red (<1σ) data points. The significance of the bin with the highest decrement is stated below the corresponding data point. Borders of X-ray cavities are marked by dashed lines and distinguished by colour to the W cavity (blue) and NE cavity (orange). *Lower right:* comparison of an azimuthally averaged radial profile excluding detected cavities, which served as a background for radial significance calculations, with radial profiles across detected X-ray cavities. Significances of individual radial bins were calculated similarly as in azimuthal profiles. We state the significance of the most significant radial bins for individual cavities in the legend. Borders of individual X-ray cavities are marked by blue (N cavity) and orange (S cavity) dashed lines.

A.2.4 Parameter distributions

Table A.2.1: References for detections or non-detections of X-ray cavities and radio lobes for the sample of 70 early-type galaxies.

Galaxy	X-ray cavities [a]	Radio lobes [b]
3C 449	DU10†, L13	L13, G22
IC 1262	DU10, P14	B20
IC 1459	S16†	T15
IC 1860	-	DU10, G22†
IC 4296	P14†	G19
IC 4765	-	-
NGC 57	-	G22†
NGC 193	C10, B14	G11, B20
NGC 315	-	G11, C22, G22
NGC 383	DU10†	G11, C22
NGC 499	P14*, K19*	DU10†, B20†, G22†
NGC 507	DO10*, C10	DU10, G11, C22, G22
NGC 533	DO10, P14†, S16	DU10, G22
NGC 708	DO10, P14, S16	DU10, B20, C22, G22
NGC 720	-	-
NGC 741	DO10*, S17	G11, B20, G22
NGC 777	C10, P14*	B20†, C22, G22
NGC 1132	DO10, S16†	G22†
NGC 1275	S16	G20
NGC 1316	C10, S16	G22
NGC 1380	-	-
NGC 1387	-	-
NGC 1399	P14, S16	DU10, G22
NGC 1404	S16	DU10, G22†
NGC 1407	DO10*, S16†	G11, G22
NGC 1521	-	-
NGC 1550	DO10*, P14	DU10, G22
NGC 1553	C10	-
NGC 1600	C10	G22
NGC 1700	-	-
NGC 2300	DO10*	B20†, G22†
NGC 2305	-	DU10†
NGC 2563	-	K18†
NGC 3091	DO10†	G22†
NGC 3402	DO10†, P14	G11
NGC 3923	-	G22†
NGC 4073	DO10†, P14†, S16†	G22†
NGC 4104	DO10, P14†	B20
NGC 4125	DO10†	G22†
NGC 4261	C10*, O11, S16†	G22
NGC 4291	-	W23†
NGC 4325	R07, DO10†, P14*	R07†
NGC 4342	-	-
NGC 4374	C10, S16	G22
NGC 4382	-	C09†
NGC 4406	-	G22†
NGC 4472	C10, P14, S16	DU10, G22
NGC 4477	L18	L18†
NGC 4486	S16	DU10, G22
NGC 4526	-	-
NGC 4552	C10, S16	G22
NGC 4555	-	C22†
NGC 4636	C10, P14, S16	DU10, G11, G22
NGC 4649	PAG14, S16†	DU10, C22, G22
NGC 4696	P14, S16	DU10, G22
NGC 4778	DO10, P14, S16	G11, G22†
NGC 4936	P14†	G22†
NGC 5044	DO10, C10, P14, S16	DU10, G11, G22
NGC 5129	DO10†	G22
NGC 5171	P14†	-
NGC 5813	C10, P14	G11, B20, G22
NGC 5846	DO10, C10, P14, S16	DU10†, G11, B20, G22
NGC 6107	-	-
NGC 6166	P14, S16	B20
NGC 6338	DO10, C10, P14, S16	B20
NGC 6482	P14†, S16†	M14
NGC 6868	M10*, P14†	-
NGC 7618	S16†	K06†
NGC 7619	DO10†, S16†	G11†, G22†
NGC 7796	-	-

[a] For X-ray cavities, sources marked with † are reported as non-detections and sources marked with * are reported as cavity candidates.
[b] For radio lobes marked with †, no emission, point-like emission or radio relics are reported.
References: [K06] Kraft et al. (2006) [R07] Russell et al. (2007) [C09] Capetti et al. (2009) [DO10] Dong et al. (2010) [DU10] Dunn et al. (2010) [C10] Cavagnolo et al. (2010) [M10] Machacek et al. (2010) [G11] Giacintucci et al. (2011) [O11] O'Sullivan et al. (2011) [L13] Lal et al. (2013) [B14] Bogdán et al. (2014) [M14] Miraghaei et al. (2014) [P14] Panagoulia et al. (2014) [PAG2014] Paggi et al. (2014) [T15] Tingay and Edwards (2015) [S16] Shin et al. (2016) [S17] Schellenberger et al. (2017) [K18] Kolokythas et al. (2018) [L18] Li et al. (2018) [G19] Grossová et al. (2019) [K19] Kim et al. (2019) [P19] Pandge et al. (2019) [B20] Bîrzan et al. (2020) [G20] Gendron-Marsolais et al. (2020) [C22] Capetti et al. (2022) [G22] Grossová et al. (2022) [W23] Wójtowicz et al. (2023)

Table A.2.2: Parameters Parameters obtained from β-modelling the whole sample of galaxies: galaxy name, original size of the image region in *Chandra* pixels (1 pixel ≈ 0.492 arcsec), the total number of counts; first component parameters: core radius r_c, amplitude A, beta parameter β, ellipticity e; second component parameters: core radius $r_{c,2}$, amplitude A_2, beta parameter β_2; and the background level c_0.

Galaxy	Size	Counts	r_c	A	α	e	$r_{c,2}$	A_2	α_2	$c0$
3C 449	768	46202	$0.49^{+0.04}_{-0.05}$	453^{+60}_{-53}	1 ± 0.02	0.18 ± 0.01	200 ± 10	0.208 ± 0.005	1.0 ± 0.1	0.049 ± 0.006
IC 1262	512	118849	$12.3^{+0.6}_{-0.5}$	4.8 ± 0.2	0.98 ± 0.01	0.109 ± 0.005	85.6 ± 2.1	1.77 ± 0.03	0.99 ± 0.1	0.1 ± 0.01
IC 1459	512	18660	0.49 ± 0.01	4410^{+250}_{-200}	$1.36^{+0.014}_{-0.006}$	0.11 ± 0.01	$58.6^{+4.3}_{-3.7}$	0.19 ± 0.02	1.4 ± 0.1	0.022 ± 0.001
IC 1860	512	27841	5.9 ± 0.4	5.5 ± 0.3	0.65 ± 0.01	0.15 ± 0.01	0	0	0	0.013 ± 0.002
IC 4296	512	9632	0.98 ± 0.04	294^{+18}_{-17}	1.13 ± 0.01	0.18 ± 0.02	0	0	0	0.017 ± 0.002
IC 4765	512	6090	4.1 ± 0.6	$3.4^{+0.5}_{-0.4}$	0.94 ± 0.05	0	$127.1^{+4.7}_{-4.8}$	0.24 ± 0.02	10 ± 1	0.01 ± 0.001
NGC 57	128	823	4.2 ± 0.5	3.1 ± 0.4	1.06 ± 0.04	0.15 ± 0.05	0	0	0	0.12 ± 0.01
NGC 193	512	29406	$0.72^{+0.04}_{-0.05}$	280^{+25}_{-21}	1.43 ± 0.04	0	$274.6^{+6}_{-5.7}$	0.19 ± 0.002	1.4 ± 0.1	0.068 ± 0.007
NGC 315	512	16673	$0.208^{+0.009}_{-0.006}$	6990^{+220}_{-550}	$0.99^{+0.003}_{-0.004}$	0.05 ± 0.01	0	0	0	0.01 ± 0.001
NGC 383	512	13471	$0.35^{+0.04}_{-0.06}$	670^{+180}_{-140}	1.16 ± 0.04	0	3.9 ± 0.4	$11.1^{+1.9}_{-1.4}$	1.1 ± 0.1	0.037 ± 0.001
NGC 499	640	34211	$2.6^{+0.4}_{-0.3}$	6 ± 0.9	0.84 ± 0.01	$0.087^{+0.011}_{-0.01}$	$51^{+2.3}_{-2}$	0.7 ± 0.03	0.84 ± 0.08	0.13 ± 0.01
NGC 507	512	56224	2.2 ± 0.2	$31.4^{+2.6}_{-2.5}$	1.06 ± 0.03	$0.02^{+0.011}_{-0.01}$	176.6 ± 3.8	0.432 ± 0.005	1.1 ± 0.1	0.088 ± 0.009
NGC 533	512	21546	3.7 ± 0.4	$13.8^{+1.1}_{-0.9}$	0.82 ± 0.02	0	$44.1^{+7}_{-6.4}$	1.2 ± 0.2	$2.6^{+0.5}_{-0.4}$	$0.017^{+0.001}_{-0.002}$
NGC 708	640	425100	$18.5^{+0.4}_{-0.3}$	16.6 ± 0.2	0.67 ± 0.006	0.233 ± 0.003	0	0	0	0.234 ± 0.007
NGC 720	640	35400	6.4 ± 0.4	$6.0^{+0.4}_{-0.3}$	0.72 ± 0.01	$0.12^{+0.02}_{-0.01}$	0	0	0	0.028 ± 0.001
NGC 741	512	40443	2.2 ± 0.1	54 ± 3	0.81 ± 0.01	0.07 ± 0.01	0	0	0	0.063 ± 0.001
NGC 777	512	3474	$4.3^{+0.3}_{-0.4}$	$3.4^{+0.4}_{-0.3}$	0.84 ± 0.01	0.11 ± 0.03	0	0	0	0.13 ± 0.01
NGC 1132	512	21967	4.4 ± 0.4	9.6 ± 0.4	$1.06^{+0.03}_{-0.02}$	0.11 ± 0.02	$51.7^{+5.6}_{-5.2}$	0.17 ± 0.01	$0.35^{+0.04}_{-0.03}$	0.13 ± 0.01
NGC 1275	768	15323417	1.5 ± 0.03	3251^{+63}_{-61}	1.65 ± 0.02	0.11 ± 0.01	193.8 ± 0.4	91.88 ± 0.07	1.268 ± 0.002	0.093 ± 0.009
NGC 1316	512	58438	$0.94^{+0.07}_{-0.06}$	164^{+11}_{-10}	0.764 ± 0.007	0	52.1 ± 0.8	6.5 ± 0.3	10 ± 1	0.096 ± 0.002
NGC 1380	512	7017	7 ± 0.6	2.6 ± 0.2	1.07 ± 0.04	0.1 ± 0.04	0	0	0	0.018 ± 0.002
NGC 1387	512	5354	$1.3^{+0.2}_{-0.1}$	$7^{+1}_{-0.9}$	0.67 ± 0.02	0.22 ± 0.03	0	0	0	0.006 ± 0.001
NGC 1399	640	328646	5.44 ± 0.06	$190.5^{+2.4}_{-2.3}$	0.942 ± 0.003	0	0	0	0	0.336 ± 0.002
NGC 1404	512	305846	4.88 ± 0.05	296 ± 3.3	0.902 ± 0.002	0	0	0	0	0.113 ± 0.003
NGC 1407	512	23152	$0.22^{+0.03}_{-0.02}$	246^{+38}_{-34}	0.67 ± 0.07	0.1 ± 0.01	59.9 ± 1.2	0.81 ± 0.04	2.3 ± 0.2	0.013 ± 0.001
NGC 1521	512	9164	$5.3^{+0.6}_{-0.5}$	2.7 ± 0.3	0.82 ± 0.02	0.21 ± 0.03	0	0	0	0.018 ± 0.001
NGC 1550	640	230601	3.9 ± 0.3	$31.4^{+1.9}_{-2}$	1.07 ± 0.07	0.235 ± 0.004	16.4 ± 0.5	10.3 ± 0.5	0.616 ± 0.003	0.059 ± 0.006
NGC 1553	640	5878	0.46 ± 0.06	408^{+89}_{-68}	$1.37^{+0.06}_{-0.05}$	0.16 ± 0.03	8.7 ± 0.9	0.151 ± 0.002	0.4 ± 0.04	0.037 ± 0.004
NGC 1600	512	50980	$18.5^{+1.6}_{-1.4}$	$9.9^{+0.4}_{-0.3}$	2.3 ± 0.2	$0.13^{+0.02}_{-0.01}$	52.2 ± 5.2	0.27 ± 0.02	0.5 ± 0.1	$0.08^{+0.01}_{-0.03}$
NGC 1700	512	6361	1.6 ± 0.2	13.4 ± 1.6	0.87 ± 0.02	0.27 ± 0.03	0	0	0	$0.015^{+0.002}_{-0.001}$
NGC 2300	512	29865	8.8 ± 0.4	6.6 ± 0.3	0.92 ± 0.02	0.06 ± 0.02	0	0	0	0.057 ± 0.001
NGC 2305	512	3756	2.1 ± 0.2	6 ± 0.8	0.78 ± 0.02	$0.08^{+0.03}_{-0.04}$	0	0	0	0.003 ± 0.0003
NGC 2563	512	6910	2.7 ± 0.3	6.8 ± 0.8	0.87 ± 0.02	0.1 ± 0.04	0	0	0	0.016 ± 0.002
NGC 3091	512	10206	$3.7^{+0.5}_{-0.4}$	5.7 ± 0.6	$0.87^{+0.05}_{-0.04}$	0	$160.6^{+3.8}_{-3.7}$	0.2 ± 0.01	4.8 ± 0.5	0.008 ± 0.001
NGC 3402	768	49730	5.7 ± 0.2	16.2 ± 0.6	0.755 ± 0.003	0.061 ± 0.009	0	0	0	0.06 ± 0.006
NGC 3923	512	27664	6.1 ± 0.2	25.1 ± 0.8	1.09 ± 0.01	0.16 ± 0.01	0	0	0	0.044 ± 0.001

Table A.2.2: Continued.

Galaxy	Size	Counts	r_c	A	α	e	$r_{c,2}$	A_2	α_2	$c0$
NGC 4073	768	59275	$11.4^{+0.4}_{-0.3}$	7.3 ± 0.2	$0.796^{+0.008}_{-0.007}$	$0.173^{+0.007}_{-0.008}$	0	0	0	0.016 ± 0.001
NGC 4104	512	13991	4.7 ± 0.2	14.1 ± 0.7	1.11 ± 0.02	0.25 ± 0.02	0	0	0	0.033 ± 0.001
NGC 4125	512	14521	1.1 ± 0.1	$16.8^{+1.9}_{-1.6}$	$0.595^{+0.01}_{-0.008}$	0.21 ± 0.02	0	0	0	0.002 ± 0.001
NGC 4261	512	50099	1.19 ± 0.03	756^{+23}_{-24}	1.038 ± 0.004	0	0	0	0	0.076 ± 0.001
NGC 4291	512	7468	$0.54^{+0.08}_{-0.07}$	8.2 ± 1.1	0.505 ± 0.006	$0.21^{+0.02}_{-0.03}$	0	0	0	0.12 ± 0.01
NGC 4325	768	42117	$6.6^{+1.3}_{-1.1}$	$1.7^{+0.4}_{-0.3}$	1.41 ± 0.02	$0.155^{+0.007}_{-0.008}$	48.2 ± 1.3	2.3 ± 0.06	1.4 ± 0.1	0.013 ± 0.001
NGC 4342	512	13071	0.2 ± 0.01	677 ± 68	1.01 ± 0.03	0.18 ± 0.04	$59.5^{+4.8}_{-4.3}$	0.11 ± 0.01	1 ± 0.1	0.032 ± 0.001
NGC 4374	512	212811	0.26 ± 0.02	3790^{+420}_{-350}	0.774 ± 0.004	0	92.1 ± 1	3.3 ± 0.1	3.4 ± 0.3	$0.354^{+0.004}_{-0.005}$
NGC 4382	512	7780	0.14 ± 0.02	$26.5^{+3}_{-3.8}$	0.5 ± 0.01	0.07 ± 0.04	0	0	0	0.006 ± 0.001
NGC 4406	512	514275	$4.1^{+0.3}_{-0.2}$	$35.9^{+1.9}_{-1.7}$	0.76 ± 0.04	0.315 ± 0.003	135 ± 7.1	$3.8^{+0.2}_{-0.1}$	1.8 ± 0.1	1 ± 0.02
NGC 4472	640	734419	8.6 ± 0.1	$175.8^{+1.9}_{-1.8}$	0.944 ± 0.007	0	331^{+21}_{-20}	$1.42^{+0.04}_{-0.03}$	$1.17^{+0.09}_{-0.08}$	0.11 ± 0.01
NGC 4477	512	19800	1.0 ± 0.1	$30.6^{+5.1}_{-4.6}$	$1.14^{+0.07}_{-0.06}$	0.14 ± 0.03	$33.3^{+2.3}_{-2.2}$	0.51 ± 0.03	1.1 ± 0.1	0.052 ± 0.001
NGC 4486	640	3605386	$0.4^{+0.02}_{-0.03}$	1247^{+96}_{-83}	0.731 ± 0.004	0.168 ± 0.001	40.1 ± 0.3	62.4 ± 0.3	0.73 ± 0.07	2.14 ± 0.03
NGC 4526	512	4955	1.1 ± 0.1	$39^{+6.2}_{-4.9}$	1.7 ± 0.1	0.22 ± 0.03	20.1 ± 1.7	0.78 ± 0.06	1.7 ± 0.2	0.013 ± 0.001
NGC 4552	512	61952	3.4 ± 0.1	66.2 ± 3.2	1.62 ± 0.02	0	22.6 ± 0.5	14 ± 0.3	1.6 ± 0.2	0.089 ± 0.001
NGC 4555	512	4958	1.8 ± 0.2	$16.6^{+2}_{-1.7}$	0.98 ± 0.02	$0.05^{+0.04}_{-0.03}$	0	0	0	0.012 ± 0.001
NGC 4636	640	299549	71.2 ± 0.4	21 ± 0.2	10 ± 1	0	393.2 ± 1.2	3.19 ± 0.02	10 ± 1	0.222 ± 0.001
NGC 4649	512	281760	9.21 ± 0.08	152.5 ± 1.4	1.033 ± 0.003	0.056 ± 0.003	0	0	0	0.123 ± 0.003
NGC 4696	768	6853500	$13.1^{+0.07}_{-0.08}$	278.8 ± 1.3	0.58 ± 0.06	0.132 ± 0.001	153.3 ± 0.6	42.3 ± 0.2	10 ± 1	0.12 ± 0.01
NGC 4778	512	148213	11.5 ± 0.4	18.6 ± 0.4	$0.83^{+0.02}_{-0.01}$	0.043 ± 0.005	$242.9^{+3.2}_{-2.9}$	1.75 ± 0.05	10 ± 1	$0.088^{+0.007}_{-0.006}$
NGC 4936	512	4330	$0.16^{+0.04}_{-0.03}$	$34^{+11.4}_{-7.3}$	0.61 ± 0.02	0.15 ± 0.05	0	0	0	0.008 ± 0.001
NGC 5044	512	1314389	14.4 ± 0.5	31.4 ± 0.7	0.81 ± 0.01	0	146.1 ± 0.5	13.17 ± 0.06	1.3 ± 0.1	0.096 ± 0.01
NGC 5129	512	33361	1.06 ± 0.08	$80^{+7.5}_{-6.5}$	0.87 ± 0.02	0	240^{+33}_{-29}	$0.136^{+0.011}_{-0.008}$	0.86 ± 0.09	$0.01^{+0.01}_{-0.02}$
NGC 5171	512	6678	$3.1^{+0.8}_{-0.7}$	$1^{+0.3}_{-0.2}$	$0.8^{+0.07}_{-0.06}$	$0.22^{+0.08}_{-0.09}$	0	0	0	0.023 ± 0.001
NGC 5813	512	953760	$35.5^{+1.6}_{-1.5}$	47.3 ± 0.6	2.9 ± 0.2	0.131 ± 0.002	$415.9^{+1.1}_{-1}$	$10.88^{+0.05}_{-0.06}$	10 ± 1	0.852 ± 0.006
NGC 5846	512	88165	11.6 ± 0.4	8.9 ± 0.2	0.665 ± 0.008	$0.209^{+0.007}_{-0.006}$	0	0	0	0.01 ± 0.005
NGC 6107	512	5168	$1.6^{+0.2}_{-0.3}$	3.3 ± 0.5	0.62 ± 0.02	$0.06^{+0.05}_{-0.04}$	0	0	0	0.007 ± 0.001
NGC 6166	512	954398	$18.8^{+1}_{-0.8}$	$26.9^{+0.5}_{-0.6}$	$1.12^{+0.06}_{-0.05}$	0	334^{+13}_{-15}	6.5 ± 0.1	$4.4^{+0.3}_{-0.4}$	1.03 ± 0.02
NGC 6338	512	33798	3.7 ± 0.3	$15.6^{+1.5}_{-1.4}$	$1.58^{+0.06}_{-0.05}$	0.18 ± 0.01	$29.1^{+1.3}_{-1.2}$	3.7 ± 0.1	1.6 ± 0.2	0.064 ± 0.001
NGC 6482	512	9424	4.4 ± 0.3	$9.7^{+0.7}_{-0.6}$	0.87 ± 0.01	$0.02^{+0.02}_{-0.01}$	0	0	0	0.002 ± 0.001
NGC 6868	640	20924	$0.066^{+0.008}_{-0.007}$	1720^{+300}_{-250}	$0.748^{+0.008}_{-0.007}$	0.16 ± 0.03	0	0	0	0.034 ± 0.001
NGC 7618	512	34814	$2.8^{+0.3}_{-0.2}$	$33.4^{+3.3}_{-3.1}$	$1.35^{+0.06}_{-0.05}$	0.06 ± 0.01	$48.7^{+2.4}_{-2.2}$	1.32 ± 0.04	1.4 ± 0.1	0.047 ± 0.002
NGC 7619	640	22579	2.6 ± 0.1	21.5 ± 1.4	0.793 ± 0.008	0.11 ± 0.02	0	0	0	0.02 ± 0.001
NGC 7796	512	12166	1.12 ± 0.1	24.1 ± 2.6	0.76 ± 0.01	0	0	0	0	0.026 ± 0.001

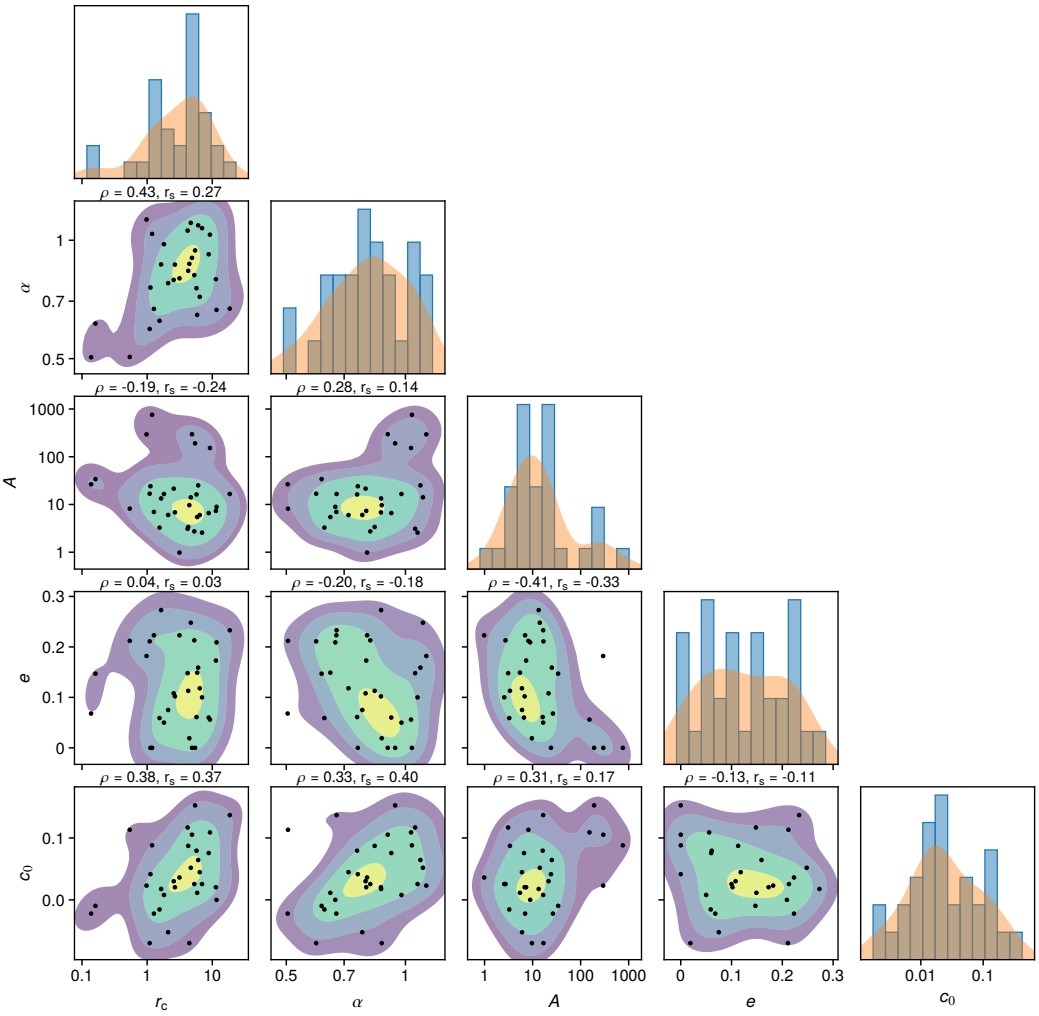

Figure A.2.4: Corner plot showing distributions of β-model parameters of galaxies fitted by single β-model: core radius r_c, alpha parameter α, amplitude A, ellipticity e and level of background c_0. Contours in parameter pair plots correspond to 90 %, 75 %, 50 % and 10 % intervals in terms of cumulative probability of Gaussian KDE. Pearson and Spearman correlation coefficients are stated above individual plots of parameter pairs.

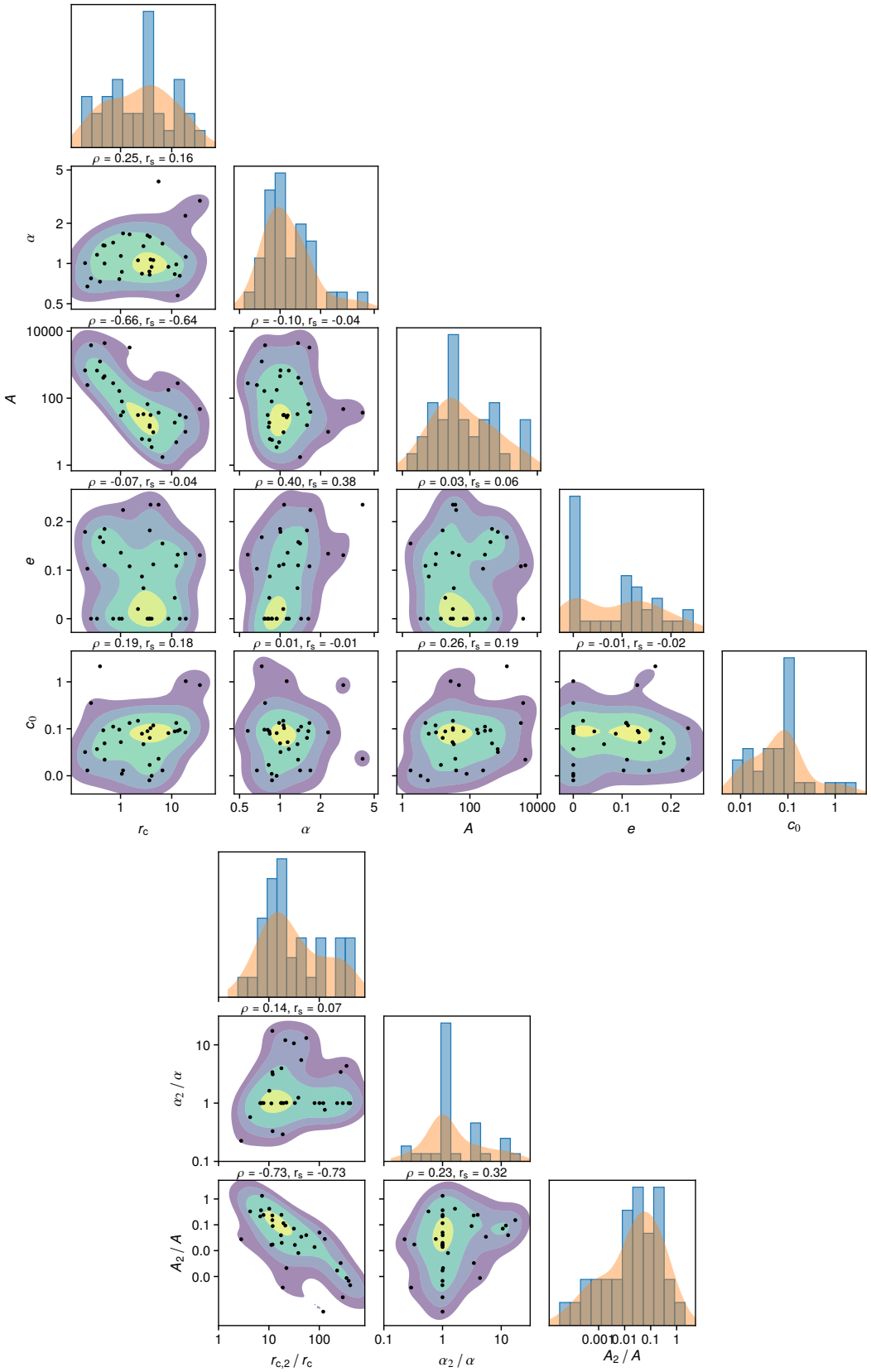

Figure A.2.5: Upper: corner plot showing distributions of the first β-component parameters for galaxies fitted by double β-model: core radius r_c, alpha parameter α, amplitude A, ellipticity e and level of background c_0. Lower: corner plot showing distributions of ratios of core radii $r_{c,2}/r_c$, alpha parameters α_2/α and amplitudes A_2/A between the second and the first β-component. Contours in parameter pair plots correspond to 90 %, 75 %, 50 % and 10 % intervals in terms of cumulative probability of Gaussian KDE. Pearson and Spearman correlation coefficients are stated above individual plots of parameter pairs.

Table A.2.3: Parameters of visually estimated X-ray cavities.

Galaxy	Cav.	$a('')$	$b('')$	$d('')$	$\phi(^\circ)$	$\varphi(^\circ)$
3C 449	S1	32.0	24.1	91.5	280.0	77.0
	N1	32.5	24.8	110	88.4	259.2
IC 1262	SE1	14.9	8.15	17.1	232.2	97.1
	N1	20.5	15.3	27.2	94.3	263.1
NGC 193	W1	59.3	40.2	17.0	338.8	3.7
	E1	36.8	30.8	79.0	172.1	79.9
NGC 507	NW1	2.04	1.92	3.75	48.2	6.1
	SE1	2.66	1.72	3.63	245.1	6.2
	N2	15.4	9.05	18.3	104.4	64.6
	W2	14.5	8.34	19.2	340.8	62.9
NGC 533	NE1	2.00	1.56	1.97	138.7	172.4
	SW1	2.80	2.09	3.56	336.4	333.1
NGC 708	NE1	3.05	2.37	7.04	144.7	176.9
	W1	2.25	2.25	4.43	337.8	337.8
NGC 741	SW1	7.16	3.19	9.29	300.7	44.2
	NW1	4.13	2.38	8.71	44.4	270.9
	E2	23.1	16.7	38.1	169.6	180.9
	SW2	33.3	24.4	69.5	333.4	2.5
NGC 777	SW1	4.24	3.05	5.19	292.6	274.5
	E1	4.73	3.51	6.26	159.8	126.0
NGC 1132	W1	4.67	3.95	13.5	10.2	12.5
	SE1	4.57	3.27	9.15	244.9	179.2
NGC 1275	SW1	19.9	17.3	26.4	298.8	288.6
	N1	17.5	13.9	17.0	95.5	42.0
	NW2	38.8	20.5	74.7	33.2	8.6
	S2	37.5	29.3	95.7	261.6	96.3
NGC 1316	SE1	5.86	4.99	6.66	223.8	196.3
	NW1	5.61	4.24	6.78	44.6	40.7
NGC 1399	N1	4.5	2.25	6.06	81.0	3.8
	S1	4.58	2.42	6.30	264.9	1.9
	N2	33.5	11.8	71.0	86.2	5.0
	S2	37.8	12.7	77.2	262.1	0.6
NGC 1404	E1	4.21	2.94	5.37	163.3	187.1
	W1	3.13	1.67	3.21	341.9	327.7
NGC 1550	NW1	14.6	11.3	18.4	60.0	289.2
	S1	13.8	11.5	30.1	273.2	67.7
NGC 1553	NE1	21.2	16.2	25.7	126.2	177.9
	SW1	21.4	14.4	24.9	310.4	10.0
NGC 1600	N1	3.67	2.23	2.72	68.2	185.0
	S1	3.01	2.23	3.99	286.3	35.4
NGC 3402	SW1	5.72	3.28	13.5	325.0	12.3
	NE1	6.76	4.45	15.7	124.6	122.0
NGC 4104	W1	1.96	1.86	1.13	346.1	6.3
NGC 4261	W1	30.4	25.3	50.2	11.8	1.2
	E1	33.1	23.1	47.5	186.0	177.7
NGC 4325	W1	13	8.78	15.7	354.9	34.1
	SE1	15.7	12.7	17.0	205.8	205.8
NGC 4374	NE1	21.3	17.4	24.7	124.8	182.3
	S1	30.4	22	59	279.5	31.3
NGC 4472	N1	5.47	2.59	7.72	110.6	105.6
	W1	4.43	2.51	8.11	342.4	3.2
	NW1	29.5	14.3	43.7	25.8	9.6
	E1	28.3	15	47.3	158.9	148.9
NGC 4477	SE1	10.9	9.37	13.4	210.4	168.8
	NW1	9.15	6.76	10.6	25.3	15.4
NGC 4486	E1	14.7	12.3	16.6	196.9	180.1
	W1	14.8	11.7	20.3	12.7	4.8
NGC 4552	N1	7.95	4.85	7.43	93.1	10.7
	SW1	9.13	4.85	6.47	296.7	202.5
NGC 4636	E1	2.78	1.69	2.11	190.3	179.9
	NW1	3.56	1.8	5.49	43.3	2.1
	NE2	9.55	7.38	15	116.3	25.9
	SW2	9.49	7.08	17.1	321.7	180.5
	E3	27.3	18.5	40.3	197.7	189.2
	W3	27.9	20.1	56.5	10.8	228.4
	NE4	38.1	23	90.7	155.5	200.4
	SW4	39.8	23.2	87.2	331.6	9.4
NGC 4649	N1	6.01	4.67	12.5	98.9	92.3
	S1	6.45	5.03	12.7	287.3	281.5
NGC 4696	SE1	9.82	6.16	10.1	228.8	225.5
	W1	11.3	6.31	18.2	350.9	336.1
NGC 4778	N1	2.33	1.39	7.19	79.2	248.5
	SE1	2.16	1.1	4.39	230.4	90.8
	S2	13	9.63	19.6	287.8	183.5
	NE2	18.6	11.9	35.2	127.2	219.3
NGC 5044	NE1	9.73	3.58	20	123.7	28.8
	SW1	9.74	4.95	19.1	320.6	18.7
	S2	20.8	15.9	27.2	248.2	138.0
	NW2	18.6	15.7	25.9	53.7	1.3
	E3	35.9	19.5	46.5	179.0	167.4
	W3	23	18.4	55.3	346.7	1.1
NGC 5813	N1	5.79	3.99	7.38	98.8	19.9
	SW1	5.78	4.42	7.1	307.0	183.8
	NE2	15.8	10.9	29.7	127.1	20.6
	SW2	25.9	25	44.8	321.5	173.8
	NE3	50.7	21.4	121	133.0	17.3
	SW3	47.4	22.1	154	310.2	197.8
NGC 5846	NE1	6.35	3.73	5.38	137.8	7.7
	SW1	5.28	3.74	7.53	304.5	181.2
	SE2	20.0	14.8	47.2	213.6	130.1
	W2	17.8	16.1	39.4	352.6	226.8
NGC 6166	W1	3.55	2.0	4.6	10.2	3.5
	NE1	3.13	2.18	4.81	125.5	0.1
	E2	20.5	13.2	33.9	181.5	163.8
	W2	17.2	14	38.3	357.9	162.3
NGC 6338	SW1	8.25	7.57	11.5	319.8	259.0
	NE1	12.8	7.35	12.9	156.9	195.7

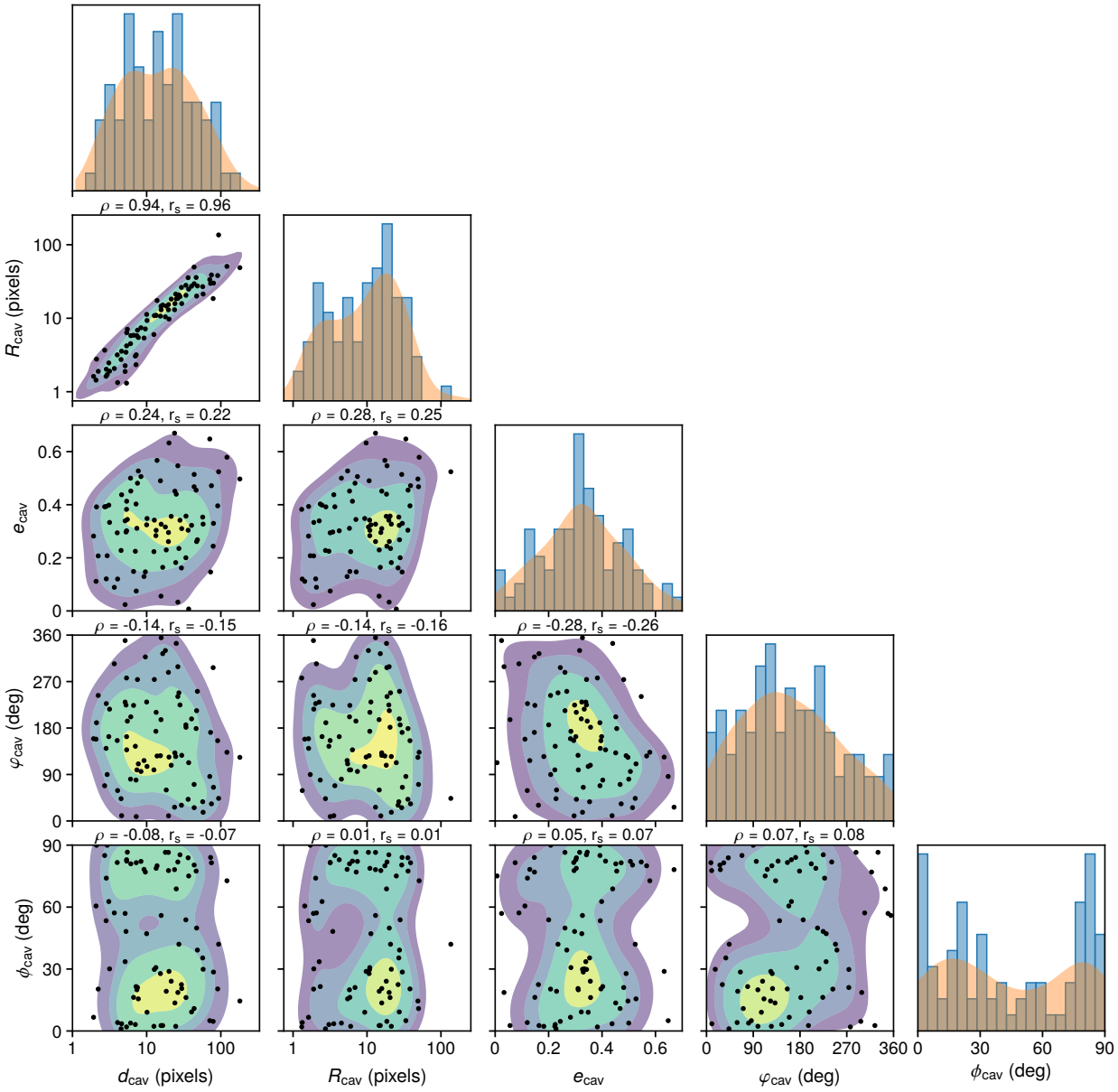

Figure A.2.6: Corner plot showing distributions and correlations between primary cavity parameters: distance from the centre of the galaxy $d_{\rm cav}$, semi-major axis $R_{\rm cav}$, ellipticity $e_{\rm cav}$ and rotational angle $\phi_{\rm cav}$ (angle between semi-major axis and the direction towards the centre of galaxy). Contours in parameter pair plots correspond to 90 %, 75 %, 50 % and 10 % intervals in terms of cumulative probability of Gaussian KDE. Pearson and Spearman correlation coefficients are stated above individual plots of parameter pairs.

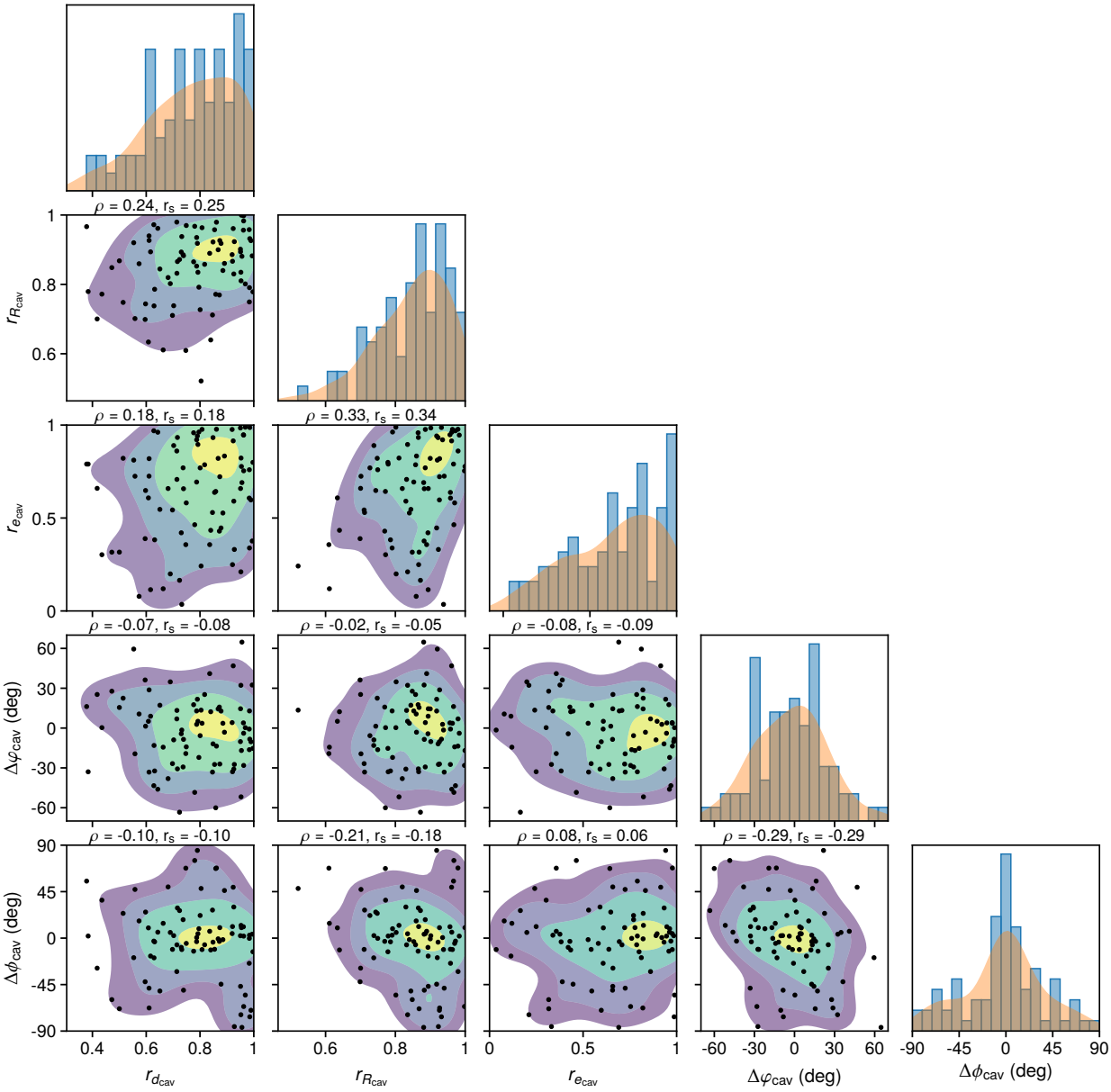

Figure A.2.7: Corner plot showing distributions and correlations of secondary cavity parameters (ratios and differences between individual cavity parameters within a cavity pair): relative distance r_d, relative semi-major axis r_R, difference between ellipticity $r_{e_{\mathrm{cav}}}$, difference between positional angles $d\phi$ and difference between rotational angles $d\varphi$. Contours in parameter pair plots correspond to 90 %, 75 %, 50 % and 10 % intervals in terms of cumulative probability of Gaussian KDE. Pearson and Spearman correlation coefficients are stated above individual plots of parameter pairs.

A.2.5 Exemplary mock images

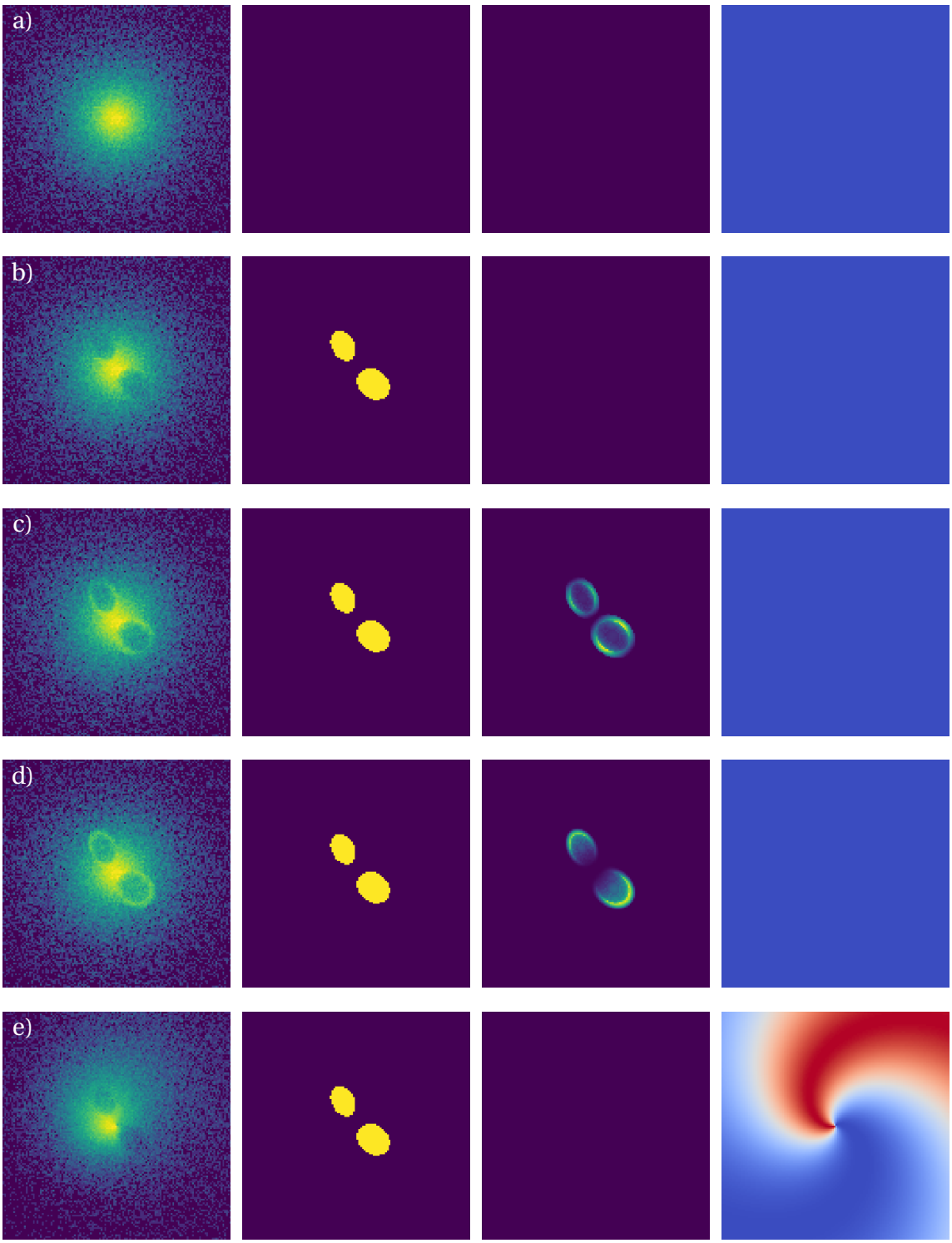

Figure A.2.8: Examples of artificially generated images with various features: **a)** single beta model without cavities, **b)** beta model with cavities, **c)** beta model with cavities and type I rims, **d)** beta model with cavities and type II rims, **e)** beta model with cavities and gas sloshing. Individual columns show: 1) the resulting noisy image, 2) binary cavity mask, 3) cavity rim pattern, and 4) sloshing pattern.

A.2.6 CADET architecture

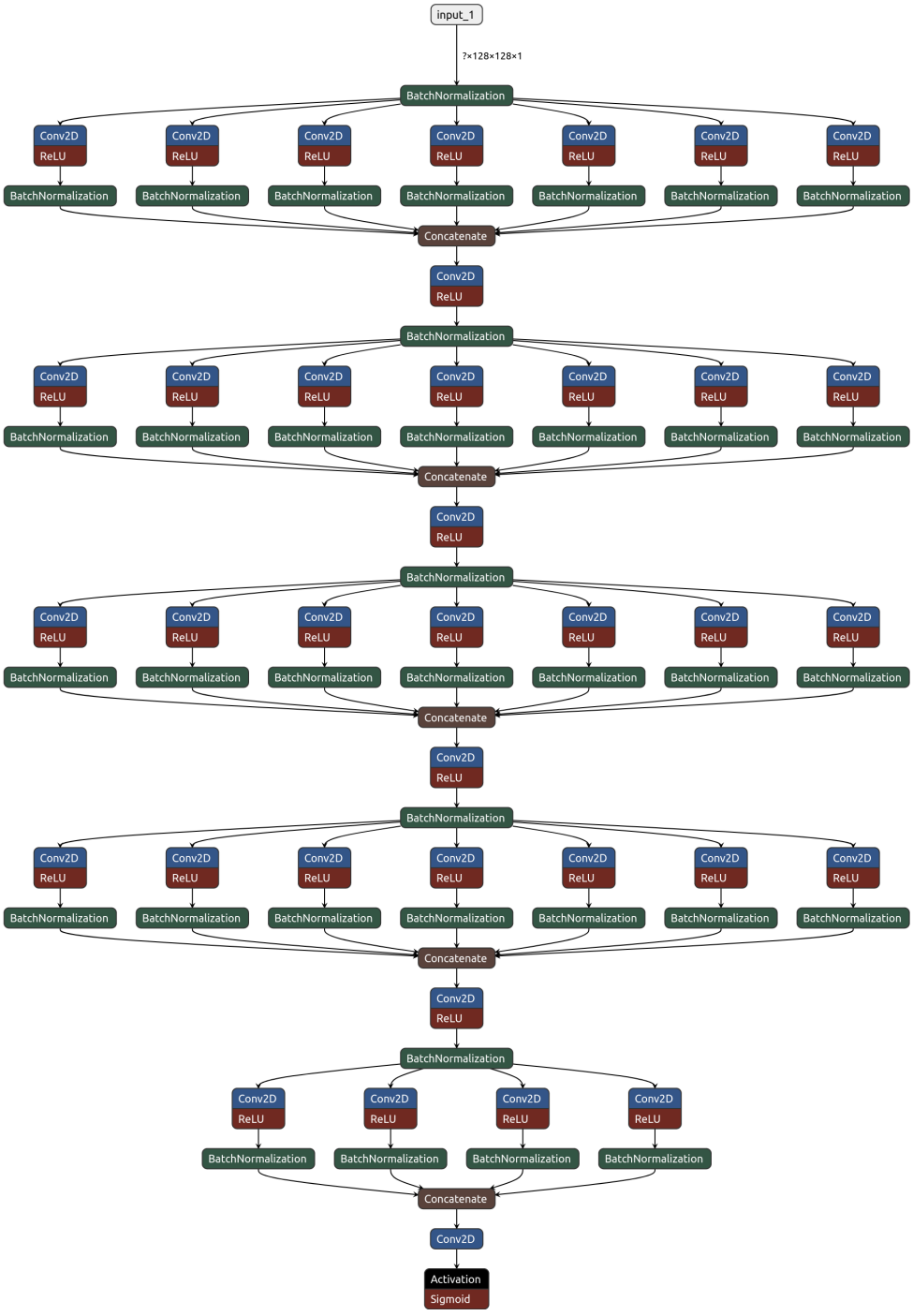

Figure A.2.9: The schematic picture of the convolutional neural network composed of 5 Inception-like blocks. Each block consists of a series of parallel convolutional layers each composed of various numbers of convolutional filters with various sizes. The output of all parallel convolutional layers is then concatenated into a single output, followed by a convolutional layer with 32 of 1×1 filters and a dropout layer, which was for simplicity omitted. The scheme was created using the Netron visualisation tool.

A.2.7 *Chandra* OBSIDs

Table A.2.4: Listed *Chandra* observations (OBSIDs) for individual sources.

Galaxy	OBSID	Instrument	Date	Exptime (ks)
3C 449	4057	ACIS-S	2003-09-18	24.98
	11737	ACIS-S	2010-09-14	52.34
	13123	ACIS-S	2010-09-20	59.92
IC 1262	2018	ACIS-S	2001-08-23	30.47
	6949	ACIS-I	2006-04-17	38.6
	7321	ACIS-I	2006-04-19	37.55
	7322	ACIS-I	2006-04-22	37.54
IC 1459	2196	ACIS-S	2001-08-12	55.21
IC 1860	10537	ACIS-S	2009-09-12	37.28
IC 4296	3394	ACIS-S	2001-12-15	24.84
IC 4765	15637	ACIS-S	2013-03-29	14.87
NGC 57	10547	ACIS-S	2008-10-29	9.78
NGC 193	4053	ACIS-S	2003-09-01	23.25
	11389	ACIS-S	2009-08-21	93.92
NGC 315	4156	ACIS-S	2003-02-22	54.75
NGC 383	2147	ACIS-S	2000-11-06	43.6
NGC 499	10536	ACIS-S	2009-02-12	18.4
	10865	ACIS-S	2009-02-04	5.12
	10866	ACIS-S	2009-02-05	8.04
	10867	ACIS-S	2009-02-07	7.06
NGC 507	317	ACIS-S	2000-10-11	17.67
	2882	ACIS-I	2002-01-08	43.36
NGC 533	2880	ACIS-S	2002-07-28	36.74
NGC 708	2215	ACIS-S	2001-08-03	28.75
	7921	ACIS-S	2006-11-20	110.68
NGC 720	492	ACIS-S	2000-10-12	23.24
	7062	ACIS-S	2006-10-09	22.86
	7372	ACIS-S	2006-08-06	49.25
	8448	ACIS-S	2006-10-12	8.06
	8449	ACIS-S	2006-10-12	18.91
NGC 741	2223	ACIS-S	2001-01-28	29.93
	17198	ACIS-S	2015-12-04	91.42
	18718	ACIS-S	2015-12-06	55.9
NGC 777	5001	ACIS-I	2004-12-23	10.04
NGC 1132	801	ACIS-S	1999-12-10	12.9
	3576	ACIS-S	2003-11-16	32.35
NGC 1275	4946	ACIS-S	2004-10-06	23.66
	4947	ACIS-S	2004-10-11	29.79
	4948	ACIS-S	2004-10-09	118.16
	4949	ACIS-S	2004-10-12	29.38
	4950	ACIS-S	2004-10-12	82.91
	4951	ACIS-S	2004-10-17	95.97
	4952	ACIS-S	2004-10-14	163.15
	4953	ACIS-S	2004-10-18	30.08
	6139	ACIS-S	2004-10-04	56.01
	6145	ACIS-S	2004-10-19	84.59
	6146	ACIS-S	2004-10-20	46.99
	11713	ACIS-S	2009-11-29	112.25
	11714	ACIS-S	2009-12-07	91.99
	11715	ACIS-S	2009-12-02	73.36
	11716	ACIS-S	2009-10-10	39.64
	12025	ACIS-I	2009-11-25	17.94
	12033	ACIS-I	2009-11-27	18.89
	12036	ACIS-I	2009-12-02	47.93
	12037	ACIS-I	2009-12-05	84.37
NGC 1316	2022	ACIS-S	2001-04-17	28.2
	20340	ACIS-S	2019-04-16	44.95
	20341	ACIS-S	2019-04-22	51.39
	22179	ACIS-S	2019-04-17	38.95
	22180	ACIS-S	2019-04-20	13.57
	22187	ACIS-S	2019-04-25	53.18
NGC 1380	9526	ACIS-S	2008-03-26	40.68
NGC 1387	4168	ACIS-I	2003-05-20	45.63
NGC 1399	319	ACIS-S	2000-01-18	56.03
	9530	ACIS-S	2008-06-08	59.35
	14527	ACIS-S	2013-07-01	27.8
NGC 1399	14529	ACIS-S	2015-11-06	31.48
	16639	ACIS-S	2014-10-12	29.67
NGC 1404	2942	ACIS-S	2003-02-13	29.23
	4174	ACIS-I	2003-05-28	45.0
	9798	ACIS-S	2007-12-24	18.3
	9799	ACIS-S	2007-12-27	21.29
	16231	ACIS-S	2014-10-20	60.5
	16232	ACIS-S	2014-11-12	69.01
	16233	ACIS-S	2014-11-09	98.76
	17540	ACIS-S	2014-11-02	28.47
	17541	ACIS-S	2014-10-23	24.74
	17548	ACIS-S	2014-11-11	48.22
	17549	ACIS-S	2015-03-28	61.66
NGC 1407	791	ACIS-S	2000-08-16	45.19
NGC 1521	10539	ACIS-S	2009-07-04	49.41
NGC 1550	3186	ACIS-I	2002-01-08	9.99
	3187	ACIS-I	2002-01-08	9.65
	5800	ACIS-S	2005-10-22	44.55
	5801	ACIS-S	2005-10-24	44.45
NGC 1553	783	ACIS-S	2000-01-02	17.6
NGC 1600	4283	ACIS-S	2002-09-18	22.87
	4371	ACIS-S	2002-09-20	26.75
	21374	ACIS-S	2018-12-03	25.72
	21375	ACIS-S	2019-11-28	42.21
	21998	ACIS-S	2018-12-03	13.88
	22878	ACIS-S	2019-11-25	44.97
	22911	ACIS-S	2019-11-01	31.01
	22912	ACIS-S	2019-11-02	35.64
NGC 1700	2069	ACIS-S	2000-11-03	32.92
NGC 2300	4968	ACIS-S	2004-06-23	45.57
	15648	ACIS-S	2013-05-24	20.81
	21383	ACIS-S	2020-06-14	46.44
	23033	ACIS-S	2020-06-01	45.38
	23034	ACIS-S	2019-12-04	45.37
NGC 2305	10549	ACIS-S	2009-07-19	9.92
NGC 2563	7925	ACIS-I	2007-09-18	48.11
NGC 3091	3215	ACIS-S	2002-03-26	31.55
NGC 3402	3243	ACIS-S	2002-11-05	28.57
NGC 3923	1563	ACIS-S	2001-06-14	18.13
	9507	ACIS-S	2008-04-11	81.0
NGC 4073	3234	ACIS-S	2002-11-24	29.96
NGC 4104	6939	ACIS-S	2006-02-16	35.88
NGC 4125	2071	ACIS-S	2001-09-09	63.69
NGC 4261	834	ACIS-S	2000-05-06	32.93
	9569	ACIS-S	2008-02-12	100.94
NGC 4291	11778	ACIS-S	2010-12-11	29.78
NGC 4325	3232	ACIS-S	2003-02-04	29.68
NGC 4342	4687	ACIS-S	2005-02-11	37.72
	12955	ACIS-S	2011-02-17	71.59
NGC 4374	20539	ACIS-S	2019-04-05	39.22
	20540	ACIS-S	2019-02-26	30.17
	20541	ACIS-S	2019-04-10	11.29
	20542	ACIS-S	2019-03-18	34.61
	20543	ACIS-S	2019-04-27	54.35
	21845	ACIS-S	2019-03-28	27.7
	21852	ACIS-S	2019-02-18	15.61
	21867	ACIS-S	2019-03-13	23.63
	22113	ACIS-S	2019-02-20	21.82
	22126	ACIS-S	2019-02-28	35.1
	22127	ACIS-S	2019-03-02	22.71
	22128	ACIS-S	2019-03-03	23.75
	22142	ACIS-S	2019-03-14	20.77
	22143	ACIS-S	2019-03-16	22.75
	22144	ACIS-S	2019-03-15	31.72
	22153	ACIS-S	2019-03-23	21.08

Table A.2.3: Continued.

Galaxy	OBSID	Instrument	Date	Exptime (ks)
NGC 4374	22163	ACIS-S	2019-03-29	35.6
	22164	ACIS-S	2019-03-31	32.64
	22166	ACIS-S	2019-04-06	38.56
	22174	ACIS-S	2019-04-11	49.41
	22175	ACIS-S	2019-04-12	27.2
	22176	ACIS-S	2019-04-13	51.39
	22177	ACIS-S	2019-04-14	36.58
	22195	ACIS-S	2019-04-28	38.07
	22196	ACIS-S	2019-05-07	20.3
NGC 4382	2016	ACIS-S	2001-05-29	39.61
	16968	ACIS-I	2015-04-04	19.83
	19331	ACIS-S	2017-02-20	22.33
	20012	ACIS-S	2017-02-22	26.06
	20013	ACIS-S	2017-02-23	31.69
	20014	ACIS-S	2017-02-24	51.93
NGC 4406	318	ACIS-S	2000-04-07	11.65
	16967	ACIS-I	2016-05-02	19.81
NGC 4472	321	ACIS-S	2000-06-12	34.58
	11274	ACIS-S	2010-02-27	39.67
	12888	ACIS-S	2011-02-21	159.31
	12889	ACIS-S	2011-02-14	134.64
	16260	ACIS-S	2014-08-04	24.74
	16261	ACIS-S	2015-02-24	22.76
	16262	ACIS-S	2016-04-30	24.73
	21647	ACIS-S	2019-04-17	29.68
NGC 4477	9527	ACIS-S	2008-04-27	37.68
NGC 4486	352	ACIS-S	2000-07-29	35.38
	2707	ACIS-S	2002-07-06	88.65
NGC 4486	352	ACIS-S	2000-07-29	37.7
	2707	ACIS-S	2002-07-06	98.7
	18232	ACIS-S	2016-04-27	18.2
	18233	ACIS-S	2016-02-23	37.2
	18781	ACIS-S	2016-02-24	39.5
	18782	ACIS-S	2016-02-26	34.1
	18783	ACIS-S	2016-04-20	36.1
	18836	ACIS-S	2016-04-28	38.9
	18837	ACIS-S	2016-04-30	13.7
	18838	ACIS-S	2016-05-28	56.3
	18856	ACIS-S	2016-06-12	25.5
	20034	ACIS-S	2017-04-11	13.1
	20035	ACIS-S	2017-04-14	13.1
	21457	ACIS-S	2019-03-27	14.1
	21458	ACIS-S	2019-03-28	12.8
NGC 4526	3925	ACIS-S	2003-11-14	41.36
NGC 4552	2072	ACIS-S	2001-04-22	54.28
	13985	ACIS-S	2012-04-22	49.41
	14358	ACIS-S	2012-08-10	49.41
	14359	ACIS-S	2012-04-23	48.14
NGC 4555	2884	ACIS-S	2003-02-04	29.56
NGC 4636	323	ACIS-S	2000-01-26	46.43
	3926	ACIS-I	2003-02-14	74.7
	4415	ACIS-I	2003-02-15	74.37
NGC 4649	785	ACIS-S	2000-04-20	25.92
	8182	ACIS-S	2007-01-30	49.77
	8507	ACIS-S	2007-02-01	17.39
	12975	ACIS-S	2011-08-08	84.79
	12976	ACIS-S	2011-02-24	101.04
	14328	ACIS-S	2011-08-12	13.93
NGC 4696	504	ACIS-S	2000-05-22	31.62
	505	ACIS-S	2000-06-08	9.96
	4954	ACIS-S	2004-04-01	88.29
	4955	ACIS-S	2004-04-02	44.68
	5310	ACIS-S	2004-04-04	49.33
	16223	ACIS-S	2014-05-26	178.97
	16224	ACIS-S	2014-04-09	42.29
	16225	ACIS-S	2014-04-26	30.1
NGC 4696	16534	ACIS-S	2014-06-05	55.44
	16607	ACIS-S	2014-04-12	45.65
	16608	ACIS-S	2014-04-07	34.11
	16609	ACIS-S	2014-05-04	82.33
	16610	ACIS-S	2014-04-27	17.34
NGC 4778	921	ACIS-S	2000-01-25	48.4
	10462	ACIS-S	2009-03-02	67.15
	10874	ACIS-S	2009-03-03	51.36
NGC 4936	4997	ACIS-I	2004-02-09	13.97
	4998	ACIS-I	2004-02-15	14.95
NGC 5044	798	ACIS-S	2000-03-19	20.47
	9399	ACIS-S	2008-03-07	82.68
	17195	ACIS-S	2015-06-06	78.03
	17196	ACIS-S	2015-05-11	88.87
	17653	ACIS-S	2015-05-07	35.52
	17654	ACIS-S	2015-05-10	25.05
	17666	ACIS-S	2015-08-23	88.55
NGC 5129	6944	ACIS-S	2006-04-13	20.91
	7325	ACIS-S	2006-05-14	25.84
NGC 5171	3216	ACIS-S	2002-12-10	34.68
NGC 5813	5907	ACIS-S	2005-04-02	48.4
	9517	ACIS-S	2008-06-05	98.76
	12951	ACIS-S	2011-03-28	74.0
	12952	ACIS-S	2011-04-05	143.07
	12953	ACIS-S	2011-04-07	31.76
	13246	ACIS-S	2011-03-30	45.02
	13247	ACIS-S	2011-03-31	35.76
	13253	ACIS-S	2011-04-08	118.02
	13255	ACIS-S	2011-04-10	43.41
NGC 5846	788	ACIS-S	2000-05-24	23.88
	7923	ACIS-I	2007-06-12	90.03
NGC 6107	8180	ACIS-S	2007-09-29	19.8
NGC 6166	497	ACIS-S	2000-05-13	18.66
	498	ACIS-S	1999-12-11	17.16
	10748	ACIS-I	2009-11-19	40.58
	10803	ACIS-I	2009-11-17	30.16
	10804	ACIS-I	2009-06-23	18.79
	10805	ACIS-I	2009-11-23	30.29
NGC 6338	4194	ACIS-I	2003-09-17	46.65
	18892	ACIS-S	2017-06-24	11.88
	18893	ACIS-S	2017-07-21	44.58
	19934	ACIS-S	2017-07-12	28.67
	19935	ACIS-S	2017-06-05	35.09
	19937	ACIS-S	2017-06-08	19.79
	20089	ACIS-S	2017-06-11	18.53
	20104	ACIS-S	2017-06-21	14.86
NGC 6338	20112	ACIS-S	2017-07-13	41.5
	20113	ACIS-S	2017-07-15	25.02
	20117	ACIS-S	2017-07-23	12.75
NGC 6482	3218	ACIS-S	2002-05-20	18.52
	19584	ACIS-S	2017-11-14	27.61
	19585	ACIS-S	2018-02-22	19.7
	20850	ACIS-S	2017-11-24	19.7
	20857	ACIS-S	2017-11-26	22.96
	20978	ACIS-S	2018-02-22	19.89
	20979	ACIS-S	2018-02-23	9.82
	20980	ACIS-S	2018-05-29	75.64
NGC 6868	3191	ACIS-I	2002-11-01	23.46
	11753	ACIS-I	2009-08-19	72.59
NGC 7618	802	ACIS-S	1999-12-10	11.4
	7895	ACIS-S	2007-09-08	34.06
NGC 7619	2074	ACIS-I	2001-08-20	26.6
	3955	ACIS-S	2003-09-24	31.84
NGC 7796	7061	ACIS-S	2006-08-28	53.07
	7401	ACIS-S	2006-09-03	19.95

A.3 Chemical enrichment in M89

A.3.1 Abundance measurement comparison of different temperature models

We present the abundance and α/Fe ratios from Table 3.2 for comparison. In Figure A.3.1, the abundance and ratios measured with 1T `vapec`, 1T 2×`vapec` and `vgadem` temperature models from ACIS-S, EPIC and RGS data are presented. Moreover, similar comparison plots of the Core and Tail regions derived with different temperature models are presented in Figure A.3.2. In this plot, the derived values are from ACIS-S data.

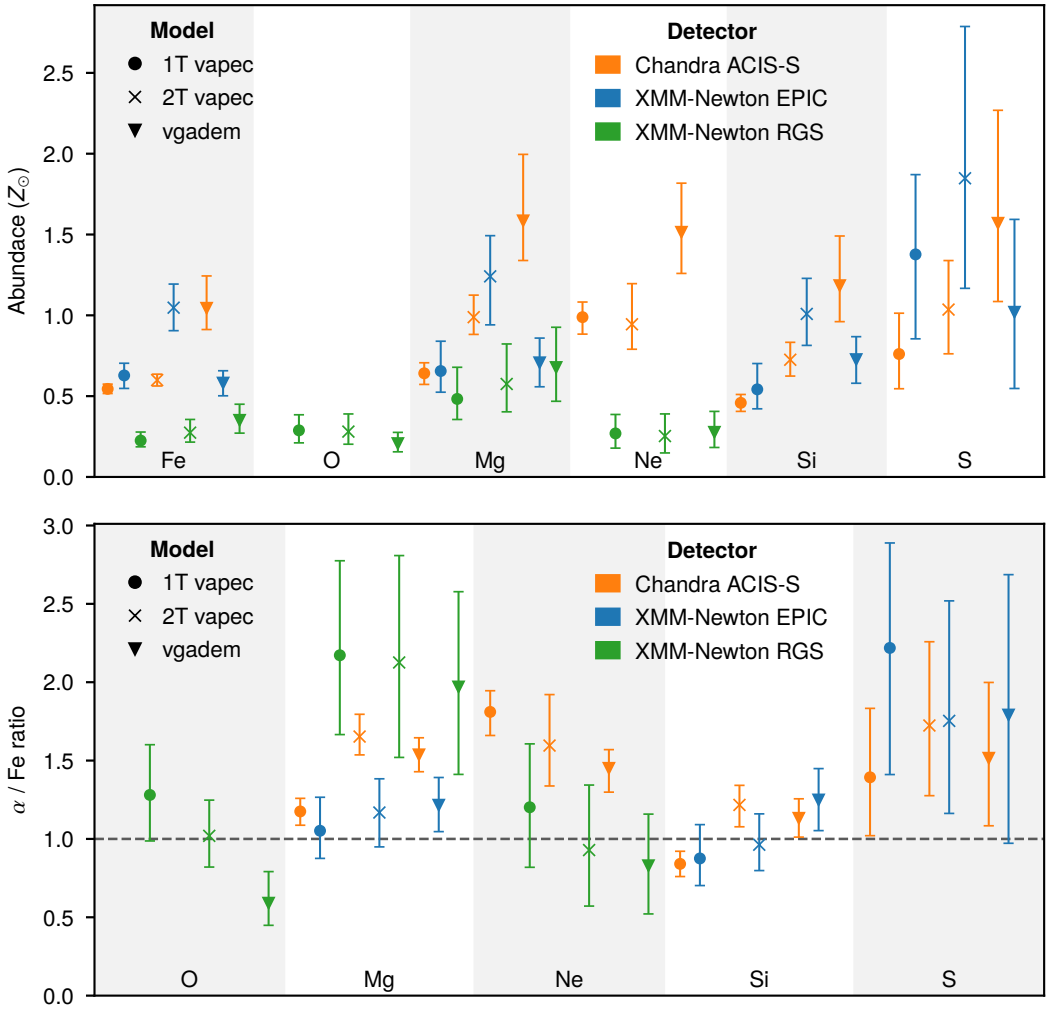

Figure A.3.1: Abundance and ratio measurements with different temperature models using ACIS-S, EPIC and RGS data.

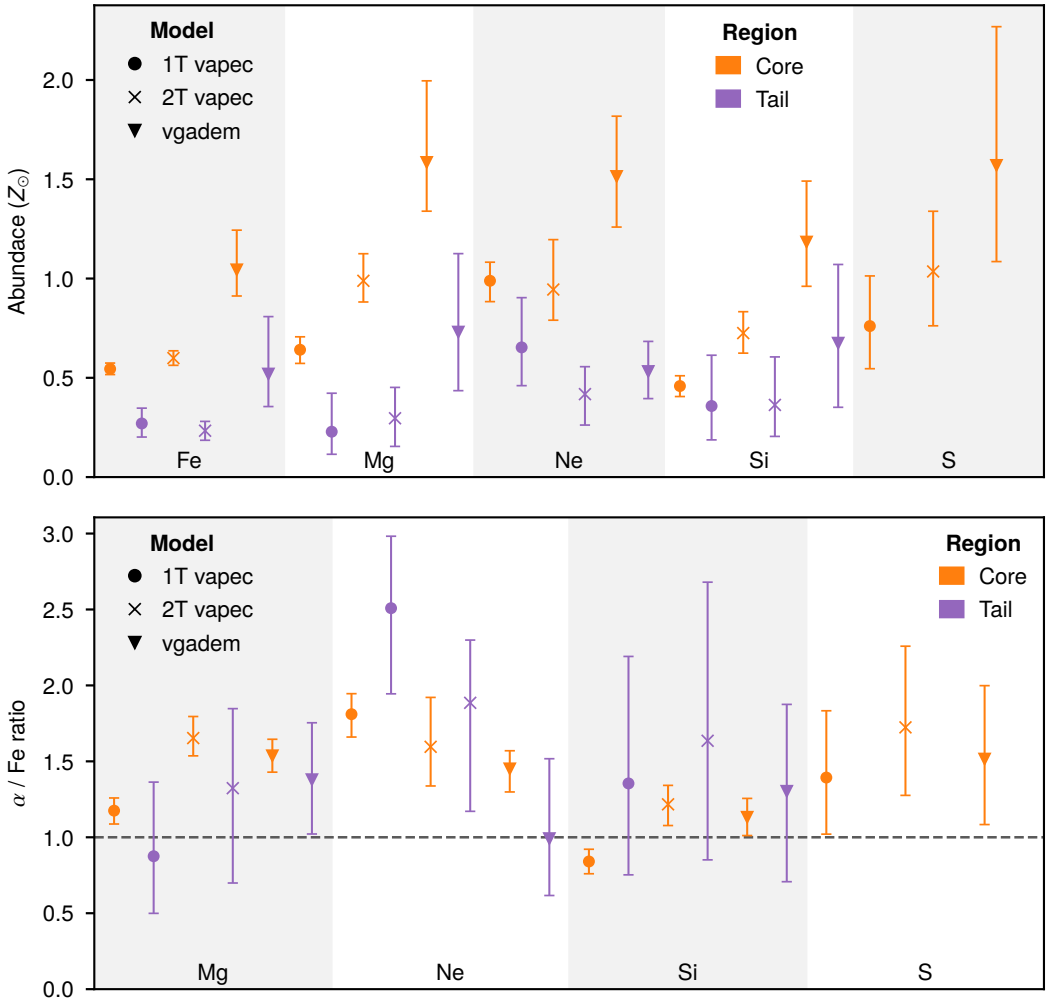

Figure A.3.2: Abundance and ratio measurement comparison of Tail and Core regions using ACIS-S data.

A.4 Missing metals in the Centaurus cluster

A.4.1 Comparison of central spectral fits

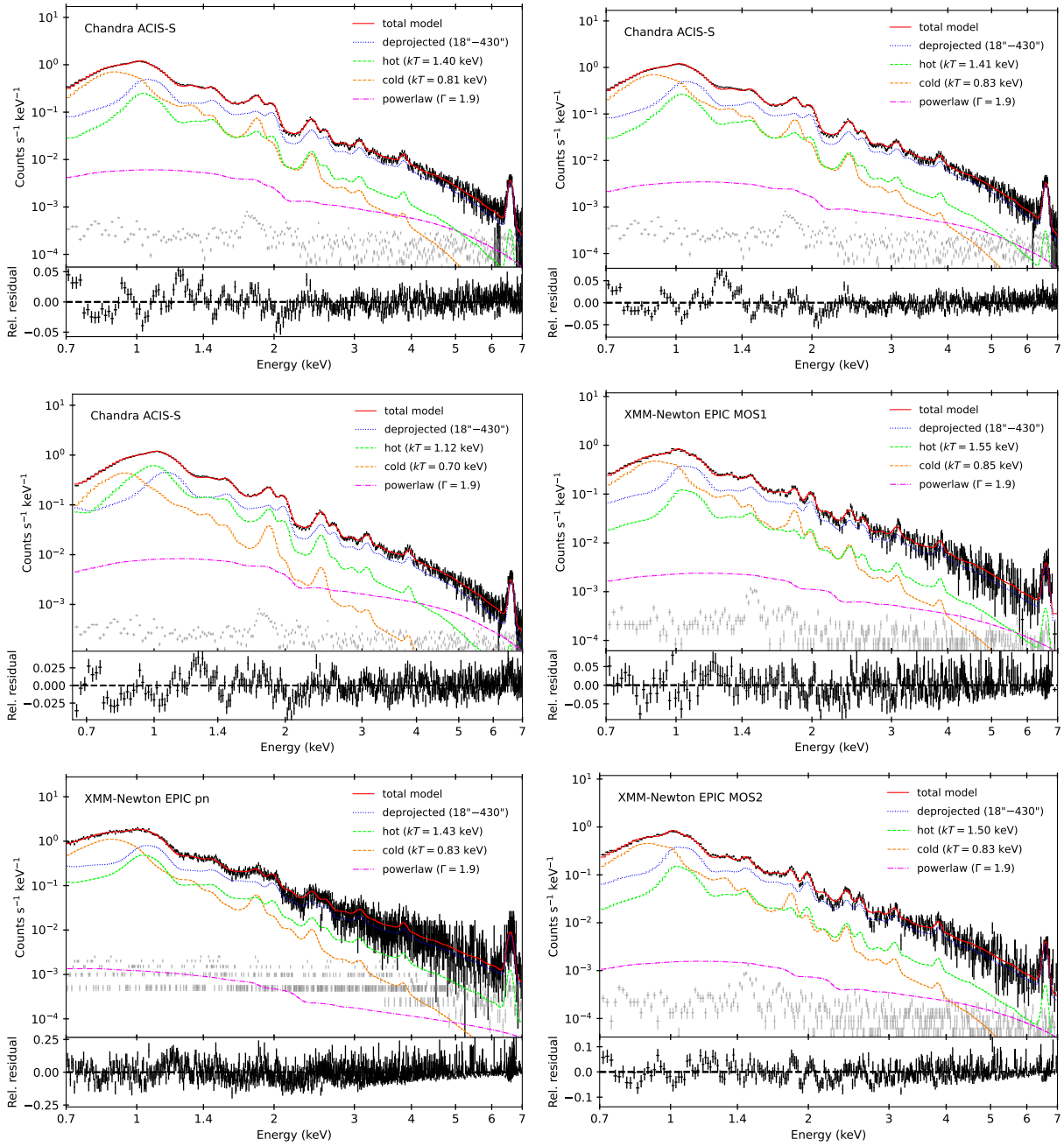

Figure A.4.1: Spectra of the innermost radial bin (central 18.5 arcsec) for individual X-ray instruments used in the analysis: *Chandra* ACIS-S with AtomDB 3.1.3 (*upper left*), *Chandra* ACIS-S with AtomDB 3.0.9 (*upper right*), *Chandra* ACIS-S with SPEXACT 3.08.01 (*center left*), *XMM-Newton* EPIC MOS1 (*center right*), *XMM-Newton* EPIC pn (*lower left*), and *XMM-Newton* EPIC MOS2 (*lower right.*

A.4.2 Posterior distribution of central parameters

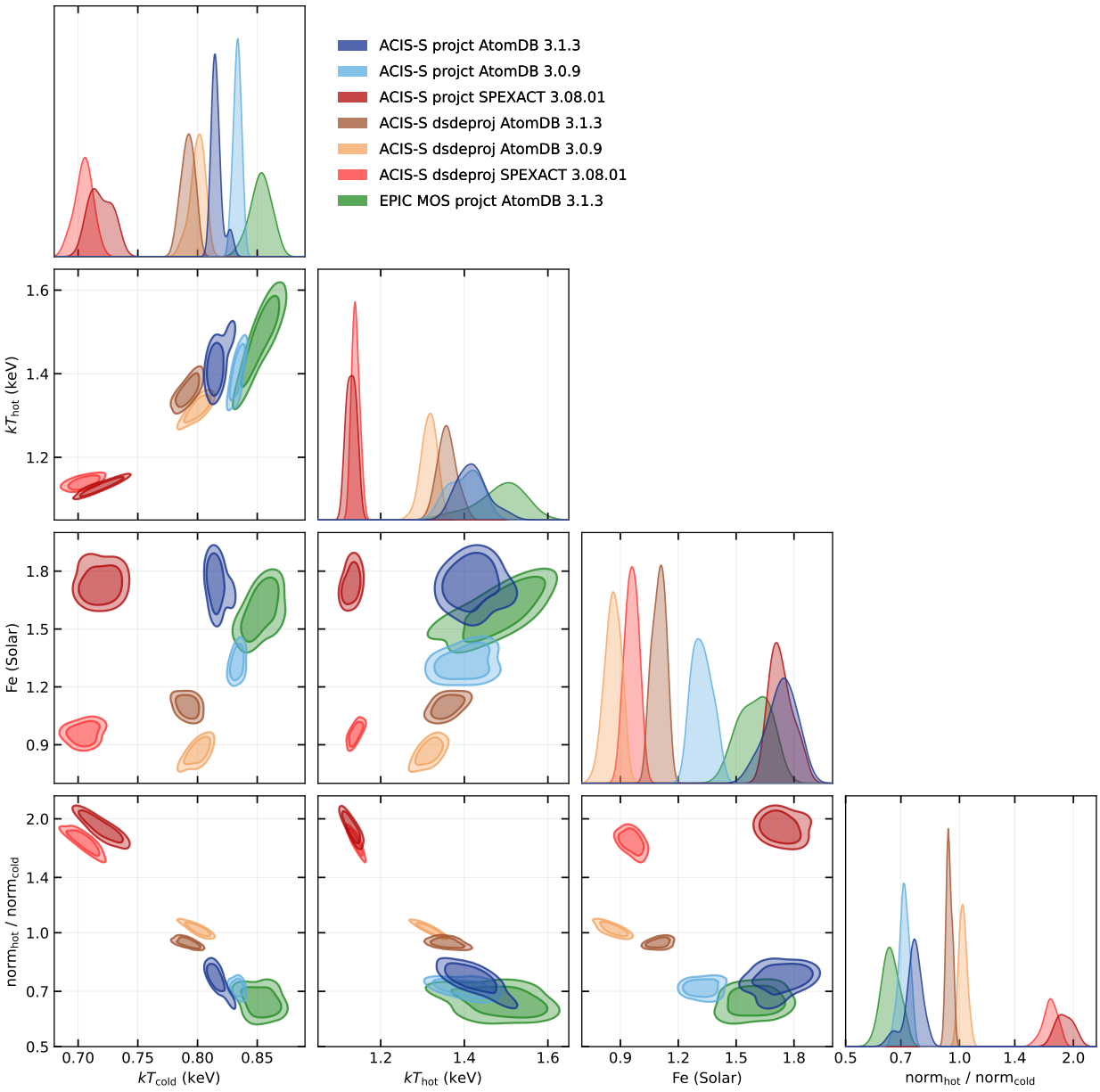

Figure A.4.2: Contours representing 68% and 90% confidence intervals of the following parameters of the innermost radial bin: temperature of the colder plum-like component ($kT_{\rm cold}$), temperature of the hotter volume-filling component ($kT_{\rm hot}$), iron metallicity of both components (Fe), and ratio of norms of hot and cold components ($\rm norm_{hot}/norm_{cold}$). We compare posteriors of the following configurations of data, atomic database, and projection method: *Chandra* ACIS-S AtomDB 3.1.3, *Chandra* ACIS-S AtomDB 3.0.9, *Chandra* ACIS-S SPEXACT 3.08.01, EPIC MOS AtomDB 3.1.3, *Chandra* ACIS-S dsdeproj AtomDB 3.1.3, and *Chandra* ACIS-S dsdeproj AtomDB 3.0.9.

A.4.3 Radial profiles of individual heavy elements

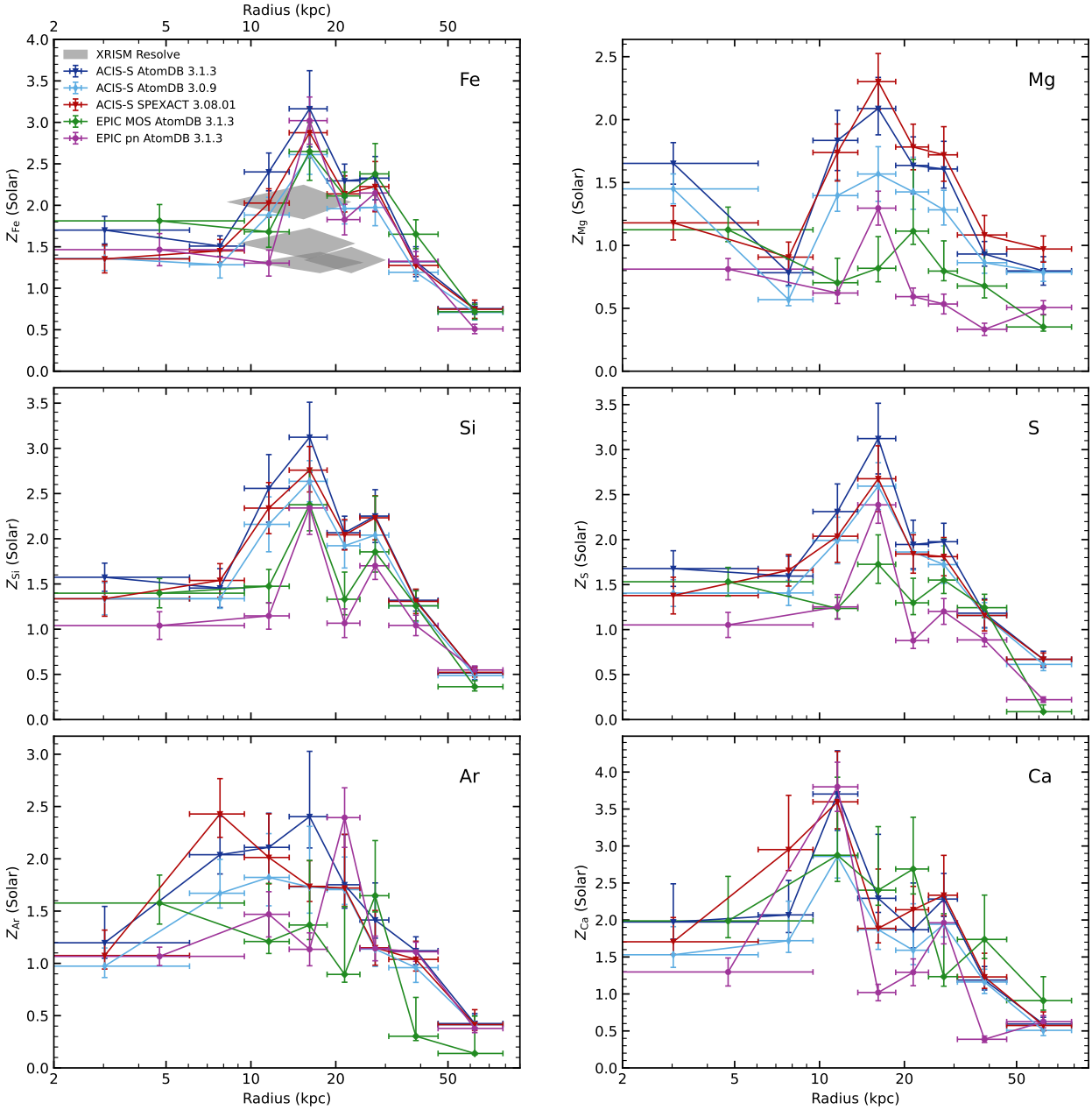

Figure A.4.3: Metallicity profiles of all heavier elements identified in the *Chandra* and *XMM-Newton* spectra and fitted separately: iron (Fe), magnesium (Mg), silicon (Si), sulphur (S), argon (Ar), and calcium (Ca). The profiles compare estimates obtained with *Chandra* using AtomDB version 3.1.3 and 3.0.9, and SPEXACT 3.08.01, as well as *XMM-Newton* EPIC MOS and pn.

References

M. Abadi, A. Agarwal, P. Barham, E. Brevdo, Z. Chen, C. Citro, G. S. Corrado, A. Davis, J. Dean, M. Devin, S. Ghemawat, I. Goodfellow, A. Harp, G. Irving, M. Isard, Y. Jia, R. Jozefowicz, L. Kaiser, M. Kudlur, J. Levenberg, D. Mané, R. Monga, S. Moore, D. Murray, C. Olah, M. Schuster, J. Shlens, B. Steiner, I. Sutskever, K. Talwar, P. Tucker, V. Vanhoucke, V. Vasudevan, F. Viégas, O. Vinyals, P. Warden, M. Wattenberg, M. Wicke, Y. Yu, and X. Zheng. TensorFlow: Large-scale machine learning on heterogeneous systems, 2015. URL `https://www.tensorflow.org/`. Software available from tensorflow.org.

Z. Abdulla, J. E. Carlstrom, A. B. Mantz, D. P. Marrone, C. H. Greer, J. W. Lamb, E. M. Leitch, S. Muchovej, C. O'Donnell, T. J. Plagge, and D. Woody. Constraints on the Thermal Contents of the X-Ray Cavities of Cluster MS 0735.6+7421 with Sunyaev-Zel'dovich Effect Observations. *ApJ*, 871(2):195, Feb. 2019. doi: 10.3847/1538-4357/aaf888.

W. Alhassan, A. R. Taylor, and M. Vaccari. The FIRST Classifier: compact and extended radio galaxy classification using deep Convolutional Neural Networks. *MNRAS*, 480(2):2085–2093, Oct. 2018. doi: 10.1093/mnras/sty2038.

S. W. Allen, R. J. H. Dunn, A. C. Fabian, G. B. Taylor, and C. S. Reynolds. The relation between accretion rate and jet power in X-ray luminous elliptical galaxies. *MNRAS*, 372(1):21–30, Oct. 2006. doi: 10.1111/j.1365-2966.2006.10778.x.

K. A. Arnaud. XSPEC: The First Ten Years. In G. H. Jacoby and J. Barnes, editors, *Astronomical Data Analysis Software and Systems V*, volume 101 of *Astronomical Society of the Pacific Conference Series*, page 17, Jan. 1996.

M. Balucinska-Church and D. McCammon. Photoelectric Absorption Cross Sections with Variable Abundances. *ApJ*, 400:699, Dec. 1992. doi: 10.1086/172032.

E. M. Berkhuijsen. A Survey of the Continuum Radiation at 820 MHz between Declinations -7° and +85°. A Study of the Galactic Radiation and the Degree of Polarization with Special Reference to the Loops and Spurs. *A&A*, 14:359, Oct. 1971.

N. Biava, M. Brienza, A. Bonafede, and M. Gitti. Constraining the AGN duty cycle in the cluster MS 0735.6+7421. In *44th COSPAR Scientific Assembly. Held 16-24 July*, volume 44, page 2330, July 2022.

V. Biffi, S. Planelles, S. Borgani, D. Fabjan, E. Rasia, G. Murante, L. Tornatore, K. Dolag, G. L. Granato, M. Gaspari, and A. M. Beck. The history of chemical enrichment in the intracluster medium from cosmological simulations. *MNRAS*, 468(1):531–548, 02 2017. ISSN 0035-8711. doi: 10.1093/mnras/stx444. URL `https://doi.org/10.1093/mnras/stx444`.

J. Binney and S. Tremaine. *Galactic dynamics*. Princeton: Princeton Univ. Press, 1987.

L. Bîrzan, D. A. Rafferty, B. R. McNamara, M. W. Wise, and P. E. J. Nulsen. A Systematic Study of Radio-induced X-Ray Cavities in Clusters, Groups, and Galaxies. *ApJ*, 607(2):800–809, June 2004. doi: 10.1086/383519.

L. Birzan, D. A. Rafferty, B. R. McNamara, M. W. Wise, and P. E. J. Nulsen. A Systematic Study of Radio-induced X-Ray Cavities in Clusters, Groups, and Galaxies. *ApJ*, 607(2):800–809, Jun 2004. ISSN 1538-4357. doi: 10.1086/383519. URL `http://dx.doi.org/10.1086/383519`.

L. Bîrzan, B. R. McNamara, P. E. J. Nulsen, C. L. Carilli, and M. W. Wise. Radiative Efficiency and Content of Extragalactic Radio Sources: Toward a Universal Scaling Relation between Jet Power and Radio Power. *ApJ*, 686(2): 859–880, Oct. 2008. doi: 10.1086/591416.

L. Bîrzan, D. A. Rafferty, M. Brüggen, A. Botteon, G. Brunetti, V. Cuciti, A. C. Edge, R. Morganti, H. J. A. Röttgering, and T. W. Shimwell. LOFAR observations of X-ray cavity systems. *MNRAS*, 496(3):2613–2635, Aug. 2020. doi: 10.1093/mnras/staa1594.

J. P. Blakeslee, J. R. Lucey, B. J. Barris, M. J. Hudson, and J. L. Tonry. A synthesis of data from fundamental plane and surface brightness fluctuation surveys. *MNRAS*, 327(3):1004–1020, Nov. 2001. doi: 10.1046/j.1365-8711.2001.04800.x.

J. P. Blakeslee, A. Jordán, S. Mei, P. Côté, L. Ferrarese, L. Infante, E. W. Peng, J. L. Tonry, and M. J. West. The ACS Fornax Cluster Survey. V. Measurement and Recalibration of Surface Brightness Fluctuations and a Precise Value of the Fornax-Virgo Relative Distance. *ApJ*, 694(1):556–572, Mar. 2009. doi: 10.1088/0004-637X/694/1/556.

E. L. Blanton, C. L. Sarazin, B. R. McNamara, and M. W. Wise. Chandra Observation of the Radio Source/X-Ray Gas Interaction in the Cooling Flow Cluster Abell 2052. *ApJ Lett.*, 558(1):L15–L18, Sept. 2001. doi: 10.1086/323269.

H. Boehringer, W. Voges, A. C. Fabian, A. C. Edge, and D. M. Neumann. A ROSAT HRI study of the interaction of the X-ray emitting gas and radio lobes of NGC 1275. *MNRAS*, 264:L25–L28, Oct. 1993. doi: 10.1093/mnras/264.1.L25.

Á. Bogdán and A. D. Goulding. Connecting Dark Matter Halos with the Galaxy Center and the Supermassive Black Hole. *ApJ*, 800(2):124, Feb. 2015. doi: 10.1088/0004-637X/800/2/124.

Á. Bogdán, R. J. van Weeren, R. P. Kraft, W. R. Forman, S. Randall, S. Giacintucci, E. Churazov, C. P. O'Dea, S. A. Baum, J. Noell-Storr, and C. Jones. Young AGN Outburst Running over Older X-Ray Cavities. *ApJ Lett.*, 782(2): L19, Feb. 2014. doi: 10.1088/2041-8205/782/2/L19.

P. T. Boggs and J. E. Rogers. Orthogonal distance regression. In *Statistical analysis of measurement error models and applications: proceedings of the AMS-IMS-SIAM joint summer research conference held June 10-16, 1989*, volume 112, 1990.

H. Böhringer and N. Werner. X-ray spectroscopy of galaxy clusters: studying astrophysical processes in the largest celestial laboratories. *A&AR*, 18(1-2):127–196, Feb. 2010. doi: 10.1007/s00159-009-0023-3.

H. Böhringer, E. Belsole, J. Kennea, K. Matsushita, S. Molendi, D. M. Worrall, R. F. Mushotzky, M. Ehle, M. Guainazzi, I. Sakelliou, G. Stewart, W. T. Vestrand, and S. Dos Santos. XMM-Newton observations of M 87 and its X-ray halo. *A&A*, 365:L181–L187, Jan. 2001. doi: 10.1051/0004-6361:20000092.

H. Böhringer, K. Matsushita, E. Churazov, Y. Ikebe, and Y. Chen. The new emerging model for the structure of cooling cores in clusters of galaxies. *A&A*, 382:804–820, Feb. 2002. doi: 10.1051/0004-6361:20011708.

H. Böhringer, K. Matsushita, E. Churazov, A. Finoguenov, and Y. Ikebe. Implications of the central metal abundance peak in cooling core clusters of galaxies. *A&A*, 416:L21–L25, Mar. 2004. doi: 10.1051/0004-6361:20040047.

B. D. Boizelle, J. L. Walsh, A. J. Barth, D. A. Buote, A. J. Baker, J. Darling, L. C. Ho, J. Cohn, and K. M. Kabasares. Black Hole Mass Measurements of Radio Galaxies NGC 315 and NGC 4261 Using ALMA CO Observations. *ApJ*, 908(1): 19, Feb. 2021. doi: 10.3847/1538-4357/abd24d.

H. Bondi. On spherically symmetrical accretion. *MNRAS*, 112:195, Jan. 1952. doi: 10.1093/mnras/112.2.195.

A. Boselli, M. Fossati, A. Longobardi, K. Kianfar, N. Z. Dametto, P. Amram, J. P. Anderson, P. Andreani, S. Boissier, M. Boquien, V. Buat, G. Consolandi, L. Cortese, P. Côté, J. C. Cuillandre, L. Ferrarese, L. Galbany, G. Gavazzi, S. Gwyn, G. Hensler, J. Hutchings, E. W. Peng, J. Postma, J. Roediger, Y. Roehlly, P. Serra, and G. Trinchieri. A Virgo Environmental Survey Tracing Ionised Gas Emission (VESTIGE).XII. Ionised gas emission in the inner regions of lenticular galaxies. *arXiv e-prints*, art. arXiv:2111.06635, Nov. 2021.

Boselli, A., Fossati, M., Longobardi, A., Kianfar, K., Dametto, N. Z., Amram, P., Anderson, J. P., Andreani, P., Boissier, S., Boquien, M., Buat, V., Consolandi, G., Cortese, L., Côté, P., Cuillandre, J. C., Ferrarese, L., Galbany, L., Gavazzi, G., Gwyn, S., Hensler, G., Hutchings, J., Peng, E. W., Postma, J., Roediger, J., Roehlly, Y., Serra, P., and Trinchieri, G. A virgo environmental survey tracing ionised gas emission (vestige) - xii. ionised gas emission in the inner regions of lenticular galaxies. *A&A*, 659:A46, 2022. doi: 10.1051/0004-6361/202142482. URL `https://doi.org/10.1051/0004-6361/202142482`.

J. Bradbury, R. Frostig, P. Hawkins, M. J. Johnson, C. Leary, D. Maclaurin, G. Necula, A. Paszke, J. VanderPlas, S. Wanderman-Milne, and Q. Zhang. JAX: composable transformations of Python+NumPy programs, 2018. URL `http://github.com/google/jax`.

J. N. Bregman and J. R. Parriott. Mass Loss from Planetary Nebulae in Elliptical Galaxies. *ApJ*, 699(2):923–932, July 2009. doi: 10.1088/0004-637X/699/2/923.

M. Brüggen, E. Scannapieco, and S. Heinz. Evolution of X-ray cavities. *MNRAS*, 395(4):2210–2220, June 2009. doi: 10.1111/j.1365-2966.2009.14684.x.

J. Buchner. A statistical test for Nested Sampling algorithms. *Statistics and Computing*, 26(1-2):383–392, Jan. 2016. doi: 10.1007/s11222-014-9512-y.

J. Buchner. Collaborative Nested Sampling: Big Data versus Complex Physical Models. *PASP*, 131(1004):108005, Oct. 2019. doi: 10.1088/1538-3873/aae7fc.

J. Buchner. UltraNest - a robust, general purpose Bayesian inference engine. *The Journal of Open Source Software*, 6(60):3001, Apr. 2021. doi: 10.21105/joss.03001.

D. A. Buote. Iron Gradients in Cooling Flow Galaxies and Groups. *ApJ*, 539(1):172–186, Aug. 2000. doi: 10.1086/309224.

D. A. Buote and A. C. Fabian. X-ray spectral analysis of elliptical galaxies from ASCA: the Fe abundance in a multi-phase medium. *MNRAS*, 296(4):977–994, June 1998. doi: 10.1046/j.1365-8711.1998.01478.x.

C. R. Canizares, G. W. Clark, T. H. Markert, C. Berg, M. Smedira, D. Bardas, H. Schnopper, and K. Kalata. High-resolution X-ray spectroscopy of M87 with the Einstein Observatory: the detection of an O VIII emission line. *ApJ Lett.*, 234:L33–L37, Nov. 1979. doi: 10.1086/183104.

M. Cantiello, J. P. Blakeslee, G. Raimondo, S. Mei, E. Brocato, and M. Capaccioli. Detection of Radial Surface Brightness Fluctuations and Color Gradients in Elliptical Galaxies with the Advanced Camera for Surveys. *ApJ*, 634(1):239–257, Nov. 2005. doi: 10.1086/491694.

A. Capetti, P. Kharb, D. J. Axon, D. Merritt, and R. D. Baldi. A Very Large Array Radio Survey of Early-Type Galaxies in the Virgo Cluster. *AJ*, 138(6):1990–1997, Dec. 2009. doi: 10.1088/0004-6256/138/6/1990.

A. Capetti, M. Brienza, B. Balmaverde, P. N. Best, R. D. Baldi, A. Drabent, G. Gürkan, H. J. A. Rottgering, C. Tasse, and B. Webster. The LOFAR view of giant, early-type galaxies: Radio emission from active nuclei and star formation. *A&A*, 660:A93, Apr. 2022. doi: 10.1051/0004-6361/202142911.

M. Cappellari, N. Scott, K. Alatalo, L. Blitz, M. Bois, F. Bournaud, M. Bureau, A. F. Crocker, R. L. Davies, T. A. Davis, P. T. de Zeeuw, P.-A. Duc, E. Emsellem, S. Khochfar, D. Krajnović, H. Kuntschner, R. M. McDermid, R. Morganti, T. Naab, T. Oosterloo, M. Sarzi, P. Serra, A.-M. Weijmans, and L. M. Young. The ATLAS^{3D} project - XV. Benchmark for early-type galaxies scaling relations from 260 dynamical models: mass-to-light ratio, dark matter, Fundamental Plane and Mass Plane. *MNRAS*, 432(3):1709–1741, July 2013. doi: 10.1093/mnras/stt562.

W. Cash. Parameter estimation in astronomy through application of the likelihood ratio. *ApJ*, 228:939–947, Mar. 1979. doi: 10.1086/156922.

K. W. Cavagnolo, B. R. McNamara, P. E. J. Nulsen, C. L. Carilli, C. Jones, and L. Bîrzan. A Relationship Between AGN Jet Power and Radio Power. *ApJ*, 720(2):1066–1072, Sept. 2010. doi: 10.1088/0004-637X/720/2/1066.

K. W. Cavagnolo, B. R. McNamara, M. W. Wise, P. E. J. Nulsen, M. Brüggen, M. Gitti, and D. A. Rafferty. A Powerful AGN Outburst in RBS 797. *ApJ*, 732(2):71, May 2011. doi: 10.1088/0004-637X/732/2/71.

A. Cavaliere and R. Fusco-Femiano. Reprint of 1976A&A....49..137C. X-rays from hot plasma in clusters of galaxies. *A&A*, 500:95–102, May 1976.

S. Chandrasekhar. *Hydrodynamic and hydromagnetic stability*. Oxford University Press, 1961.

F. Chollet et al. Keras. `https://keras.io`, 2015.

E. Churazov, M. Brüggen, C. R. Kaiser, H. Böhringer, and W. Forman. Evolution of Buoyant Bubbles in M87. *ApJ*, 554(1):261–273, June 2001. doi: 10.1086/321357.

E. Churazov, R. Sunyaev, W. Forman, and H. Böhringer. Cooling flows as a calorimeter of active galactic nucleus mechanical power. *MNRAS*, 332:729–734, May 2002. doi: 10.1046/j.1365-8711.2002.05332.x.

E. Churazov, W. Forman, C. Jones, and H. Böhringer. XMM-Newton Observations of the Perseus Cluster. I. The Temperature and Surface Brightness Structure. *ApJ*, 590(1):225–237, June 2003. doi: 10.1086/374923.

E. Churazov, W. Forman, C. Jones, R. Sunyaev, and H. Böhringer. XMM-Newton observations of the Perseus cluster - II. Evidence for gas motions in the core. *MNRAS*, 347(1):29–35, Jan. 2004. doi: 10.1111/j.1365-2966.2004.07201.x.

L. Ciotti, A. D'Ercole, S. Pellegrini, and A. Renzini. Winds, Outflows, and Inflows in X-Ray Elliptical Galaxies. I. *ApJ*, 376:380, Aug. 1991. doi: 10.1086/170289.

J. Condon, J. Darling, Y. Y. Kovalev, and L. Petrov. VLBA observations of a complete sample of 2MASS galaxies. *arXiv e-prints*, art. arXiv:1110.6252, Oct. 2013.

C. Conroy, G. J. Graves, and P. G. van Dokkum. EARLY-TYPE GALAXY ARCHEOLOGY: AGES, ABUNDANCE RATIOS, AND EFFECTIVE TEMPERATURES FROM FULL-SPECTRUM FITTING. *ApJ*, 780(1):33, dec 2013. doi: 10.1088/0004-637x/780/1/33. URL `https://doi.org/10.1088/0004-637x/780/1/33`.

H.-J. Cui, H.-G. Xu, J.-H. Gu, J.-Y. Wang, L.-Y. Gu, Y. Wang, Z.-Z. Qin, and T. An. Metal enrichment via ram pressure stripping in the IGM of the compact galaxy group RGH 80. *Research in Astronomy and Astrophysics*, 10(4):301–308, Apr. 2010. doi: 10.1088/1674-4527/10/4/002.

B. Dai and U. Seljak. Learning effective physical laws for generating cosmological hydrodynamics with Lagrangian deep learning. *Proceedings of the National Academy of Science*, 118(16):2020324118, Apr. 2021. doi: 10.1073/pnas.2020324118.

S. De Grandi and S. Molendi. Metallicity Gradients in X-Ray Clusters of Galaxies. *ApJ*, 551(1):153–159, Apr. 2001. doi: 10.1086/320098.

S. de Grandi and S. Molendi. Metal abundances in the cool cores of galaxy clusters. *A&A*, 508(2):565–574, Dec. 2009. doi: 10.1051/0004-6361/200912745.

De Luca and Molendi. The 2-8 keV cosmic X-ray background spectrum as observed with XMM-Newton. *A&A*, 419(3):837–848, 2004. doi: 10.1051/0004-6361:20034421. URL `https://doi.org/10.1051/0004-6361:20034421`.

J. de Plaa, N. Werner, J. A. M. Bleeker, J. Vink, J. S. Kaastra, and M. Méndez. Constraining supernova models using the hot gas in clusters of galaxies. *A&A*, 465(2):345–355, Apr. 2007. doi: 10.1051/0004-6361:20066382.

J. de Plaa, N. Werner, A. Simionescu, J. S. Kaastra, Y. G. Grange, and J. Vink. Cold fronts and multi-temperature structures in the core of Abell 2052. *A&A*, 523:A81, Nov. 2010. doi: 10.1051/0004-6361/201015198.

J. de Plaa, J. S. Kaastra, N. Werner, C. Pinto, P. Kosec, Y. Y. Zhang, F. Mernier, L. Lovisari, H. Akamatsu, G. Schellenberger, F. Hofmann, T. H. Reiprich, A. Finoguenov, J. Ahoranta, J. S. Sanders, A. C. Fabian, O. Pols, A. Simionescu, J. Vink, and H. Böhringer. CHEERS: The chemical evolution RGS sample. *A&A*, 607:A98, Nov. 2017. doi: 10.1051/0004-6361/201629926.

J. W. den Herder, A. C. Brinkman, S. M. Kahn, G. Branduardi-Raymont, K. Thomsen, H. Aarts, M. Audard, J. V. Bixler, A. J. den Boggende, J. Cottam, T. Decker, L. Dubbeldam, C. Erd, H. Goulooze, M. Güdel, P. Guttridge, C. J. Hailey, K. A. Janabi, J. S. Kaastra, P. A. J. de Korte, B. J. van Leeuwen, C. Mauche, A. J. McCalden, R. Mewe, A. Naber, F. B. Paerels, J. R. Peterson, A. P. Rasmussen, K. Rees, I. Sakelliou, M. Sako, J. Spodek, M. Stern, T. Tamura, J. Tandy, C. P. de Vries, S. Welch, and A. Zehnder. The Reflection Grating Spectrometer on board XMM-Newton. *A&A*, 365: L7–L17, Jan. 2001. doi: 10.1051/0004-6361:20000058.

T. Di Matteo, S. W. Allen, A. C. Fabian, A. S. Wilson, and A. J. Young. Accretion onto the Supermassive Black Hole in M87. *ApJ*, 582:133–140, Jan. 2003. doi: 10.1086/344504.

J. M. Dickey and B. P. Lientz. The Weighted Likelihood Ratio, Sharp Hypotheses about Chances, the Order of a Markov Chain. *The Annals of Mathematical Statistics*, 41(1):214 – 226, 1970. doi: 10.1214/aoms/1177697203. URL `https://doi.org/10.1214/aoms/1177697203`.

S. Diehl, H. Li, C. L. Fryer, and D. Rafferty. Constraining the Nature of X-Ray Cavities in Clusters and Galaxies. *ApJ*, 687(1):173–192, Nov. 2008. doi: 10.1086/591310.

S. Dieleman, K. W. Willett, and J. Dambre. Rotation-invariant convolutional neural networks for galaxy morphology prediction. *MNRAS*, 450(2):1441–1459, June 2015. doi: 10.1093/mnras/stv632.

A. D'Isanto and K. L. Polsterer. Photometric redshift estimation via deep learning. Generalized and pre-classification-less, image based, fully probabilistic redshifts. *A&A*, 609:A111, Jan. 2018. doi: 10.1051/0004-6361/201731326.

R. Dong, J. Rasmussen, and J. S. Mulchaey. A Systematic Search for X-ray Cavities in the Hot Gas of Galaxy Groups. *ApJ*, 712(2):883–900, Apr. 2010. doi: 10.1088/0004-637X/712/2/883.

B. T. Dullo, A. Gil de Paz, and J. H. Knapen. Ultramassive Black Holes in the Most Massive Galaxies: M_{BH}-σ versus M_{BH}-R_b. *ApJ*, 908(2):134, Feb. 2021. doi: 10.3847/1538-4357/abceae.

R. J. H. Dunn, S. W. Allen, G. B. Taylor, K. F. Shurkin, G. Gentile, A. C. Fabian, and C. S. Reynolds. The radio properties of a complete, X-ray selected sample of nearby, massive elliptical galaxies. *MNRAS*, 404(1):180–197, May 2010. doi: 10.1111/j.1365-2966.2010.16314.x.

S. C. Ellis and E. O'Sullivan. Correlations of near-infrared, optical and X-ray luminosity for early-type galaxies. *MNRAS*, 367(2):627–645, Apr. 2006. doi: 10.1111/j.1365-2966.2005.09982.x.

T. A. Enßlin and S. Heinz. Radio and X-ray detectability of buoyant radio plasma bubbles in clusters of galaxies. *A&A*, 384:L27–L30, Mar. 2002. doi: 10.1051/0004-6361:20020207.

M. K. Erdim, C. Ezer, O. Ünver, F. Hazar, and M. Hudaverdi. The relative supernovae contribution to the chemical enrichment history of Abell 1837. *MNRAS*, 508(3):3337–3344, 10 2021. ISSN 0035-8711. doi: 10.1093/mnras/stab2730. URL `https://doi.org/10.1093/mnras/stab2730`.

M. Ester, H.-P. Kriegel, J. Sander, and X. Xu. A density-based algorithm for discovering clusters in large spatial databases with noise. In *Proceedings of the Second International Conference on Knowledge Discovery and Data Mining*, KDD'96, page 226–231. AAAI Press, 1996.

S. Ettori. Note on a polytropic β-model to fit the X-ray surface brightness of clusters of galaxies. *MNRAS*, 311(2): 313–316, Jan. 2000. doi: 10.1046/j.1365-8711.2000.03037.x.

S. Ettori and A. C. Fabian. Effects of sedimented helium on the X-ray properties of galaxy clusters. *MNRAS*, 369(1): L42–L46, June 2006. doi: 10.1111/j.1745-3933.2006.00170.x.

S. Ettori, A. Donnarumma, E. Pointecouteau, T. H. Reiprich, S. Giodini, L. Lovisari, and R. W. Schmidt. Mass Profiles of Galaxy Clusters from X-ray Analysis. *Space Sci. Rev.*, 177(1-4):119–154, Aug. 2013. doi: 10.1007/s11214-013-9976-7.

Event Horizon Telescope Collaboration. First M87 Event Horizon Telescope Results. VI. The Shadow and Mass of the Central Black Hole. *ApJ Lett.*, 875(1):L6, Apr. 2019. doi: 10.3847/2041-8213/ab1141.

A. C. Fabian. Cooling Flows in Clusters of Galaxies. *ARA&A*, 32:277–318, Jan. 1994. doi: 10.1146/annurev.aa.32.090194.001425.

A. C. Fabian. Observational Evidence of Active Galactic Nuclei Feedback. *ARA&A*, 50:455–489, Sept. 2012. doi: 10.1146/annurev-astro-081811-125521.

A. C. Fabian, J. S. Sanders, S. Ettori, G. B. Taylor, S. W. Allen, C. S. Crawford, K. Iwasawa, R. M. Johnstone, and P. M. Ogle. Chandra imaging of the complex X-ray core of the Perseus cluster. *MNRAS*, 318(4):L65–L68, Nov. 2000. doi: 10.1046/j.1365-8711.2000.03904.x.

A. C. Fabian, A. Celotti, K. M. Blundell, N. E. Kassim, and R. A. Perley. The properties of the X-ray holes in the intracluster medium of the Perseus cluster. *MNRAS*, 331(2):369–375, Mar. 2002. doi: 10.1046/j.1365-8711.2002.05182.x.

A. C. Fabian, J. S. Sanders, G. B. Taylor, S. W. Allen, C. S. Crawford, R. M. Johnstone, and K. Iwasawa. A very deep Chandra observation of the Perseus cluster: shocks, ripples and conduction. *MNRAS*, 366(2):417–428, Feb. 2006. doi: 10.1111/j.1365-2966.2005.09896.x.

A. C. Fabian, G. J. Ferland, J. S. Sanders, B. R. McNamara, C. Pinto, and S. A. Walker. Hidden cooling flows in clusters of galaxies. *MNRAS*, 515(3):3336–3345, Sept. 2022. doi: 10.1093/mnras/stac2003.

A. C. Fabian, G. J. Ferland, J. S. Sanders, H. R. Russell, B. R. McNamara, C. Pinto, J. Hlavacek-Larrondo, S. A. Walker, L. R. Ivey, and M. McDonald. Hidden cooling flows - IV. More details on Centaurus and the efficiency of AGN feedback in clusters. *MNRAS*, 535(3):2173–2188, Dec. 2024. doi: 10.1093/mnras/stae2414.

M. E. Filho, F. Fraternali, S. Markoff, N. M. Nagar, P. D. Barthel, L. C. Ho, and F. Yuan. Further clues to the nature of composite LINER/H II galaxies. *A&A*, 418:429–443, May 2004. doi: 10.1051/0004-6361:20034486.

M. Fink, M. Kromer, I. R. Seitenzahl, F. Ciaraldi-Schoolmann, F. K. Röpke, S. A. Sim, R. Pakmor, A. J. Ruiter, and W. Hillebrandt. Three-dimensional pure deflagration models with nucleosynthesis and synthetic observables for Type Ia supernovae. *MNRAS*, 438(2):1762–1783, 12 2014. ISSN 0035-8711. doi: 10.1093/mnras/stt2315. URL `https://doi.org/10.1093/mnras/stt2315`.

A. Finoguenov, L. P. David, and T. J. Ponman. An ASCA Study of the Heavy-Element Distribution in Clusters of Galaxies. *ApJ*, 544(1):188–203, Nov. 2000. doi: 10.1086/317173.

R. Fisher. *Statistical Methods for Research Workers*. Biological monographs and manuals. Oliver and Boyd, 1944. URL `https://books.google.cz/books?id=-L9OzAEACAAJ`.

S. Fort. Towards understanding feedback from supermassive black holes using convolutional neural networks. *arXiv e-prints*, art. arXiv:1712.00523, Dec. 2017.

A. R. Foster, L. Ji, R. K. Smith, and N. S. Brickhouse. Updated Atomic Data and Calculations for X-Ray Spectroscopy. *ApJ*, 756(2):128, Sept. 2012. doi: 10.1088/0004-637X/756/2/128.

P. Freeman, S. Doe, and A. Siemiginowska. Sherpa: a mission-independent data analysis application. In J.-L. Starck and F. D. Murtagh, editors, *Astronomical Data Analysis*, volume 4477 of *Society of Photo-Optical Instrumentation Engineers (SPIE) Conference Series*, pages 76–87, Nov. 2001. doi: 10.1117/12.447161.

A. Fruscione, J. C. McDowell, G. E. Allen, N. S. Brickhouse, D. J. Burke, J. E. Davis, N. Durham, M. Elvis, E. C. Galle, D. E. Harris, D. P. Huenemoerder, J. C. Houck, B. Ishibashi, M. Karovska, F. Nicastro, M. S. Noble, M. A. Nowak, F. A. Primini, A. Siemiginowska, R. K. Smith, and M. Wise. CIAO: Chandra's data analysis system. In D. R. Silva and R. E. Doxsey, editors, *Society of Photo-Optical Instrumentation Engineers (SPIE) Conference Series*, volume 6270 of *Society of Photo-Optical Instrumentation Engineers (SPIE) Conference Series*, page 62701V, June 2006. doi: 10.1117/12.671760.

Y. Fujita, N. Tawa, K. Hayashida, M. Takizawa, H. Matsumoto, N. Okabe, and T. H. Reiprich. High Metallicity of the X-Ray Gas Up to the Virial Radius of a Binary Cluster of Galaxies: Evidence of Galactic Superwinds at High-Redshift. *PASJ*, 60:S343, Jan. 2008. doi: 10.1093/pasj/60.sp1.S343.

Y. Fukazawa, T. Ohashi, A. C. Fabian, C. R. Canizares, Y. Ikebe, K. Makishima, R. F. Mushotzky, and K. Yamashita. Metal Concentration and X-Ray Cool Spectral Component in the Central Region of the Centaurus Cluster of Galaxies. *PASJ*, 46(3):L55–L58, June 1994. doi: 10.1093/pasj/46.3.55.

K. Fukushima. Cognitron: A self-organizing multilayer neural network. *Biological Cybernetics*, 20:121–136, 1975.

K. Fukushima, S. B. Kobayashi, and K. Matsushita. Chemical enrichment in the cool core of the Centaurus cluster of galaxies. *MNRAS*, 514(3):4222–4238, Aug. 2022. doi: 10.1093/mnras/stac1590.

M. Gaspari, M. Ruszkowski, and P. Sharma. Cause and Effect of Feedback: Multiphase Gas in Cluster Cores Heated by AGN Jets. *ApJ*, 746(1):94, Feb. 2012. doi: 10.1088/0004-637X/746/1/94.

M. Gaspari, D. Eckert, S. Ettori, P. Tozzi, L. Bassini, E. Rasia, F. Brighenti, M. Sun, S. Borgani, S. D. Johnson, G. R. Tremblay, J. M. Stone, P. Temi, H. Y. K. Yang, F. Tombesi, and M. Cappi. The X-Ray Halo Scaling Relations of Supermassive Black Holes. *ApJ*, 884(2):169, Oct. 2019. doi: 10.3847/1538-4357/ab3c5d.

F. Gastaldello, A. Simionescu, F. Mernier, V. Biffi, M. Gaspari, K. Sato, and K. Matsushita. The Metal Content of the Hot Atmospheres of Galaxy Groups. *Universe*, 7(7):208, June 2021. doi: 10.3390/universe7070208.

E. Gatuzz, J. S. Sanders, K. Dennerl, A. Liu, A. C. Fabian, C. Pinto, D. Eckert, H. Russell, T. Tamura, S. A. Walker, and J. ZuHone. Chemical enrichment of the ICM within the virgo cluster – I. Radial profiles. *MNRAS*, 520(3): 4793–4800, 02 2023. ISSN 0035-8711. doi: 10.1093/mnras/stad447. URL `https://doi.org/10.1093/mnras/stad447`.

M. Gendron-Marsolais, J. Hlavacek-Larrondo, R. J. van Weeren, L. Rudnick, T. E. Clarke, B. Sebastian, T. Mroczkowski, A. C. Fabian, K. M. Blundell, E. Sheldahl, K. Nyland, J. S. Sanders, W. M. Peters, and H. T. Intema. High-resolution VLA low radio frequency observations of the Perseus cluster: radio lobes, mini-halo, and bent-jet radio galaxies. *MNRAS*, 499(4):5791–5805, Dec. 2020. doi: 10.1093/mnras/staa2003.

S. Giacintucci, E. O'Sullivan, J. Vrtilek, L. P. David, S. Raychaudhury, T. Venturi, R. M. Athreya, T. E. Clarke, M. Murgia, P. Mazzotta, M. Gitti, T. Ponman, C. H. Ishwara-Chandra, C. Jones, and W. R. Forman. A Combined Low-radio Frequency/X-ray Study of Galaxy Groups. I. Giant Metrewave Radio Telescope Observations at 235 MHz AND 610 MHz. *ApJ*, 732(2):95, May 2011. doi: 10.1088/0004-637X/732/2/95.

M. R. Gilfanov, R. A. Syunyaev, and E. M. Churazov. Radial Brightness Profiles of Resonance X-Ray Lines in Galaxy Clusters. *Soviet Astronomy Letters*, 13:3, Jan. 1987.

R. Gilli, A. Comastri, and G. Hasinger. The synthesis of the cosmic X-ray background in the Chandra and XMM-Newton era. *A&A*, 463(1):79–96, Feb. 2007. doi: 10.1051/0004-6361:20066334.

M. Gitti, L. Feretti, and S. Schindler. Multifrequency VLA radio observations of the X-ray cavity cluster of galaxies RBS797: evidence of differently oriented jets. *A&A*, 448(3):853–860, Mar. 2006. doi: 10.1051/0004-6361:20053998.

J. Goodman and J. Weare. Ensemble samplers with affine invariance. *Communications in Applied Mathematics and Computational Science*, 5(1):65 – 80, 2010. doi: 10.2140/camcos.2010.5.65. URL `https://doi.org/10.2140/camcos.2010.5.65`.

R. Grossová, N. Werner, K. Rajpurohit, F. Mernier, K. Lakhchaura, K. Gabányi, R. E. A. Canning, P. Nulsen, F. Massaro, M. Sun, T. Connor, A. King, S. W. Allen, R. L. S. Frisbie, M. Donahue, and A. C. Fabian. Powerful AGN jets and unbalanced cooling in the hot atmosphere of IC 4296. *MNRAS*, 488(2):1917–1925, Sept. 2019. doi: 10.1093/mnras/stz1728.

R. Grossová, N. Werner, F. Massaro, K. Lakhchaura, T. Plšek, K. Gabányi, K. Rajpurohit, R. E. A. Canning, P. Nulsen, E. O'Sullivan, S. W. Allen, and A. Fabian. Very Large Array Radio Study of a Sample of Nearby X-Ray and Optically Bright Early-type Galaxies. *ApJS*, 258(2):30, Feb. 2022. doi: 10.3847/1538-4365/ac366c.

K. Gültekin, S. Burke-Spolaor, T. R. Lauer, T. J. W. Lazio, L. A. Moustakas, P. Ogle, and M. Postman. Chandra Observations of Abell 2261 Brightest Cluster Galaxy, a Candidate Host to a Recoiling Black Hole. *ApJ*, 906(1):48, Jan. 2021. doi: 10.3847/1538-4357/abc483.

J. E. Gunn and I. Gott, J. Richard. On the Infall of Matter Into Clusters of Galaxies and Some Effects on Their Evolution. *ApJ*, 176:1, Aug. 1972. doi: 10.1086/151605.

F. Guo. The Shape of X-Ray Cavities in Galaxy Clusters: Probing Jet Properties and Viscosity. *ApJ*, 803(1):48, Apr. 2015. doi: 10.1088/0004-637X/803/1/48.

F. Guo. Probing the Physics of Mechanical AGN Feedback with Radial Elongations of X-Ray Cavities. *ApJ*, 903(1):3, Nov. 2020. doi: 10.3847/1538-4357/abb777.

H. Gursky, E. Kellogg, S. Murray, C. Leong, H. Tananbaum, and R. Giacconi. A Strong X-Ray Source in the Coma Cluster Observed by UHURU. *ApJ Lett.*, 167:L81, Aug. 1971. doi: 10.1086/180765.

R. Hausen and B. E. Robertson. Morpheus: A Deep Learning Framework for the Pixel-level Analysis of Astronomical Image Data. *ApJS*, 248(1):20, May 2020. doi: 10.3847/1538-4365/ab8868.

K. He, X. Zhang, S. Ren, and J. Sun. Delving deep into rectifiers: Surpassing human-level performance on imagenet classification. In *2015 IEEE International Conference on Computer Vision (ICCV)*, pages 1026–1034, 2015. doi: 10.1109/ICCV.2015.123.

S. He, Y. Li, Y. Feng, S. Ho, S. Ravanbakhsh, W. Chen, and B. Póczos. Learning to predict the cosmological structure formation. *Proceedings of the National Academy of Sciences*, 116(28):13825–13832, 2019. doi: 10.1073/pnas.1821458116. URL `https://www.pnas.org/content/116/28/13825`.

HI4PI Collaboration, N. Ben Bekhti, L. Flöer, R. Keller, J. Kerp, D. Lenz, B. Winkel, J. Bailin, M. R. Calabretta, L. Dedes, H. A. Ford, B. K. Gibson, U. Haud, S. Janowiecki, P. M. W. Kalberla, F. J. Lockman, N. M. McClure-Griffiths, T. Murphy, H. Nakanishi, D. J. Pisano, and L. Staveley-Smith. HI4PI: A full-sky H I survey based on EBHIS and GASS. *A&A*, 594:A116, Oct. 2016. doi: 10.1051/0004-6361/201629178.

R. C. Hickox and D. M. Alexander. Obscured Active Galactic Nuclei. *ARA&A*, 56:625–671, Sept. 2018. doi: 10.1146/annurev-astro-081817-051803.

Hitomi Collaboration. Solar abundance ratios of the iron-peak elements in the perseus cluster. *Nature*, 551 (7681):478–480, Nov 2017. ISSN 1476-4687. doi: 10.1038/nature24301. URL `https://doi.org/10.1038/nature24301`.

J. Hlavacek-Larrondo, A. C. Fabian, A. C. Edge, H. Ebeling, J. S. Sanders, M. T. Hogan, and G. B. Taylor. Extreme AGN feedback in the MAssive Cluster Survey: a detailed study of X-ray cavities at z>0.3. *MNRAS*, 421(2):1360–1384, Apr. 2012. doi: 10.1111/j.1365-2966.2011.20405.x.

J. Hlavacek-Larrondo, M. McDonald, B. A. Benson, W. R. Forman, S. W. Allen, L. E. Bleem, M. L. N. Ashby, S. Bocquet, M. Brodwin, J. P. Dietrich, C. Jones, J. Liu, C. L. Reichardt, B. R. Saliwanchik, A. Saro, T. Schrabback, J. Song, B. Stalder, A. Vikhlinin, and A. Zenteno. X-Ray Cavities in a Sample of 83 SPT-selected Clusters of Galaxies: Tracing the Evolution of AGN Feedback in Clusters of Galaxies out to z=1.2. *ApJ*, 805(1):35, May 2015. doi: 10.1088/0004-637X/805/1/35.

M. T. Hogan, B. R. McNamara, F. A. Pulido, P. E. J. Nulsen, A. N. Vantyghem, H. R. Russell, A. C. Edge, I. Babyk, R. A. Main, and M. McDonald. The Onset of Thermally Unstable Cooling from the Hot Atmospheres of Giant Galaxies in Clusters: Constraints on Feedback Models. *ApJ*, 851(1):66, Dec. 2017. doi: 10.3847/1538-4357/aa9af3.

Z. Huang and C. L. Sarazin. A High-Resolution ROSAT X-Ray Study of Abell 4059. *ApJ*, 496(2):728–736, Mar. 1998. doi: 10.1086/305406.

D. S. Hudson, R. Mittal, T. H. Reiprich, P. E. J. Nulsen, H. Andernach, and C. L. Sarazin. What is a cool-core cluster? a detailed analysis of the cores of the X-ray flux-limited HIFLUGCS cluster sample. *A&A*, 513:A37, Apr. 2010. doi: 10.1051/0004-6361/200912377.

Y. Ichinohe and S. Yamada. Neural network-based anomaly detection for high-resolution X-ray spectroscopy. *MNRAS*, 487(2):2874–2880, Aug. 2019. doi: 10.1093/mnras/stz1528.

Y. Ichinohe, S. Yamada, N. Miyazaki, and S. Saito. Neural network-based preprocessing to estimate the parameters of the X-ray emission of a single-temperature thermal plasma. *MNRAS*, 475(4):4739–4744, Apr. 2018. doi: 10.1093/mnras/sty161.

S. Ioffe and C. Szegedy. Batch normalization: Accelerating deep network training by reducing internal covariate shift. In *ICML'15: Proceedings of the 32nd International Conference on International Conference on Machine Learning*, ICML'15, page 448–456. JMLR.org, 2015.

J. A. Irwin, A. E. Athey, and J. N. Bregman. X-Ray Spectral Properties of Low-Mass X-Ray Binaries in Nearby Galaxies. *ApJ*, 587(1):356–366, Apr. 2003. doi: 10.1086/368179.

F. Jansen, D. Lumb, B. Altieri, J. Clavel, M. Ehle, C. Erd, C. Gabriel, M. Guainazzi, P. Gondoin, R. Much, R. Munoz, M. Santos, N. Schartel, D. Texier, and G. Vacanti. XMM-Newton observatory. I. The spacecraft and operations. *A&A*, 365:L1–L6, Jan. 2001. doi: 10.1051/0004-6361:20000036.

J. B. Jensen, J. L. Tonry, B. J. Barris, R. I. Thompson, M. C. Liu, M. J. Rieke, E. A. Ajhar, and J. P. Blakeslee. Measuring Distances and Probing the Unresolved Stellar Populations of Galaxies Using Infrared Surface Brightness Fluctuations. *ApJ*, 583(2):712–726, Feb. 2003. doi: 10.1086/345430.

J. Ji, J. A. Irwin, A. Athey, J. N. Bregman, and E. J. Lloyd-Davies. Elemental Abundances in the X-Ray Gas of Early-Type Galaxies with XMM-Newton and Chandra Observations. *ApJ*, 696(2):2252–2268, May 2009. doi: 10.1088/0004-637X/696/2/2252.

R. M. Johnstone, S. W. Allen, A. C. Fabian, and J. S. Sanders. Chandra observations of abell 2199. *Monthly Notices of the Royal Astronomical Society*, 336(1):299–308, 10 2002. ISSN 0035-8711. doi: 10.1046/j.1365-8711.2002.05743.x. URL `https://doi.org/10.1046/j.1365-8711.2002.05743.x`.

C. Jones, W. Forman, A. Vikhlinin, M. Markevitch, L. David, A. Warmflash, S. Murray, and P. E. J. Nulsen. Chandra Observations of NGC 4636-an Elliptical Galaxy in Turmoil. *ApJ Lett.*, 567(2):L115–L118, Mar. 2002. doi: 10.1086/340114.

W. A. Joye and E. Mandel. New Features of SAOImage DS9. In H. E. Payne, R. I. Jedrzejewski, and R. N. Hook, editors, *Astronomical Data Analysis Software and Systems XII*, volume 295 of *Astronomical Society of the Pacific Conference Series*, page 489, Jan. 2003.

J. S. Kaastra and J. A. M. Bleeker. Optimal binning of X-ray spectra and response matrix design. *A&A*, 587:A151, Mar. 2016. doi: 10.1051/0004-6361/201527395.

J. S. Kaastra, R. Mewe, and H. Nieuwenhuijzen. SPEX: a new code for spectral analysis of X & UV spectra. In K. Yamashita and T. Watanabe, editors, *UV and X-ray Spectroscopy of Astrophysical and Laboratory Plasmas*, pages 411–414, Jan. 1996.

J. S. Kaastra, T. Tamura, J. R. Peterson, J. A. M. Bleeker, C. Ferrigno, S. M. Kahn, F. B. S. Paerels, R. Piffaretti, G. Branduardi-Raymont, and H. Böhringer. Spatially resolved X-ray spectroscopy of cooling clusters of galaxies. *A&A*, 413:415–439, Jan. 2004. doi: 10.1051/0004-6361:20031512.

J. S. Kaastra, J. de Plaa, L. Gu, et al. Spex: X-ray spectral fitting package, 2022. URL `https://doi.org/10.5281/zenodo.7037609`.

J. S. Kaastra, A. J. J. Raassen, J. de Plaa, and L. Gu. SPEX X-ray spectral fitting package, Mar. 2024.

E. Kellogg, H. Gursky, C. Leong, E. Schreier, H. Tananbaum, and R. Giacconi. X-Ray Observations of the Virgo Cluster, NGC 5128, and 3c 273 from the UHURU Satellite. *ApJ Lett.*, 165:L49, Apr. 1971. doi: 10.1086/180714.

B. C. Kelly. Some Aspects of Measurement Error in Linear Regression of Astronomical Data. *ApJ*, 665(2):1489–1506, Aug. 2007. doi: 10.1086/519947.

M. G. Kendall. A new measure of rank correlation. *Biometrika*, 30(1/2):81–93, 1938. ISSN 00063444. URL `http://www.jstor.org/stable/2332226`.

D.-W. Kim, C. Anderson, D. Burke, R. D'Abrusco, G. Fabbiano, A. Fruscione, J. Lauer, M. McCollough, D. Morgan, A. Mossman, E. O'Sullivan, A. Paggi, S. Vrtilek, and G. Trinchieri. Chandra Early-type Galaxy Atlas. *ApJS*, 241(2): 36, Apr. 2019. doi: 10.3847/1538-4365/ab0ca4.

D. P. Kingma and J. Ba. Adam: A Method for Stochastic Optimization. *arXiv e-prints*, art. arXiv:1412.6980, Dec. 2014.

C. C. Kirkpatrick, M. Gitti, K. W. Cavagnolo, B. R. McNamara, L. P. David, P. E. J. Nulsen, and M. W. Wise. Direct Evidence for Outflow of Metal-Enriched Gas Along the Radio Jets of Hydra A. *ApJ Lett.*, 707(1):L69–L72, Dec. 2009. doi: 10.1088/0004-637X/707/1/L69.

K. Kolokythas, E. O'Sullivan, S. Raychaudhury, S. Giacintucci, M. Gitti, and A. Babul. The Complete Local-volume Groups Sample - II. A study of the central radio galaxies in the high-richness sub-sample. *MNRAS*, 481(2):1550–1577, Dec. 2018. doi: 10.1093/mnras/sty2030.

J. Kormendy and L. C. Ho. Coevolution (Or Not) of Supermassive Black Holes and Host Galaxies. *ARA&A*, 51(1): 511–653, Aug. 2013. doi: 10.1146/annurev-astro-082708-101811.

M. Kosiba, M. Lieu, B. Altieri, N. Clerc, L. Faccioli, S. Kendrew, I. Valtchanov, T. Sadibekova, M. Pierre, F. Hroch, N. Werner, L. Burget, C. Garrel, E. Koulouridis, E. Gaynullina, M. Molham, M. E. Ramos-Ceja, and A. Khalikova. Multiwavelength classification of X-ray selected galaxy cluster candidates using convolutional neural networks. *MNRAS*, 496(4):4141–4153, Aug. 2020. doi: 10.1093/mnras/staa1723.

R. P. Kraft, C. Jones, P. E. J. Nulsen, and M. J. Hardcastle. The Complex X-Ray Morphology of NGC 7618: A Major Group-Group Merger in the Local Universe? *ApJ*, 640(2):762–767, Apr. 2006. doi: 10.1086/500123.

R. P. Kraft, E. Roediger, M. Machacek, W. R. Forman, P. E. J. Nulsen, C. Jones, E. Churazov, S. Randall, Y. Su, and A. Sheardown. Stripped Elliptical Galaxies as Probes of ICM Physics. III. Deep Chandra Observations of NGC 4552: Measuring the Viscosity of the Intracluster Medium. *ApJ*, 848(1):27, Oct. 2017. doi: 10.3847/1538-4357/aa8a6e.

K. Lakhchaura, N. Werner, M. Sun, R. E. A. Canning, M. Gaspari, S. W. Allen, T. Connor, M. Donahue, and C. Sarazin. Thermodynamic properties, multiphase gas, and AGN feedback in a large sample of giant ellipticals. *MNRAS*, 481(4):4472–4504, Dec. 2018. doi: 10.1093/mnras/sty2565.

K. Lakhchaura, F. Mernier, and N. Werner. Possible depletion of metals into dust grains in the core of the Centaurus cluster of galaxies. *A&A*, 623:A17, Mar. 2019a. doi: 10.1051/0004-6361/201834755.

K. Lakhchaura, N. Truong, and N. Werner. Correlations between supermassive black holes, hot atmospheres, and the total masses of early-type galaxies. *MNRAS*, 488(1):L134–L142, Sept. 2019b. doi: 10.1093/mnrasl/slz114.

D. V. Lal, R. P. Kraft, S. W. Randall, W. R. Forman, P. E. J. Nulsen, E. Roediger, J. A. ZuHone, M. J. Hardcastle, C. Jones, and J. H. Croston. Gas Sloshing and Radio Galaxy Dynamics in the Core of the 3C 449 Group. *ApJ*, 764(1):83, Feb. 2013. doi: 10.1088/0004-637X/764/1/83.

L. Landau and E. Lifshitz. *Fluid Mechanics*, chapter IX. Pergamon Press, 1959.

S. M. Lea, R. Mushotzky, and S. S. Holt. Einstein Observatory solid state spectrometer observations of M87 and the Virgo cluster. *ApJ*, 262:24–32, Nov. 1982. doi: 10.1086/160392.

K. Levenberg. A method for the solution of certain non-linear problems in least squares. *Quarterly of applied mathematics*, 2(2):164–168, 1944.

Y. Li, Y. Su, and C. Jones. X-ray cavities in the hot corona of the lenticular galaxy NGC 4477. *MNRAS*, 480(4): 4279–4286, Nov. 2018. doi: 10.1093/mnras/sty2125.

A. Liu, M. Zhai, and P. Tozzi. On the origin of central abundance drops in the intracluster medium of galaxy groups and clusters. *Monthly Notices of the Royal Astronomical Society*, 485(2):1651–1664, 02 2019. ISSN 0035-8711. doi: 10.1093/mnras/stz533. URL `https://doi.org/10.1093/mnras/stz533`.

K. Lodders. Solar System Abundances and Condensation Temperatures of the Elements. *ApJ*, 591(2):1220–1247, July 2003. doi: 10.1086/375492.

K. Lodders, H. Palme, and H. P. Gail. Abundances of the Elements in the Solar System. *Landolt Börnstein*, 4B:712, Jan. 2009. doi: 10.1007/978-3-540-88055-4_34.

I. Lonoce, A. Feldmeier-Krause, and W. L. Freedman. The stellar initial mass function and population properties of m89 from optical and nir spectroscopy: Addressing biases in spectral index analysis*. *ApJ*, 920(2):93, oct 2021. doi: 10.3847/1538-4357/ac11f9. URL https://dx.doi.org/10.3847/1538-4357/ac11f9.

Z. Ma, J. Zhu, W. Li, and H. Xu. An Approach to Detect Cavities in X-Ray Astronomical Images Using Granular Convolutional Neural Networks. *IEICE Transactions on Information and Systems*, 100(10):2578–2586, Jan. 2017. doi: 10.1587/transinf.2017EDP7079.

M. Machacek, A. Dosaj, W. Forman, C. Jones, M. Markevitch, A. Vikhlinin, A. Warmflash, and R. Kraft. Infall of the Elliptical Galaxy NGC 1404 into the Fornax Cluster. *ApJ*, 621(2):663–672, Mar. 2005. doi: 10.1086/427548.

M. Machacek, C. Jones, W. R. Forman, and P. Nulsen. Chandra Observations of Gas Stripping in the elliptical galaxy ngc 4552 in the virgo Cluster. *ApJ*, 644(1):155–166, Jun 2006. ISSN 1538-4357. doi: 10.1086/503350. URL http://dx.doi.org/10.1086/503350.

M. Machacek, P. E. J. Nulsen, C. Jones, and W. R. Forman. Chandra Observations of Nuclear Outflows in the Elliptical Galaxy NGC 4552 in the Virgo Cluster. *ApJ*, 648(2):947–955, Sept. 2006. doi: 10.1086/505963.

M. E. Machacek, E. O'Sullivan, S. W. Randall, C. Jones, and W. R. Forman. The Mysterious Merger of NGC 6868 and NGC 6861 in the Telescopium Group. *ApJ*, 711(2):1316–1332, Mar. 2010. doi: 10.1088/0004-637X/711/2/1316.

P. Madau and M. Dickinson. Cosmic star-formation history. *ARA&A*, 52(1):415–486, 2014. doi: 10.1146/annurev-astro-081811-125615. URL https://doi.org/10.1146/annurev-astro-081811-125615.

R. A. Main, B. R. McNamara, P. E. J. Nulsen, H. R. Russell, and A. N. Vantyghem. A relationship between halo mass, cooling, active galactic nuclei heating and the co-evolution of massive black holes. *MNRAS*, 464(4):4360–4382, Feb. 2017. doi: 10.1093/mnras/stw2644.

D. Makarov, P. Prugniel, N. Terekhova, H. Courtois, and I. Vauglin. HyperLEDA. III. The catalogue of extragalactic distances. *A&A*, 570:A13, Oct. 2014. doi: 10.1051/0004-6361/201423496.

M. Markevitch and A. Vikhlinin. Shocks and cold fronts in galaxy clusters. *Physics Reports*, 443(1):1–53, May 2007. doi: 10.1016/j.physrep.2007.01.001.

I. Martín-Navarro, J. N. Burchett, and M. Mezcua. Black hole feedback and the evolution of massive early-type galaxies. *MNRAS*, 491(1):1311–1319, Jan. 2020. doi: 10.1093/mnras/stz3073.

W. G. Mathews. Interstellar Events in Elliptical Galaxies. *ApJ*, 354:468, May 1990. doi: 10.1086/168708.

W. G. Mathews and F. Brighenti. Hot Gas in and around Elliptical Galaxies. *ARA&A*, 41:191–239, Jan. 2003. doi: 10.1146/annurev.astro.41.090401.094542.

K. Matsushita, H. Böhringer, I. Takahashi, and Y. Ikebe. The abundance pattern of O, Mg, Si, and Fe in the intracluster medium of the Centaurus cluster observed with XMM-Newton. *A&A*, 462(3):953–963, Feb. 2007. doi: 10.1051/0004-6361:20041577.

L. D. Matthews and M. J. Reid. Very Large Array Observations of H I in the Circumstellar Envelopes of Asymptotic Giant Branch Stars. *AJ*, 133(5):2291–2309, May 2007. doi: 10.1086/512613.

M. McCourt, P. Sharma, E. Quataert, and I. J. Parrish. Thermal instability in gravitationally stratified plasmas: implications for multiphase structure in clusters and galaxy haloes. *MNRAS*, 419(4):3319–3337, Feb. 2012. doi: 10.1111/j.1365-2966.2011.19972.x.

R. M. McDermid, E. Emsellem, K. L. Shapiro, R. Bacon, M. Bureau, M. Cappellari, R. L. Davies, T. De Zeeuw, J. Falcón-Barroso, D. Krajnović, H. Kuntschner, R. F. Peletier, and M. Sarzi. The SAURON project – VIII. OASIS/CFHT integral-field spectroscopy of elliptical and lenticular galaxy centres*. *MNRAS*, 373(3):906–958, 11 2006. ISSN 0035-8711. doi: 10.1111/j.1365-2966.2006.11065.x. URL https://doi.org/10.1111/j.1365-2966.2006.11065.x.

M. McDonald, B. R. McNamara, M. S. Calzadilla, C.-T. Chen, M. Gaspari, R. C. Hickox, E. Kara, and I. Korchagin. Observational Evidence for Enhanced Black Hole Accretion in Giant Elliptical Galaxies. *ApJ*, 908(1):85, Feb. 2021. doi: 10.3847/1538-4357/abd47f.

J. P. McMullin, B. Waters, D. Schiebel, W. Young, and K. Golap. CASA Architecture and Applications. In R. A. Shaw, F. Hill, and D. J. Bell, editors, *Astronomical Data Analysis Software and Systems XVI*, volume 376 of *Astronomical Society of the Pacific Conference Series*, page 127, Oct. 2007.

B. R. McNamara and P. E. J. Nulsen. Heating Hot Atmospheres with Active Galactic Nuclei. *ARA&A*, 45(1):117–175, Sept. 2007. doi: 10.1146/annurev.astro.45.051806.110625.

B. R. McNamara and P. E. J. Nulsen. Mechanical feedback from active galactic nuclei in galaxies, groups and clusters. *New Journal of Physics*, 14(5):055023, May 2012. doi: 10.1088/1367-2630/14/5/055023.

B. R. McNamara, M. Wise, P. E. J. Nulsen, L. P. David, C. L. Sarazin, M. Bautz, M. Markevitch, A. Vikhlinin, W. R. Forman, C. Jones, and D. E. Harris. Chandra X-Ray Observations of the Hydra A Cluster: An Interaction between the Radio Source and the X-Ray-emitting Gas. *ApJ Lett.*, 534(2):L135–L138, May 2000a. doi: 10.1086/312662.

B. R. McNamara, M. W. Wise, L. P. David, P. E. J. Nulsen, and C. L. Sarazin. New Perspectives on Cooling Flows and Cluster Radio Sources. In F. Durret and D. Gerbal, editors, *Constructing the Universe with Clusters of Galaxies*, page 6.6, Jan. 2000b.

B. R. McNamara, M. W. Wise, P. E. J. Nulsen, L. P. David, C. L. Carilli, C. L. Sarazin, C. P. O'Dea, J. Houck, M. Donahue, S. Baum, M. Voit, R. W. O'Connell, and A. Koekemoer. Discovery of Ghost Cavities in the X-Ray Atmosphere of Abell 2597. *ApJ Lett.*, 562(2):L149–L152, Dec. 2001. doi: 10.1086/338326.

B. R. McNamara, P. E. J. Nulsen, M. W. Wise, D. A. Rafferty, C. Carilli, C. L. Sarazin, and E. L. Blanton. The heating of gas in a galaxy cluster by X-ray cavities and large-scale shock fronts. *Nature*, 433(7021):45–47, Jan. 2005. doi: 10.1038/nature03202.

B. R. McNamara, M. Rohanizadegan, and P. E. J. Nulsen. Are Radio Active Galactic Nuclei Powered by Accretion or Black Hole Spin? *ApJ*, 727(1):39, Jan. 2011. doi: 10.1088/0004-637X/727/1/39.

P. J. Mendygral, S. M. O'Neill, and T. W. Jones. Synthetic Observations of Simulated Active Galactic Nucleus Jets: X-ray Cavities. *ApJ*, 730(2):100, Apr. 2011. doi: 10.1088/0004-637X/730/2/100.

P. J. Mendygral, T. W. Jones, and K. Dolag. MHD Simulations of Active Galactic Nucleus Jets in a Dynamic Galaxy Cluster Medium. *ApJ*, 750(2):166, May 2012. doi: 10.1088/0004-637X/750/2/166.

Mernier, de Plaa, J., Lovisari, L., Pinto, C., Zhang, Y.-Y., Kaastra, J. S., Werner, N., and Simionescu, A. Abundance and temperature distributions in the hot intra-cluster gas of abell9. *A&A*, 575:A37, 2015a. doi: 10.1051/0004-6361/201425282. URL https://doi.org/10.1051/0004-6361/201425282.

F. Mernier and V. Biffi. Chemical enrichment in groups and clusters. *arXiv e-prints*, art. arXiv:2202.07097, Feb. 2022.

F. Mernier, J. de Plaa, L. Lovisari, C. Pinto, Y. Y. Zhang, J. S. Kaastra, N. Werner, and A. Simionescu. Abundance and temperature distributions in the hot intra-cluster gas of Abell 4059. *A&A*, 575:A37, Mar. 2015b. doi: 10.1051/0004-6361/201425282.

F. Mernier, J. de Plaa, C. Pinto, J. S. Kaastra, P. Kosec, Y. Y. Zhang, J. Mao, and N. Werner. Origin of central abundances in the hot intra-cluster medium. I. Individual and average abundance ratios from XMM-Newton EPIC. *A&A*, 592:A157, Aug. 2016. doi: 10.1051/0004-6361/201527824.

F. Mernier, J. de Plaa, J. S. Kaastra, Y. Y. Zhang, H. Akamatsu, L. Gu, P. Kosec, J. Mao, C. Pinto, T. H. Reiprich, J. S. Sanders, A. Simionescu, and N. Werner. Radial metal abundance profiles in the intra-cluster medium of cool-core galaxy clusters, groups, and ellipticals. *A&A*, 603:A80, July 2017. doi: 10.1051/0004-6361/201630075.

F. Mernier, V. Biffi, H. Yamaguchi, P. Medvedev, A. Simionescu, S. Ettori, N. Werner, J. S. Kaastra, J. de Plaa, and L. Gu. Enrichment of the Hot Intracluster Medium: Observations. *Space Sci. Rev.*, 214(8):129, Dec. 2018a. doi: 10.1007/s11214-018-0565-7.

F. Mernier, J. de Plaa, N. Werner, J. S. Kaastra, A. J. J. Raassen, L. Gu, J. Mao, I. Urdampilleta, N. Truong, and A. Simionescu. Mass-invariance of the iron enrichment in the hot haloes of massive ellipticals, groups, and clusters of galaxies. *MNRAS*, 478(1):L116–L121, July 2018b. doi: 10.1093/mnrasl/sly080.

F. Mernier, N. Werner, J. de Plaa, J. S. Kaastra, A. J. J. Raassen, L. Gu, J. Mao, I. Urdampilleta, and A. Simionescu. Solar chemical composition in the hot gas of cool-core ellipticals, groups, and clusters of galaxies. *MNRAS: Letters*, 480(1):L95–L100, 07 2018. ISSN 1745-3925. doi: 10.1093/mnrasl/sly134. URL https://doi.org/10.1093/mnrasl/sly134.

F. Mernier, N. Werner, K. Lakhchaura, J. de Plaa, L. Gu, J. S. Kaastra, J. Mao, A. Simionescu, and I. Urdampilleta. How do atomic code uncertainties affect abundance measurements in the intracluster medium? *Astronomische Nachrichten*, 341(2):203–209, Feb. 2020. doi: 10.1002/asna.202023779.

F. Mernier, N. Werner, Y. Su, C. Pinto, R. Grossová, A. Simionescu, E. Iodice, M. Sarzi, and A. Görgei. The cycle of metals in the infalling elliptical galaxy NGC1404. *MNRAS*, 511(3):3159–3178, 01 2022. ISSN 0035-8711. doi: 10.1093/mnras/stac253. URL https://doi.org/10.1093/mnras/stac253.

F. Mernier, K. Fukushima, A. Simionescu, M. Kondo, A. Majumder, T. Plšek, N. Werner, Y. Fujita, K. Sato, K. Matsushita, M. Loewenstein, R. Mushotzky, J.-P. Breuer, R. Fujimoto, Y. Fukazawa, I. Hatsukade, K. Nakazawa, M. Urata, and N. Yamasaki. Chemical composition and enrichment of the Centaurus cluster core seen by XRISM/Resolve. *arXiv e-prints*, art. arXiv:2512.11028, Dec. 2025. doi: 10.48550/arXiv.2512.11028.

E. T. Million, S. W. Allen, N. Werner, and G. B. Taylor. Ram-pressure stripping of the cool core of the ophiuchus cluster. *Monthly Notices of the Royal Astronomical Society*, 405(3):1624–1633, 06 2010. ISSN 0035-8711. doi: 10.1111/j.1365-2966.2010.16596.x. URL https://doi.org/10.1111/j.1365-2966.2010.16596.x.

H. Miraghaei, H. G. Khosroshahi, H. R. Klöckner, T. J. Ponman, N. N. Jetha, and S. Raychaudhury. IGM heating in fossil galaxy groups. *MNRAS*, 444(1):651–666, Oct. 2014. doi: 10.1093/mnras/stu1323.

R. J. Mitchell, J. L. Culhane, P. J. N. Davison, and J. C. Ives. Ariel 5 observations of the X-ray spectrum of the Perseus cluster. *MNRAS*, 175:29P–34P, May 1976. doi: 10.1093/mnras/175.1.29P.

J. S. Mulchaey. X-ray Properties of Groups of Galaxies. *ARA&A*, 38:289–335, Jan. 2000. doi: 10.1146/annurev.astro.38.1.289.

R. F. Mushotzky and M. Loewenstein. Lack of Evolution in the Iron Abundance in Clusters of Galaxies and Implications for the Global Star Formation Rate at High Redshift. *ApJ Lett.*, 481(2):L63–L66, June 1997. doi: 10.1086/310651.

R. F. Mushotzky, P. J. Serlemitsos, B. W. Smith, E. A. Boldt, and S. S. Holt. OSO 8 X-ray spectra of clusters of galaxies. I. Observations of twenty clusters: physical correlations. *ApJ*, 225:21–39, Oct. 1978. doi: 10.1086/156465.

R. F. Mushotzky, S. S. Holt, E. A. Boldt, P. J. Serlemitsos, and B. W. Smith. Observation of the core of the Perseus cluster with the Einstein solid state spectrometer - Cooling gas and elemental abundances. *ApJ Lett.*, 244:L47–L51, Mar. 1981. doi: 10.1086/183477.

K. Nomoto, C. Kobayashi, and N. Tominaga. Nucleosynthesis in stars and the chemical enrichment of galaxies. *ARA&A*, 51(1):457–509, 2013. doi: 10.1146/annurev-astro-082812-140956. URL https://doi.org/10.1146/annurev-astro-082812-140956.

P. Nulsen, C. Jones, W. Forman, E. Churazov, B. McNamara, L. David, and S. Murray. Radio Mode Outbursts in Giant Elliptical Galaxies. In S. Heinz and E. Wilcots, editors, *The Monster's Fiery Breath: Feedback in Galaxies, Groups, and Clusters*, volume 1201 of *American Institute of Physics Conference Series*, pages 198–201, Dec. 2009. doi: 10.1063/1.3293033.

P. E. J. Nulsen. Thermal instability in cooling flows. *MNRAS*, 221:377–392, July 1986. doi: 10.1093/mnras/221.2.377.

P. E. J. Nulsen, D. C. Hambrick, B. R. McNamara, D. Rafferty, L. Birzan, M. W. Wise, and L. P. David. The Powerful Outburst in Hercules A. *ApJ Lett.*, 625(1):L9–L12, May 2005. doi: 10.1086/430945.

A. Ogorzalek, I. Zhuravleva, S. W. Allen, C. Pinto, N. Werner, A. B. Mantz, R. E. A. Canning, A. C. Fabian, J. S. Kaastra, and J. de Plaa. Improved measurements of turbulence in the hot gaseous atmospheres of nearby giant elliptical galaxies. *MNRAS*, 472(2):1659–1676, Dec. 2017. doi: 10.1093/mnras/stx2030.

J. Orlowski-Scherer, S. K. Haridas, L. Di Mascolo, K. Perez Sarmiento, C. E. Romero, S. Dicker, T. Mroczkowski, T. Bhandarkar, E. Churazov, T. E Clarke, M. Devlin, M. Gaspari, I. Lowe, B. Mason, C. L. Sarazin, J. Sievers, and R. Sunyaev. GBT/MUSTANG-2 9" resolution imaging of the SZ effect in MS0735.6+7421: Confirmation of the SZ Cavities through direct imaging. *arXiv e-prints*, art. arXiv:2207.07100, July 2022.

E. O'Sullivan, D. M. Worrall, M. Birkinshaw, G. Trinchieri, A. Wolter, A. Zezas, and S. Giacintucci. Interaction between the intergalactic medium and central radio source in the NGC 4261 group of galaxies. *MNRAS*, 416(4): 2916–2931, Oct. 2011. doi: 10.1111/j.1365-2966.2011.19239.x.

A. Paggi, G. Fabbiano, D.-W. Kim, S. Pellegrini, F. Civano, J. Strader, and B. Luo. Active Galactic Nucleus Feedback in the Hot Halo of NGC 4649. *ApJ*, 787(2):134, June 2014. doi: 10.1088/0004-637X/787/2/134.

E. K. Panagoulia, A. C. Fabian, J. S. Sanders, and J. Hlavacek-Larrondo. A volume-limited sample of X-ray galaxy groups and clusters - II. X-ray cavity dynamics. *MNRAS*, 444(2):1236–1259, Oct. 2014. doi: 10.1093/mnras/stu1499.

E. K. Panagoulia, J. S. Sanders, and A. C. Fabian. A volume-limited sample of X-ray galaxy groups and clusters - III. Central abundance drops. *Monthly Notices of the Royal Astronomical Society*, 447:417–437, 2015. doi: 10.1093/mnras/stu2469.

M. B. Pandge, S. S. Sonkamble, V. Parekh, P. Dabhade, A. Parmar, M. K. Patil, and S. Raychaudhury. AGN Feedback in Galaxy Groups: A Detailed Study of X-Ray Features and Diffuse Radio Emission in IC 1262. *ApJ*, 870(2):62, Jan. 2019. doi: 10.3847/1538-4357/aaf105.

M. B. Pandge, B. Sebastian, R. Seth, and S. Raychaudhury. A detailed study of X-ray cavities in the intracluster environment of the cool core cluster Abell 3017. *MNRAS*, 504(2):1644–1656, June 2021. doi: 10.1093/mnras/stab384.

V. Parekh, F. Durret, P. Padmanabh, and M. B. Pandge. A hot X-ray filament associated with A3017 galaxy cluster. *MNRAS*, 470(3):3742–3749, Sept. 2017. doi: 10.1093/mnras/stx1457.

J. R. Parriott and J. N. Bregman. Mass loss from evolved stars in elliptical galaxies. *ApJ*, 681(2):1215, jul 2008. doi: 10.1086/588033. URL `https://dx.doi.org/10.1086/588033`.

F. Pedregosa, G. Varoquaux, A. Gramfort, V. Michel, B. Thirion, O. Grisel, M. Blondel, P. Prettenhofer, R. Weiss, V. Dubourg, J. Vanderplas, A. Passos, D. Cournapeau, M. Brucher, M. Perrot, and E. Duchesnay. Scikit-learn: Machine learning in Python. *Journal of Machine Learning Research*, 12:2825–2830, 2011.

R. Perley, P. Napier, J. Jackson, B. Butler, B. Carlson, D. Fort, P. Dewdney, B. Clark, R. Hayward, S. Durand, M. Revnell, and M. McKinnon. The Expanded Very Large Array. *IEEE Proceedings*, 97(8):1448–1462, Aug. 2009. doi: 10.1109/JPROC.2009.2015470.

R. A. Perley, C. J. Chandler, B. J. Butler, and J. M. Wrobel. The Expanded Very Large Array: A New Telescope for New Science. *ApJ Lett.*, 739(1):L1, Sept. 2011. doi: 10.1088/2041-8205/739/1/L1.

J. R. Peterson and A. C. Fabian. X-ray spectroscopy of cooling clusters. *Physics Reports*, 427(1):1–39, Apr. 2006. doi: 10.1016/j.physrep.2005.12.007.

J. R. Peterson, F. B. S. Paerels, J. S. Kaastra, M. Arnaud, T. H. Reiprich, A. C. Fabian, R. F. Mushotzky, J. G. Jernigan, and I. Sakelliou. X-ray imaging-spectroscopy of Abell 1835. *A&A*, 365:L104–L109, Jan. 2001. doi: 10.1051/0004-6361:20000021.

L. Petrov. The Wide-field VLBA Calibrator Survey: WFCS. *AJ*, 161(1):14, Jan. 2021. doi: 10.3847/1538-3881/abc4e1.

T. Plšek, N. Werner, M. Topinka, and A. Simionescu. CAvity DEtection Tool (CADET): pipeline for detection of X-ray cavities in hot galactic and cluster atmospheres. *MNRAS*, 527(2):3315–3346, Jan. 2024. doi: 10.1093/mnras/stad3371.

T. Plšek, N. Werner, R. Grossová, M. Topinka, A. Simionescu, and S. W. Allen. The relation between accretion rate and jet power in early-type galaxies with thermally unstable hot atmospheres. *Monthly Notices of the Royal Astronomical Society*, 09 2022. ISSN 0035-8711. doi: 10.1093/mnras/stac2770. URL `https://doi.org/10.1093/mnras/stac2770`. stac2770.

T. J. Ponman, A. J. R. Sanderson, and A. Finoguenov. The Birmingham-CfA cluster scaling project - III. Entropy and similarity in galaxy systems. *MNRAS*, 343(1):331–342, July 2003. doi: 10.1046/j.1365-8711.2003.06677.x.

D. A. Rafferty, B. R. McNamara, P. E. J. Nulsen, and M. W. Wise. The Feedback-regulated Growth of Black Holes and Bulges through Gas Accretion and Starbursts in Cluster Central Dominant Galaxies. *ApJ*, 652(1):216–231, Nov. 2006. doi: 10.1086/507672.

D. A. Rafferty, L. Bîrzan, P. E. J. Nulsen, B. R. McNamara, W. N. Brandt, M. W. Wise, and H. J. A. Röttgering. A deep Chandra observation of the active galactic nucleus outburst and merger in Hickson compact group 62. *MNRAS*, 428(1):58–70, Jan. 2013. doi: 10.1093/mnras/sts007.

S. W. Randall, P. E. J. Nulsen, C. Jones, W. R. Forman, E. Bulbul, T. E. Clarke, R. Kraft, E. L. Blanton, L. David, N. Werner, M. Sun, M. Donahue, S. Giacintucci, and A. Simionescu. A Very Deep Chandra Observation of the Galaxy Group NGC 5813: AGN Shocks, Feedback, and Outburst History. *ApJ*, 805(2):112, June 2015. doi: 10.1088/0004-637X/805/2/112.

A. Renzini and S. Andreon. Chemical evolution on the scale of clusters of galaxies: a conundrum? *MNRAS*, 444(4):3581–3591, 09 2014. ISSN 0035-8711. doi: 10.1093/mnras/stu1689. URL `https://doi.org/10.1093/mnras/stu1689`.

E. Roediger, R. P. Kraft, P. E. J. Nulsen, W. R. Forman, M. Machacek, S. Randall, C. Jones, E. Churazov, and R. Kokotanekova. STRIPPED ELLIPTICAL GALAXIES AS PROBES OF ICM PHYSICS. i. TAILS, WAKES, AND FLOW PATTERNS IN AND AROUND STRIPPED ELLIPTICALS. *ApJ*, 806(1):103, jun 2015a. doi: 10.1088/0004-637x/806/1/103. URL `https://doi.org/10.1088/0004-637x/806/1/103`.

E. Roediger, R. P. Kraft, P. E. J. Nulsen, W. R. Forman, M. Machacek, S. Randall, C. Jones, E. Churazov, and R. Kokotanekova. STRIPPED ELLIPTICAL GALAXIES AS PROBES OF ICM PHYSICS. II. STIRRED, BUT MIXED? VISCOUS AND INVISCID GAS STRIPPING OF THE VIRGO ELLIPTICAL m89. *ApJ*, 806(1):104, jun 2015b. doi: 10.1088/0004-637x/806/1/104. URL `https://doi.org/10.1088/0004-637x/806/1/104`.

H. R. Russell, J. S. Sanders, and A. C. Fabian. Direct X-ray spectral deprojection of galaxy clusters. *MNRAS*, 390(3):1207–1216, Nov. 2008. doi: 10.1111/j.1365-2966.2008.13823.x.

H. R. Russell, B. R. McNamara, A. C. Edge, M. T. Hogan, R. A. Main, and A. N. Vantyghem. Radiative efficiency, variability and Bondi accretion on to massive black holes: the transition from radio AGN to quasars in brightest cluster galaxies. *MNRAS*, 432(1):530–553, June 2013. doi: 10.1093/mnras/stt490.

H. R. Russell, A. C. Fabian, B. R. McNamara, and A. E. Broderick. Inside the Bondi radius of M87. *MNRAS*, 451(1):588–600, July 2015. doi: 10.1093/mnras/stv954.

H. R. Russell, A. C. Fabian, B. R. McNamara, J. M. Miller, P. E. J. Nulsen, J. M. Piotrowska, and C. S. Reynolds. The imprints of AGN feedback within a supermassive black hole's sphere of influence. *MNRAS*, 477(3):3583–3599, July 2018. doi: 10.1093/mnras/sty835.

P. A. Russell, T. J. Ponman, and A. J. R. Sanderson. Bayesian modelling of the cool core galaxy group NGC 4325. *MNRAS*, 378(4):1217–1228, July 2007. doi: 10.1111/j.1365-2966.2007.11660.x.

R. P. Saglia, M. Opitsch, P. Erwin, J. Thomas, A. Beifiori, M. Fabricius, X. Mazzalay, N. Nowak, S. P. Rusli, and R. Bender. The SINFONI Black Hole Survey: The Black Hole Fundamental Plane Revisited and the Paths of (Co)evolution of Supermassive Black Holes and Bulges. *ApJ*, 818(1):47, Feb. 2016. doi: 10.3847/0004-637X/818/1/47.

E. E. Salpeter. The Luminosity Function and Stellar Evolution. *ApJ*, 121:161, Jan. 1955. doi: 10.1086/145971.

J. S. Sanders and A. C. Fabian. Spatially resolved x-ray spectroscopy of the core of the centaurus cluster. *Monthly Notices of the Royal Astronomical Society*, 331(2):273–283, 03 2002. ISSN 0035-8711. doi: 10.1046/j.1365-8711.2002.05211.x. URL https://doi.org/10.1046/j.1365-8711.2002.05211.x.

J. S. Sanders and A. C. Fabian. Resonance scattering, absorption and off-centre abundance peaks in clusters of galaxies. *MNRAS*, 370(1):63–73, July 2006. doi: 10.1111/j.1365-2966.2006.10497.x.

J. S. Sanders and A. C. Fabian. A deeper X-ray study of the core of the Perseus galaxy cluster: the power of sound waves and the distribution of metals and cosmic rays. *MNRAS*, 381(4):1381–1399, Nov. 2007. doi: 10.1111/j.1365-2966.2007.12347.x.

J. S. Sanders, A. C. Fabian, and R. J. H. Dunn. Non-thermal X-rays, a high-abundance ridge and fossil bubbles in the core of the Perseus cluster of galaxies. *MNRAS*, 360(1):133–140, June 2005. doi: 10.1111/j.1365-2966.2005.09016.x.

J. S. Sanders, A. C. Fabian, K. A. Frank, J. R. Peterson, and H. R. Russell. Deep high-resolution X-ray spectra from cool-core clusters. *MNRAS*, 402(1):127–144, Feb. 2010. doi: 10.1111/j.1365-2966.2009.15902.x.

J. S. Sanders, A. C. Fabian, G. B. Taylor, H. R. Russell, K. M. Blundell, R. E. A. Canning, J. Hlavacek-Larrondo, S. A. Walker, and C. K. Grimes. A very deep Chandra view of metals, sloshing and feedback in the Centaurus cluster of galaxies. *MNRAS*, 457(1):82–109, Mar. 2016. doi: 10.1093/mnras/stv2972.

C. L. Sarazin. X-ray emission from clusters of galaxies. *Reviews of Modern Physics*, 58(1):1–115, Jan. 1986. doi: 10.1103/RevModPhys.58.1.

G. Schellenberger, J. M. Vrtilek, L. David, E. O'Sullivan, S. Giacintucci, M. Johnston-Hollitt, S. W. Duchesne, and S. Raychaudhury. NGC 741—Mergers and AGN Feedback on a Galaxy-group Scale. *ApJ*, 845(1):84, Aug. 2017. doi: 10.3847/1538-4357/aa7f2e.

G. Schellenberger, L. P. David, J. Vrtilek, E. O'Sullivan, S. Giacintucci, W. Forman, C. Jones, and T. Venturi. A New Feedback Cycle in the Archetypal Cooling Flow Group NGC 5044. *ApJ*, 906(1):16, Jan. 2021. doi: 10.3847/1538-4357/abc488.

S. Schindler, W. Kapferer, W. Domainko, M. Mair, E. van Kampen, T. Kronberger, S. Kimeswenger, M. Ruffert, O. Mangete, and D. Breitschwerdt. Metal enrichment processes in the intra-cluster medium. *A&A*, 435(2):L25–L28, May 2005. doi: 10.1051/0004-6361:200500107.

R. W. Schmidt, A. C. Fabian, and J. S. Sanders. Chandra temperature and metallicity maps of the Perseus cluster core. *MNRAS*, 337(1):71–78, Nov. 2002. doi: 10.1046/j.1365-8711.2002.05804.x.

K. M. Schure, D. Kosenko, J. S. Kaastra, R. Keppens, and J. Vink. A new radiative cooling curve based on an up-to-date plasma emission code. *A&A*, 508(2):751–757, Dec. 2009. doi: 10.1051/0004-6361/200912495.

J. Secká. Určování výkonů jetů v obřích eliptických galaxiích [online]. https://is.muni.cz/th/rnxoz/, 2018.

I. R. Seitenzahl, F. Ciaraldi-Schoolmann, F. K. Röpke, M. Fink, W. Hillebrandt, M. Kromer, R. Pakmor, A. J. Ruiter, S. A. Sim, and S. Taubenberger. Three-dimensional delayed-detonation models with nucleosynthesis for Type Ia supernovae. *MNRAS*, 429(2):1156–1172, 12 2013. ISSN 0035-8711. doi: 10.1093/mnras/sts402. URL `https://doi.org/10.1093/mnras/sts402`.

P. J. Serlemitsos, B. W. Smith, E. A. Boldt, S. S. Holt, and J. H. Swank. X-radiation from clusters of galaxies: spectral evidence for a hot evolved gas. *ApJ Lett.*, 211:L63–L66, Jan. 1977. doi: 10.1086/182342.

J. L. Sérsic. Influence of the atmospheric and instrumental dispersion on the brightness distribution in a galaxy. *Boletin de la Asociacion Argentina de Astronomia La Plata Argentina*, 6:41–43, Feb. 1963.

P. Sharma, M. McCourt, I. J. Parrish, and E. Quataert. On the structure of hot gas in haloes: implications for the L_X-T_X relation and missing baryons. *MNRAS*, 427(2):1219–1228, Dec. 2012. doi: 10.1111/j.1365-2966.2012.22050.x.

I. Shilon, M. Kraus, M. Büchele, K. Egberts, T. Fischer, T. L. Holch, T. Lohse, U. Schwanke, C. Steppa, and S. Funk. Application of deep learning methods to analysis of imaging atmospheric Cherenkov telescopes data. *Astroparticle Physics*, 105:44–53, Feb. 2019. doi: 10.1016/j.astropartphys.2018.10.003.

J. Shin, J.-H. Woo, and J. S. Mulchaey. A Systematic Search for X-Ray Cavities in Galaxy Clusters, Groups, and Elliptical Galaxies. *ApJS*, 227(2):31, Dec. 2016. doi: 10.3847/1538-4365/227/2/31.

A. Siemiginowska, V. Kashyap, B. Refsdal, D. van Dyk, A. Connors, and T. Park. pyblocxs: Bayesian Low-Counts X-ray Spectral Analysis in Sherpa. In I. N. Evans, A. Accomazzi, D. J. Mink, and A. H. Rots, editors, *Astronomical Data Analysis Software and Systems XX*, volume 442 of *Astronomical Society of the Pacific Conference Series*, page 439, July 2011.

A. Simionescu, N. Werner, A. Finoguenov, H. Böhringer, and M. Brüggen. Metal-rich multi-phase gas in M 87. AGN-driven metal transport, magnetic-field supported multi-temperature gas, and constraints on non-thermal emission observed with XMM-Newton. *A&A*, 482(1):97–112, Apr. 2008. doi: 10.1051/0004-6361:20078749.

A. Simionescu, N. Werner, H. Böhringer, J. S. Kaastra, A. Finoguenov, M. Brüggen, and P. E. J. Nulsen. Chemical enrichment in the cluster of galaxies Hydra A. *A&A*, 493(2):409–424, Jan. 2009. doi: 10.1051/0004-6361:200810225.

A. Simionescu, S. Nakashima, H. Yamaguchi, K. Matsushita, F. Mernier, N. Werner, T. Tamura, K. Nomoto, J. de Plaa, S.-C. Leung, A. Bamba, E. Bulbul, M. E. Eckart, Y. Ezoe, A. C. Fabian, Y. Fukazawa, L. Gu, Y. Ichinohe, M. N. Ishigaki, J. S. Kaastra, C. Kilbourne, T. Kitayama, M. Leutenegger, M. Loewenstein, Y. Maeda, E. D. Miller, R. F. Mushotzky, H. Noda, C. Pinto, F. S. Porter, S. Safi-Harb, K. Sato, T. Takahashi, S. Ueda, and S. Zha. Constraints on the chemical enrichment history of the Perseus Cluster of galaxies from high-resolution X-ray spectroscopy. *MNRAS*, 483(2):1701–1721, Feb. 2019. doi: 10.1093/mnras/sty3220.

R. K. Smith, N. S. Brickhouse, D. A. Liedahl, and J. C. Raymond. Collisional Plasma Models with APEC/APED: Emission-Line Diagnostics of Hydrogen-like and Helium-like Ions. *ApJ Lett.*, 556(2):L91–L95, Aug. 2001. doi: 10.1086/322992.

Y. Sofue. Giant Explosion at the Galactic Center and Huge Shocked Shells in the Halo. *ApJ Lett.*, 431:L91, Aug. 1994. doi: 10.1086/187480.

Y. Su and J. A. Irwin. Investigating the Potential Dilution of the Metal Content of Hot Gas in Early-type Galaxies by Accreted Cold Gas. *ApJ*, 766(1):61, Mar. 2013. doi: 10.1088/0004-637X/766/1/61.

Y. Su, J. A. Irwin, I. White, Raymond E., and M. C. Cooper. The Scatter in the Hot Gas Content of Early-type Galaxies. *ApJ*, 806(2):156, June 2015. doi: 10.1088/0004-637X/806/2/156.

Y. Su, R. P. Kraft, E. Roediger, P. Nulsen, W. R. Forman, E. Churazov, S. W. Randall, C. Jones, and M. E. Machacek. Deep chandra observations of ngc 1404: Cluster plasma physics revealed by an infalling early-type galaxy. *ApJ*, 834(1):74, jan 2017. doi: 10.3847/1538-4357/834/1/74. URL `https://dx.doi.org/10.3847/1538-4357/834/1/74`.

C. Szegedy, W. Liu, Y. Jia, P. Sermanet, S. Reed, D. Anguelov, D. Erhan, V. Vanhoucke, and A. Rabinovich. Going deeper with convolutions. In *2015 IEEE Conference on Computer Vision and Pattern Recognition (CVPR)*, pages 1–9, 2015. doi: 10.1109/CVPR.2015.7298594.

P. Temi, A. Amblard, M. Gitti, F. Brighenti, M. Gaspari, W. G. Mathews, and L. David. ALMA Observations of Molecular Clouds in Three Group-centered Elliptical Galaxies: NGC 5846, NGC 4636, and NGC 5044. *ApJ*, 858(1):17, May 2018. doi: 10.3847/1538-4357/aab9b0.

P. Temi, M. Gaspari, F. Brighenti, N. Werner, R. Grossova, M. Gitti, M. Sun, A. Amblard, and A. Simionescu. Probing multiphase gas in local massive elliptical galaxies via multiwavelength observations. *ApJ*, 928(2):150, apr 2022. doi: 10.3847/1538-4357/ac5036. URL https://dx.doi.org/10.3847/1538-4357/ac5036.

G. Theureau, M. O. Hanski, N. Coudreau, N. Hallet, and J. M. Martin. Kinematics of the Local Universe. XIII. 21-cm line measurements of 452 galaxies with the Nançay radiotelescope, JHK Tully-Fisher relation, and preliminary maps of the peculiar velocity field. *A&A*, 465(1):71–85, Apr. 2007. doi: 10.1051/0004-6361:20066187.

D. Thomas, C. Maraston, K. Schawinski, M. Sarzi, and J. Silk. Environment and self-regulation in galaxy formation. *MNRAS*, 404(4):1775–1789, 05 2010. ISSN 0035-8711. doi: 10.1111/j.1365-2966.2010.16427.x. URL https://doi.org/10.1111/j.1365-2966.2010.16427.x.

J. Thomas, C.-P. Ma, N. J. McConnell, J. E. Greene, J. P. Blakeslee, and R. Janish. A 17-billion-solar-mass black hole in a group galaxy with a diffuse core. *Nature*, 532(7599):340–342, Apr. 2016. doi: 10.1038/nature17197.

S. J. Tingay and P. G. Edwards. The multifrequency parsec-scale structure of PKS 2254-367 (IC 1459): a luminosity-dependent break in morphology for the precursors of radio galaxies? *MNRAS*, 448(1):252–257, Mar. 2015. doi: 10.1093/mnras/stu2756.

N. Truong, E. Rasia, V. Biffi, F. Mernier, N. Werner, M. Gaspari, S. Borgani, S. Planelles, D. Fabjan, and G. Murante. Mass-metallicity relation from cosmological hydrodynamical simulations and X-ray observations of galaxy groups and clusters. *MNRAS*, 484(2):2896–2913, Apr. 2019. doi: 10.1093/mnras/stz161.

N. Truong, A. Pillepich, and N. Werner. Correlations between supermassive black holes and hot gas atmospheres in IllustrisTNG and X-ray observations. *MNRAS*, 501(2):2210–2230, Feb. 2021. doi: 10.1093/mnras/staa3880.

R. B. Tully, H. M. Courtois, A. E. Dolphin, J. R. Fisher, P. Héraudeau, B. A. Jacobs, I. D. Karachentsev, D. Makarov, L. Makarova, S. Mitronova, L. Rizzi, E. J. Shaya, J. G. Sorce, and P.-F. Wu. Cosmicflows-2: The Data. *AJ*, 146(4):86, Oct. 2013. doi: 10.1088/0004-6256/146/4/86.

F. Ubertosi, M. Gitti, F. Brighenti, G. Brunetti, M. McDonald, P. Nulsen, B. McNamara, S. Randall, W. Forman, M. Donahue, A. Ignesti, M. Gaspari, S. Ettori, L. Feretti, E. L. Blanton, C. Jones, and M. Calzadilla. The Deepest Chandra View of RBS 797: Evidence for Two Pairs of Equidistant X-ray Cavities. *ApJ Lett.*, 923(2):L25, Dec. 2021. doi: 10.3847/2041-8213/ac374c.

F. Ubertosi, F. Brighenti, E. O'Sullivan, G. Schellenberger, M. Gitti, S. Giacintucci, P. Temi, L. P. David, J. Vrtilek, T. Venturi, E. Liuzzo, M. Massardi, and K. Rajpurohit. Multiphase Gas Offsets in the Atmospheres of Central Galaxies and Their Consequences for SMBH Activation. I. The Hot and Warm Ionized Gas Phases. *ApJ*, 994(2):247, Dec. 2025. doi: 10.3847/1538-4357/ae1013.

O. Urban, N. Werner, S. W. Allen, A. Simionescu, and A. Mantz. A uniform metallicity in the outskirts of massive, nearby galaxy clusters. *MNRAS*, 470(4):4583–4599, 06 2017. ISSN 0035-8711. doi: 10.1093/mnras/stx1542. URL https://doi.org/10.1093/mnras/stx1542.

A. N. Vantyghem, B. R. McNamara, H. R. Russell, R. A. Main, P. E. J. Nulsen, M. W. Wise, H. Hoekstra, and M. Gitti. Cycling of the powerful AGN in MS 0735.6+7421 and the duty cycle of radio AGN in clusters. *MNRAS*, 442(4):3192–3205, Aug. 2014. doi: 10.1093/mnras/stu1030.

G. M. Voit. Tracing cosmic evolution with clusters of galaxies. *Reviews of Modern Physics*, 77(1):207–258, Apr. 2005. doi: 10.1103/RevModPhys.77.207.

G. M. Voit and M. Donahue. The Fate of Stellar Mass Loss in Central Cluster Galaxies. *ApJ Lett.*, 738(2):L24, Sept. 2011. doi: 10.1088/2041-8205/738/2/L24.

G. M. Voit and M. Donahue. Cooling Time, Freefall Time, and Precipitation in the Cores of ACCEPT Galaxy Clusters. *ApJ Lett.*, 799(1):L1, Jan. 2015. doi: 10.1088/2041-8205/799/1/L1.

L. Štofanová, A. Simionescu, and J. S. Kaastra. The clus model in SPEX: Projection and resonant scattering effects on the iron abundance and temperature profiles of galaxy clusters. *A&A*, 694:A149, Feb. 2025. doi: 10.1051/0004-6361/202451431.

M. C. Weisskopf, B. Brinkman, C. Canizares, G. Garmire, S. Murray, and L. P. Van Speybroeck. An Overview of the Performance and Scientific Results from the Chandra X-Ray Observatory. *PASP*, 114(791):1–24, Jan. 2002. doi: 10.1086/338108.

N. Werner and F. Mernier. *Hot Atmospheres of Galaxies, Groups, and Clusters of Galaxies*, pages 279–310. Springer International Publishing, 2020. doi: 10.1007/978-3-030-38509-5_10.

N. Werner, J. de Plaa, J. S. Kaastra, J. Vink, J. A. M. Bleeker, T. Tamura, J. R. Peterson, and F. Verbunt. Xmm-newton spectroscopy of the cluster of galaxies 2a 0335+096. *A&A*, 449(2):475–491, 2006. doi: 10.1051/0004-6361:20053868. URL `https://doi.org/10.1051/0004-6361:20053868`.

N. Werner, F. Durret, T. Ohashi, S. Schindler, and R. P. C. Wiersma. Observations of Metals in the Intra-Cluster Medium. *Space Sci. Rev.*, 134(1-4):337–362, Feb. 2008. doi: 10.1007/s11214-008-9320-9.

N. Werner, I. Zhuravleva, E. Churazov, A. Simionescu, S. W. Allen, W. Forman, C. Jones, and J. S. Kaastra. Constraints on turbulent pressure in the X-ray haloes of giant elliptical galaxies from resonant scattering. *MNRAS*, 398(1):23–32, Sept. 2009. doi: 10.1111/j.1365-2966.2009.14860.x.

N. Werner, A. Simionescu, E. T. Million, S. W. Allen, P. E. J. Nulsen, A. von der Linden, S. M. Hansen, H. Böhringer, E. Churazov, A. C. Fabian, W. R. Forman, C. Jones, J. S. Sanders, and G. B. Taylor. Feedback under the microscope-II. Heating, gas uplift and mixing in the nearest cluster core. *MNRAS*, 407(4):2063–2074, Oct. 2010. doi: 10.1111/j.1365-2966.2010.16755.x.

N. Werner, O. Urban, A. Simionescu, and S. W. Allen. A uniform metal distribution in the intergalactic medium of the perseus cluster of galaxies. *Nature*, 502(7473):656–658, Oct 2013. ISSN 1476-4687. doi: 10.1038/nature12646. URL `https://doi.org/10.1038/nature12646`.

N. Werner, B. R. McNamara, E. Churazov, and E. Scannapieco. Hot Atmospheres, Cold Gas, AGN Feedback and the Evolution of Early Type Galaxies: A Topical Perspective. *Space Sci. Rev.*, 215(1):5, Jan. 2019. doi: 10.1007/s11214-018-0571-9.

D. R. Wilkins, S. W. Allen, E. D. Miller, M. Bautz, T. Chattopadhyay, R. Foster, C. E. Grant, S. Herrmann, R. Kraft, R. G. Morris, P. Nulsen, and G. Schellenberger. Reducing the background in x-ray imaging detectors via machine learning. In J.-W. A. den Herder, S. Nikzad, and K. Nakazawa, editors, *Space Telescopes and Instrumentation 2022: Ultraviolet to Gamma Ray*, volume 12181 of *Society of Photo-Optical Instrumentation Engineers (SPIE) Conference Series*, page 121816S, Aug. 2022. doi: 10.1117/12.2629496.

R. Willingale, A. D. P. Hands, R. S. Warwick, S. L. Snowden, and D. N. Burrows. The X-ray spectrum of the North Polar Spur. *MNRAS*, 343(3):995–1001, Aug. 2003. doi: 10.1046/j.1365-8711.2003.06741.x.

R. Willingale, R. L. C. Starling, A. P. Beardmore, N. R. Tanvir, and P. T. O'Brien. Calibration of X-ray absorption in our Galaxy. *MNRAS*, 431(1):394–404, May 2013. doi: 10.1093/mnras/stt175.

A. S. Wilson and Y. Yang. Chandra X-Ray Imaging and Spectroscopy of the M87 Jet and Nucleus. *ApJ*, 568(1):133–140, Mar. 2002. doi: 10.1086/338887.

A. Wójtowicz, Ł. Stawarz, C. C. Cheung, N. Werner, and D. Rudka. Radio Emission of Nearby Early-type Galaxies in the Low and Very Low Radio Luminosity Range. *ApJ*, 944(2):195, Feb. 2023. doi: 10.3847/1538-4357/acb498.

K.-W. Wong, J. A. Irwin, M. Yukita, E. T. Million, W. G. Mathews, and J. N. Bregman. Resolving the Bondi Accretion Flow toward the Supermassive Black Hole of NGC 3115 with Chandra. *ApJ Lett.*, 736:L23, July 2011. doi: 10.1088/2041-8205/736/1/L23.

K.-W. Wong, J. A. Irwin, R. V. Shcherbakov, M. Yukita, E. T. Million, and J. N. Bregman. The Megasecond Chandra X-Ray Visionary Project Observation of NGC 3115: Witnessing the Flow of Hot Gas within the Bondi Radius. *ApJ*, 780:9, Jan. 2014. doi: 10.1088/0004-637X/780/1/9.

C. Wu, O. I. Wong, L. Rudnick, S. S. Shabala, M. J. Alger, J. K. Banfield, C. S. Ong, S. V. White, A. F. Garon, R. P. Norris, H. Andernach, J. Tate, V. Lukic, H. Tang, K. Schawinski, and F. I. Diakogiannis. Radio Galaxy Zoo: CLARAN - a deep learning classifier for radio morphologies. *MNRAS*, 482(1):1211–1230, Jan. 2019. doi: 10.1093/mnras/sty2646.

K. K. S. Wu, A. C. Fabian, and P. E. J. Nulsen. Non-gravitational heating in the hierarchical formation of X-ray clusters. *MNRAS*, 318(3):889–912, Nov. 2000. doi: 10.1046/j.1365-8711.2000.03828.x.

Xrism Collaboration. The bulk motion of gas in the core of the Centaurus galaxy cluster. *Nature*, 638(8050):365–369, Feb. 2025. doi: 10.1038/s41586-024-08561-z.

C. Zhang, E. Churazov, W. R. Forman, and C. Jones. Standoff distance of bow shocks in galaxy clusters as proxy for mach number. *MNRAS*, 482(1):20–29, Sep 2018. ISSN 1365-2966. doi: 10.1093/mnras/sty2501. URL `http://dx.doi.org/10.1093/mnras/sty2501`.

C. Zhang, I. Zhuravleva, A. Heinrich, E. Bellomi, N. Truong, J. ZuHone, E. Churazov, M. E. Eckart, Y. Fujita, J. Hlavacek-Larrondo, Y. Ichinohe, M. Markevitch, K. Matsushita, F. Mernier, E. D. Miller, K. Mori, H. Nakajima, A. Ogorzalek, F. S. Porter, A. Tümer, S. Ueda, and N. Werner. Mapping the Perseus galaxy cluster with XRISM: Gas kinematic features and their implications for turbulence. *A&A*, 707:A109, Mar. 2026. doi: 10.1051/0004-6361/202557660.

X. Zhang, A. Simionescu, H. Akamatsu, J. S. Kaastra, J. de Plaa, and R. J. van Weeren. X-ray study of the merging galaxy cluster Abell 3411-3412 with XMM-Newton and Suzaku. *A&A*, 642:A89, Oct. 2020. doi: 10.1051/0004-6361/202037965.